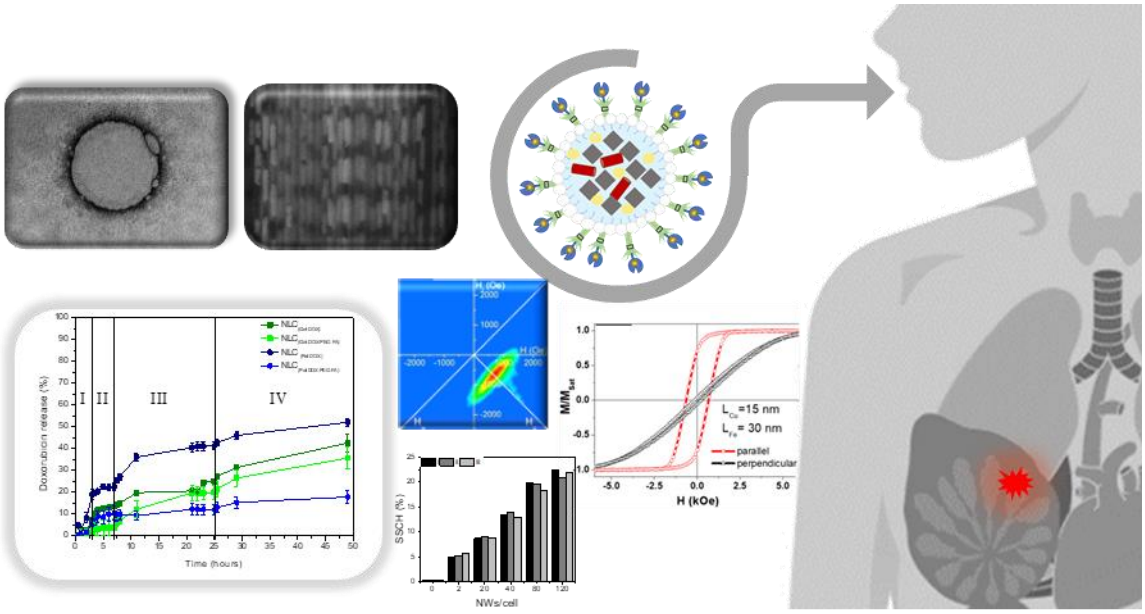

Multimodal Magnetic Lipid Nanocarriers for Cancer Therapies

Suellen Silveira Moraes
Doutoramento em Física
Departamento de Física e Astronomia
2021

Supervisor
Célia Tavares de Sousa, Doutora, FCUP
co-Supervisor
Cláudia Nunes, Doutora, FFUP
co-Supervisor
João Pedro Esteves de Araújo, Professor Doutor, FCUP

Suellen Silveira Moraes

Multimodal Magnetic Lipid Nanocarriers for Cancer Therapies

Supervisor: Doutora Célia Tavares de Sousa

Co-Supervisor: Doutora Cláudia Nunes

Co-Supervisor: Professor Doutor João Pedro Esteves de Araújo

*Thesis submitted to the Faculty of Sciences of the U*niversity of Porto in partial fulfilment of the requirements for the degree *of Doctor in Physics*

Department of Physics and Astronomy

Faculty of Sciences of the University of Porto

2021

Institutions involved in this thesis:

Funding:

This PhD work was supported by Conselho Nacional de Desenvolvimento Científico (CNPq, Brazil) for financial support through the grant No. 234513/2014-4. This work was also supported by the Portuguese Fundação para a Ciência e Tecnologia (FCT) and COMPETE 2020 (FEDER) under the projects: POCI-01-0145-FEDER-031302; POCI-01-0141-FEDER-032527; POCI- 01-0145-FEDER-028676; POCI-01-0145-FEDER-031302; Network of Extreme Conditions Laboratories (NECL)-NORTE-01-0145-FEDER- 022096; and the European Union's Horizon 2020 research and innovation program under the Marie Sklodowska-Curie Grant Agreement No. 734801

To my daughter Lívia and my son Leonardo

To my nieces Luanna and Arianna

my little sunshine

O correr da vida embrulha tudo.
A vida é assim: esquenta e esfria,
aperta e daí afrouxa,
sossega e depois desinquieta.
O que ela quer da gente é coragem

(Guimarães Rosa)

Acknowledgements

Gratidão e empatia deveriam ser palavras-chave nesta tese pois esse é o sentimento que está impregnado em cada página desde documento. Vossa empatia, minha gratidão, sem isso não teria chegado aqui, todos foram verdadeiros gigantes que me carregaram nos ombros nos dias mais sóbrios e me ajudaram a enxergar horizontes verdejantes.

Por isso agradeço…

À Deus, pois sem a fé que deposito em Sua justiça e em Sua bondade não teria forças para superar todos os obstáculos que me foram aparecendo no caminho e a Ele também agradeço ter colocado em minha vida pessoas tão maravilhosas a quem também só devo gratidão.

À Doutora Célia Tavares de Sousa, a quem aprendi a admirar ainda mais sua força, disciplina, conhecimento e amabilidade, expresso o meu profundo agradecimento por essa orientação e apoio incondicional que muito elevaram os meus conhecimentos científicos e que, sem dúvida, muito estimularam o meu desejo de querer saber mais, alimentando uma vontade constante de querer fazer melhor. E reconheço, com gratidão, não só a confiança em mim depositada, desde o início, mas também, o sentido de responsabilidade que me incutiu em todas as fases desse doutoramento.

À Doutora Cláudia Nunes, a pessoa mais alegre, comprometida e empática com quem pude conviver, o meu sincero agradecimento pela co-orientação neste doutoramento. Muito obrigada pelo profissionalismo, pela sincera amizade, pela alegria e simpatia contagiante com que conduziste nossos dias de trabalho e pela total disponibilidade com que sempre me tratou. O seu apoio foi determinante na elaboração desta tese.

Ao Professor Doutor João Pedro Araújo agradeço a co-orientação, o apoio nas apresentações dos congressos e a oportunidade que me deu de integrar no Grupo de Investigação do IFMUP e ainda por me ter proporcionado todas as condições necessárias para a elaboração da minha Tese. Não me esquecendo da eterna simpatia e amizade com que sempre me tratou. Sei que mesmo dos bastidores tens um amável e inteligente toque em tudo que se é produzido, tens esse lugar ingrato de ser onipresente, mas só quem foca nas soluções e não nos problemas é quem o pode ocupar.

À Professora Doutora Salette Reis por permitir a minha integração no Grupo de Investigação da FFUP e por me ter proporcionado as condições necessárias para a

conclusão da nossa pesquisa, o que tornou possível o desenvolvimento de um trabalho verdadeiramente multidisciplinar. Agradeço também a sua simpatia e disponibilidade! Consigo aprendi que a sabedoria das palavras está num olhar e isso basta.

Ao Dr. David Navas, agradeço a simpatia com que sempre me tratou e pela enorme ajuda com as simulações.

À Dra. Sofia Lima, agradeço desde seu exemplo de organização e a proatividade até a enorme paciência que tiveste com meus erros no trabalho com a células e por sempre confiar que eu era capaz (mesmo que isso precisasse ser no ensaio seguinte). Obrigada!

À Dra. Mariana Proença agradeço toda dedicação em nossas colaborações e pelo carinho de sempre.

Aos Professores Klebert Pirota e Fanny Beron, por me receberem na UNICAMP-BRASIL, e colaborarem com nosso trabalho.

À nossa queria Isabel Alves, por todo carinho, alegria e dedicação com que resolve nossos eternos problemas e a Dra. Armanda por toda paciência em tratar das nossas viagens, encomendas e inscrições sempre para ontem.

À Florbela Texeira, pelo carinho com o qual me tratou sempre que a burocracia nos batia a porta. E muito obrigada ainda pela paciência e dedicação.

Ás minhas queridas Maria Armanda Silva e Filomena Dara agradeço todo carinho desde os meus primeiros dias na Universidade do Porto e por essa amizade querida que se perpetua.

À Maria Sant'Ana, por toda dedicação e carinho com que sempre me atendeu na pós-graduação.

Ao Engenheiro Francisco agradeço primeiro a amizade, mas sem sua assistência técnica altamente qualificada, feita ao pormenor não teria as amostras e os resultados aqui apresentados. Ao Engenheiro Fernando obrigada pelo óptimo trabalho com a retificação das células e para disponibilidade e simpatia com que sempre me tratou.

À sete colegas que se tornaram minhas queridas amigas do coração: Andréa Marinho (foste um anjo que de repente se materializou do meu lado num ensaio de release, e muita cumplicidade surgiu a partir desse momento, obrigada por sua amizade genuína), Paula Quitério (a eterna senhora dos fornos, te adoro), Vívian Andrade (mulher, sim senhor, maluca, mas não te devo nada e a pessoa mais meiga que conheci em minha vida, obrigada amiga por sua alegria e disposição de entrar numa briga por mim), Ana Silva (o amor e a doçura em forma de gente, adorei cada momento contigo), Ana Pires (nossa coelhinha quântica do país das maravilhas… sempre a correr e sempre presente, te adoro), Sofia Caspani (obrigada por toda ajuda

quando não pude estar presente, trabalhar contigo foi muito divertido, um dia vamos fazer nosso cemitério de amostras) e Isabel Barbosa (sua amizade foi a pioneira na minha integração ao grupo, és a maior anfitriã de laboratório que conheço, obrigada pelos abraços e sorrisos ao fim do dia). Vossa companhia foi como um repouso para minha alma nos dias conturbados e nunca vou esquece vosso carinho.

À Paula Quitério, agradeço por tudo! Foi um prazer atravessar o oceano contigo que até repetimos. Todos os congressos, todos os momentos como vizinhas de mesa, todas as madrugadas a trabalhar em várias partes do mundo! Literalmente por tudo. És a pessoa mais empática que eu conheço, pois renuncias ao que tens de mais preciso (tempo e saúde) para ajudar as pessoas, todas elas, sem distinção. Adorei ir conhecendo essa caixinha de surpresas que és tu!

Aos Coordenadores do MAP-Fis a oportunidade e o privilégio que tive em frequentar este programa que muito contribuiu para o enriquecimento da minha formação académica e científica e nomeadamente ao professor João Santos agradeço a simpatia e aos inúmeros pareceres.

Ao Departamento de Física e Astronomia, IFIMUP e Universidade do Porto, todos os docentes e não docentes por terem colaborado de alguma forma como facilitadores desse meu percurso até aqui.

A todos os integrantes dos grupos IFIMUP e MB_2, agradeço toda simpatia, amizade e companheirismo e por mostrar, em todos os dias convividos, o quão gratificante é poder trabalhar em um ambiente harmónico onde o respeito e a boa disposição estão sempre presentes. Nomeadamente Ana Rita (MB_2), Adréia Granja (MB_2), Arlete (IFIMUP), Joana Magalhães (MB_2).e Ricardo Magalhães (IFMUP).

Ao Bruno Oliveira, agradeço os dois filhos maravilhosos que vieram junto com esse doutoramento e a toda dedicação e paciência desprendida, por me acalmar nos dias turbulentos e por me inspirar que melhores dias estariam por vir. Agradeço também a cumplicidade e por sempre confiar em mim.

À Margarida Lopes, Paulo Novais e Antônio Barbosa, por toda alegria e carinho com que sempre me trataram em vossa casa. Obrigada por tudo!

Aos meus queridos amigos Laura Castro e Mário Pêgo, minha eterna gratidão por me adotaram como filha do coração e receberem meus filhos como netos da alma e por cuidarem deles quando precisei.

Aos amigos brazucas Bruna, Bruno, Bianca, Vitor, Kelly e Valério, obrigada pelo carinho e pelos dias leves que me proporcionaram.

Às minhas eternas amigas Rosane Castro e Giovanna Parizotto, agradeço toda cumplicidade, que nem a distância consegue destruir.

Aos meus irmãos Anderson Moraes Filho e Suelaine Moraes por todo apoio nos momentos difíceis e pelo carinho de sempre. O amor que une é mais forte que qualquer aventura. Obrigada por esse amor correspondido.

Aos meus filhos Lívia e Leonardo por me proporcionarem as maiores felicidades e motivos para continuar. Só vosso sorriso já é suficiente!

Aos meus pais Anderson Moraes e Suelene Sousa agradeço primeiramente a compreensão com que sempre aceitaram minhas escolhas, mesmo que esta lhes custasse a eterna saudade e preocupação de me ver sair de casa para caminhos tão longe de vossa proteção. Agradeço ainda o amor incondicional, toda renúncia que fizeram para me proporcionar uma vida com maiores possibilidade e todos os exemplos de honestidade, trabalho e amor que me ensinaram mais que qualquer palavra. É a vocês que dedico todas as minhas conquistas.

Obrigada!

Resumo

O cancro é uma das doenças mais letais do mundo. Em particular nas mulheres, o cancro da mama representa 25% do total de casos de cancro. A maior parte das terapias clínicas no combate ao cancro levam a muitos efeitos colaterais, principalmente devido à ação dos fármacos nas células saudáveis e aos mecanismos de resistência aos fármacos. Os nanossistemas multifuncionais são cada vez mais apresentados na literatura como possíveis soluções para tais limitações, pois proporcionam um aumento na eficácia do tratamento, devido ao seu direcionamento local, o que permite uma terapia direcionada e a redução das doses dos fármacos. Adicionalmente, estes sistemas podem possibilitar simultaneamente diagnóstico e terapia. Assim, as nanopartículas multifuncionais são constituídas por diferentes componentes, escolhidos de forma a direcioná-las aos tecidos alvo e aí exercer a sua ação. As nanopartículas multifuncionais são constituídas por um transportador, moléculas localizadas à superfície que possibilitam o seu direcionamento a um alvo, fármacos e/ou outras nanopartículas magnéticas ou plasmónicas, polímeros sensíveis, etc., que atuam como um controlador de libertação ou dispositivo de ablação.

Neste contexto, esta tese teve como principal objetivo o desenvolvimento de nanopartículas multifuncionais utilizando transportadores lipídicos nanoestruturados (NLCs) como agentes de transporte de um fármaco anticancerígeno, no caso a doxorrubicina (DOX) e um núcleo magnético composto por nanofios magnéticos ou nanopartículas superparamagnéticas de óxido de ferro (SPIONs). Estas formulações podem ser usadas como agentes em aplicações polivalentes que podem fornecer simultaneamente imagens de ressonância magnética, administração aprimorada de fármaco, hipertermia magnética e morte celular por ação magneto-mecânica. A superfície das NLCs foi funcionalizada com moléculas conjugadas de ácido fólico e polietilenoglicol (FA-PEG) para aumentar o tempo de circulação dessas nanopartículas e promover a libertação seletiva do fármaco para as células cancerígenas, mesmo por via oral.

Duas formulações distintas de NLCs foram projetadas e otimizadas levando a uma eficiência de encapsulação de mais de 65%. O potencial citotóxico e de direcionamento das NLCs foi estudado *in vitro*, usando a linha celular MDA-MB-231. Os resultados mostraram uma internalização maior das NLCs conjugados com FA-PEG. Estudos de libertação *in vitro* que simulam o trajeto no corpo humano após a administração oral, mostram que todas as formulações poderiam chegar ao microambiente tumoral contendo 50% da DOX encapsulada. Além disso, os NLCs

demonstraram estabilidade de armazenamento a 25 °C por pelo menos 42 dias. Em geral, os resultados revelaram que os NLCs desenvolvidos possibilitam a administração oral e são uma abordagem promissora para a libertação direcionada de DOX nas células do cancro da mama.

Paralelamente, foram fabricados dois tipos de nanoestruturas magnéticas: SPIONs e nanofios. Os SPIONs foram produzidos por um método de co-precipitação por microondas. Estas nanopartículas magnéticas com diâmetro médio de aproximadamente 12 ± 3 nm no estado superparamagnético apresentaram uma taxa de absorção específica (SAR) de 64 W/g para uma frequência de 103 kHz e um campo magnético (H) de 20 mT (200 Oe). Os SPIONs e a DOX foram encapsulados com sucesso nas NLCs que, por sua vez, foram funcionalizadas com FA-PEG. A formulação final mostrou cerca de 277 ± 10 nm de diâmetro médio e boa estabilidade por mais de 10 semanas.

Para desenvolver nanofios magnéticos com dimensões e composição controláveis, foi utilizada uma abordagem de nanofabricação por métodos assistidos por membranas. Primeiro, as membranas anódicas de óxido de alumínio (AAO) foram sintetizadas pelo método de anodização de substratos de alumínio em duas etapas. Posteriormente foi empregue eletrodeposição pulsada usando um único banho para crescer nanofios de Fe/Cu multissegmentados. As camadas de Cu foram utilizadas como camadas removíveis visando uma produção em larga escala de nanofios de Fe com dimensões nanométricas. Este método de fabricação permitiu um estudo sistemático das propriedades magnéticas destas nanoestruturas, alterando as suas dimensões e a distância entre elas. Em primeiro lugar, para estudar as interações magnéticas entre os nanofios de Fe, o comprimento e o diâmetro do segmento de Fe foram mantidos constantes a (30 ± 7) e (45 ± 5) nm, respectivamente, e o comprimento do Cu variou entre (15 ± 5) e (120 ± 10) nm. A influência da variação da espessura da camada não magnética nas propriedades magnéticas dos nanofios foi investigada com medidas das curvas de reversão de primeira ordem (FORC) e simulações micromagnéticas. A nossa análise confirmou que, nos nanofios de Fe/Cu multissegmentados com segmentos de Cu mais curtos, o acoplamento dipolar entre os segmentos de Fe controla o comportamento magnético do nanofio e o seu desempenho é semelhante a um nanofio contínuo de Fe de dimensões semelhantes. Por outro lado, nanofios de Fe/Cu multissegmentados com segmentos de Cu maiores agem como uma matriz de entidades magnéticas sem interação entre elas (ao longo do eixo do nanofio), onde o comportamento global é controlado fundamentalmente pelas interações dipolares entre vizinhos. Os nanofios de Fe e Fe/Au/Fe foram desprendidos da membrana de AAO e utilizados para estudar a sua viabilidade e

internalização celular com diferentes concentrações (de 0 a 120 NWs/célula), por citometria de fluxo. Observou-se que os nanofios foram internalizados nas células até 120 nanofios/célula sem atingir um valor de saturação. Nenhuma das concentrações resultou numa toxicidade celular superior a 15% (viabilidade celular de 85%), o que significa que os nanofios são inócuos, sem campo magnético aplicado.

Palavras-chave: Nanopartículas multifuncionais, nanofios, transportadores lipídicos nanoestruturados, terapia do cancro, entrega controlada de fármaco, hipertermia magnética.

Abstract

Cancer is one of the most lethal diseases in the world. In particular, for women, breast cancer accounts for 25% of all cancer cases. Most clinical cancer-fighting therapies lead to many deleterious side effects mainly due to drugs' distribution to non-target cells and mechanisms of drug resistance. Multifunctional nanosystems are increasingly presented in the literature as possible solutions to such limitations, as they provide an increase in the effectiveness of treatment, owing to their local targeting, which allows a targeted therapy and the reduction of drug doses. Moreover, they may also allow theragnostic. Thus, multi-functional nanoparticles present several agents with specific roles that enable the nanoparticle to reach the target and fight it. In general, multifunctional nanoparticles have a carrier, molecules that bind to the target, drugs and/or other magnetic and plasmonic nanoparticles, sensitive polymers, etc., that act as a release controller or ablation device.

This thesis aimed the design and development of multifunctional nanocarriers using nanostructured lipid carriers (NLCs) as the shell structure to transport the anticancer drug doxorubicin (DOX) and a magnetic core, composed either by magnetic nanowires or superparamagnetic iron oxide nanoparticles, SPIONs. These formulations can be agents to be used in multipurpose applications that can simultaneously provide magnetic resonance images, enhanced drug delivery, magnetic fluidic hyperthermia and magneto-mechanical cell death. The NLCs surface was functionalized with conjugate molecules of folic acid and polyethylene glycol (FA-PEG) to increase the time circulation of these nanoparticles and promote a selective drug delivery to cancer cells, even using oral administration.

Two distinct NLCs formulations were designed and optimized leading to an encapsulation efficiency of more than 65%. Cytotoxic and targeting potential of NLCs were studied *in vitro*, using MDA-MB-231 cell line. Results showed an enhanced cellular uptake of conjugated NLCs with FA-PEG. In vitro release studies mimicking the path in the body after oral administration, show that all formulations would reach the tumor microenvironment bearing 50% of the encapsulated DOX. Moreover, NLCs demonstrated storage stability at 25 °C for at least 42 days. Overall, results revealed that the developed NLCs enable the possibility of oral administration and are a promising approach for the targeted delivery of DOX to breast cancer cells.

In parallel, two types of magnetic nanostructures were fabricated: SPIONs and nanowires. SPIONs were produced by a microwave co-precipitation method. These magnetic nanoparticles with an average diameter of approximately 12 ± 3 nm in a

superparamagnetic state presented a specific absorption rate (SAR) of 64 W/g for a frequency of 103 kHz and a magnetic field (H) of 20 mT (200 Oe). The SPIONs and the DOX were successfully encapsulated in the NLC and functionalized with FA-PEG. The final formulation showed about 277 ± 10 nm of average diameter and good stability for more than 10 weeks.

To develop magnetic nanowires with controllable dimensions and composition, a template assisted nanofabrication approach was used. First, anodic aluminum oxide (AAO) membranes were synthesized by a two-step anodization of aluminum substrates. Then pulsed electrodeposition using a single bath was employed to grow multi-segmented Fe/Cu nanowires. The Cu layers were used as dead layers aiming at a large-scale production of Fe nanowires with nanometric dimensions. This manufacturing method allowed a systematic study of the magnetic properties of these nanostructures by changing their dimensions and the distance between them. First, to study the magnetic interactions between the Fe nanowires, both Fe segment length and diameter were kept constant to (30 ± 7) and (45 ± 5) nm, respectively and Cu length was varied between (15 ± 5) and (120 ± 10) nm. The influence of the non-magnetic layer thickness variation on the nanowire magnetic properties was investigated through first-order reversal curve (FORC) measurements and micromagnetic simulations. Our analysis confirmed that in the multi-segmented Fe/Cu nanowires with shorter Cu segments, the dipolar coupling between Fe segments controls the nanowire magnetic behavior, and its performance is like that of a continuous Fe nanowire array of similar dimensions. On the other hand, multi-segmented Fe/Cu nanowires with larger Cu segments act as a collection of non-interacting magnetic entities (along the nanowire axis), and their global behavior is mainly controlled by the neighbor-to-neighbor dipolar nanostructures interactions. Fe and Fe/Au/Fe nanowires were released from the AAO membrane and used to study their cell viability and uptake, with different concentrations (from 0 to 120 NWs/cell), by flow cytometry. The nanowires were observed to have been internalized up to 120 nanowires/cell without reaching a saturation value. None of the concentrations resulted in cell toxicity higher than 15 % (cell viability of 85%), which means that the nanowires are innocuous, without an applied magnetic field.

Keywords: Multifunctional nanoparticles, nanowires, nanostructured lipid carriers, cancer therapy, drug delivery, magnetic hyperthermia.

Contents

List of Figures

List of Tables

List of Abbreviations and Symbols

AAO, Anodic Alumina Oxide

AMF, alternating magnetic fields

APTES, aminopropyltriethoxysilane

BB, Bragg-Brentano

BSA, bovine serum albumin

BSE, backscattered electrons

CE, Counter electrode

CT, computed tomography

D, Diameter

d_{hkl}, plane spacing

DOX, Doxorubicin

DOX-NLCs, Nanostructured lipid carriers with Doxorubicin

D_{int}, interpore distances

D_{XRD}, Crystallite size

DSPE Disteroylphosphatidylethanolamine

e^{-}, electron

E, Electric field

EE, entrapment efficiency

EDS, Energy dispersive X-ray spectroscopy

FA-PEG, folic acid and polyethylene glycol

FDA, Food and Drug Administration

FES, fetal bovine serum

FC, field-cooled magnetization

FORC, First-order reversal curve
ρFORC, FORC Distribution

FWHM, Full width at half maximum

GS, grain-size

*H*c, coercive fields

HA, hard anodization

HCPA, Hexagonal Cose-Packed Arrays

IONs, iron oxide nanoparticles

IC_{50}, 50% cellular growth inhibitions

j, current density

L, length

LC, loading capacity

MFH, Magnetic fluid hyperthermia

MTT, Methylthiazolyldiphenyl-tetratozium

mr, Reduced remanence

NLCs, Nanostructured lipid carriers

NPs, Nanoparticles

NRs, Nanorods

NWs, Nanowire

NTs, Nanotubes

PEG_{2000}, poly(ethylene glycol)2000

SAR, Specific absorption rate

SEM, Scanning electron microscopy

SSC-H, Height of the side scattered light

SQUID, Superconducting quantum interference device

SPIONs, Superparamagnetic iron oxide nanoparticles

T_C, Curie temperature

T_M, Morin transition

TEM, Transmission electron microscopy

UV, Ultra-violet

V, Voltage

VSM, Vibrating sample magnetometer

w, Full width at half-maximum (FWHM) of Bragg peaks

W, Wall thickness

WE, Working electrode

XPS, X-ray photoelectron spectroscopy

XRD, X-ray diffraction

ZFC-FC, Zero field cooled -field cooled

θ, Diffraction angle

λ, Wavelength of irradiation

ε, Microstrain

δ_b, Oxide barrier layer

υ, Frequency

η, Viscosity

k, Scherrer constant

Thesis Outline

Recent advances in nanotechnology have contributed to the development of multifunctional nanoparticles for biomedical applications. Due to their unique characteristics, including multifunctionality, large surface area, structural diversity and long circulation time in the blood compared to small molecules, nanoparticles have emerged as attractive alternatives for optimized therapies through personalized medicine.

To enable practical applications of nanometric materials, structures consisting of nanoelements with precise and uniform shape and size must be synthesized and functionalized for the specific application and organized in two-dimensional or three-dimensional architectures. In addition, it is of great importance developing nanostructured materials that are structurally and dimensionally controlled, whose physical properties are easier to understand and more receptive to theoretical treatment, because a wide range of material properties critically depends on the size, shape, and regularity of its substructure.

Anodic alumina oxide (AAO) models and standard aluminum sheets with a self-organized hierarchical structure proved to be suitable not only as a template for the preparation of structurally well-controlled nanostructured materials but also as a non-lithographic replication template for the preparation of two-dimensional or three-dimensional matrices of periodic nanostructures such as multi-segmented nanowires prepared by electrodeposition.

The pathway adopted for this work can be divided into three main steps: (i) the first consists in the synthesis and characterization of high aspect ratio nanoparticles namelymulti-segmented nanowires by electrodeposition, using AAO as templates; (ii) in the second part we developed nanostructured lipid carriers for oral delivery; (iii) finally a coordinated effort was made to encapsulate the magnetic core and the drug in the lipid core and functionalize the surface of the multifunctional nanoparticles for potential breast cancer treatment.

This PhD work was developed under the collaboration between the research group of Multifunctional Magnetic Materials and Nanostructures from the Institute of Physics for Advanced Materials, Nanotechnology and Photonics (IFIMUP), at the Faculty of Sciences of the University of Porto (FCUP), led by Prof. João Pedro Araújo, and the

research laboratory LAQV, REQUIMTE at the Faculty of Pharmacy of Porto University, in the research group of Prof. Salette Reis.

This thesis is structured in 6 chapters, comprising an introduction, the experimental techniques, three chapters describing the main results and their discussion, and a final chapter with conclusions and future perspectives.

A brief summary is given:

Chapter 1 - This chapter includes the state-of-the-art regarding the application of nanoparticles to cancer treatment, an overview of the various types of nanoparticles, their advantages, and applications. A review of the magnetic properties of these nanostructures is also presented. The physical-chemical processes involved in the synthesis of electrodeposited nanowires in AAO are referred, as well as the general aspects of lipid nanoparticles, in particular the nanostructured lipid carriers (NLCs) and their advantages in oral administration.

Chapter 2 - In this chapter, it is presented a description of the experimental methods and characterization techniques used. The first section includes the synthesis methods to obtain the diverse nanoparticles, such as nanowires, superparamagnetic iron oxide nanoparticles (SPIONs), or NLCs. In the second section are described the characterization techniques, in particular the morphological, structural, optical, magnetic characterization of the produced nanostructures. Finally, *in vitro* studies and procedures are described.

Chapter 3 – This chapter describes the synthesis of Fe/Cu multi-segmented nanowires (NWs) obtained from electrodeposition in AAO templates, followed by a structural and magnetic characterization, to better understand the main physical properties of these biocompatible nanostructures. To reveal the role of the Cu and Fe segment length in the NW magnetic properties measurements were performed. Micromagnetic simulations were also performed to better understand the magnetic interactions between the Fe nanostructures (this part of this chapter is already published in Moraes, S.; Navas, D.; Béron, F.; Proenca, M.P.; Pirota, K.R.; Sousa, C.T.; Araújo, J.P. The Role of Cu Length on the Magnetic Behaviour of Fe/Cu Multi-Segmented Nanowires. Nanomaterials 2018, 8, 490).

Chapter 4 – In this chapter, we present the doxorubicin (DOX) loaded NLCs preparation by a hot-homogenization process followed by ultrasonication. Studies involving different NLCs matrixes were performed to assess the composition that held

the most convenient physical features as size, zeta potential and encapsulation efficiency are concerned. All parameters were optimized towards NLCs shelf stability and suitable size for oral administration. A conjugate of PEG-FA was synthesized and added to the NLCs formulations to confer active targeting. Thus, this modification showed to allow DOX-NLCs to remain in circulation for longer periods and release the drug into site-specific targets (part of this chapter is already published in Moraes, S., Marinho, A., Lima, S., Granja, A., Araújo, J. P., Reis, S., Sousa,C.T. & Nunes, C. (2020). Targeted nanostructured lipid carriers for doxorubicin oral delivery. International Journal of Pharmaceutics, 592, 120029).

Chapter 5 – In this chapter, we describe the cytotoxic and targeting potential of a new targeted drug delivery system based on functionalized NLCs. The cytotoxicity and cell internalization were also evaluated for several types of magnetic nanostructures and for multifunctional nanostructures after the internalization of the magnetic core in the NLCs (part of this chapter is already published in Moraes, S., Marinho, A., Lima, S., Granja, A., Araújo, J. P., Reis, S., Sousa,C.T. & Nunes, C. (2020). Targeted nanostructured lipid carriers for doxorubicin oral delivery. International Journal of Pharmaceutics, 592, 120029).

Chapter 6 – In this last chapter, the main conclusions and future work are summarized.

Chapter 1

Introduction

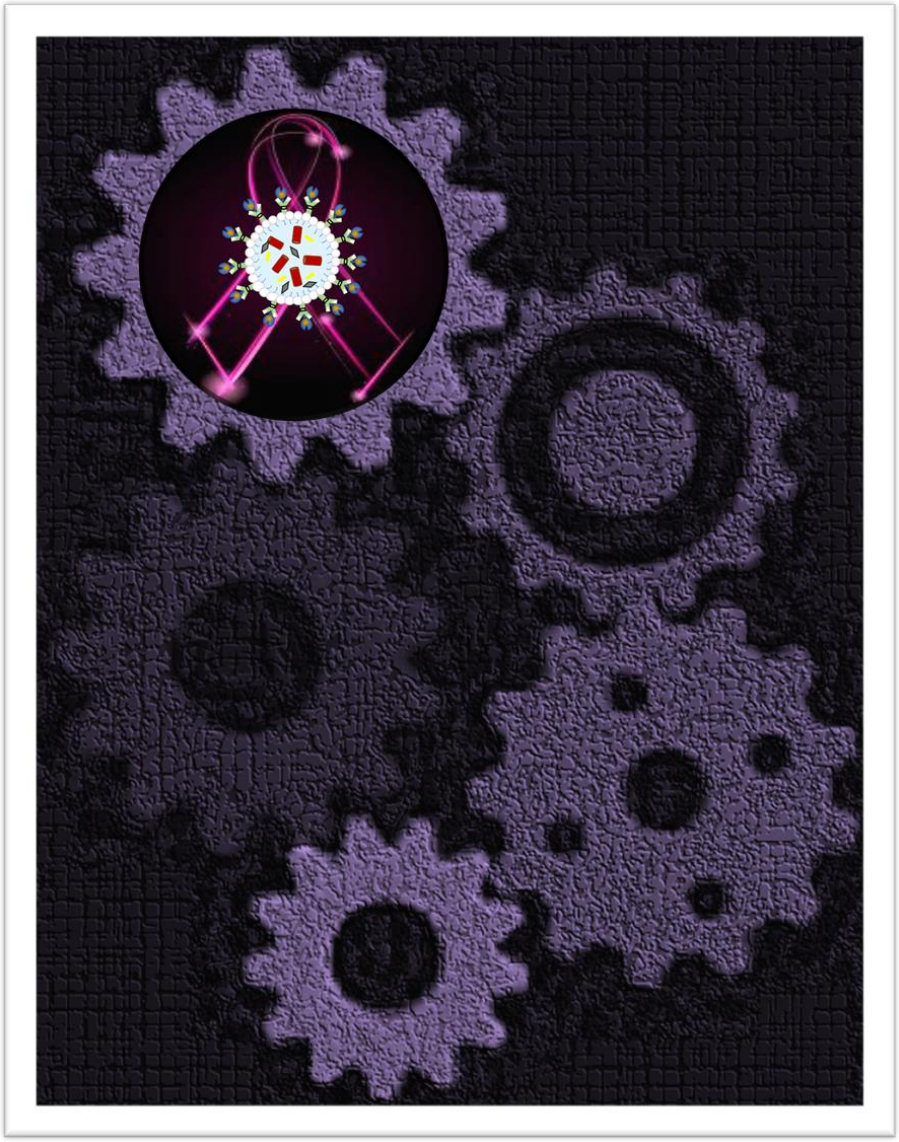

Chapter 1

Introduction

In this chapter, it is presented an overview of the most recent advances in nanotechnology for cancer treatment using different kind of nanoparticles. The main advantages and physical properties of magnetic nanostructures were detailed, particularly focused in the synthesis and characterization of multi-segmented magnetic nanowires by template-assisted electrodeposition method. Finally, the general aspects of lipid nanoparticles are presented, in particular the potential use of nanostructured lipid carriers with encapsulated magnetic nanostructures and chemotherapeutic agents for cancer therapy.

1.1. Nanotechnology in cancer treatment

In this chapter, it is presented an overview of the most recent advances in nanotechnology for cancer treatment using different kind of nanoparticles. The main advantages and physical properties of magnetic nanostructures were detailed, particularly focused in the synthesis and characterization of multi-segmented magnetic nanowires by template-assisted electrodeposition method. Finally, the general aspects of lipid nanoparticles are presented, in particular the potential use of nanostructured lipid carriers with encapsulated magnetic nanostructures and chemotherapeutic agents for cancer therapy.

1.1.1. Drug delivery

The drug delivery concept consists of micro and nanosystems for targeted transportation and local release of drugs [1, 2]. Compared to conventional chemotherapeutic therapies, these delivery systems show less side effects and are capable of targeted delivery of the therapeutic agents based on their ligands [3, 4].

For more than 5 decades, the literature has shown the development of increasingly sophisticated and effective drug delivery systems. Some of these, such as liposomes

[5], polymeric micelles [6], carbon nanotubes [7], solid lipid nanoparticles (SLN) [8], nanostructured lipid carriers (NLC) [9], fullerenes (C60) [10], and magnetic nanoparticles [11], have a particular interest for application in cancer therapy (Fig. 1.1). These nanosystems can be adapted to obtain various biological functionalities and therefore be used in a big range of settings, providing a safer and effective targeted drug delivery [12].

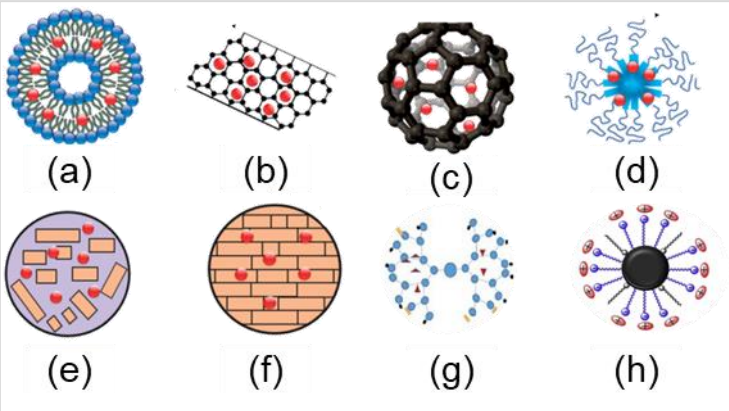

Fig. 1.1: Scheme of drug delivery systems with special interest for application in cancer therapy: (a) liposomes, (b) carbon nanotubes, (c) fullerenes (C60), (d) polymeric micelles, (e) nanostructured lipid carriers, (f) solid lipid nanoparticles, (g) dendrites and (h) magnetic nanoparticles. (adapted from [13]).

Although, tens of thousands reports on the topic of drug carriers for cancer treatment have been published, there is still a gap between technological advances in research and clinical therapies. Figure 1.2 shows a chronological view of the development of some drug delivery systems. In 1965, liposomes were discovered by the group led by Bangham [14], then in 1995, the US Food and Drug Administration (FDA) approved the Doxil, the first liposomal formulation of doxorubicin [15]. In 2005, Abraxane has been approved by FDA for clinical use in the treatment of breast and pancreatic cancer. Abraxane is an albumin-based nanoparticle with protein-bound paclitaxel [16]. After that, with the development of nanomedicine, other nanosystems have been approved for clinical use [17, 18].

Several studies [19-21] demonstrated that nanomaterials have several advantages as drug carriers, such as:

i) improving the pharmacokinetic and pharmacological properties of the drugs once increase water solubility and protect drugs dissolution in the blood stream;

ii) limitation of drug accumulation in non-targeted organs and enhancing therapeutic efficacy in the specific targeted tissue or cell to be treated;

iii) real-time monitoring of drug delivery by combining imaging and therapeutic agents [19].

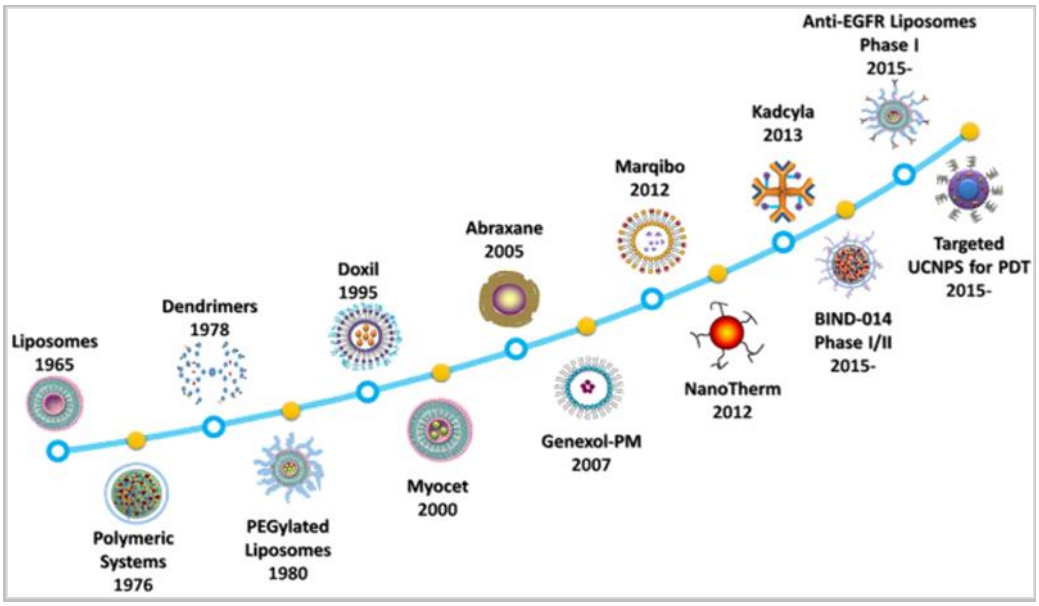

Fig. 1.2: Timeline of the development of drug delivery systems [19].

At the moment, most of the efforts in cancer therapy have been devoted to the efficiency improvement of tumor cells elimination reducing side effects. For that proposal, one of the great tools is the integration of magnetic nanoparticles in the drug delivery systems and use their physical properties as a therapeutic alternative [22]. These magnetic nanoparticles can be also functionalized with cancer specific antibodies or folic acid to improve the treatment specificity [3]. In particular, nanoparticles functionalized with folic acid are successfully recognized by folate receptors and internalized into cells via folate receptor mediated endocytosis, since cell surface receptors for folic acid are overexpressed across a broad spectrum of cancer and inflammatory cells [1].

However, magnetic nanoparticles conjugated with specific drugs have some limitations, e.g., difficult control of drug release and low drug loading capacity. Therefore, for drug delivery applications, magnetic nanoparticles must be pre-coated with substances that assure their stability, biodegradability, high loading and release capability and nontoxicity in the physiological medium combined with the intrinsic properties of the magnetic core (high magnetic saturation, biocompatibility, and interactive functions on the surface) [23].

High-aspect-ratio nanoparticles with enhanced surface area and new physical properties are fertile grounds for scientific research in the next years, leading possible breakthroughs in targeted delivery systems. In particular, polymeric nanotubes and

multisegmented nanowires (NWs) with the possibility of providing double different functionalization are fascinate candidates for these applications [24-27]. Sousa *et al.* [25] demonstrated the functionalization of silica nanotubes (SNTs) fabricated in anodic alumina oxide (AAO) membranes (Fig.1.3). The surface of SNTs was functionalized with aminosilane and their inner voids were used to incorporate a non-steroidal anti-inflammatory drug (NSAIDs), naproxen, by means of an electrostatic interaction (Fig. 1.3 (left)). The system is pH-sensitive and presents an improved drug delivery in the inflammation local where the pH is lower whereas at physiological pH the linkage between the drug and the SNTs is stable (Fig. 1.3 (right)).

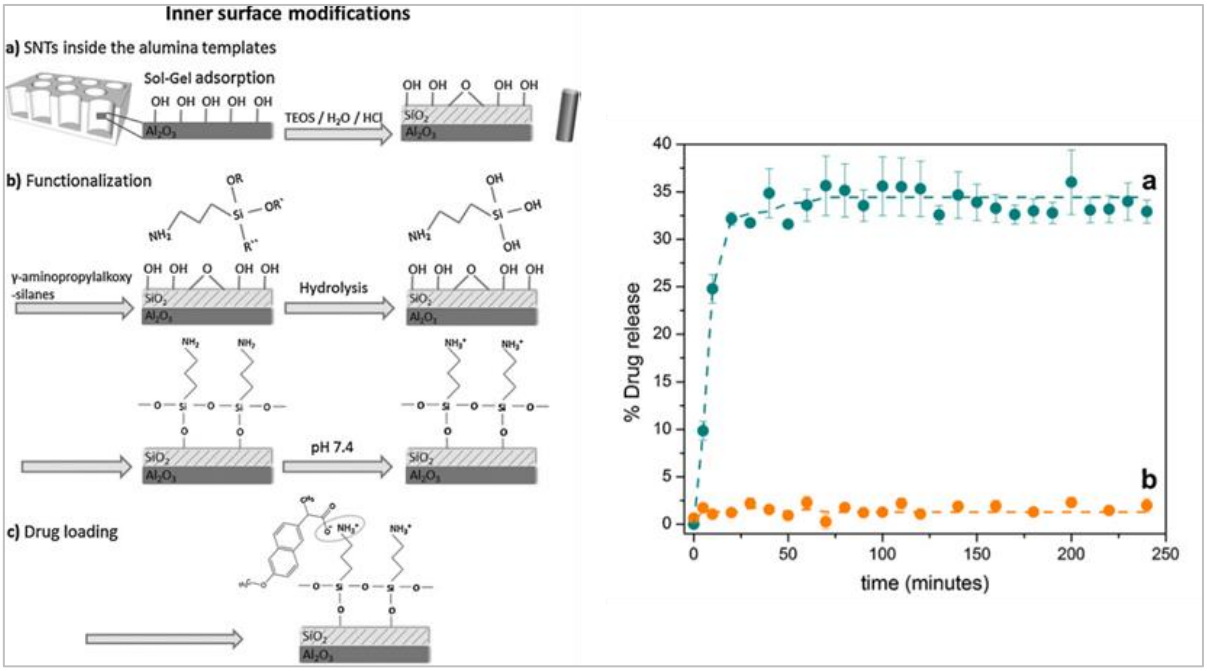

Fig. 1.3: (Left) Schematic representation of: (a) formation of silica nanotubes (SNTs) inside nanoporous alumina templates; (b) SNTs inner surface functionalization and (c) drug loading in the inner voids of SNTs (Right) Release profile of naproxen from the inner voids of silica nanotubes at pH 5.0 (a) and at pH 7.4 (b), assessed by fluorescence measurements. Results are reported as mean ± SD (n = 3) [25].

Özkale *et al.* [27] presented a study about the influence of magnetic tuning on the performance of protein release on demand, three types of NWs, namely, non-magnetic (rich in Cu), totally magnetic (rich in FeCo) and multi-segmented FeCo15nm/Cu15nm (Fig 1.4). An improved release of 83% was achieved fully magnetic FeCo nanowires, where on oscillating magnetic field was applied compared with only 45% for multi-segmented FeCo15nm/Cu15nm nanowires (Fig.1.4), which suggests that the controlled release of the drug can be obtained by taking advantage of the magnetic architecture of the NWs.

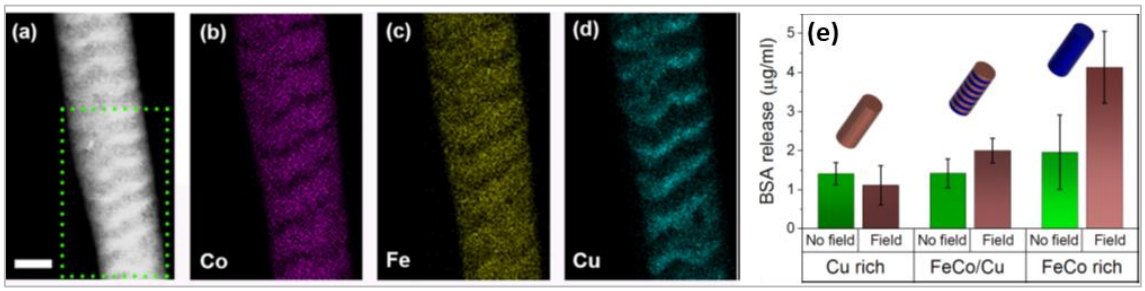

Fig. 1.4: (a) Scanning transmission electron microscopy (STEM) image of a FeCo15nm/Cu15nm multissegmented NWs and the corresponding element distribution EDX (energy dispersive X-ray) mappings for (b) Co, (c) Fe, and (d) Cu. Scale bar corresponds to 50 nm. (e) bovine serum albumin (BSA) release amount for the three studied NW composition is shown. The schematic NWs are for Cu-rich, segmented FeCo15nm/Cu15nm, and FeCo-rich NWs [27].

1.1.2. Photothermal therapy

In recent years, much attention has been paid to photothermal therapy (PTT) for selective treatment of cancer based in thermal ablation by laser radiation. Thermal therapies can be classified into two major subtypes: hyperthermia (or moderate-temperature hyperthermia) and thermal ablation [28]. In hyperthermia, the temperature is raised a few degrees above physiological level (41- 45 ºC) usually during 15 to 60 minutes [28]. Thermal ablation is the use of extreme temperatures (above 45 ºC) for direct damage or destruction of the tumor tissues [28]. Both types of thermal laser therapies finds growing applications in cancer therapy [23, 29]. One of the main drawbacks in laser treatment is the requirement of high-power lasers for the effective stimulation of the tumor cell death, therefore photothermal agents can be used to help the selective heating at the local environment [30]. For this propose is necessary to find biocompatible agents with a large absorption coefficient in the near infrared regions where the absorption of tissues is minimal [23]. Thus, metallic nanoparticles or even semiconducting carbon nanotubes or graphene are examples of materials that can be used since they can be activated by near-infrared light [31]. Some metals, for example gold (Au) or silver (Ag), are promising candidates for several applications in chemistry, physics, and biology owing to their unique properties, such as large optical field enhancements due to the strong scattering and absorption of light [23]. In particular, Au nanoparticles are very photostable, biocompatible and capable to induce cellular damage via thermal effects such as photo hyperthermia [32].

Feng *et al.* [33] developed a hybrid system by capping DOX-loaded hollow mesoporous CuS nanoparticles (HMCuS) with iron oxide nanoparticles (IONs) and coated with polyethylene glycol (PEG) (HMCuS/DOX@ION-PEG) that can be used as either a photothermal or photodynamic agent. The photothermal effect is depicted in Fig. 1.5. where it is represented the temperatures achieved after three min of irradiation by an optical laser of 808 nm for all types of nanoparticles studied, with the highest temperature reached for HMCuS/DOX@ION-PEG. Figure 1.5 (b) revealed that the photothermal effect for HMCuS/DOX@ION-PEG with different concentrations after irradiation by an 808 nm laser; occur in both concentration- and time-dependent manners. In Fig. 1.5 (c) can be observed that the no-laser treated group displayed a sustained-release property along with the time progress and only a small amount of DOX (24.4%) released within 14 h. By contrast, a burst release of DOX occurred with NIR irradiation, indicating an NIR-responsive controlled drug release profile in an impulsive manner.

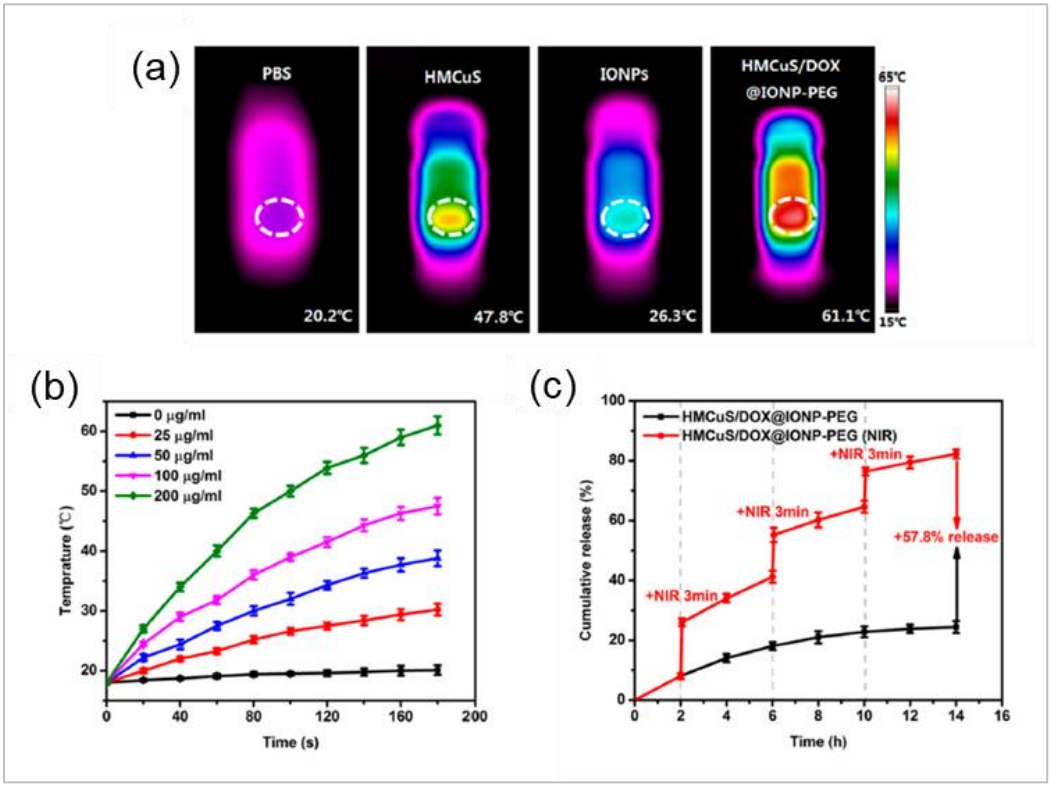

Fig. 1.5: (a) Infra-red (IR) thermal images of tubes with phosphate buffer (PBS), hollow mesoporous CuS nanoparticles (HMCuS), iron oxide nanoparticles (IONs) and HMCuS/DOX@ION-polyethylene glycol (PEG) after irradiation by a 808 nm laser for 3 min; (b) the photothermal heating curves of HMCuS/DOX@ION-PEG with different concentrations after irradiation by an 808 nm laser; (c) release curves of doxorubicin (DOX) from the hybrid system with or without Near infra-red (NIR) irradiation [33].

Martínez-Banderas *et al.* [34] presents results on the development of NWs with an iron core and iron oxide shell of about 3.0 ± 1.2 μm in length, functionalized with an anticancer drug for photothermal therapy. As shown in Fig. 1.6, thermal images of both suspensions of incubated control and NW cells before and during laser irradiation were acquired and temperature profiles were shown in Fig. 1.6 (b). During irradiation, the suspension of cells incubated with NWs reached a temperature of almost 40 °C (Fig. 1.6 (a-IV), which translates to a ΔT of ~20 °C, while the control cells (Fig. 1.6 (a-II)) showed only a slight increase temperature of ~2 °C. This result indicates that cell confinement did not prevent the photothermal efficiency of NWs when a high cell density is used. The core-shell nanostructure presents an improved light-matter interaction in the near infrared region, resulting in a high photothermal conversion efficiency of more than 80% which is in the range of the best Au-based nanomaterials.

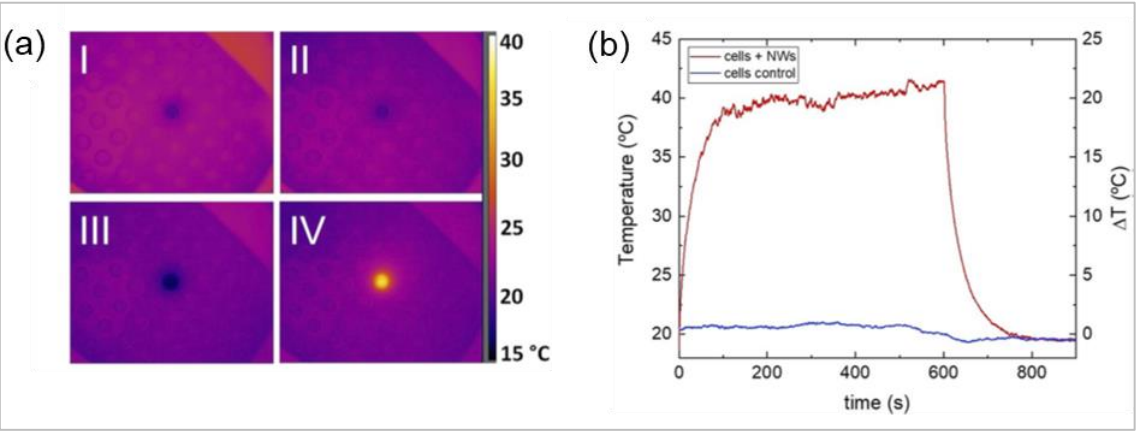

Fig. 1.6: Photothermal effect of BSA coated NWs in breast cancer cells. (a) Thermal images acquired with an infrared camera of a concentrated suspension of breast cancer cells. Cells without NWs before (a-I) and after (a-II) NIR laser irradiation. Cells incubated with BSA coated NWs before (a-III) and after (a-IV) NIR laser irradiation. The laser was applied with a power density of 0.8 W/cm^2, and the images correspond to the view from the top of a 96 well plate. (b) Temperature response curves of concentrated suspensions of breast cancer cells nonincubated (control) and incubated with BSA coated NWs (0.02 mg Fe/mL) that were irradiated with a NIR laser (808 nm) [34].

Li *et al.* showed for the first time that PEGylated CuNWs were able to convert near-infrared (NIR, 808 nm) light into heat at a photothermal efficiency of 12.5%. The PEGylated CuNWs exhibited good reusability and enabled rapid temperature rise to more than 50 °C in 6 min by NIR irradiation (Fig. 1.7 (a)). The PEGylated CuNWs were flexible and intertwined around the cancer cells, which, upon NIR irradiation, allowed for direct heat transmission to cells and effectively triggered cancer cell ablation in *in vitro* bearing mice and ensuing NIR irradiation for 6 min significantly raised the local

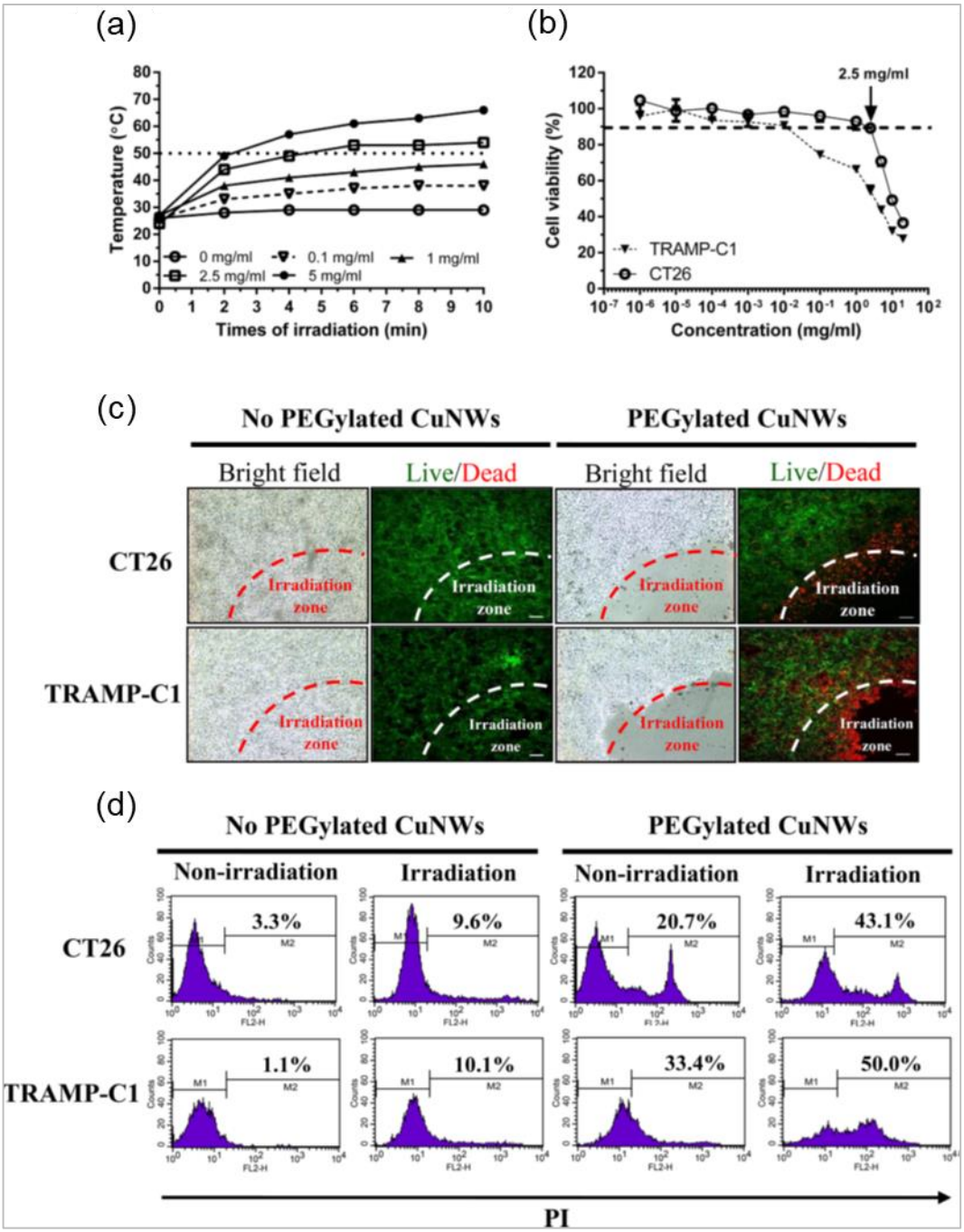

Fig. 1.7: *In vitro* photothermal effect of PEGylated CuNWs. (a) Temperature elevation of PEGylated CuNWs (0−5 mg/mL, in 0.5 mL PBS) under NIR laser irradiation within 10 min (808 nm, 1.5 W/cm2). (b) Cytotoxicity of PEGylated CuNWs on CT26 and TRAMP-C1 cell as measured by MTT assay. (c) Cell death analysis by Live/Dead staining. (d) Cell death analysis by PI staining/flow cytometry. In all experiments, PEGylated CuNWs were dispersed in PBS. For *in vitro* tumor cell ablation, we incubated CT26 and TRAMP-C1 cells in 12-well plates (2 × 105 cells/well) with or without 2.5 mg/mL of PEGylated CuNWs (1 mL/well) for 1 h, and exposed the cells to local NIR laser irradiation (808 nm, 1.5 W/cm^2) for 6 min. After irradiation, the cells were subjected to Live/Dead staining (c) or PI staining/flow cytometry (d). The red and green fluorescence indicated dead and viable cells, respectively [35].

temperature to >50 °C, induced necrosis, and suppressed tumor growth (Fig. 1.7 (c) and (d)).

1.1.3. Magnetic hyperthermia

Magnetic hyperthermia mediated by biocompatible magnetic nanoparticles is a thermo-therapeutic approach that has been studied for many years. However, it remains a promising, efficient and safe technique for the treatment of cancer. The structural and magnetic properties of magnetic nanoparticles, together with the parameters of the external magnetic field, are responsible for a controlled heating performance imperative for clinical success [36].

The dynamic response of a dipole with its magnetic moment in a single direction due to an external alternating magnetic field (AMF) during the transformation of magnetic energy into heat is governed mainly by thermal fluctuations. The main heat generation mechanisms can be attributed to two different phenomena: relaxation and hysteresis loss (Fig. 1.8). The relaxation is of two types: Néel and Brownian relaxations [37]. The Néel relaxation is an internal dynamic process that occurs due to rapid changes in the direction of magnetic moments relative to crystal lattice it is hindered by anisotropic energy that tends to orient the magnetic domain in each direction relative to the crystal lattice. On the other hand, Brownian relaxation is an external process that occurs due to the physical rotation of particles in a fluidic medium where they are placed. The last is hindered by the viscosity of the medium that tends to oppose the particles rotation. The Néel and Brownian sources of friction that lead to a phase lag between the applied magnetic field and the direction of the magnetic moments tends to generate thermal losses. The mechanism that governs heating capacity of a given magnetic nanoparticles is based on the induction of rapid variation of magnetic moments. The extra cellular medium and/or other intracellular components generally hinder the movement of the particles resulting in total heat contribution largely coming from Néel relaxation [37].

The heat efficiency produced by magnetic nanoparticles suspended in liquid medium is quantified by the specific absorption rate (SAR) or specific loss power (SLP) and is defined as the amount of heat released by a unit quantity of active material per unit of time during exposure to an AC magnetic field of defined frequency and field strength (Eq. 1.1).

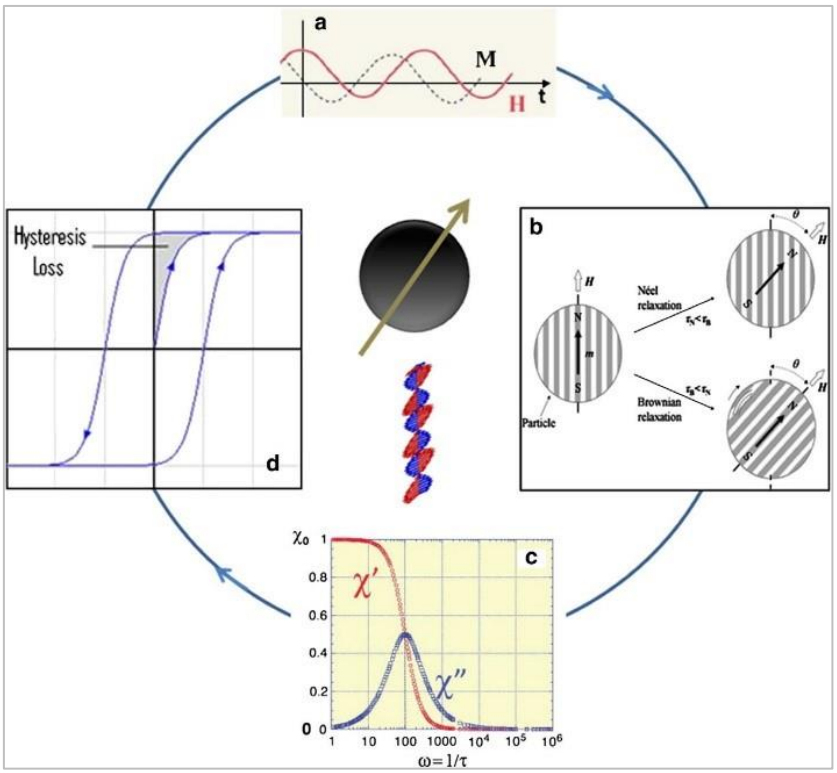

Fig. 1.8: A schematic representation of possible mechanisms for conversion of magnetic energy into heat [37].

$$SAR = C\left(\frac{\Delta T}{\Delta t}\right)_{t\to\infty} \quad (1.1)$$

where C is specific heat capacity expressed as average absorbed power per mass unit (W/g) and $\Delta T/\Delta t$ is the temperature increase per unit time which compounds to the initial slope of the temperature versus time dependence. Several parameters can affect magnetic-induced hyperthermia and consequently the SAR: applied magnetic field and frequency [38-40], particle size [41-43], particle morphology [37, 44, 45], composition anisotropy [46-50], dipolar interactions [51-54] , viscosity [41, 55, 56], or coating with organic ligands [57, 58].

In particular, superparamagnetic iron oxide nanoparticles (SPIONs) are considered promising magnetic nanoparticles for hyperthermia applications due to their biocompatibility, low-cost manufacturing and tuning of unique magnetic properties of monodomain. Many studies presented in the literature promote SPIONs for use in local heating therapy. Ziba *et al.* [59] shows that SPIONs induction heating efficiency under exposure to various alternating magnetic fields (AMF), resulted in a remarkable SAR rate of 168 W/g, keeping the average temperature within the safe hyperthermia range and resulting in 49% cell viability (see Fig. 1.9).

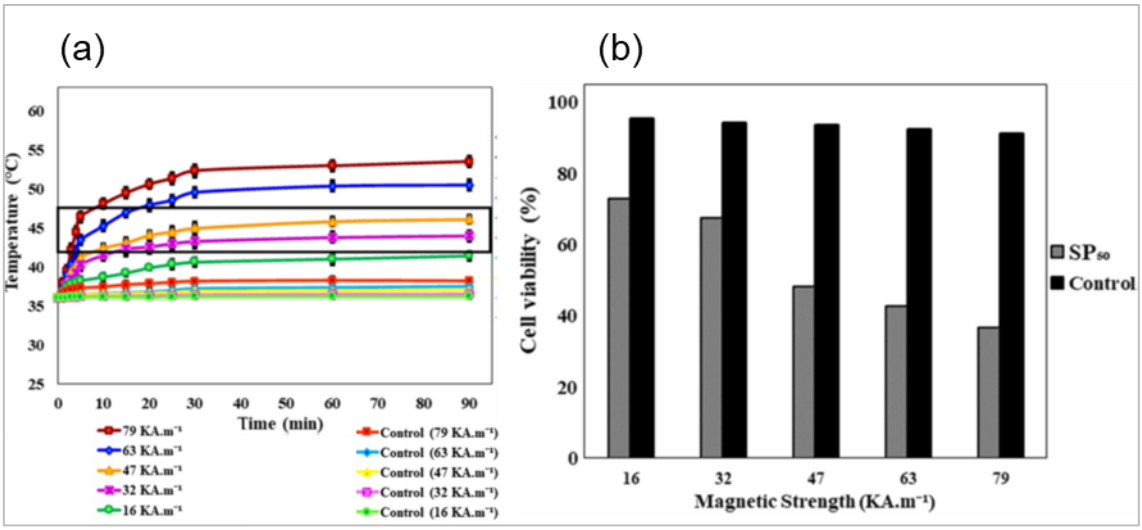

Fig. 1.9: (a) The thermal profiles of the HepG2 cells treated with and without the SP_{50} exposed to five varied AMF strengths. The band illustrates the hyperthermia range. (b) Cytotoxicity profiles of HepG2 cells treated with and without SP_{50} exposed to varied AMF strengths. [59].

More recently also magnetic NWs represent a very promising candidate for enhanced magnetic hyperthermia [24, 60-62]. Remarkably, theoretical studies have predicted that the use of magnetic nanoparticles with larger magnetic moments and larger magnetic anisotropy would be more desirable than spherical nanoparticles, as the larger values of SAR can be achieved at smaller particle sizes [24]. Cho *et al.* [24] carried out a comparative study of the magnetic hyperthermia properties of FeCo nanowires with different lengths and diameters and concluded that when the applied field is higher than the coercive field of the nanowires, the nanowires are aligned in the direction of the magnetic field during hyperthermia experiments, due to their aspect ratio and dipolar interactions. This results in greater heating efficiency. The SAR of the nanowires increases with an increase in the wire length (especially above 10 μm) as can be seen in Fig. 1.10, and as the nanowires get smaller (2 μm) the SAR values obtained are notable, indicating that the FeCo nanowires are a promising candidate for increased magnetic hyperthermia.

However, neither application of magnetic nanoparticles has yet become part of the standard for cancer diagnosis or treatment. Although magnetic hyperthermia is especially attractive for cancer treatment, some challenges, such as accurate thermometry within the tumor mass and the high needed concentration of magnetic nanoparticles, impede its successful application [28]. Another drawback of these magnetic nanoparticles is the inability to monitor the tumor evolution during the hyperthermia treatment by MRI due to the generation of artifacts [28, 63]. Moreover, the high concentration of magnetic nanoparticles in prolonged treatments can increase

the therapeutic agent's accumulation and thereby their toxicity [28, 64]. Also, the high magnetic fields used in MHF oblige the removal of dental fillings, implants and crowns prior to AMF exposure and are incompatible with the use of pacemakers and defibrillators due to electromagnetic interference.

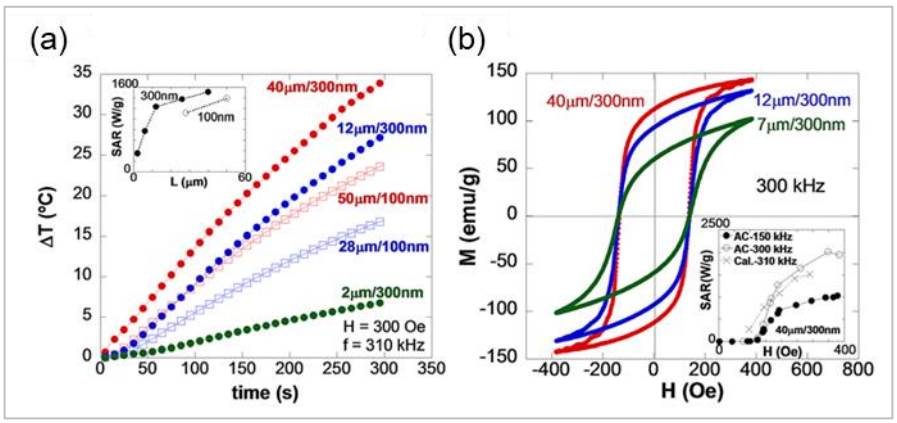

Fig. 1.10: Magnetic hyperthermia measurements: (a) heating curves measured by calorimetric methods for the FeCo NWs with different lengths and diameters; (b) The hysteresis loops measured using AC magnetometry; the inset of (a) shows SAR as a function of the length, while the inset of (b) shows the SAR *vs.* H curves obtained from both methods [24].

1.1.4. Magneto-mechanical induced cellular annihilation

The magneto-mechanical induced cell death is a technique that consists in exerting forces or torques on cells by using magnetic nanostructures controlled by low frequency external magnetic fields, inducing cell apoptosis [65-67]. The basic physical principle of magneto-mechanical actuation in cells is the spatial rotation due to the high magnetic torque of the nanostructure to align themselves with an applied magnetic field through the Brown relaxation process (see Fig.1.11) [28, 68]. The torque produced depends on the applied magnetic field characteristics and the magnetic moment, and the magnetic susceptibility of the nanostructure [65, 69].

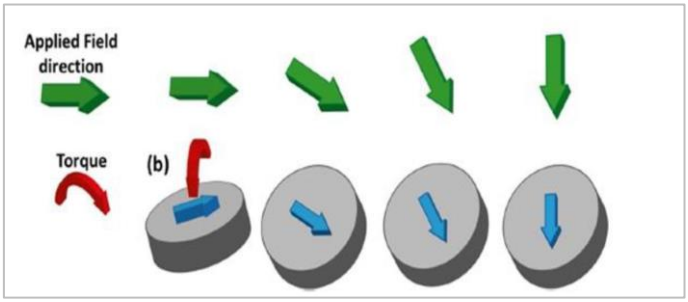

Fig. 1.11: Schematic of nanostructure rotation when an external magnetic field is applied [68].

This cancer therapy presents several advantages, such as:

- The possibility to specifically target cancer cells by functionalizing the surface of the magnetic nanostructures, which would significantly reduce the toxic side effects of chemotherapy;
- Required considerably lower strength and frequency of the magnetic field in comparison to magnetic hyperthermia, making it easier to implement while eliminating the risk of destroying healthy tissues by undesired local overheating [65, 70];
- High saturation magnetization at low saturation fields, no remanent magnetization and coercive field which avoids the nanostructures agglomeration in the absence of a magnetic field [69, 71, 72];
- Low concentration of magnetic nanostructures are required, in principle only one nanostructure per cell is sufficient to induce the cell death [28];

In this sense, several studies are being driven to improve this technique, namely by optimizing the magnetic nanostructure dimensions, composition and the applied magnetic field and frequency [68].

Figure 1.12 shows a schematic representation of the magneto-mechanical cellular annihilation using micro/nanodiscs in a spin vortex state, i.e., an in-plane flux closure spin distribution study done by Kim *et al.* [73], in which after the incorporation of the functionalized microdiscs by the cells, they were exposed to spatially uniform

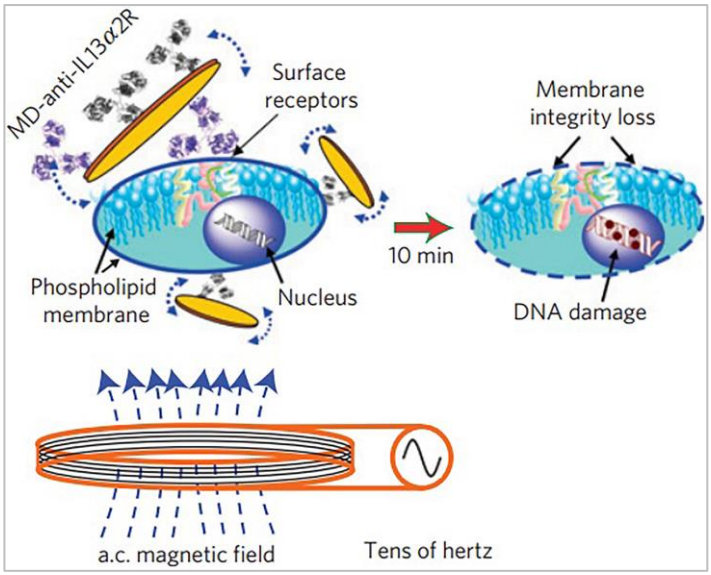

Fig. 1.12: Representative scheme of the cancer cells annihilation by magnetomechanics employing magnetic disk-shaped structures in vortex state [73].

alternating current (AC) magnetic fields with different intensities and frequencies. In this study a relevant cell damage (90% of cell death) was obtained by applying a considerably weak magnetic fields (<10 mT), with frequencies of few tens of Hertz (10–20 Hz) during only 10 minutes. Therefore, this technique shows a great advantage with the typical heating-induced cell death, using superparamagnetic particles, where considerably stronger AC magnetic fields and high magnetic nanoparticles concentration are needed, with frequencies of hundreds of kilo Hertz [73].

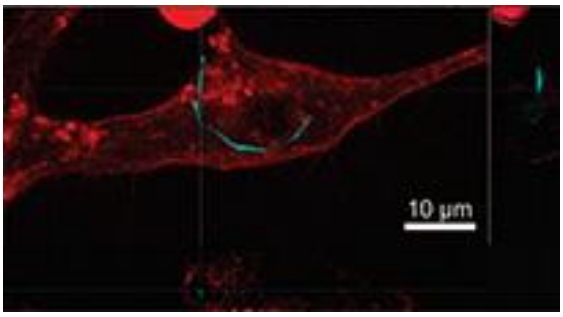

Fig. 1.13: Confocal projection and cross sections of a 3T3 fibroblast (red) with various Ni nanowires internalized (blue) [48].

Magnetic nanowires have also been studied in the context of magnetomechanical induced cell damage by various authors. One of the first reports addressing this one-dimensional nanostructure in such biomedical applications is by Fung *et al.* [26]. In their work ferromagnetic Ni nanowires, with diameters ranging from 198 nm to 280 nm and an average length of 4:4 µm, presenting longitudinal magnetic anisotropy. These NWs are prepared by electrodeposition in porous aluminum oxide templates and then incubated with fibroblast (NIH/3T3) for about 12 h (Fig. 1.13). These nanostructures did not significantly affect the cell viability in the absence of a magnetic field, in spite of Ni being an agent of hypersensitivity and moderately cytotoxic. Then, the nanowires were exposed to a weak (240 mT) and low-frequency (1 Hz) rotating magnetic field for 20 min. After this process, a viability reduction of the cell cultures by 89% was observed, indicating that this process effectively induced cell death. Complementing this work, Choi *et al.* [74] demonstrated the death of human embryonic kidney cells (HEK-293) due to the rotation of internalized Ni nanowires, with an average nominal diameter of 150 nm and longitudinal magnetic anisotropy, caused by the application of an external AC magnetic field. This study also verified that the AC modulation amplitude and rate were fundamental parameters to determine the rotation of the nanowire inside the cell; however, the authors do not specify field intensity and frequency or the cell death rate achieved using this technique. Also, in this context, Contreras *et al.* [75] analyzed the magnetomechanical effect in human colon cancer cells (HCT116) incubated with two

concentrations of Ni nanowires (2.4 and 12 mg/ml). These nanostructures had a diameter of 35 nm and a length of 4 µm and presented longitudinal magnetic anisotropy. After the incubation, the viability of the cells was confirmed, and subsequently, they were exposed to an AC magnetic field (0.5 mT; 1 Hz or 1 kHz) for 10 or 30 min. Similar to the previous reports.

A different study by Contreras [76] considered the application of Fe and Ni nanowires, with longitudinal shape anisotropy, in the same experimental conditions, and revealed that the first nanostructures are better tolerated by the used cell lines (HCT 116 and HeLa). Different lengths of nanowires (1 µm and 5 µm) were also analyzed; however, a significant influence of this parameter on the cell viability for nanostructures of the same material was not observed. Afterward, both types of nanowires (with a diameter of 35 nm and 4 µm long) were incubated with cells (HCT 116) at two different nanowire-to-cell concentrations (100:1 and 500:1), and then AC magnetic fields (0.5 mT and 1 Hz or 1 kHz) were applied. Similar to the previous study, it was verified that the magnetomechanical action resulted in the death of up to 60% of cancer cells when using Ni nanostructures at a 500:1 concentration, with a 1 h exposure. Additionally, it was found that a one hour incubation time seemed to be optimal for the application of this treatment.

1.1.5. Magnetic resonance image

Magnetic Resonance Imaging (MRI) is a noninvasive and nondestructive acquisition image technique, capable of providing three-dimensional (3D) images of living organisms [77]. This technique uses the relaxation times of the water protons and, therefore, contrast agents can be used for modifying the magnitude of the signal in the body regions where the agent is incorporated, increasing significantly the sensitivity and specificity of MRI, since these agents change the intrinsic properties of the tissues within a living organism, increasing the information present in the images [78]. Advances in nanotechnology and materials science have been the driving forces that are propelling forward the use of magnetic nanostructures as promising alternatives to commercial contrast agents used in MRI [79].

Superparamagnetic iron oxides nanoparticles (SPIONs) have been considered a substitute for commercial options due to their high saturation magnetization, biocompatibility, ease of metabolization and surface functionalization [80-83]. Figure 1.14 shows a study by Hobson *et al.* [84] where they were able to verify that the SPIONs significantly improved the contours and details of MRI the images. Recently, it was also demonstrated that several types of nanoparticles were able to cross the blood

brain barrier, increasing the possibility of early diagnosis of several diseases in the brain [85].

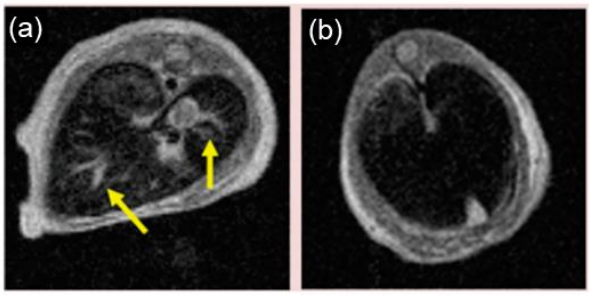

Fig. 1.14: T2-weighted axial MRI pictures illustrating a mice liver cross section 60 min pos-administration of (a) raspberry SPIONs; (b) commercially available contrast agent Ferucarbotran®. The arrows in (a) show hepatic liver vessels, that are not observed in (b) [84].

New lines of research considered the NWs and NDs promising contrast agents due to their shape anisotropy induced by the high aspect ratio and higher magnetic moments moreover, this kind of nanostructure can be combined with other biomedical applications [86-90].

1.1.6. Multifunctional magnetic nanoparticles

Multifunctional magnetic nanoparticles are a generation of nanoparticles that have attracted considerable attention in nanotechnology research for medical application, since they are able to be used for several proposals in a single intervention. These nanoparticles offer an opportunity to create multi-functionality with potential applications in diagnosis and therapy of several types of diseases like cancer [37]. The design of multifunctional nanoparticles for biomedical applications is based in core-shell structures and depends mainly on the magnetic functionality of the core, the properties of the shell and their interaction with the biological medium [3].

The use of multifunctional magnetic nanoparticles, with magnetic core offers new technical possibilities for biomedical applications such as hyperthermia and enhanced MRI. Nanoparticles with small sizes present a unique opportunity to interfere, in a highly localized and specific way, with natural processes involving viruses, bacteria or cells and allows interference in the development of complex diseases like many types of cancer and neuropathies [31]. Many studies on multifunctional magnetic nanoparticles have already proven its efficiency in several types of cancers, for example, colon cancer, breast cancer, prostate cancer and brain tumor as summarized in Table 1.1.

Table 1.1: Some exemples of available nanoparticles for multifunctional medical aplication.

Core	Coating	Size	Loaded drug	Targeting ligand	Cell in vivo model	Application	Ref.
Bismuth iron oxide NPs	Dextran	98 nm	Nono	None	Human liver carcinoma cells (Hep G2) BJ5ta fibroblasts C57BL/6J mice	Dual CT and MRI T2 contrast agents were successfully deployed in an in vivo murine model	[91]
Iron oxide NPs	None	35 nm	None	Anti-prostate specific membrane antigen J591 antibody	LNCaP cells (CRL-1740) DUI145 cells (HTB-81)	MRI T2 contrast agents that specifically target prostate cancer cells were developed	[92]
Iron oxide NPs	Dextran	40 nm	Flutax1DiR Doxorubicin	None	LNCaP cells Mice with PC3 flank xenografts Mice with BT20 flank xenografts	Drug delivery vehicles that release their therapeutics in mildly acidic environments were created; these particles also exhibit changes in MR relaxivity values upon drug release and may thus be used to monitor drug delivery	[93]
Iron oxide NPs	Chitosan	50 nm	Temozo-lomide	Chlorotoxin	Glioblastoma cells (U-118 MG) C57BL/6Jmice	Drug delivery vehicles capa-ble of carrying the chemothe-rapeutic temo-zolomide specifically to glioblastoma brain cancer cells were tested *in vitro*	[94]
Iron oxide NPs	PEG	100 nm	siRNA targeting human telomerasereverse transcript-tase		MCF-7 cells PC3 cells SKOV-3 cells Hep G2 cells BALB/c mice with Hep G2 xenograft tumors	Redox-sensitive gene and siRNA delivery was achieved *in vitro* and in vivo to induce apoptosis and inhibit growth of liver cancer.	[95]
Iron oxide NPs	PEG	19 nm	None	None	Immunodeficient athymic NMRI mice Human epidermoid carcinoma xenografts (A431 cells)	SPIONs injected intratumorally into skin cancer xenografts induced localized hyperthermia when irradiated with an external magnetic field, arresting tumor growth	[96]
Gold-iron oxide composite	PEG	25 nm	None	A33 scFv antibody	Colorectal cancer cells (SW1222 and HT 29)	Active targeting of colorectal cancer cells and subsequent selective photothermal ablation of tumor tissue *in vivo*	[97]
Iron oxide NPs	APTES	15 nm	Pheophorbide-A	None	Epithelial cancer77 cells (KB cells)	Simultaneous photodynamic therapy and dual-mode fluorescence/MR imaging of epithelial cancer cells *in vitro* was demonstrated	[98]
Iron NWs	APTS and BSA		Doxorubicin		Brest Cancer cells (MDA-MB-231)	Combination of the chemotoxic and magnetomechanical treatment.	[71]

Note: aminopropyltriethoxysilane (APTES) or with bovine serum albumin (BSA) Polyethylene glycol (PEG)

The combination with other materials like gold coating or carbon nanomaterials, can result in hybrid nanostructures with enhanced physicochemical properties. For example, gold iron-oxide hybrid nanoparticles exhibit enhanced optical properties, so they are suitable for optical sensing applications [3], computed tomography (CT) [99], and photothermal therapy (PTT) [100]. Espinosa *et al.* [101] presented a study with Janus nanoparticles composed of an iron oxide nanosphere and a gold nanostar (both magnetic and plasmonic) for magneto-photo-thermal activation and magnetic guidance aiming co-application in MHT and PTT. Initially the study that availed heating properties of Janus gold-iron oxide in the cellular environment under MHT and PTT conclude that MHT heating performance is much lower ($\Delta T \approx 1 - 2$ °C) compared to PTT response ($\Delta T \approx 30$ °C). Then it was investigated an alternative asset from the magnetic component: the possibility for the nanoparticles to be remotely guided by a magnet. Figure 1.15 show the results of these assay that confirmed the enhanced internalization of the nanoparticles under magnet application, with more nanoparticles observed per cell, densely packed within endosomes and this tallows for considerable improvement in hyperthermia results.

On the other hand, multifunctional magnetic nanoparticles with a shell functionalized with specifics target and drugs allows the controlled drug delivery [11]. To combine MRI and controlled drug release, Hayashi *et al*. [102] present a study that enhancing heat-generation power and relativity of encapsulated SPIONs and DOX (doxorubicin) into a carboxylic polymer modified with amine and FA-hetero bi-functionalized polyethylene glycol. The results conclude that controlled release of DOX was trigged by the heat generated from the alternating magnetic field.

Currently, there are only few works in the literature that reported multifunctional high aspect ratio nanoparticles. However, multifunctional magnetic NWs are a type of magnetic carrier that offers significant advantages over commercially available spherical magnetic particles [103]. The NWs composition can be modulated along the wire length, which in turn enables the precise control of their architecture and magnetic properties. In addition, by using specific ligands that bind selectively to different segments of the wire, it is possible to perform multiple functionalization [104].

Martínez-Banderas *et al.* [71] presents a bimodal strategy to induce the death of breast cancer cells by combining the chemotoxic effect caused by an anticancer drug (DOX) with the mechanical disturbance caused by Fe NWs with an average length of (6.4 ± 1.3) µm and a diameter of 30 to 40 nm, when exposed to a low frequency (10 Hz) AC magnetic field (1mT) for 10 min. For the study of internalization, the nanostructures were incubated with cells at a concentration of 0.05 Fe mg/mL for 24 h

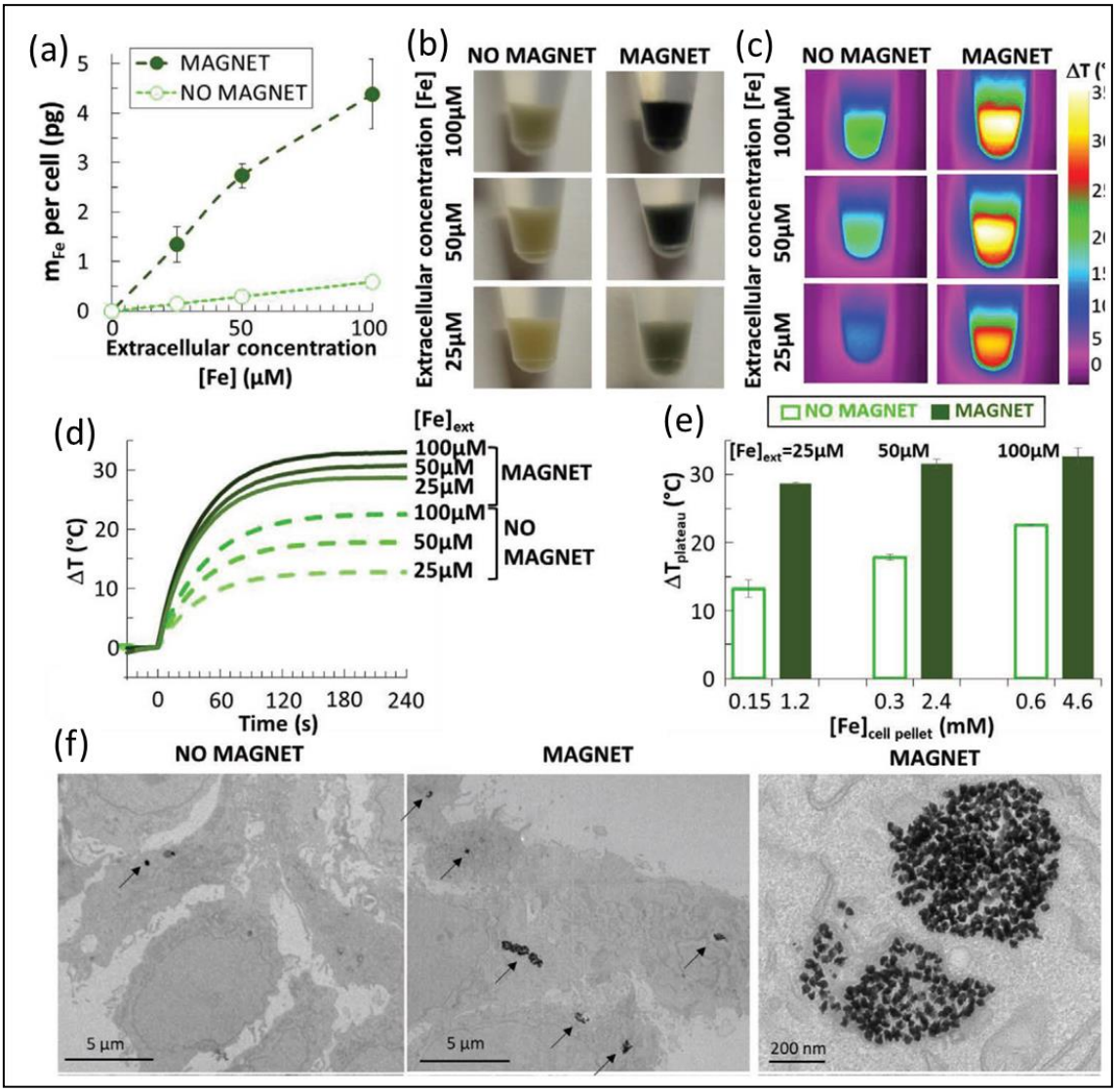

Fig. 1.15: ***I****n vitro* assay of magnetic guiding-assisted photothermia of Janus gold-iron oxide. (a) Magnetic guiding effect (b) Camera images of cell pellets under different incubation conditions. (c) Infrared thermal images, (d) typical heating curves, and (e) average plateau temperature elevation of cell pellets illuminated with laser (680 nm laser 0.5 W cm−2) after 5 min, for all conditions and (f) TEM images of CT-26 cells incubated with nanoparticles with and without Magnet applicated [101].

and using Prussian blue staining for iron oxide detection it was found that the functionalized nanowires demonstrated a high degree of internalization by the cells, becoming efficient carriers for drug delivery. In addition, NWs coated with BSA showed better internalization (26 ± 63 of NW Fe per cell) with a greater distribution within cells and smaller clusters. Figure 1.16 shows the NWs coated with 3-aminopropyl-triethoxysilane (APTES) (Fig. 1.16 (a)) or with bovine serum albumin (BSA) (Fig. 1.16 (b)), to allow the connection with doxorubicin (DOX) and ensure the functionalization on the surface of the NWs. Viability result of breast cancer cells (MDA-MB-231) (Fig.1.16

(c)) shows the efficiency of this technique in inducing cell death. A large cytotoxic effect was observed in breast cancer cells caused by the double effect of functionalized nanowires, with a maximum reduction of 73% in cell viability. Therefore, it was demonstrated that the combination of these two treatment modes (chemotoxic and magneto-mechanical) using functionalized magnetic NWs, had synergistic effects, turning this technique into an attractive approach for new cancer therapies.

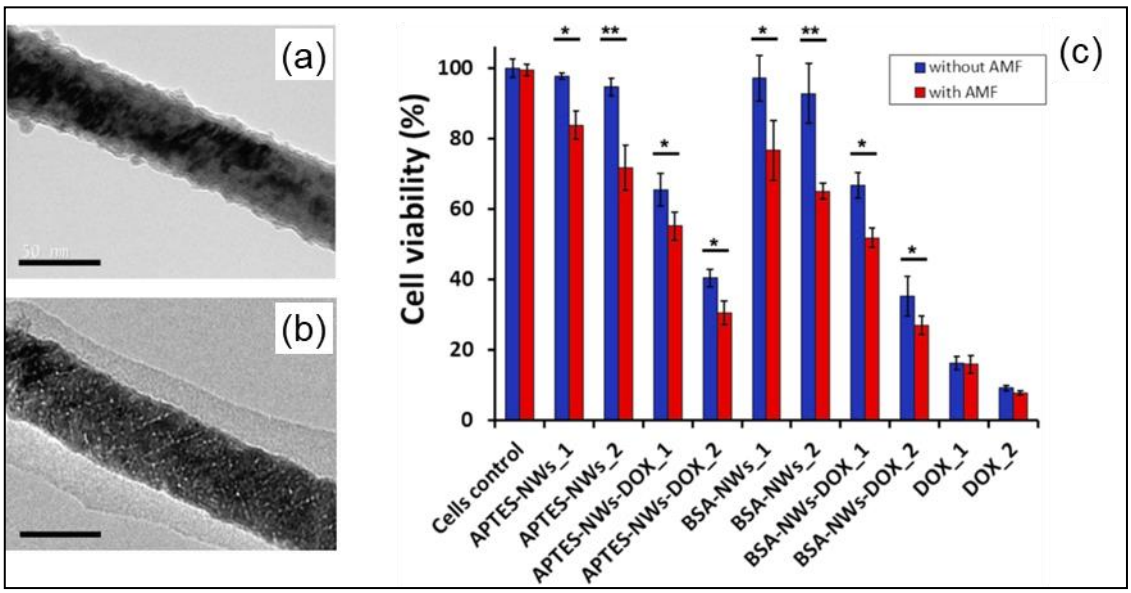

Fig. 1.16: TEM micrographs of APTES-NWs (b) and BSA-NWs (a). The scale bars correspond to 50 nm. Viability of MDA-MB-231 cells incubated with different formulations and with or without application of a low frequency alternating magnetic field (AMF) (c) [71].

1.1.7. Spherical versus high aspect ratio nanoparticles

The new top-down and bottom-up manufacturing techniques allowed the exploration of different nanoparticle geometries, including cylindrical and discoid shapes (see Fig. 1.17) For different forms of nanostructures we can also expect different magnetic behavior responses as well as different effects on pharmacokinetics and biodistribution [105]. The size, shape and surface charge of the nanoparticles determine the biodistribution between different organs, including the lungs, liver, spleen and kidneys [106]. Blanco *et al.* [64]. Regarding the particle size, diameters around 100 nm demonstrated long-lasting in the circulation [64]. Nanoparticles with diameters lower than 5 nm when intravenous administrated are rapidly undergo upon renal clearance [107]. Larger particles are accumulated in the liver due to the presence of a noncontinuous endothelia with vascular fenestrations of 50 - 100 nm [108]. Long half-lives in blood can be increased by increasing the particle size to 380 - 780 nm, which

improves the propensity of nanoparticles to extravasate through the tumor vasculature [109], However particles with more than 200 nm are retained by splenic filtration due to the dimensions of the interendothelial cell slits (200 - 500 nm) [110]. Particles in the micrometer range (2 - 5 μm) showed an advantage when targeting the metastatic sites of disease but accumulates readily within capillaries of the lungs and are also uptake by resident macrophages of the liver, spleen and lungs. However the nanoparticles geometry (i.e. discs or nanowires) and surface functionalization ultimately determines successful completion of uptake as summarized in Fig. 1.18 [64].

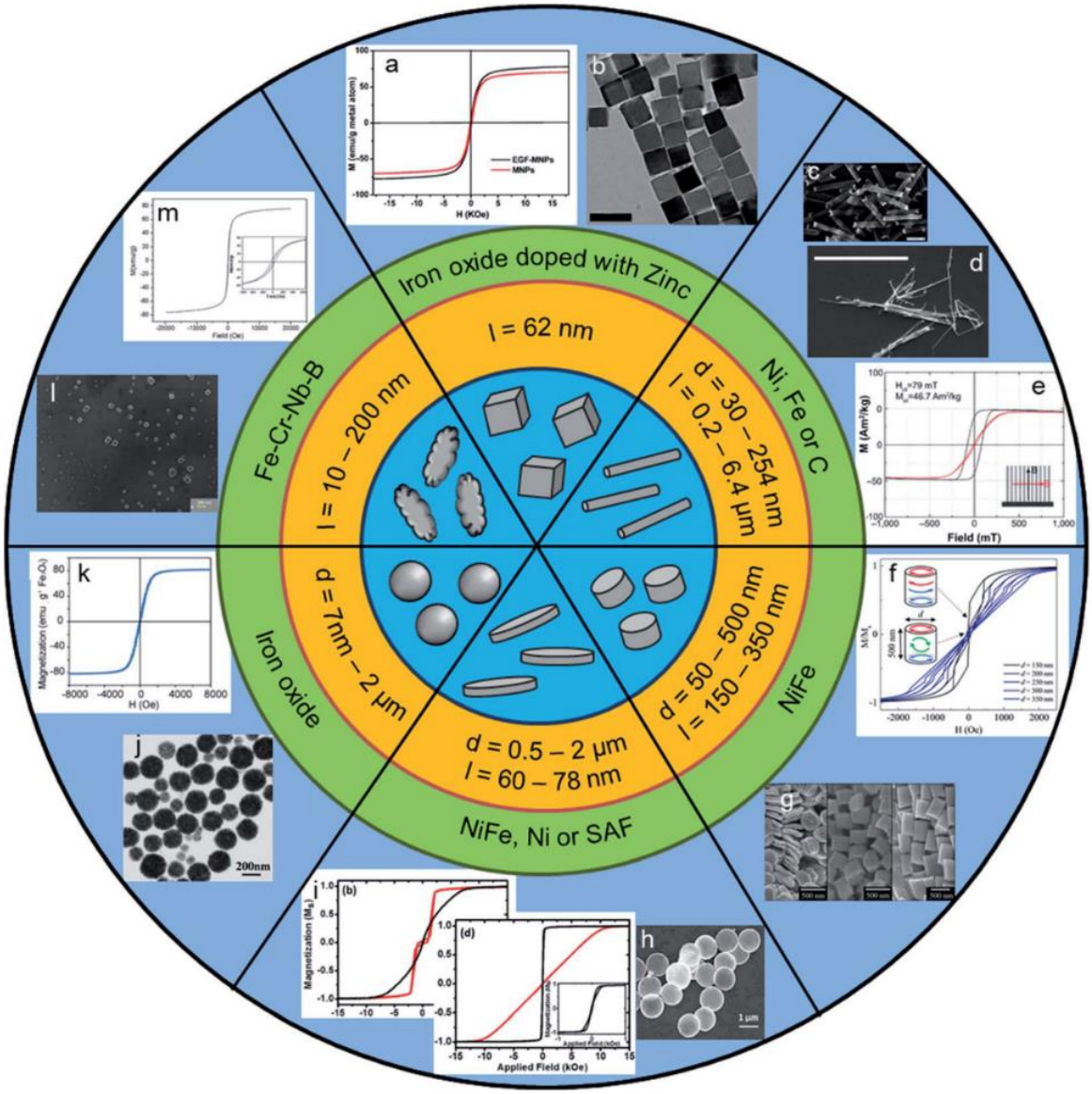

Fig. 1.17: Representative scheme showing properties of particles with different shapes, associated sizes and materials [105].

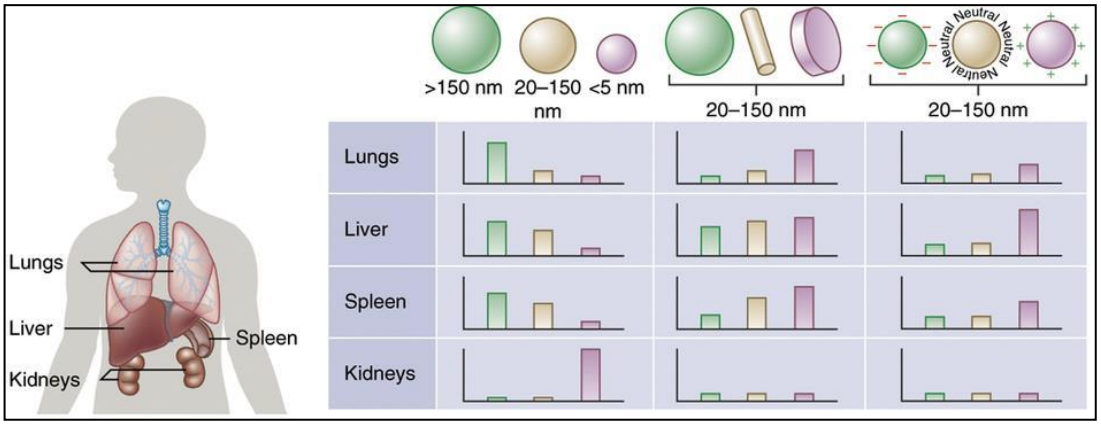

Fig. 1.18: Biodistribution among the different organs (lungs, liver, spleen and kidneys) depending on the nanoparticle size, shape and surface charge [64].

Spherical shaped nanoparticles such as liposomes or quantum dots, have been used as gene, drug and dye carriers since they circulate *in vivo* for a few hours or until a day and they also can enter in the cells [61]. High aspect ratio nanoparticles have not received the same attention as the spherical ones. Only the carbon nanotubes were more explored since they can circulate several hours after intravenous injection and also enter in mammalian cells [111].

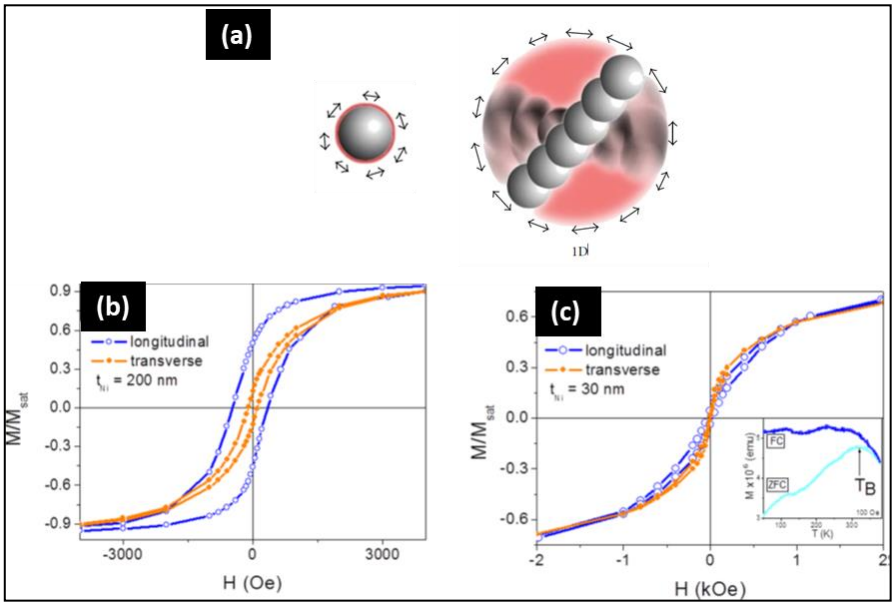

Fig. 1.19: a) One-dimensional materials have large spinning radii [61]. b) M(H) curves at 300 K with magnetic field applied parallel and transverse to the nanowires longitudinal axis for Ni nanowires of (b) 200 nm and (c) 30 nm. Inset shows ZFC and FC magnetization measurements of Ni nanowires with 30 nm length [112] .

Sousa *et al.* [112] shows the magnetization versus applied field (M(H)) measurements for AAO embedded double segmented nanowires (Au (200 nm)/Ni(30

or 200 nm)) with Cu filled dendrites. For the nanowires with thicker Ni elements (200 nm) (Fig. 1.20 a), we observe an anisotropic M(H) behavior. The ZFC magnetization curve shows a maximum, with a bifurcation between FC and ZFC data below a certain temperature (inset Fig.1.20 b). This behavior is typically present in an assembly of ferromagnetic nanoparticles exhibiting superparamagnetic above a certain temperature, as expected for Ni nanoparticles with diameter below 50. A similar study is presented by Suzano *et al*. [113] where is reported the magnetic properties of Ni/Cu multisegmented NWs embedded in the anodic aluminium oxide (AAO) membrane. The magnetic hysteresis loops M(H) recorded for the Ni/Cu NWs with L_{Ni}= 10 nm and L_{Ni} = 100 nm, with the applied magnetic field parallel (II) and perpendicular (⊥) to the NWs long axis. The results illustrate a magnetic anisotropic behaviour for Ni/Cu NWs with the easy magnetization axis lying parallel to the wire axis, arising from the competition between the magnetocrystalline anisotropy and the shape anisotropy factors [113].

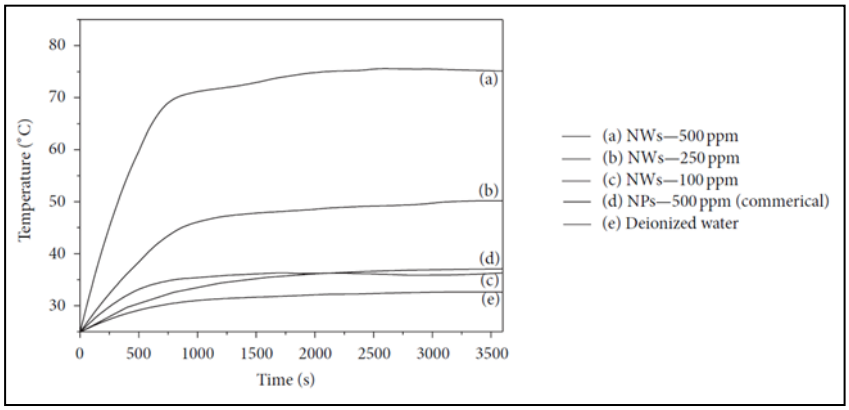

Fig. 1.20 The heating effectiveness of iron NWs with different concentrations: (a) 500 ppm of iron NWs (0.5 mg/mL), (b) 250 ppm of iron NWs (0.25 mg/mL), (c) 100 ppm of iron NWs (0.1 mg/mL), (d) 250 ppm of commercial iron nanoparticles (0.5 mg/mL), and (e) deionized water. (From reference [61]).

Lin and his group *et al.* [61] (Fig. 1.20), demonstrated that Fe nanowires can improve an order of magnitude the SAR in comparison with Fe nanoparticles, since high magnetic moments per volume can originate large forces and torques. While the magnetic anisotropy of nanowires can be enhanced by considering shape anisotropy, only a few studies have taken into account the possibility of changing their aspect ratio (shape anisotropy) and, hence, tuning their effective anisotropy. The NWs heated and stirred in an alternating magnetic field have larger reactive areas due to its higher spinning radii. This fact makes the Fe NWs the best candidates for high heating efficiency. When applied in hyperthermia one-dimensional Fe NWs an provide larger frictional areas. Some studies concluded that one-dimensional nanostructures can be

potential candidates to achieve a better heating efficiency, which reduces the time and increases the efficiency of the treatment [61].

1.2. Magnetism at the nanoscale

In nanotechnology, there is a wide range of systems related to the unique magnetic properties that emerge from the material size reduced to the nanoscale. A fundamental aspect to take into account when the material size is reduced to the nanometer scale is the size of the critical length scales, that is, when a material is reduced to a typical size of 1 - 100 nm, its dimensions become comparable to those scales of critical length of physical phenomena, below which new properties may emerge[113-115].

One of the elementary magnetic length scales is the exchange length, which characterizes the competition between the exchange and dipolar energies in a material and is defined as $L_{ex} = \sqrt{\frac{2A}{\mu_0 M_{sat}^2}}$, where A is the magnetic stiffness constant, $\mu_0 = 4\pi \times 10^{-7}$ NA^{-2} is the magnetic vacuum permeability and M_{sat} is the saturation magnetization of the magnetic material. This length is in the range of 2 to 10 nm for most ferromagnetic materials and represents the shortest scale on which the magnetization can be twisted to minimize dipolar interaction [114, 116].

The width of the magnetic domain wall is another important length because it represents the transition region between two different magnetic domains, $\delta_w \sim 20$ - 130 nm; as well as the coherence radius (maximum size of a uniformly magnetized particle in which the magnetization reversal occurs by coherent rotation; $R_{Coh} \sim 10$ - 25 nm); the superparamagnetic blocking radius (below which particles undergo spontaneous thermal fluctuations in the direction of magnetization; $R_b \sim 5$ - 20 nm); and the size of the Imry-Ma domain (below which the system is in a correlated spin glass regime) [116].

The combination of the high surface area and the unique properties exhibited by materials reduced to the nanoscale are of great interest in the development of new technological strategies, since these nanostructures, presenting properties different from conventional materials and can give rise to innovative operating principles for new materials and devices. In particularly, research in nanomedicine also stimulates the understanding of the physics of new phenomena and processes at the nanoscale, driving the development of new nanostructures, and medical devices [114].

1.2.1. Superparamagnetism

Superparamagnetism is characterized by zero coercivity and a large magnetic moment in the presence of an external magnetic field. An example of nanoparticles where superparamagnetism is observed is the iron oxide nanoparticle with very small dimensions (up to about 20 nm) [82], These nanostructures have a unique magnetic domain where a decoupling of the particle magnetization from the network due to the thermal energy exceeds the anisotropy energy [117]. This happens when the sample volume is reduced below a critical value, or superparamagnetic limit, at which more energy is needed to create a domain wall than to support the external magnetostatic energy of the single domain state. The energy of the magnetic anisotropy, which is responsible for all magnetic moments along the same direction, is presented in Eq. 1.2 [118]:

$$E\ (\theta) = K_{eff} V sen^2(\theta) \qquad (1.2)$$

Where K_{eff} is the anisotropy constant, V corresponds to the volume of the nanoparticle and θ is the angle between the easy axis and the magnetization. Therefore, $K_{eff} V$ is the energy barrier between the two reverse easy directions of magnetization that are energetically equivalent. With decreasing particle size, $K_{eff} V$ decreases until the value of thermal energy and fluctuations of the overall magnetic moment can take place within the particle. These thermal fluctuations then affect the orientation of the magnetization if they are large enough to overcome the magnetic anisotropy barrier. This change in magnetization resembles the behavior of a paramagnetic material, albeit involving a magnetic moment that is several orders of magnitude larger, leading to the creation of a superparamagnet [119, 120]. Two key features describe a superparamagnetic system: lack of hysteresis and data of different temperatures superimposed onto a universal curve of $\mathrm{M\ vs.\ H/T}$ [121].

The superparamagnetic state is distinguished by its thermal response. The thermal relaxation time (τ) describes the average time the ensemble magnetic moment at a given temperature (T) reverses from one direction in space to another over a uniaxial activation energy and is given by the Néel-Brown expression in Eq. 1.3:

$$\tau = \tau_0 \left(\frac{K_{eff}\ V}{k_B T}\right) \qquad 1.3$$

where k_B is the Boltzmann constant, $1/\tau_0$ is the reversal attempt frequency with $\tau_0 \approx 10^{-9}$ and V is the particle volume

As illustrated in Fig. 1.21, for measurement times $\tau_m \ll \tau$, the average time between magnetic reversals is much larger than the measurement time. If the total magnetization of the particles reverses at shorter times than the experimental timescales, the system will appear to be superparamagnetic. If not, the system is in the blocked state [117, 119, 120, 122, 123], where the temperature at which the ambient thermal energy becomes equal to the volume magnetic anisotropy energy is defined as the blocking temperature T_B.

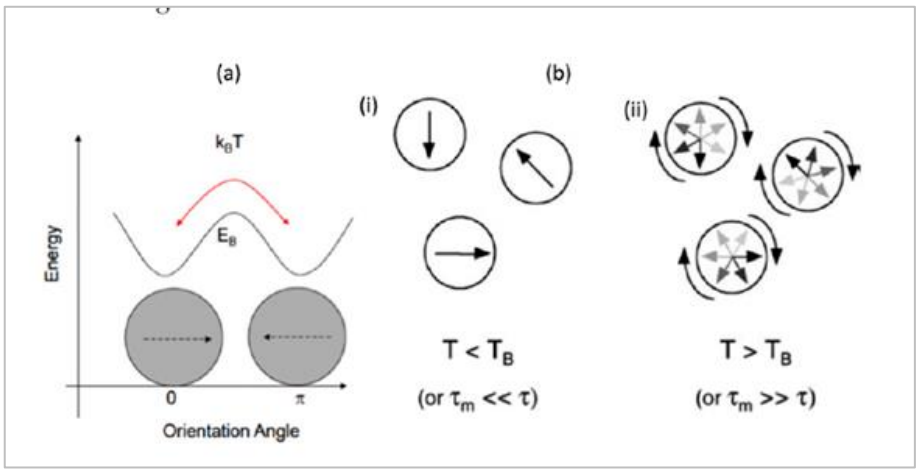

Fig. 1.21: (a) Scheme of the energy needed, EB, for the magnetization of a nanoparticle to flip between the parallel and antiparallel orientations along the easy axis. (b) Superparamagnetic nanoparticles in a (i) quasi-stable blocked state, and (ii) a freely rotating [123].

1.2.2. Magnetic anisotropy

When considering nanoscaled materials, the importance of anisotropy contributions in the understanding of the corresponding magnetic properties is highly increased [114, 124]. The magnetic properties of a material are determined by the magnetic anisotropies of such material that, in most cases them have a preferential direction (energetically more favorable) for their magnetic moments to align, usually called the easy axis of magnetization [105].

The primary sources of magnetic anisotropy are shape, magnetoelastic, magneto-crystalline and exchange anisotropies. The first is related to the shape of the material for non-spherical materials, and the demagnetization field will not be the same in all directions, creating one or more axes that are easy to magnetize. When applying pressure to a material, it can change its magnetization behavior due to stress-induced

anisotropy, also called magnetoelastic anisotropy. In magneto-crystalline anisotropy, the crystallographic structure of a material will influence its magnetic response, as some crystallographic directions are preferred for the alignment of the magnetization. Exchange anisotropy, on the other hand, is related to the interface interactions between two magnetically ordered systems, thus changing the magnetic properties of the material.

The intrinsic anisotropic properties of nanostructures with higher aspect ratios, such as nanowires (NWs), nanorods (NRs) and nanotubes (NTs) allows them to interact differently depending on the direction in which the field is applied [125]. The increased surface area in relation to the volume and magnetic moments are also superior when compared with the spherical counterpart, originating an anisotropic behavior that makes these magnetic NWs subject of intense study in recent years [86, 126, 127].

Several authors have already studied the interactions between NWs and between the different layers on the multi-segmented NWs [113, 128-131]. For real systems, even with a weak crystal anisotropy, the magnetization reversal is must be described in terms of nucleation propagation mechanisms. Ferré *et al.* [132] investigated the magnetic properties of Ni and Co NWs with different diameters (35–500 nm)). This study shows that intrinsic differences between magnetization reversal mechanisms are originated from the difference in interactions between magneto-crystalline and shape anisotropies and concluded that weak Ni crystal anisotropy loses to wire shape anisotropy, resulting in an easy axis parallel to the wire axis, while the easy Co axis depends heavily on the magnetocrystalline anisotropy and the orientation of the c axis of the hcp (100,101) [132].

Studies of the transition of easy axis orientation in Co nanowires have also been carried out. Pal *et al.* [133] make a study that relates aspect ratio (L/D) with experimental values and micromagnetic simulations. In these studies, they concluded that, for all aspect ratios ($R > 10$), shape anisotropy is the dominant contribution, which leads to an easy axis in the direction parallel to the wire. For proportions less than $R < 3$, magneto-crystalline anisotropy prevails and the easy axis is oriented perpendicularly to the axis of the wire, however in the intermediate proportions, anisotropies are comparable, so they are difficult to distinguish between the axis.

Elmekawy *et al.* present a study with hexagonal arrays of Fe NWs by templated electrodeposition using AAO templates. Magnetic properties of the nanowire arrays are studied using hysteresis loops and first-order reversal curves (FORC). The results show the presence of the easy direction of magnetization along the long axis of the

NWs. The anisotropy is more pronounced for long nanowires since the slope of their hysteresis curve is lower than for short ones when the field is applied perpendicular to the wires (Fig. 1.22 a and b). In short, NWs where the shape anisotropy is not so strong and the relative deviation from the average length is higher than in the long wires, the decrease of magnetization in the fields lower than H_c^k is most likely due to inhomogeneous magnetic states. In long wires, this mechanism also takes place but is prevented by shape anisotropy. Thus, the net magnetization value is reduced due to reversing of some wires (Fig. 1.22 c and d).

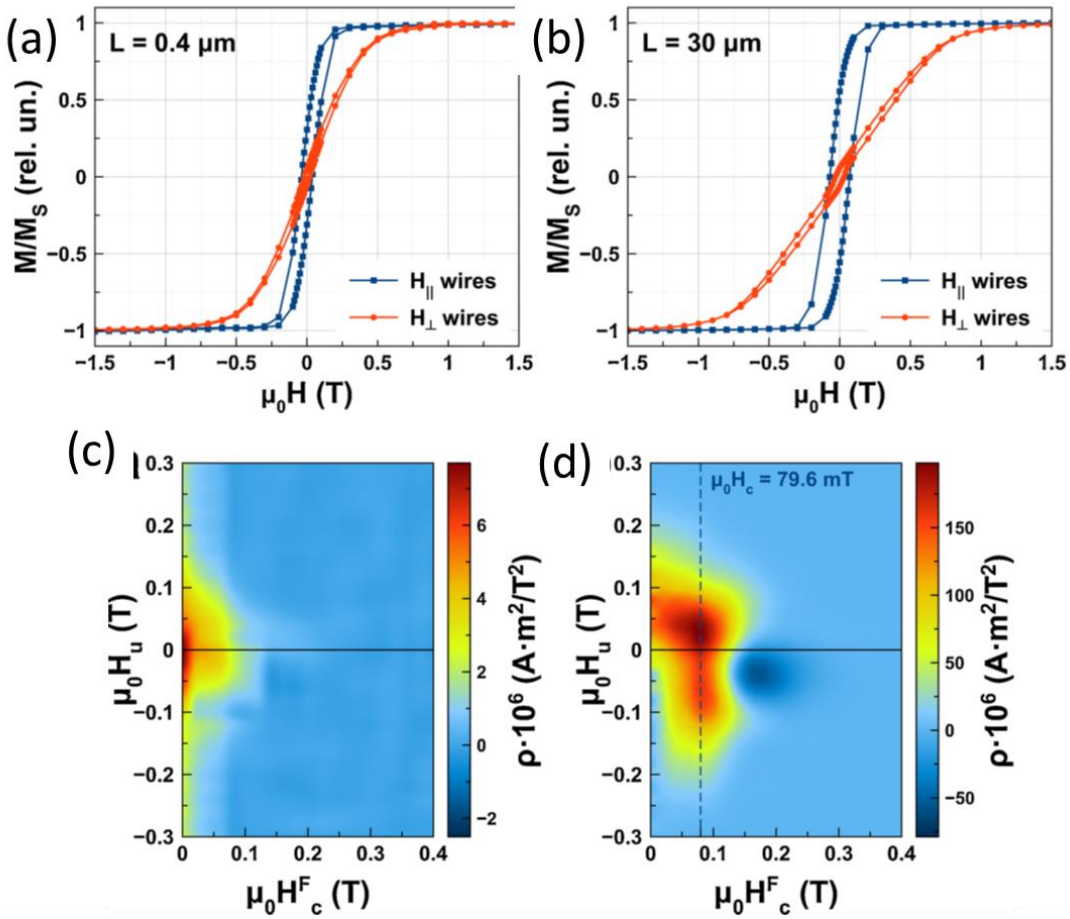

Fig. 1.22: Normalized magnetization reversal curves of iron nanowire arrays measured for (a) short (L = 0.4 μm) and (b) long (L = 30 μm) . FORC diagrams of Fe nanowire arrays containing (c) short (L = 0.4 μm) and (d) long (L = 30 μm) nanowires [134].

Several studies show different ways of influencing the easy direction of the axis, changing not only the dimensions of the wire but also its composition [135, 136] to verify how it is affected by magnetoelastic anisotropy [137].

1.2.3. First-order reversal curves (FORC)

The main hysteresis curves provide only information about the global behavior of magnetic systems, however, the first order reversal curve (FORC) and, through FORC diagrams, allows investigation of the processes that occur during the magnetization reversal of a set of magnetic entities. In 1986 Mayergoyz *et al.* [138] first proposed a mathematical model of first order reversal curves based on the Preisach model. In 1999 Pike *et al.* [139] developed the FORC diagram method, where its focus was on the various signatures of the FORC experimental diagrams for different types of samples. Since then, this technique has been widely used for the study of several systems: geomagnetic samples [140], magnetic arrays of submicron dots [141], nanopillars [142], hybrid magnetic elastomers [143] and nanowires [115, 144, 145].

1.2.3.1. FORC distribution (ρFORC)

The FORC measurement protocol is as follows: after a positive saturation, H_S +, the magnetic field decreases until a reversal field, H_{r1}, is reached. (Fig. 1.23). Then the magnetization, M, is measured as a function of the increase in the field, H, until saturation is reached again. To measure another secondary curve, the applied magnetic field is reduced from saturation to a new H_{r2} inversion field. This new inversion field is slightly larger than the previous one (H_{r1} <H_{r2}). Proceeding in a similar way to what has already been said, the applied field is increased, starting from H_{r2}, until the system saturation. In this way, repeated FORC curves are made with different reversal fields, until covering the entire area of the main hysteresis curve [142, 146].

The statistical FORC distribution r is calculated by applying a second-order mixed derivative of magnetization (M) with respect to H and to H_r.

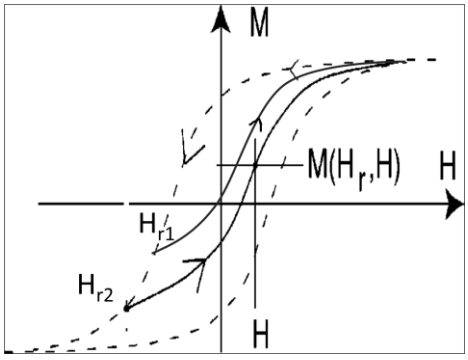

Fig. 1.23: Representation of the acquisition of a first order reversal curve (FORC) [146].

1.2.3.2. The classical Preisach model

The FORC method was based, at its origin, on the classical Preisach model. In this [147] model, the hysteresis can be modeled as a set of elementary processes. These operators are called “mathematical hysterons” to emphasize the mathematical nature of the model. In this mathematical model, the hysterons are characterized by two parameters, critical field (H_c) and interaction field (H_u) (Fig. 1.24 (b)). However, several different approaches are possible, based on in the physical hypothesis to interpret the FORC technique applied to a physical system, for example, physical analysis model, [148] or in mathematical distributions, for example, Preisach's mobile model [149].

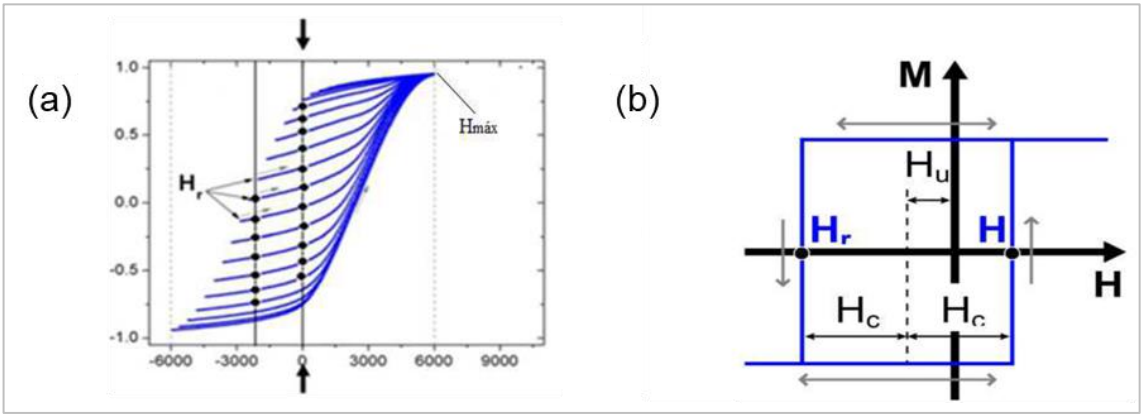

Fig. 1.24: (a) Example of a set of experimental first-order reversal curves (CoFe nanowire array, d = 15 nm, D = 55 nm, L = 1.6 μm, axial direction, ΔH = 50 Oe, ΔH_r = 100 Oe). (b) Mathematical hysteron from the classical Preisach model [147].

FORC measurement aims to recover the H_c and H_u parameters of each mathematical hysteron in the system. The difference in magnetization between the applied field and the reversal field is directly proportional to the number of hysterons that have returned to the initial state. This type of minor hysteresis curve is called the first order reversal curve. All information about hysterics in the system, the FORC distribution (ρFORC), can be obtained by applying a mixed second-order derivative of M to a set of FORCs starting at different times in order to general the process Fig. 1.24 (a) [146]:

$$\rho_{FORC}(H, H_r) = \frac{1\delta^2 M\,(H, H_r)}{2\ \ \delta H \delta H_r}(H > H_r) \tag{1.4}$$

Calculating the ρ distribution at each experimental point on the H - H_r plane (Fig. 1.25 (a), The three-dimensional diagram of the system's hysterons is obtained in a

three-dimensional diagram. The color scale ranges from blue to red, with zero representing the statistical distribution of hysterons in blue, while the maximum distribution is indicated in red as shown in Fig. 1.25 (b) [148].

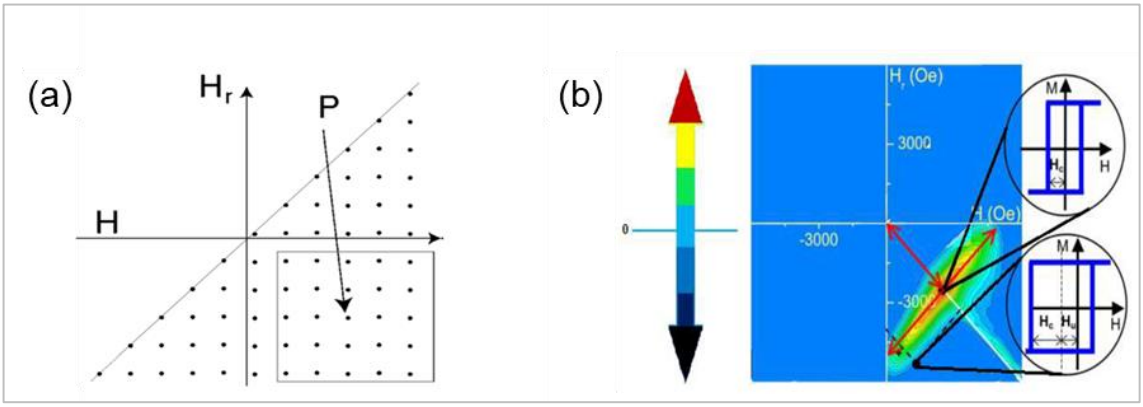

Fig. 1.25: (a) ρ distribution at each experimental point on the H - Hr plane, (b) Representation of a FORC diagram. The color scale ranges from blue, which indicates the zero of the distribution, to red, which is the positive maximum. The negative maximum of the scale is represented in black.

1.2.4. Vortex-state

The nanoscale provided new magnetic configurations due to the interaction between different energy terms, such as the contributions of dipolar energy or exchange anisotropy. Some factors are determinant for the rotation configuration present in the remance, such as geometry and aspect ratio of the structure [150]. The configuration of the magnetic vortex is being extensively studied and since it has been shown as the ground state at ferromagnetic points with different geometries (circular, elliptical or triangular). In specific micro/nanodisk conditions, energy minimization forces the spins to a wave state, where the directions of rotation gradually change, starting parallel to the surface, canceling the total energy of the dipole and also not losing much of the exchange energy [151]. In the central region of the disc the angles between adjacent rotations increase until it is no longer possible to remain in the state confined to the plane, resulting in magnetization perpendicular to the plane (vortex core) [150] as shown in Fig. 1.26.

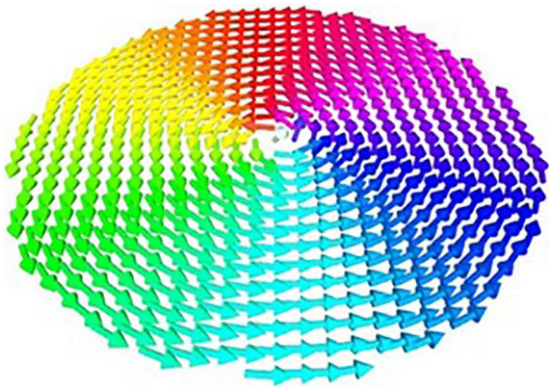

Fig. 1.26: Vortex core schematic.

Magnetic vortex state is characterized by the chirality that is related to the directions of rotating magnetization in the plane (counterclockwise or clockwise) and the direction of magnetization or polarity of the vortex core (up or down). The vortex-type remanent magnetization distribution is energetically favorable for the disks with weak magnetocrystalline anisotropy [152] and is either deduced from the hysteresis loop's shape [153] or directly observed by magnetic imaging techniques like magnetic force microscopy (MFM) [154].

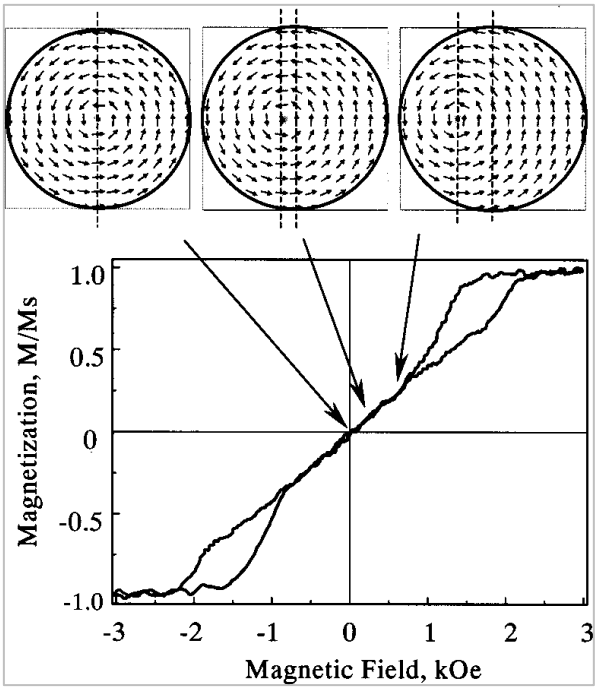

Fig. 1.27: Hysteresis loop and calculated field evolution of magnetic vortex for permalloy disk with diameter 0.2 mm and thickness 60 nm [152].

Guslienko *et al.* [152] shows the dependence of the magnetization with the applied magnetic field (Fig. 1.27). The loop was measured using a magneto-optical technique for the set of Permalloy discs (Py) with a thickness of 60 nm and a diameter of 0:2 μm. In the maximum saturation field, the disk is in a single domain state as the externally applied field decreases, leading to the nucleation of the vortex state, accompanied by an abrupt decrease in magnetization, in the so-called nucleation field, H_n. Then the magnetization responds linearly to the field, corresponding to the reversible movement of the vortex core, and includes the remaining state where the magnetization is practically null. The continuous decrease of the field causes the nucleus of the vortex to be expelled from the disk, marking the annihilation field of the vortex, H_a, after which the disk stabilizes again in a state of single domain [152, 155].

1.3. Fabrication of nanowires using electrodeposition assisted.

The main factors that make nanostructures applicable in nanoscience and nanotechnology are the possibility of being synthesized with uniformity and controllable shape and size. The manufacture of nanomaterials is generally categorized by using two different approaches: top-down and bottom-up. In the top-down approach, one starts with a bulk material and then divides it into smaller pieces until the desired nanosize is achieved, following the example of techniques that use these systems: nano-lithographic, such as electronic beam, X-ray and focused ion beam lithographs. In the bottom-up approach, atoms or molecules are used as building blocks that will constitute the final material, allowing for better precision in the manufacture of nanomaterials. production efficiency at lower costs. Among the various methods used to manufacture nanostructures, model-assisted manufacturing within the bottom-up approach is an elegant physico-chemical method and a reliable alternative to top-down approaches [156-158].

1.3.1. Multi-segmented nanowires by DC electrodeposition

Among several methods reported in the literature, self-organized nanostructuring using template assisted electrodeposition is a very promising and rapidly expanding field for the preparation of nanostructures ranging from the micrometer to few nanometers range. A well-known self-organized template to grow NWs and multi-segmented NWs in anodic alumina oxide, as it allows the low-cost and high-yield growth of highly ordered nanomagnet arrays.

1.3.1.1. Anodic alumina oxide (AAO)

The development of the anodizing process made possible to advance several techniques and methods, as it allows very precise control of template-assisted fabrication of nanostructures, such as nanowires and nanotubes [159]. In the laboratory, nanostructured anodic alumina oxide (AAO) can be produced by anodizing Al, which consists of an electrochemical process under specific conditions, with the use of an external voltage source, thus being an efficient, low cost and technologically simple process [160].

The process of the growth of AAO films relies on a balance between electrical-field-driven oxide formation at the metal/oxide interface and oxide dissolution at the electrolyte/oxide interface. In a simplified way, the occurring electrochemical processes can be represented as [161, 162]:

$$2Al(s) + 3\,H_2O\,(l) \rightarrow Al_2O_3(s) + 6H^+(aq) + \,6e^- \tag{1.5}$$

and

$$Al_2O_3(s) + 6H^+(aq) \rightarrow \,3Al^{3+}(oxide) + 3\,H_2O\,(l) \tag{1.6}$$

which correspond to the formation (Eq. (1.5)) and dissolution (Eq. (1.6)) of the oxide at the anode.

The potentiostatic regime the current density *j* (t) is monitored throughout the process. A typical curve obtained in the anodizing process is shown in Fig. 1.28. Highlighting the four main phases of pore formation and growth. First, the current density *j* (t) falls rapidly (phase I), which corresponds to the formation of the continuous non-conductive oxide barrier. Then, *j* (t) passes through a minimum value (phase II), where the oxide barrier reaches its maximum thickness. Due to fluctuations on the oxide surface, the local electric field in the low relief regions is greater, which leads to a rapid increase in current density (phase III). The damping observed in the curve corresponds to the competition of the pores during the process of self-organization. In this phase some pores fuse, inducing a slight decrease in the current density. Finally, the value becomes constant (phase IV), which corresponds to a continuous growth of the porous alumina layer [163, 164]. Thus, a longer first anodization improves the self-organization at the bottom of the pores (although always limited by the dimensions of the aluminum grains). Subsequently, AAO is removed by chemical attack.

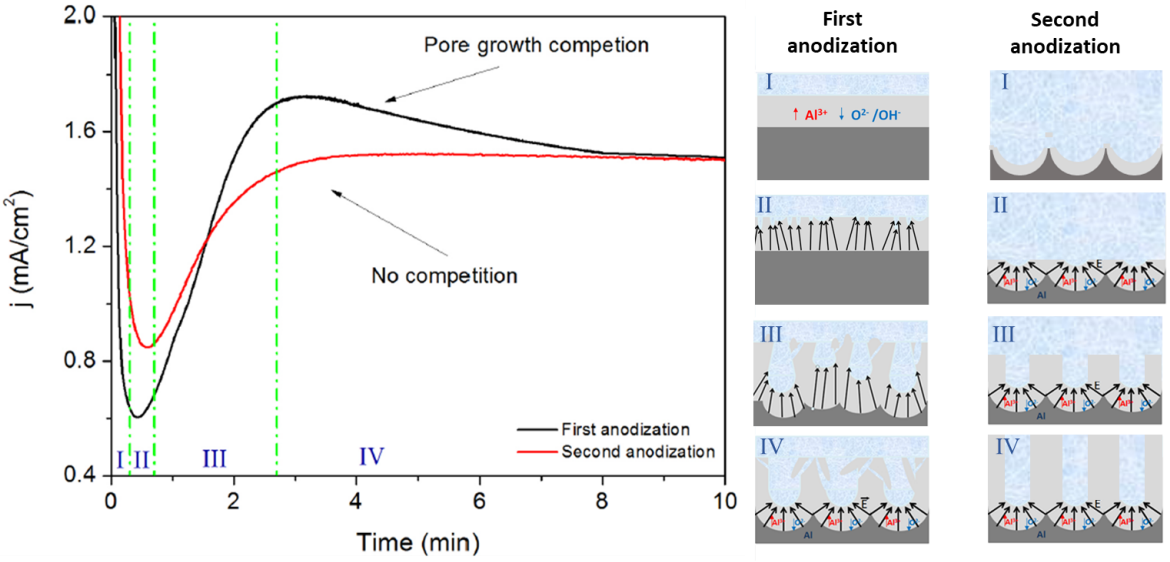

Fig. 1.28: Left: Graph of the curves j (t) of the first and second anodizing [165]. Right: Representation of the phases mentioned in the graph for the first and second anodization.

The concave and periodic patterns present on the aluminum surface serve as centers of nucleation of the pores in the second anodization. The red curves *j* (t) (Fig. 1.28) represent the second anodization, where it is possible to observe that there is no competition during the growth of the pores, as self-pattern organized regime was already achieved , so the pores grow with perfectly alignment and by using the same parameters as the first anodization [166, 167].

1.3.1.2. The hard anodization regime

Hard anodization (HA) has been used in the industry since the 1960s for high-speed manufacturing of films with better strength and low porosity Al oxide [168]. A new method for the rapid fabrication of long-range AAO membranes ordered by HA has been introduced by Lee, *et al.* [168] using oxalic acid with a reduced processing time, which provides high thickness films (100 μm) with growth rates around 50 - 100 μm/h, due to the application of high voltage (V = 100 - 150 V). The greatest difficulty of this process are rupture effects caused by high current densities, therefore to allow uniform growth it is necessary to pre-anodize an oxide layer (thickness> 400 nm) on the Al substrate surface before performing the HA process. This protective layer is created through a common MA process using 0.3 M oxalic acid at 40 V for 5 - 10 min [28]. Thereafter, the anodizing voltage is slowly increased to a targeting voltage (100-150 V) for HA at a rate of 0.5-0.9 V s^{-1} and finally HA will be continued under constant potential. In this way, highly vertically oriented AAO pores can be made much faster than the MA process.

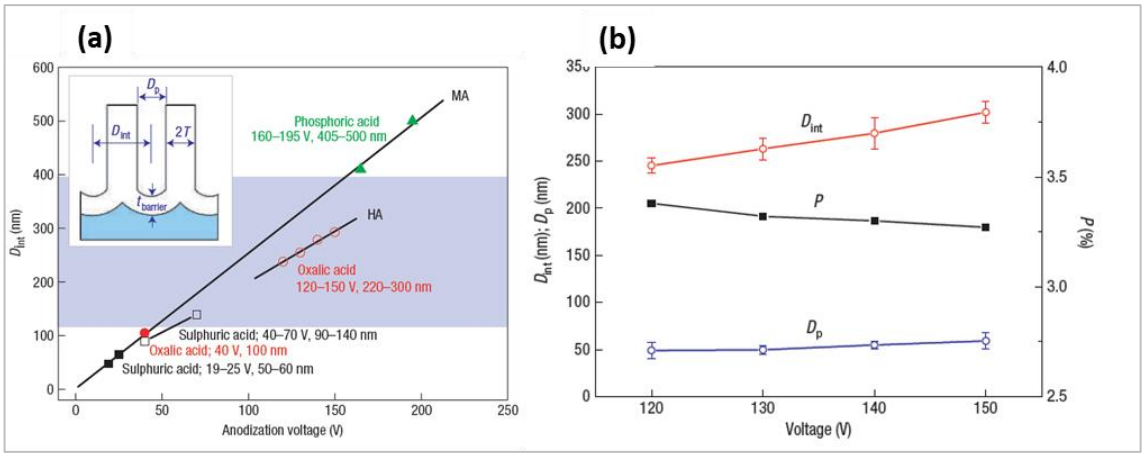

Fig. 1.29: (a) Relationship of the anodization voltage and the corresponding interpore distances (D_{int}). In conventional MA: sulfuric, oxalic and phosphoric acid and in HA: sulfuric and oxalic acids. (b) The evolution of interpore distance (*D*int), pore diameter (*D*p) and porosity (*P*)as a function of the HA voltage for 0.3M [168].

Figure 1.29 (a) shows the relationship between D_{int} and the anodizing voltage for HA compared to MA. It should be noted that the present HA process establishes a self-ordering regime in the range of D_{int} = 200–300 nm, filling the gap that was not reached by conventional MA processes. This also makes it possible to enlarge the pores of a few tens of nanometers by controlled chemical processes, without causing them to rupture [168]. The evolution of *D*int, pore diameter (*D*p) and porosity (*P*) as a function of the HA voltage for oxalic acid can be seen in the Fig. 1.29 (b). For anodization voltage from 120 to 150 V, a range for Dp of 49 - 59 nm was obtained, this relatively low value can be explained by the alumina dissolution rate, which is determined by the pH value at the bottom of the pore. For the production of NDs larger pores are needed, however, since Dint is much larger, a process of enlarging the pores by chemical attack allows the use of AAO by HA as a template for NDs with vortex state.

1.3.1.3. Electrodeposition of multi-segmented nanowires

Electrodeposition consists of the formation of a metallic layer on a substrate and occurs through the electrochemical reduction of metal ions from an electrolyte [169]. The general experimental setup, which allows the electrodeposition process in an AAO membrane, is shown in Fig. 1.30, and basically consists of immersing the membrane (cathode) and counter electrode (anode) in an electrolytic solution containing ions of the metal to be deposited , followed by the application of a potential between both electrodes to make the current flow possible [162]. The generic reaction for the metal forming process is given by [162, 169]:

$$(M_x L_y^z) + zxe \rightarrow xM^0 + yL \tag{1.7}$$

where z represents the number of electrons transferred per deposited metal atom, L a molecule, an ion, or radical hat is strongly linked to the metal ion M forming species $(M_x L_y^z)$, participating in the charge transfer process. Eq. 1.7 shows that z electron are needed to be transferred in order to perform the deposition of one metal atom. Consequently, to form the deposition of a metal molar, a charge of $N_A ne = nF$ Coulomb is required, where N_A is the Avogadro number $N_A = 6.022 \times 10^{23} mol^{-1}$. This relationship is known as Faraday's Law [162]:

$$m = \frac{QA}{nF} \tag{1.8}$$

where m is the mass of the deposited material (in grams), Q the net charge that passes through the circuit (in Coulombs) and A is the atomic mass of the metal. This equation is used to calculate the amount of metal to be deposited and to determine the electrodeposition time that is required to reach a predetermined thickness. When the substrate where we are going to deposit is a nanoporous template, it is usual to represent Eq. 1.8 in the following way [162, 169]:

$$h = \left(\frac{V_m}{zf}\right)\left(\frac{I}{S}\right)\tau \tag{1.9}$$

where $h = \mathrm{m}/\mathrm{Sd}$ and h is the length of the pore, S is the surface area, d is the density of the material, τ is the duration of electrodeposition and V_m is the molar volume of the metal. This equation highlights the importance of current density $J = \mathrm{I}/S$, since it regulates the rate of the deposition process and, therefore, it is the most practical measure to calculate the rate of any electrochemical process and its value is easily determined from knowing the area (S) of the electrode. In the deposition on nanoporous membranes, each pore represents a region of low resistivity, and the electrochemical processes start their nucleation in regions of high electric field, called active centers or growth regions, like in the anodizing process. As a consequence, J is initially non-uniform during the nucleation process and the tends to be constant during the pore growth [169].

1.4. Nanostructured lipid carriers

When talking about nanostructures for biomedical applications, it is known that the main objective of all strategies is to go unnoticed until they reach the target, and even if some materials are biocompatible, such as Fe, Au, etc. The form in which it is found can make them detectable by the immune system and thus be eliminated before reaching the target. In addition to drug delivery systems, there is also the need to confine and protect the drug and reduce its toxicity in the body. In this sense, Nanostructured lipid carriers (NLCs), which are lipid-based formulations, have been widely studied as drug delivery systems and can be the shell for a magnetic or plasmonic core. These systems have a mixed solid/ liquid lipid matrix at room temperature and are considered to have enhanced advantages when compared to many other traditional lipid-based nanocarriers, such as nanoemulsions, liposomes and solid lipid nanoparticles (SLNs) due to their physical stability, improved loading capacity and biocompatibility. This section focuses on the latest advances in the use of NLCs as drug delivery systems targeting tumors and their preparation and characterization techniques.

1.4.1. Types of lipid based carriers.

Nanotechnology has revolutionized the delivery of drugs, especially chemotherapeutic agents, providing alternative solutions with better safety and efficiency. The various types of nanoparticles with sizes between 10 to 1000 nm and a variety of special characteristics make these drug carriers suitable for an external range of applications, ranging from dermatology to complex treatments involving various therapies [170, 171]

.

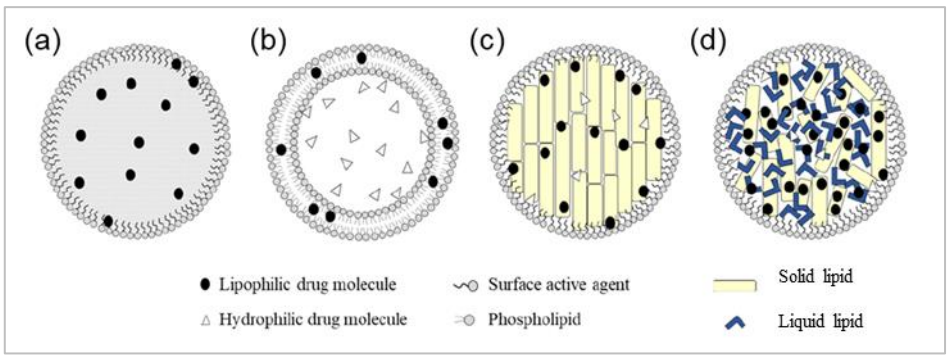

Fig. 1.30: Generic scheme of different types of lipid-based nanoparticles. (a) Nanoemulsions; (b) liposomes; (c) solid lipid nanoparticles (SLNs); and (d) nanostructured lipid carriers (NLCs) [172].

Many types of nanoparticles used as drug carriers are generally, but not necessarily, made of polymers or lipids [173]. Among these two types, we can highlight that lipid based nanoparticles, have some advantages over polymeric nanoparticles, such as cytotoxicity and the lack of adequate methods for large-scale production [174]. Lipid based delivery systems encompass different structures such as nanoemulsions, liposomes, SLNs and NLCs (Fig. 1.30).

Liposomes were the first nanoscale delivery system to be approved for clinical use in 1995 and continue to be the most used nanobased structures in clinical practice [175]. However, liposomes still present some drawbacks such as their complicated production method, low percentage entrapment efficiency (% EE), difficult large-scale manufacture, high production cost and thus SLN delivery systems have emerged.

Solid lipid nanoparticles (SLN) were first reported in the early 1990s and became known as the first generation of nanoparticles based on a solid lipid matrix at room temperature [176, 177]. These systems showed multiple advantages over other previously developed lipid systems, namely liposomes and nanoemulsions, since it is possible to avoid the use of organic solvents ensuring the protection of loaded therapeutic agents [178, 179]. However, SLN are limited by the low efficiency of the drug load and the increased risk of expelling the drug from the formulation in storage, due to polymorphic transitions of the solid lipid [180]. To overcome this limitation, Müller *et al.* [180] proposed a mixture of liquid lipids and solid lipids that form a solid amorphous matrix at body and ambient temperature and this was sufficient to significantly improve the properties of the formulation compared to SLNs. The presence of the liquid lipid creates an amorphous network that produces imperfections in a solid crystalline matrix, which makes it possible to accommodate a greater drug load [181].

With this simple change, NLCs became the second generation of lipid nanoparticles and proved capable of expanding the range of use and overcoming many of the limitations associated with conventional lipid carriers [182, 183]. For example, having solid state NLCs at room temperature has improved physical stability, which is a major barrier in emulsion-based formulations [174]. It has suitable methods for large-scale production, which solves the expensive technological requirement for mass production of liposomes [174]. In addition, NLCs are biocompatible systems, and able to adapt to various combinations of systems, including magnetic nanoparticles that allow a wider range of applications in diagnosis and therapy [28].

1.4.1.1. Types of nanostructured lipid carriers

NLCs are prepared by mixing spatially incompatible combinations of liquid lipids and solid lipids, that is, the liquid lipid molecules do not contribute to the crystalline matrix and the solid lipid crystals do not dissolve in the liquid lipid, however the liquid lipid must be present as compartments nano-size within the solid crystalline matrix [184, 185]. It forms an imperfect nucleus and a possible amorphous matrix, allowing greater loading of drugs and preventing the escape of drugs. NLCs can be classified according to the nature of their lipid content and formulation parameters into three different types [172, 183, 184]:

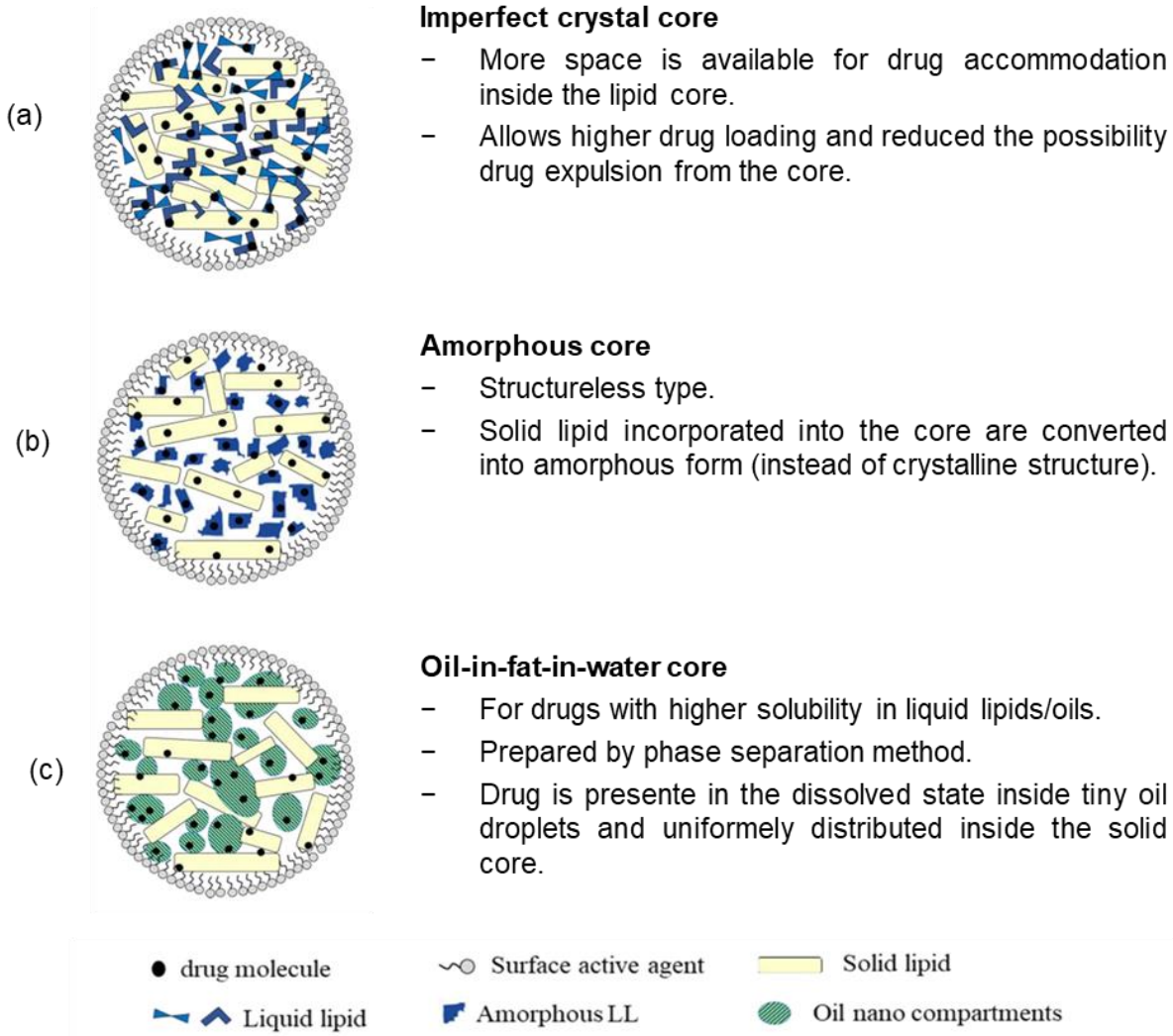

Fig. 1.31: Types of NLCs. (a) Imperfect; (b) amorphous; and (c) oil-in-fat-in-water. Adapted from [172] and [183].

NLC type I: Imperfect type. The substitution of a fraction of solid lipid by lipid / liquid oil causes the formation of an imperfect crystal matrix/reticulum. This phenomenon shows the availability of more space to accommodate the medication and allows greater loading of medications avoiding the formation of a highly structured or ordered matrix that would have expelled the medication out of the nucleus Fig. 1.32 (a).

NLC Type II: Amorphous type/without structure. The solid lipids remain in the polymorph after solidification and storage together with liquid lipids and form an amorphous core. This is advantageous in relation to NLCs of type I, since crystallization does not occur, and the drug remains incorporated in the amorphous matrix Fig. 1.32 (b).

NLC Type III: Multiple type and developed from the emulsion concept. It is basically NLC type oil in solid or fat in water, which can be developed only by the phase separation technique. Ideal when the drug shows greater oil solubility, this approach improves the drug's capacity and load stability. The oil droplets dispersed evenly in the solid lipid matrix are dispersed in the aqueous medium Fig. 1.32 (c).

In general, the formulation of NLCs involves the nanoemulsification of a lipophilic phase composed of a mixture of liquid, solid lipid and surfactants/emulsifiers, in an aqueous solution. Techniques used in the formulation of NLCs include high pressure homogenization (HPH), solvent emulsification/evaporation, microemulsification, ultrasound or high-speed homogenization, spray drying and microfluidic technology [177]. When NLCs are used as carriers of chemotherapeutic drug molecules, the selected ingredients must be biocompatible, non-toxic and suitable for systemic administration [186]. Table 1.2 lists examples of solid lipids, liquid lipids and surfactants used in the preparation of NLCs for the administration of anticancer drugs.

Table 1.2: NLCs most used components in the development of anticancer delivery systems.

Type	Name	References
Solid lipids	Glyceryl behenate (Compritol® 888 ATO)	[187-190]
	Glyceryl distearate (Precirol® ATO 5)	[188, 190-193]
	Cetil palmitate	[194-196]
	Gelucire	[197, 198]
	Stearic acid	[199-201]
Liquid lipids	Oleic acid	[189, 199, 202, 203]
	PEG-8 caprylic/capric glycerides (Labrasol®)	[193, 204]
	Squalene	[188, 205]
Surfactantes	Tween® 80	[188, 192, 206]
	Pluronic® F-68 (Poloxamer 188)	[192, 201, 203, 207]
	Soy lecithin (Epikuron—200)	[201, 207, 208]
	Pluronic F127 (poloxamer 407)	[190]

1.4.2. Cancer therapy using nanostructure lipid carriers

Special attention has been given to the use of NLCs for delivery of chemotherapeutic agents due to their capability to improve the physical and chemical stability of the incorporated drugs and to highly boost the potential of those therapeutically effective agents (usually referred by their poor pharmacokinetic properties) [180, 209, 210]. In Table 1.3 are presented several examples of NLCs used in delivery and the targeted chemotherapeutic agents, displaying enhanced IC_{50} *in vitro* and tumor inhibition rates *in vivo*. In those studies, it was demonstrated the use of NLCs as carriers for different chemotherapeutic agents and their outstanding ability to enhance the therapeutic effect to several drugs on a wide diversity of malignancies. This is accomplished by loading NLCs with either the chemotherapeutic agents alone or combined with a low dose of an adjunct or by conjugating the drug-loaded NLCs with a targeting fraction for active targeting.

In the case of breast cancer, recent clinical treatments comprise chemotherapy, radiation therapy and hormonal therapy. This leads to larger systemic exposure of drugs, with consequent systemic side effects, organ toxicities and poor compliance. Moreover, breast cancer cells are a potential cause of metastatic tumors leading to multidrug resistance (MDR). Therefore, targeted delivery in the form of nanocarriers is widely investigated to minimize all these complications [211].

Li *et al.* [212], in their work, referred the co-delivered lapachone and doxorubicin in the form of NLCs (LDNLC) for the treatment of MDR in breast cancer therapy. Lapachone was responsible for the generation of reactive oxygen species and downregulated the P-glycoprotein (Pgp) efflux pump activity. It led to an efficient accumulation of the drug in tumor cells, inhibiting tumor cell proliferation by disabling MDR. These researchers found enhanced efficacy of co-delivered LDNLC comparatively with the mono-drug delivery alone in MCF-7 ADR cells [212]. On the other hand, thymoquinone loaded NLC showed enhanced *in vivo* anticancer efficacy in mice upon oral administration, showing also inhibited metastatic properties of 4T1 cancer cells [213]. Novel C-substituted di-indolylmethane derivatives (DIM-10 and DIM-14) were developed as NLC, and their anticancer efficacy was evaluated in triple-negative breast cancer models upon oral administration. These formulations showed a significant decrease in the volume of tumor and enhanced the pharmacokinetic properties [213]. In other studies, using doxorubicin combined with NLCs and liposomes showed that NLC-DOX and liposome-DOX presented some control in the tumor dissemination, but NLC-DOX showed to be superior to liposome-DOX, indicating that NLC might be an alternative strategy to achieve the efficient antitumor activity.

Wang *et al*. [214] develop NLCs with biochanin A (BCA), and the results revealed that BCA–PEG–NLC not only have small mean particle (148.5 ± 2.88 nm) with a narrow polydispersity index (PI) (0.153 ± 0.01), encapsulation capacity (99.62 ± 0.06%), payload (9.06 ± 0.01%), zeta potential (−19.83 ± 1.19 mV), but also slower release rate compared with BCA suspension over 48 h by the dialysis method (n=3). The crystallinity of lipid matrix within BCA–PEG–NLC was evaluated by differential scanning calorimetry (DSC), which verified the BCA was successfully encapsulated into the nanoparticles. This study suggested that PEG–NLC is a novel anti-cancer nanoparticle, which could provide attractive treatment for a wide variety of tumors and improved the oral bioavailability of poorly water-soluble drugs.

1.4.3. Oral administration

Oral administration is a common method for most medications. However, some reasons make this method impossible for others, such as low solubility, stability and bioavailability. In addition, drug administration must overcome numerous obstacles, including the acidic gastric environment and the continuous secretion of mucus that protects the gastrointestinal tract. In this sense, nanoparticle drug carriers can protect drugs from degradation and deliver them to the intended locations within the gastrointestinal tract delivering drugs [215].

However, there are significant barriers in the gastrointestinal tract for nanoparticle formulations such as acidic stomach environment and degrading enzymes in the intestine. In addition, nanoparticles must penetrate the mucus barrier in the gastrointestinal tract and are secreted by the epithelium, which is not a simple process, since the unique rheological and adhesive properties of the mucus protect the epithelium from mechanical forces and pathogens and foreign particles. In addition, the rapid rates of mucus secretion and removal efficiently remove foreign materials, limiting the permanence time of the nanoparticles administered orally [215]. However, studies utilizing different sized nanoparticles demonstrated that particles with 300 nm in size or less are ideal for oral administration since they are preferentially internalized by both enterocytes and M cells and demonstrate higher intestinal transport compared to larger sized particles [216, 217].

Table 1.3: Examples of nanostructured lipid carriers (NLCs) for chemotherapeutic agents delivery (Adapted from [218]).

Treatment	Control Drug	Cancer Type	*In Vitro* Cell Line	IC50			*In Vivo* Tumor Inhibition Rate		References
				Drug-NLCs	Free Drug	Blank NLCs	Drug-NLCs	Free Drug	
Paclitaxel-NLC (PTX-NLC)	Paclitaxel	Breast cancer	MCF-7	0.075 µg/mL	0.29 µg/mL	455.49 µg/mL			[219]
		Multidrug-resistant breast cancer	MCF-7/ADR	0.065 µg/mL	8.61 µg/mL	496.74 µg/mL			
		Ovarian carcinoma	SKOV3	0.053 µg/mL	0.16 µg/mL	487.92 µg/mL			
		Multidrug-resistant ovarian carcinoma	SKOV3-TR30	0.1 µg/mL	9.35 µg/mL	498.97 µg/mL			
		Non-small cell lung carcinoma	H460	0.062 µM	0.193 µM	-	64%	26%	[220]
Doxorubicin-NLC (DOX-NLC)	Doxorubicin	Breast cancer	MCF-7	0.15 µg/mL	0.176 µg/mL	455.49 µg/mL			[219]
		Multidrug-resistant breast cancer	MCF-7/ADR	0.83 µg/mL	6.20 µg/mL	496.74 µg/mL			
		Ovarian carcinoma	SKOV3	0.33 µg/mL	0.52 µg/mL	487.92 µg/mL			
		Multidrug-resistant ovarian carcinoma	SKOV3-TR30	0.52 µg/mL	1.83 µg/mL	498.97 µg/mL			
		Non-small cell lung carcinoma	H460	0.059 µM	0.176 µgM	-	65%	26%	[220]
		Hairy cell leukemia	HC2 20d2/c	15.01 ± 0.5	17.81 ± 1.2	-			[221]
Quercetin-NLC (Q-NLC)	Quercetin	Breast cancer	MCF-7	15.8 µg/mL	>50 µg/mL	>50 µg/mL			[222]
			MDA-MB-231	14.1 µg/mL	>50 µg/mL	>50 µg/mL			
Tamoxifen NLC (TAM-NLC)	Tamoxifen	Breast cancer	MCF-7	5.56 µg/mL	2.72 µg/mL	-			[223]
			4T1	5.19 µg/mL	5.13 µg/mL	-			

Chapter 2

Experimental Techniques

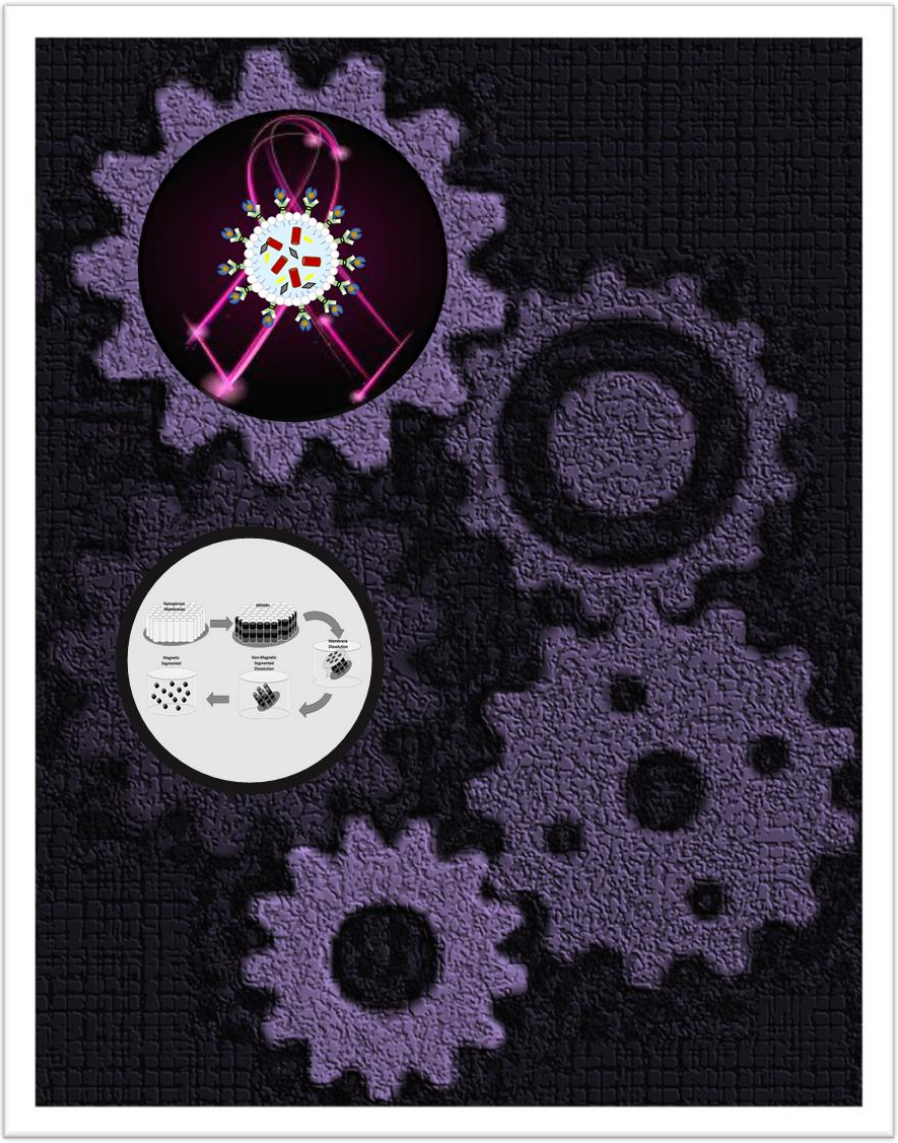

Chapter 2

Experimental Techniques

In this Chapter, it is presented a general description of the experimental techniques used in this work. First, we present the nanofabrication methods used to produce the metallic nanowires (NWs), including the anodization and electrodeposition techniques, the fabrication of superparamagnetic iron oxide nanoparticles (SPIONs) and nanostructured lipid carriers (NLC). Then, all the characterization techniques are generally described, namely morphological, structural, magnetic and optical characterization. Finally, we describe the cellular assays studies applying the fabricated NLC and NWs.

2.1. Nanofabrication

The nanofabrication processes were carried out at the IFMUP nanofabrication laboratories of the Faculty of Sciences and at the LAQV laboratory, REQUIMTE, Faculty of Pharmacy, both from the University of Porto. For both nanowires (NWs) and nanostructured lipid carriers (NLCs), it was used the same fabrication principles optimized previously by these research groups, that showed to be adequate for this work.

2.1.1. Nanowires by electrodeposition method

A set of multi-segmented Fe/Cu nanowires were synthesized using first a two-step anodization of aluminum substrates (it works as a template for the growth of the nanowires), followed by a pulsed electrodeposition technique using a single chemical bath. The fabrication of anodic alumina oxide (AAO) by mild anodization has already been extensively studied by the IFMUP research group, resulting in a highly standardized setup with well-defined parameters such as pore size, template thickness, etc [1]. On the other hand, the AAO fabrication by hard anodization, a technique still few explored, required additional optimization processes. Multi-segmented nanowires using a single bath were first developed at IFMUP for electrodepositions of Ni/Cu NWs

[113], whose setup and parameters were shown to be also suitable for the electrodeposition of Fe/Cu NWs fabricated in this work.

2.1.1.1. Aluminum pre-treatment

In the fabrication process of the AAO, the surface pre-treatment, prior to the anodization process, plays a crucial role in the formation and organization of the pore structure. The specific pre-treatment employed to the Al substrates included substrate washing for degreasing, followed by electrochemical polishing. Since detailed optimization of the Al pre-treatment was a topic intensively investigated at IFIMUP and is readily available [224-226], here we simply present a short summary describing only important details regarding the performed pre-treatments.

The Al foil was acquired in 30 cm X 30 cm plates being necessary first to cut in pieces with the desired sample dimensions, and then levelled under adequate planar pressure using a home-made pressing machine. Then, the substrates were degreased in acetone for 3 minutes in an ultrasound bath, followed by an ethanol bath also for 3 minutes to remove organic contaminations resulting from the industrial rolling process and manipulation. Before starting the electropolishing process, the Al substrates were rinsed in fresh ethanol, due to the hydrophobic nature of the electropolishing solution [1]

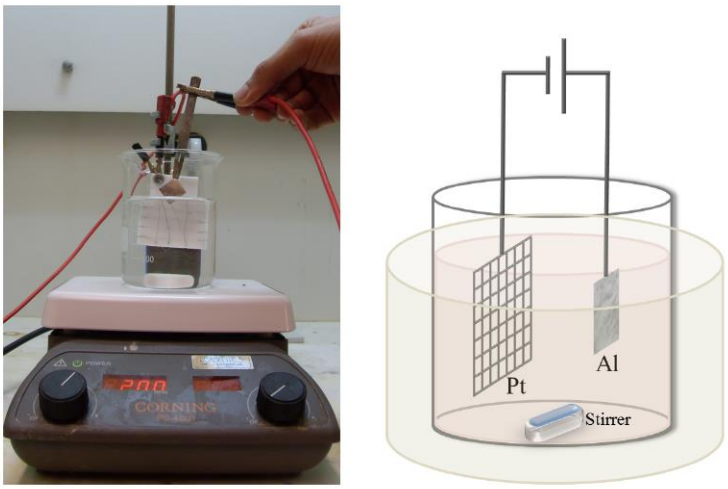

Fig. 2.1: Experimental setup for the electropolishing pre-treatment [1].

The Al surface was electrochemically polished prior to the anodization process, in order to further improve the structure and organization of AAO [226]. Electropolishing is the electrolytic removal of metal in an ionic solution by means of electrical potential and

is used to remove a thin layer of undesired materials on the surface of the metal. In the electropolishing set-up, the metal substrate is used as the anode and a Pt mesh is used as the cathode (Fig. 2.1), both submerged in an electrolyte solution of $HClO_4$: C_2H_5OH (volume ratio 1:4), establishing an electrical circuit where a DC voltage is applied. The electric field lines are more concentrated at the edges of irregular topographic points, compared to the rather smooth valleys regions. Therefore hilly points in the metal surface will be removed faster than the ones at valleys, resulting in a smooth and clean metal surface with a mirror-like finishing [227]. The electropolishing was performed at a temperature of ~10 ^{o}C, with a potential of 20 V for 2 minutes, under continuous vigorous stirring [226]. At the end, the substrates were rinsed in ethanol, followed by deionized water and dried in air.

2.1.1.2. Anodization of aluminum

A home-made set-up (scheme shown in Fig. 2.2) was implemented at IFIMUP for the growth of nanoporous templates through electrochemical oxidation (anodization) of Al foils, and also for the preparation of other nanostructures such as NWs and NTs by chemical-based template-assisted-methods [228, 229]. The anodization cell consists in a Teflon container where at the bottom we place the Al substrate (working electrode), and a Pt mesh is inserted at the top (counter electrode). The Teflon is used for being non-reactive, and adequate to be used with acidic solutions, providing at the same time good thermal insulation for the refrigerated electrolyte. The base of the cell is a Cu plate used to cool down the sample through a cooling mechanism. A mechanical stirrer used during anodization allows us to accurately control the stirring (200 - 250 rpm) of the solution during the anodization in order to improve the homogeneity of the solution concerning temperature, pH and gradients of concentration. Both the working electrode and the Pt mesh are connected to a terminal of a Keithley 2400 Sourcemeter. A computer connected to the sourcemeter controls the desired anodization or electrodeposition routines (through a LabView software), and it is also used for data acquisition during the experiment.

2.1.1.2.1. Mild anodization

The first anodization was performed using 150 ml of oxalic acid 0.3 M, for 24 h. During the anodization, the electrolyte solution was maintained at a constant temperature of 2˚C and homogeneously stirred at 200 rpm, and a potential of 40 V was applied in DC mode. In order to fabricate ordered nanopore arrays in which the holes

are straight and regularly arranged throughout the oxide film, i.e. in hexagonal close-packed arrays, a two-step anodization process similar to that reported by Masuda *et al.* [230] was employed. In the first anodization process, the hexagonally ordered pores were formed only at the bottom layer by a self-organization process. Subsequently, a chemical dissolution of the resulting AAO was achieved by submerging the sample in an aqueous solution of H_3PO_4 (0.4 M) and $H_2Cr_2O_7$ (0.2 M) at 40 ºC for about 12 hours. The remaining periodic concave patterns on the Al substrate act as pore nucleation centers for the second anodization process. An ordered nanopore array was obtained after anodizing for the second time by using the same parameters described above for the first step, however, to obtain thicker membranes (to facilitate handling during the entire process) the anodization was performed for 40 hours.

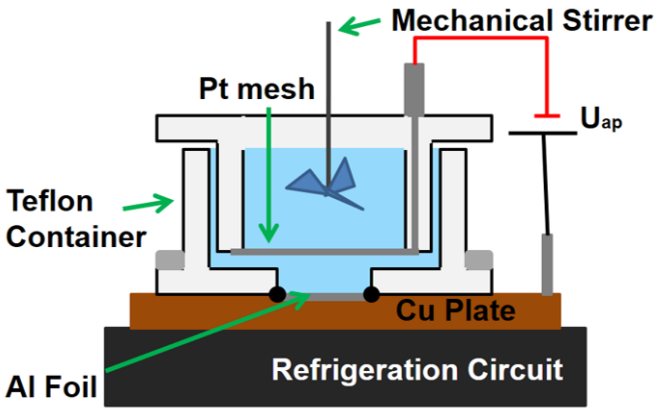

Fig. 2.2: Scheme of anodization cell.

2.1.1.2.2. Hard anodization

This method is based on high voltage regimes. The first anodization step consists in the application of 40 V for 24 h (mild anodization conditions) while keeping the temperature around 2°C, and subsequent chemical etching of the grown aluminum oxide layer. After dissolution of the oxide layer, a periodic concave-triangular features formed on the aluminum surface serve as nucleation sites for the formation of nanopores during the second anodization (second step).

In order to suppress breakdown effects caused by the high current densities, a thin oxide layer is first created by anodizing the Al foil in oxalic acid 0.3 M, in MA conditions, for 5 min. Then, without changing the electrolyte, the potential is shifted at 0.6 Vs^{-1} to the desired values, in this case, 140 V. The high potential regime is then maintained for 3 hours. In respect to the tailoring of the AAO pores, a precise controlled pulse was applied, varying the potential as desired to obtain tailored AAO templates. A home-

made LabVIEW program was developed to easily change the parameters. In the end, a transition to a MA regime is performed at 40 V for 5 min to stabilize the barrier layer at the bottom of the pores.

2.1.1.3. Aluminum removal and AAO pore widening

After the anodization process, the Al was removed from the samples using 50 mL of 0.2 M $CuCl_2$ in a 4.1 M HCl aqueous solution, at room temperature. The released AAO templates were then floated in 0.5 M phosphoric acid (H_3PO_4) aqueous solution at room temperature, to remove the nanopore bottom and increase the pore diameter; the principle of this procedure consists in put the templates laid carefully on the surface of the solution, with the bottom side in contact with the acid. The membranes float, with the top side never below the liquid level, until they start to create bubbles on the top of the surface to further sink into the solution, which means that the pores have been opened. The temperature of this process required optimization for hard anodization membranes. In fact, at room temperature, besides the amount of time needed to widen the pores (~12 h), it was observed that the acid solution started to corrode the sides of the floating membranes, leading to very thin templates that were not possible to use. Several trials with different temperatures were performed in order to obtain solid, high resolution, and well reproducible membranes. The optimum conditions were observed with the process performed in a stirred-thermic bath (to ensure temperature uniformity) at 55 °C and 500 rpm. Under these conditions, the sinking of the membranes was observed after a time of ~30 min.

2.1.1.4. Deposition of Au electrical contacts

To create electrical contacts in the bottom of the nanopores for electrodeposition, a thin gold (Au) layer was then sputtered on the backside of the AAO membranes to serve as the working electrode, using sputtering deposition.

Sputtering is a physical vapor deposition technique, where the atoms from a target material are ejected (through momentum transfer) by collision with gas ions generated by electric field [231, 232]. A sputtering system consists in two parallel plates, the target (cathode) and the substrate (anode). If inert gas argon (Ar) with low reactivity is included in the cathode gas tube, by voltage applied across the tube, some ionization is produced by collision of electrons with gas atoms. These electrons ionize the Ar atoms into Ar^+ cations. Under these conditions of glow discharge, the cathode will be bombarded with ions, resulting in the ejection of the cathode material, known as

plasma sputtering, and will be deposited on the surface of the sample (Fig. 2.3(a)) [233, 234].

A way to increase the ion density without increase the pressure is through magnetron sputtering employing DC power (works with reduced operating pressures and much higher deposition rates) [231]. In the case of magnetron sputtering, a magnetic field is placed at the surface of the target (cathode), parallel to the substrate (perpendicular to the electric field) (Fig. 2.3 (b)). By interaction between strong magnetic and electric fields, the electrons follow spiral paths at a confined superficial area of the target, increasing the collisions with Ar gas, generating more ions. The orthogonal electromagnetic field formed on the surface of the target enhances the ionization efficiency, thus increasing the plasma density and the sputtering rate. Also, avoiding the heating up of the substrates by electrons drifting in direction to the substrate [235].

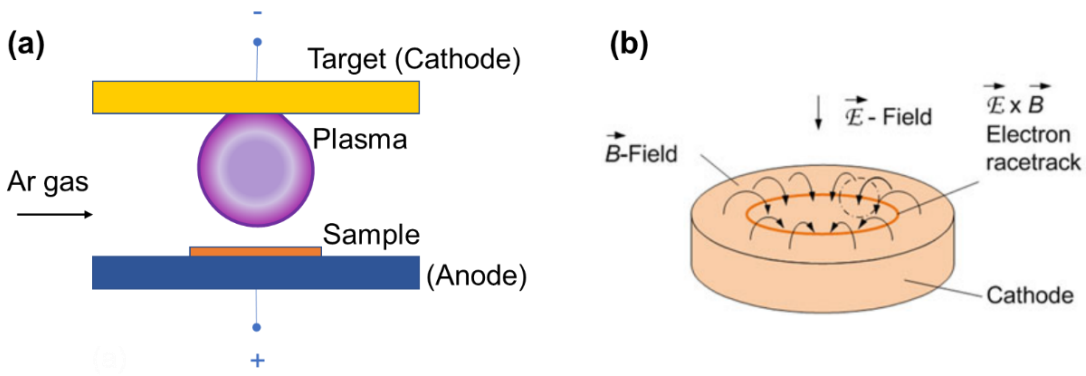

Fig. 2.3: (a) Schematic representation of sputtering configuration (Adapted from [233]). (b) Scheme of magnetron circular configuration and electron motion; the electron drift path is called racetrack. (Adapted from [235]).

By this way, the plasma can also be sustained at a lower operating pressure. Additionally, the sputtered atoms have neutral charge and thus are unaffected by the magnetic field [232, 235, 236].

A Magnetron Sputtering BOC Edwards (Scancoat six) equipment (Fig. 2.4) was used for deposition of Au contacts in the AAO membranes.

The depositions were performed using the conditions: P_{Base} = 3 X 10^{-2} mbar, P_{Work} = 3 X 10^{-1} mbar, current = 20 mA and potential = 0.9 kV, resulting in Au thin films with ~40-50 nm for a deposition time of 5 min.

Fig. 2.4: DC magnetron sputtering equipment, at IFIMUP (University of Porto).

2.1.2. Multi-segmented nanowires

After the anodization process, and sequential steps to remove the AAO nanopore bottom, pore widening, and sputtering deposition of Au film layer to provide a conductive metallic contact at the pore bottom, the AAO membranes were finally prepared for the metallic NWs electrodeposition. The electrodeposition was performed in a three-electrode cell equipped with an Ag/AgCl reference electrode, a Pt mesh as a counter electrode, and the gold-coated AAO membrane acting as the working electrode (represented in Fig. 2.5). Before the NWs electrodeposition, the Au layer was thickened by DC electrodeposition using 100 mL of a commercial gold-plating solution (Orosene E +4g/L, pH 3.5 − 4.5, from Italgalvano) at −1.0 V during 5 min. The Fe/Cu NWs were grown at room temperature by DC pulsed electrodeposition method, using 100 mL of electrolyte solution containing 0.4 M H_3BO_3, 0.1 M $FeSO_4 \cdot 7H_2O$, 0.005 M $CuSO_4 \cdot 5H_2O$, and 0.003 M ascorbic acid. The multilayer deposition was carried out with a sequence of pulses at −1.1 V to grow the Fe layer, followed by a pulse at optimized potential of −0.6 V to grow the Cu layer (that acts as separation layer). This sequence of pulses was repeatedly applied until achieving several bilayers of Fe/Cu. The deposition rate was calibrated through the electrodeposition of long NWs of each metal, accordingly with each potential (≈ 2.5 nm/s at −1.1 V for Fe, and ≈ 0.3 nm/s at −0.6 V for Cu).

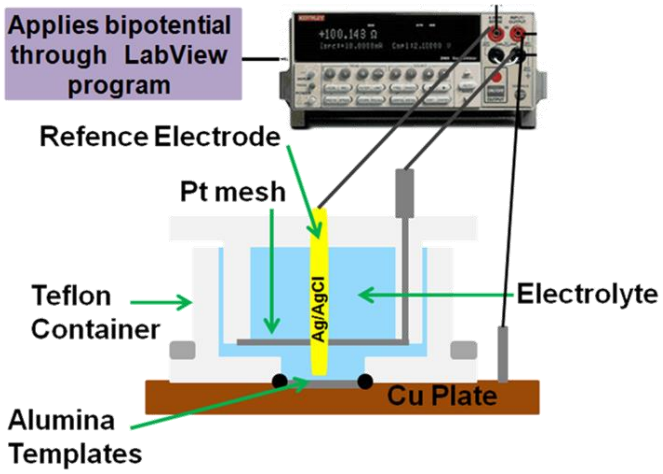

Fig. 2.5: Scheme of electrodeposition set-up, with three-electrode configuration: alumina membranes coated with Au in contact with copper plate as the working electrode, a Pt mesh as the counter-electrode and an Ag/AgCl reference electrode.

2.1.3. Nanowires removal

The Muti-segmented NWs model enables the large-scale production of Fe NWs with small lengths inside the AAO membranes, that are further released by dissolving the nanoporous membranes and the Cu separating segment of the NWs (scheme in Fig. 2.6 (a)), using a chemical etching process.

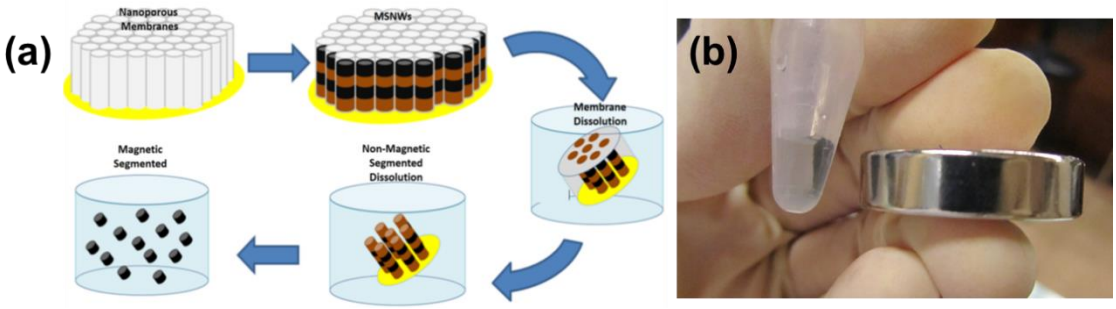

Fig. 2.6: (a) Route to obtain the multi-segmented nanowires (NWs) by AAO template-assisted method, followed by the dissolution of the membrane and Cu separating segments. (b) Separation of magnetic NWs from supernatant solution of ethanol.

The AAO template was removed in 50 mL of an aqueous solution containing 0.4 M H_3PO_4 and 0.2 M $H_2Cr_2O_7$ at 40 ºC. This etching solution also prevents the metallic NWs oxidation. The Cu branched NWs were removed in 1 mL of an aqueous solution containing 1% of nitric acid (HNO_3) 65 % for few seconds. The resulting magnetic NWs

were dispersed and washed using ethanol. Finally, the NWs can be easily separated using a magnet (Fig. 2.6(b)).

2.2. Superparamagnetic iron oxide nanoparticles

The superparamagnetic iron oxide nanoparticles (SPIONs) were produced by a microwave-assisted method Discover® SP microwave system, automated by Explorer-12 software, using 25 mL glass vessels with Teflon caps, all purchased from CEM Corporation. In this procedure, 250 mg of ferric chloride hexahydrate ($FeCl_3 \cdot 6H_2O$) and 138 mg of ferrous chloride tetrahydrate ($FeCl_2 \cdot 4H_2O$) were weighted into a glass vessel. Then, 20 mL of bi-deionized water was added under continuous magnetic stirring (with magnetic stir bar) until all the powder was dissolved. In a closed hotte, 3 mL of ammonium hydroxide (NH_4OH) solution 25% was added rapidly and drop-wise to create a black solution. The glass vessel was then sealed with a Teflon cap and left to rest until the precipitate settled down.

The vessel was placed in the microwave system, under nitrogen pressure, with the following parameters:

- Temperature: 100°C
- Stirring: maximum
- Time: 10 minutes
- Maximum wattage: 300 W
- Maximum pressure: 200 psi

After the microwave process, again in a closed hotte, the solution was removed from the glass vessel and placed it in a 50 mL Falcon®, filling with bi-deionized water up to the mark if necessary. A strong permanent magnet was approached to the suspension until all the black particles aggregated and only a clear liquid remains. The liquid was disposed quickly, to minimize any possible ammonium volatilization. The remaining ferrofluid was resuspended in 25 mL of bi-deionized water. The SPIONs formulation was finally stored at 4°C.

2.3. Nanostructured lipid carriers by ultrasonication method

In this study, it was necessary to fabricate 4 different categories of nanostructured lipid carriers (NLCs) of each group and respective formulations that are distinguished by the different solid lipids. These categories are the following (as represented in Fig. 2.7):

- NLC (composed only of lipids and surfactants),
- NLC_PEG-FA (composed of lipids and surfactants and conjugate poly(ethylene glycol) (PEG) and folic acid (FA)),
- NLC_DOX (composed of lipids and surfactants and doxorubicin),
- NLC_DOX_PEG-FA (composed of lipids, surfactants, doxorubicin and conjugate poly(ethylene glycol) (PEG) and folic acid (FA)).

Each of these compositions correspond to a permutation of the main components of the nanostructures with specific actions, which allows an effective comparison regarding the efficacy of multifunctional NLCs in the death of tumor cells. For NLCs with magnetic cores, magnetic nanoparticles were added to these same categories.

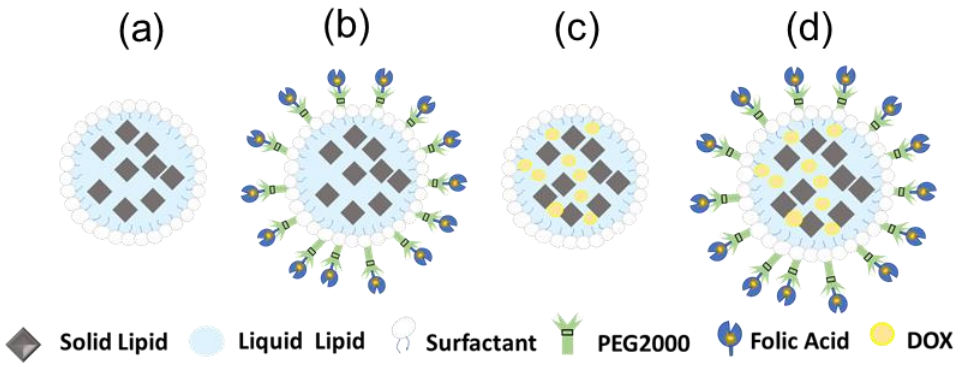

Fig. 2.7: The four different categories of nanostructured lipid carriers (NLCs) produced in this work (a) NLC, (b) NLC_PEG-FA, (c) NLC_DOX and (d) NLC_DOX_PEG-FA.

2.3.1. Synthesis of PEG-FA conjugate

In order to achieve an active targeting towards overexpressed folic acid (FA) receptors in cancer cells, a PEG-FA conjugate was synthesized and added to the lipid phase of NLCs. This conjugate is based in a phospholipid-1,2-distearoyl-*sn*-glycero-3-phosphorylethanolamine (DSPE) – coupled with poly(ethylene glycol) (PEG) with an average molecular weight of 2000 Da. The synthesis of the DSPE-PEG_{2000}-FA conjugate was obtained using the procedure described in [237]. It is a modified process that comprises four main steps:

- activation of the FA,
- coupling to DSPE-PEG_{2000}-NH_2,
- purification,
- lyophilization.

The folic acid N-hydroxysuccinimide ester (NHS-FA) was prepared by dissolving, under anhydrous conditions by stirring overnight in the dark, 1.0 g of FA in a mixture of

40 mL of anhydrous DMSO and 0.5 mL of triethylamine. This mixture was then mixed with 0.5 g of dicyclohexylcarbodiimide and 0.52 g of N-hydroxysuccinimide and stirred for another 18 h in the dark. The resulting solution was then filtered (with a 0.45 μM filter) and evaporated under vacuum, in order to remove the precipitated by-product (dicylcohexylurea (DCU)), DMSO and triethylamine. Coupling of the NHS-FA prepared solution with DSPE-PEG_{2000}-NH_2 was carried out by stirring overnight in the dark under anhydrous conditions of 2 mL of the resulting activated FA solution with 50 mg of DSPE-PEG_{2000}-NH_2 dissolved in 1 mL of DMSO. Then, 6 mL of deionized water was added and the DMSO was removed by evaporation in vacuum. The DSPE-PEG_{2000}-FA conjugate was then dialyzed against 500 mL of ultrapure water by a dialysis membrane (Cellu.Sep®T1, 3500NMWCO, Membrane Filtration Products, Inc.; Seguin, TX, USA) for 48 h to remove the unconjugated FA. The resulting solution was then lyophilized (LyoQuest −85 plus v.407, Telstar) forming a yellowish dry orange powder and the final DSPE-PEG_{2000}-FA conjugate was stored at 4 °C.

2.3.2. Production of nanostructured lipid carriers

Two types of nanostructured lipid carriers (NLCs) were prepared by a hot ultrasonication method. The NLCs composition was similar except in the solid lipids: cetyl palmitate ($NLC_{(Pal)}$) and gelucire ($NLC_{(Gel)}$) 43/01, both provided by Gattefosé SAS, France. Briefly, 225 mg of each solid lipid, 35 mg of oleic acid 90% (Sigma-Adrich, St Louis, Mo, USA), 85 mg of polysorbate 80 (Tween®80, Sigma-Aldrich, St Louis, Mo, USA) and 10 mg of DOX (LC Laboratories, Canada) were weighted and heated together (70 °C for cetyl palmitate and 55 °C for gelucire 43/01) to promote their melting. In the case of functionalized formulations, 5 mg of the conjugate PEG-FA (synthesized according to a previously optimized protocol [237]) was added. Then, 5 mL of HCl buffer (pH = 1), preheated at the same temperature, was added to the lipid mixture. This mixture was sonicated for 5 min using a sonicator (Vibra-Cell model VCX 130, Sonics and Materials Inc., Newtown, USA) with a tip diameter of 6 mm at 80% amplitude. The obtained product was then cooled to room temperature, allowing the internal oil phase to solidify, forming NLCs dispersed in the aqueous phase. A schematic representation of this procedure is presented in Fig. 2.8. As a control, drug-free NLCs were prepared in a similar manner but without the addition of DOX to the lipid phase. Non-functionalized NLCs were also produced without the presence of the conjugate PEG-FA. For the stability studies, NLCs were stored in glass vials protected from light at room temperature.

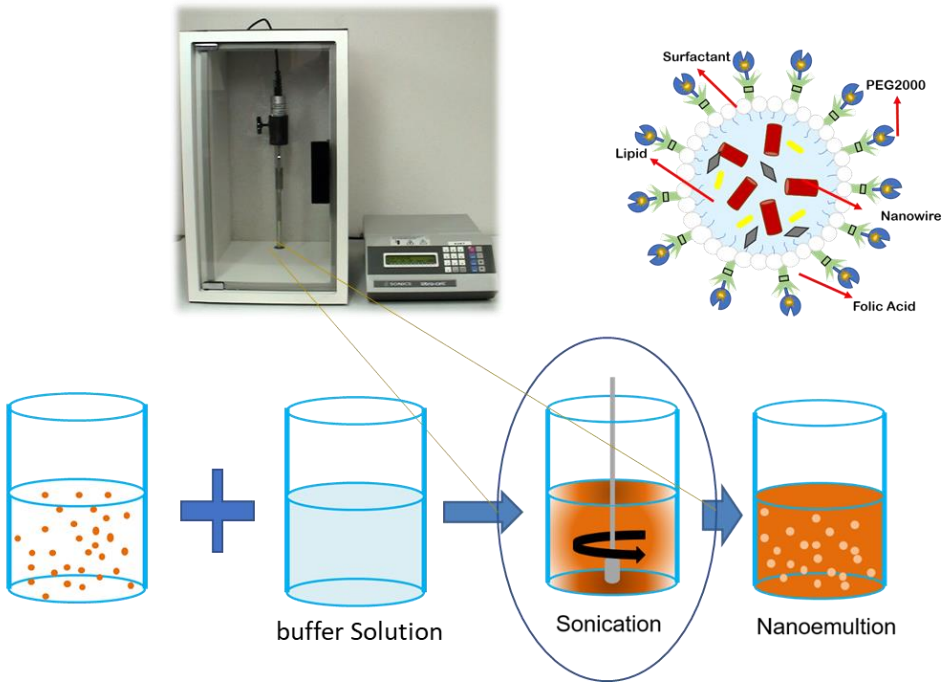

Fig. 2.8: Schematic representation of nanostructured lipid carriers (NLCs), prepared by hot ultrasonication method.

2.4. Characterization techniques

In this section, the electrochemical, morphological, structural, and magnetic characterization of the synthesized nanostructures is described. The characterization was performed at Instituto de Física de Materiais Avançados, Nanotecnologia e Fotónica da Universidade do Porto - Portugal (IFIMUP), Centro de Microscopia da Universidade do Porto - Portugal (CEMUP), Faculdade de Farmácia da Universidade do Porto - Portugal (FFUP), Instituto de Investigação e Inovação em Saúde Universidade do Porto – Portugal (I3S), Institutes for Advanced Studies, Madrid - Spain (IMDEA) and Universidade Estadual de Campinas -Brazil (UNICAMP).

2.4.1. Monitoring of the electrochemical processes

The home-made electrochemical set-up described in section 2.1 to produce AAO membranes and to perform pulsed electrodeposition (PED) is controlled by a Keithley 2400 Sourcemeter. The Keithley 2400 operates in potentiostat and galvanostat modes with working ranges of either 0 - 210 V (potentiostatic mode) and 0 - 110 mA (galvanostatic mode). This instrument provides two independent channels enabling current measurements $I(t)$ while a constant voltage (V) is applied, and voltage measurement $V(t)$ while a constant current (I) is applied. This equipment also enables

a sequential application of *I* and *V* pulses in a millisecond range, with an acquisition time per measurement of 200 ms (using LabVIEW to control Keithley 2400 equipment). A LabView application was locally developed to control automatically the anodization experiments, monitoring the current density evolution *j*(*t*) during the whole experimental run, within the user-defined conditions (anodization time and voltage). Other LabView applications were also implemented to decrease *V* in non-steady-state anodization, monitoring at the same time *j*(*t*) and the PED pulses. The temperature is controlled using a refrigerated Cu cooling plate. The refrigeration circuit uses a continuous circulating anti-freezing liquid (50% water and 50% ethylene glycol, V/V) refrigerated and propelled by a thermocirculator Fisher 100.

2.4.2. Electron microscopy

The principle of electron microscopy is the use of a beam of accelerated electrons (with controlled kinetic energy and produced under high vacuum), that interact with a sample, biological or inorganic, producing images or providing information about its composition.

Depending on several characteristics, such as the lighting system (incident electron beam generation), the detection of electrons/photons emitted by the sample or the image construction, we can find several modes of electron microscopy: Scanning Electron Microscopy (SEM), Scanning Transmission Electron Microscopy (STEM), Transmission Electron Microscopy (TEM) or Energy Dispersive X-ray Spectroscopy (EDS).

2.4.2.1. Scanning electron microscopy (SEM)

Scanning electron microscopy (SEM) is the most powerful technique that can be used for direct observation of the fabricated nanostructures, giving important information about the morphology, topography, or geometrical features (pore size, interpore distance or membrane thickness, among others). Besides, it can also provide information about the chemical composition of the synthesized nanomaterials [238]. Images with a resolution varying from a few millimeters to 5 nm, and a magnification up to 500.000 times can be provided using the SEM technique [239].

The principle of electronic microscopy consists in an electron beam with controlled kinetic energy and under high vacuum that irradiates on the sample. A set of electrostatic and magnetic lenses controls the focused electron beam to scan through a

small spot of the sample, which emits electrons and photons, and their intensity is used to form the SEM image by convolution of the sample spots hit by the beam.

The main components of an SEM microscope comprise an electron column, condenser lenses and detector, as shown in Fig. 2.9. The electron column comprises an electron source (tungsten filament cathode, for example) that emits an accelerated beam of electrons, with energies ranging from 0.1-40 keV and pressure ~10^{-4} Pa [239]. The electron beam is focused to a small diameter through a series of demagnifying magnetic focusing lenses, with defined apertures in order to converge the beam to the sample. Inside the sample chamber, there are two kinds of detectors, secondary and backscattered. For image acquisition, the electron beam is rastered over the surface of the sample in a small spot and the emitted electrons are collected by the detectors and then processed. The image is formed by mapping (point-to-point) the intensity of the detected signals with the position of the beam [238-240]

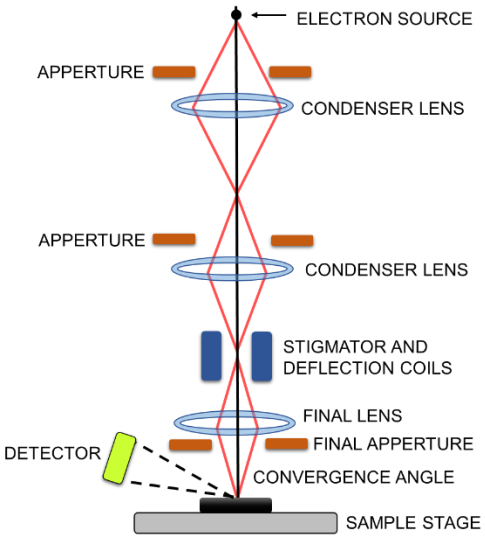

Fig. 2.9: Scheme of the scanning electron microscope main components (Adapted from [240]).

.

The signals most commonly emitted by the samples are the secondary electrons (SE), the backscattered electrons (BS) and X-rays (EDS), depending on the interaction of the electron beam with sample atoms, occurring at various depths (Fig. 2.10).

The SE are low-energy electrons (<50 eV), that result from inelastic collisions of the primary beam with superficial atoms (few nanometers from the sample surface and loosely bound), as represented in Fig. 2.10. The images originated by SE provide information about the topography of the sample [240, 241].

On the other hand, BSE are high-energy electrons (>50 eV) reflected from the sample, including Auger electrons (Fig. 2.10). BSE result from the elastic collision of

the primary-beam with atoms located deeper inside the sample. Additionally, the intensity of BSE signal is related with atomic number (Z) contrast and density, where elements with higher atomic number emit electrons more strongly than elements with low atomic number, resulting into a brighter image [239, 240].

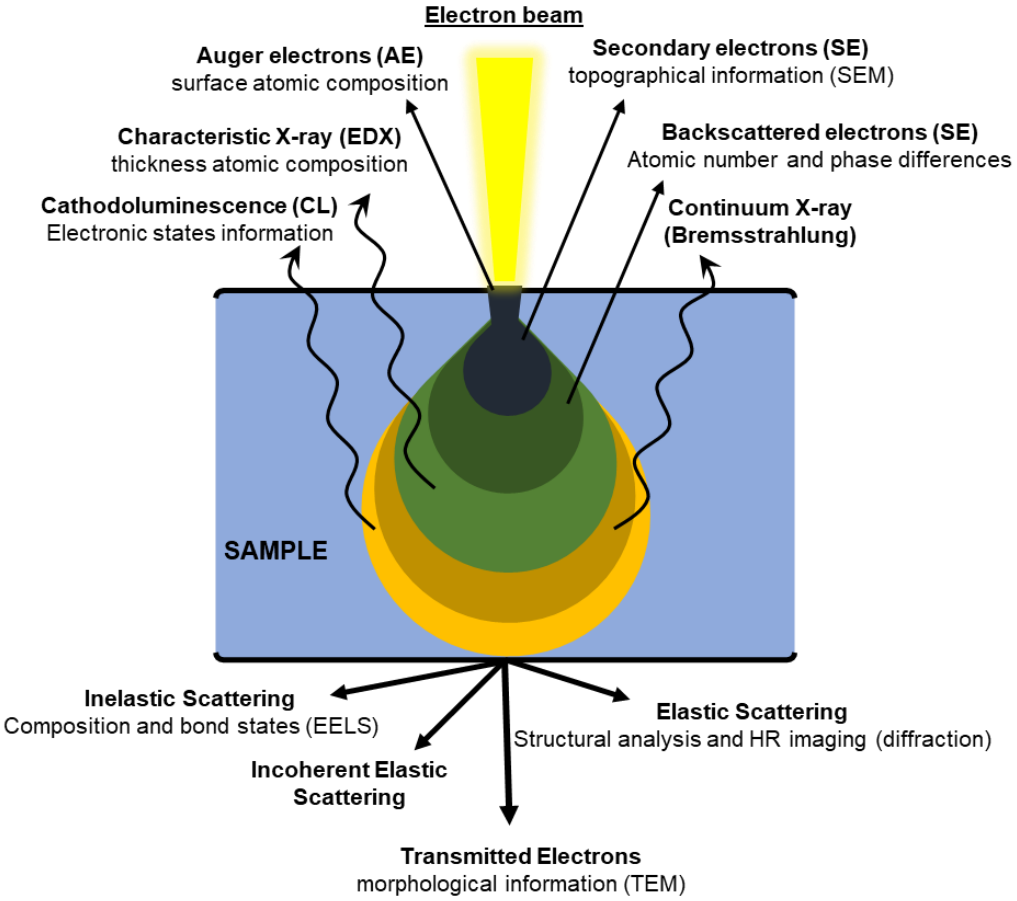

Fig. 2.10: Different signals are generated from the sample by interaction with the electron-beam (cross-section view). Adapted from [242].

During this work, the SEM images that revealed the morphological features of prepared samples were collected using a Phillips-FEI/Quanta 400 FEG high resolution scanning electron microscope (SEM), at the Materials Center from the University of Porto (CEMUP).

For SEM observation, the AAO samples were simply placed in carbon tape and fixed to a sample holder for top-view without special preparation. For cross-section view, the AAO membranes were broken in the middle of anodization area, and thenmn02< placed on the edge of the sample holder, fixed on top of carbon tape.

ImageJ software [243] was used to measure the geometrical features of the produced nanostructures, such as AAO pore diameter or nanowires thickness, taken respectively from the SEM top and cross-section images.

2.4.2.2. Electron dispersive spectroscopy (EDS)

In the course of the SEM or STEM image acquisition, the chemical information about the sample can be obtained using the Energy Dispersive Spectroscopy (EDS) analysis of X-rays. The use of characteristic X-ray peaks to provide elemental composition is commonly used coupled to the SEM technique [238-240].

The interaction (inelastic) of the electron beam with the sample just below the surface may excite an electron in an inner shell, creating an electron hole. This hole can be filled by a higher-energy shell electron, producing photon emission (energies between 0.1 and 20 keV) that are characteristic of each atomic transition of the emitting element, and can be detected by an energy dispersive X-ray detector [238-240]. However, the EDS technique only provides information about the chemical elements present in the sample, and does not give specific information about the molecular structure [244].

In this work, an EDS system EDAX Genesis X4M unit, integrated with SEM equipment described above, was used at the CEMUP center from University of Porto.

2.4.2.3. Transmission electron microscopy (TEM)

The main difference between SEM and TEM is that SEM images result from the detected electrons that were reflected from the sample which gives morphological/topography information about the sample´s surface, while TEM images uses electrons that passed through a sample (transmitted electrons), giving information about the interior of the sample, its crystalline structure, morphology and stress state information [245].

The morphology of unloaded and DOX-loaded NLCs were observed by TEM (TEM Jeol JEM-1400; JEOL Ltd., Tokyo,Japan). NLCs suspensions were diluted (1:10) in type 1 Milli-Q® Integral ultrapure water, and 10 µL were then placed on copper-mesh grids. After 2 min, the excess was removed, and 0.75% (w/v) uranyl acetate solution (10 µL) was added for 10 sec to obtain a negative staining. The images were obtained with an acceleration voltage of 80 kV.

2.4.3. X-Ray diffraction (XRD)

The X-ray diffraction (XRD) is a structural technique for the characterization of crystalline nanomaterials. With XRD technique, important information as crystalline

phases, preferred orientation, epitaxy, and structural parameters such as grain size, crystallite size and microstrain can be determined [240, 246].

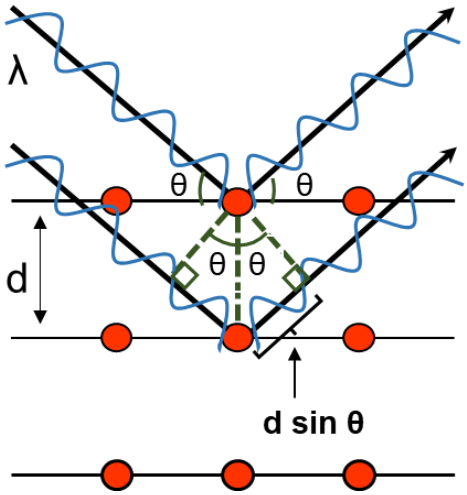

Fig. 2.11: Schematic representation of the Bragg's relation (adapted from [247]).

When X-rays beam interact with the electrons from the atoms of a sample, it results in radiation scattering. The wavelength of the X-ray radiation has values in the order of the lattice parameters of crystalline materials (1 Å). If the distance between the atoms is comparable to the wavelength of the X-rays, it occurs the interference of the scattered waves in the analysed materials, forming a diffraction pattern with constructive or destructive interferences. If the scattered waves interfere in constructive way, the X-rays are scattered by the atomic planes in a crystal (at characteristic angles based on the spaces between the atomic planes). This results in emitted beams of high intensity along certain directions, forming a diffraction peak [240]. The crystals have sets of planes passing through their atoms, each of them with a specific distance *d* between planes that originate a characteristic angle of diffracted X-rays, according to Bragg's law [248]:

$$n\lambda = 2d_{hkl}sin\theta \tag{2.1}$$

where λ is the wavelength of incident wave, n a positive integer, d_{hkl} is the atomic distance between planes (atomic spacing) and θ is the diffraction angle (as shown in Fig. 2.10).

In this work, the crystalline phases of our samples were determined using a SmartLab Rigaku® diffractometer (Fig. 2.12), with a copper Cu Kα radiation λ = 1.540593 Å, and anode x-ray tube operated at 45 kV and 200 mA.

The crystallographic analysis was assessed by XRD measurements using Bragg–Brentano *θ*/2*θ* configuration. Additionally, structural parameters such as crystallite size (D_{hkl}) was determined from peak broadening analysis, using Debye-Scherrer equation [249]:

$$D_{hkl} = k\frac{\lambda}{\beta \cos\theta} \tag{2.2}$$

with *k* a shape factor constant (typically k ~0.9 for spherical grains), *λ* the wavelength of the X-ray radiation (CuKα = 1.54056 Å), *β* the full width at half-maximum height of peaks and *θ* the Bragg diffraction angle.

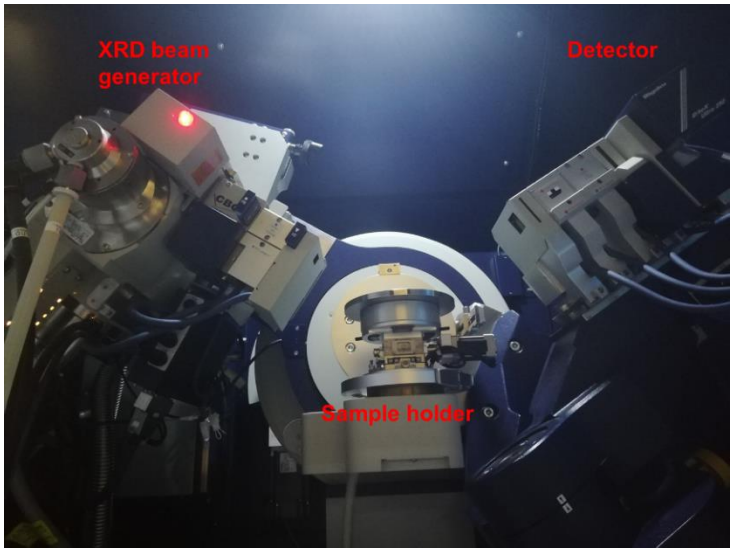

Fig. 2.12: Rigaku SmartLab XRD main components (X-ray tube generator, sample holder and X-ray detector), at IFIMUP (University of Porto).

2.4.4. Magnetometry (SQUID and VSM)

The magnetic properties of the synthesized nanowires were studied using a Quantum Design Superconducting Quantum Interference Device (SQUID) magnetometer (at IFIMUP, Universidade of Porto). The Quantum Design SQUID magnetometer is an integrated device comprising a superconducting coil in a helium bath and a corresponding control system. This system allows accurate magnetization measurements in our samples in a temperature range of 5 - 370 K, and thus the determination of the critical temperatures, such as block temperature (T_b). For this purpose, the temperature dependence of the magnetization (in low fields, H = 50 - 100 Oe) was measured in increasing temperatures, but only after the sample had been cooled without any H. The obtained M (T, H = constant, low field) curve in increasing

temperature is denominated a zero-field-cooled (ZFC) magnetization. On the other hand, when the sample is cooled with H, the obtained M(H,T = constant, low field) curve in increasing temperature is denominated a field-cooled (FC) magnetization. Isothermal M *vs* H measurements were performed as a function of the applied magnetic field (*H* varied from -5 to 5 T) to obtain the saturation magnetization (M_{sat}) and the coercive fields (H_c).

The magnetic hysteresis loops M(H) were measured with the field (*H*) applied along the parallel ($H^{//}$) and perpendicular ($H^{\perp}$) directions with respect to the NWs' longitudinal axis in a vibrating sample magnetometer (VSM), LakeShore Controller Model 7304 (Lake Shore Cryotronics Inc., Westerville, OH, USA), at room temperature. Moreover, the first-order reversal curves (FORCs) were acquired for a parallel applied magnetic field. After saturating the nanowire array at 10 kOe, 100 minor (reversal) curves were measured, covering the ± 2500 Oe region. Each curve was preceded by a saturation and consisted of a 25 Oe field spacing. The FORC distribution was calculated as the second-order mixed derivative of the magnetization, with respect to the reversal field (H_r) and applied field (H) [250]. The results are presented in a Preisach plane, with the diagonal axes being $H_c = 0.5\ (H - H_r)$ and $H_u = -0.5\ (H + H_r)$. The distribution strength is given through the color scale, ranging from blue (null value) to red (maximum value).

2.4.5. UV-VIS spectrophotometry

The UV-Vis technique was applied in this work in the studies of EE, drug release and cell viability. The technique of UV-Vis spectroscopy was applied in this work in the studies of EE, drug release and cell viability. UV-VIS spectroscopy is a technique based on the absorption of light by an unknown substance that is intended to be studied. The sample is illuminated with electromagnetic rays of various wavelengths in the visible (from ultraviolet to lower infrared) of the spectrum. Depending on the substance, the light is partially absorbed, and the transmitted part is recorded as a function of the wavelength by a suitable detector, providing the sample's UV/VIS spectrum. (see Fig.2.13).

In general, a UV / VIS spectrum is represented graphically by the absorbance as a function of the wavelength, this is appropriate because the height of the absorption peaks is directly proportional to the concentration of the species.

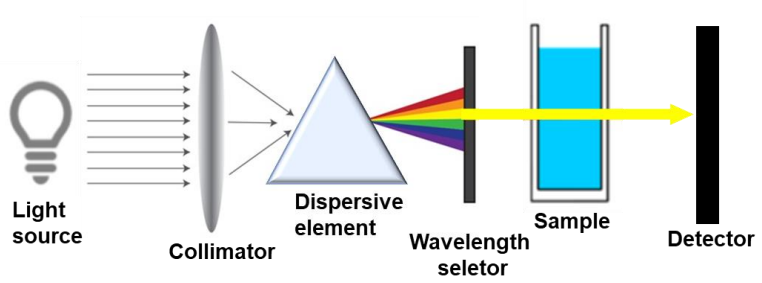

Fig. 2.13: Measurement principle in UV/VIS spectroscopy

To determine the sample concentration (c) from the measured absorbance value (A), the Lambert-Beer law is used [251]:

$$c = \frac{A}{\varepsilon \cdot d} \tag{2.3}$$

where ε is a specific sample constant that describes how much the sample is absorbing at a given wavelength, d is the length of the cuvette path is given in cm.

To obtain the best measurement results and in accordance with the Lambert-Beer Law, the absorbance must be in the linear range of the instrument. The suitable range for ideal measurements, that is, the measurement range in which the absorbance is directly proportional to the concentration. For that, the calibration line is made, where several measurements of the light absorption of the standard solution are made with different known concentrations in a fixed wavelength predefined by the characteristic peak of the studied compound.

In our case, for the study of doxorubicin (DOX) the calibration line is represented in Fig. 2.14. The graph shows the linearity of the absorption as a function of the concentrations, whose slope is ε (specific constant of the sample), and also the limit of detection (LOD) and limit of quantitation (LOQ) are presented.

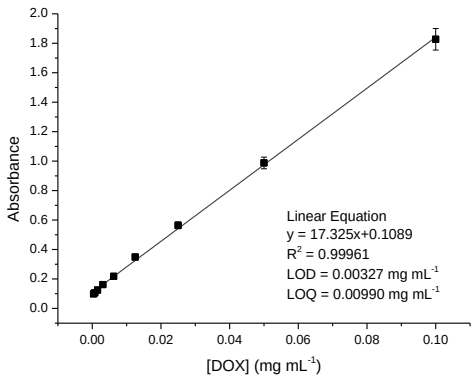

Fig. 2.14: Calibration curve of Doxorubicin, pH 1 at λ_{max} 253 nm. The linear equation, limit of detection (LOD) and limit of quantitation (LOQ) are presented.

2.4.5.1. Entrapment efficiency (EE) and loading capacity (LC)

The entrapment efficiency (*EE*) and loading capacity (*LC*) of DOX in NLCs was determined by UV-Vis spectrophotometry. Briefly, the formulations were diluted (1:100) in HCl buffer (pH = 1), transferred into Amicon®Ultra-4 Centrifugal Filter Devices (50 KDa, MERK Milipore, Ltd; Cork, Ireland) and centrifuged (HeraeusT M MultifugeT M X1R Centrifuge, USA) at 1006 x*g*, 20 ˚C during 45 min or until complete separation between the NLCs retained in the filter unit and the aqueous phase corresponding to the filtrate. The supernatant was used to quantify the amount of non-incorporated DOX by UV–vis spectrophotometry (Jasco V − 660 Spectrophotometer, USA) at λ_{max} 253 nm, which is the maximum absorption of DOX in aqueous solution. Taking into account the drug initially added to the NLCs formulation and subtracting the free DOX remaining in the filtrate, it was possible to determine the amount of drug incorporated in the NLCs and thus the entrapment efficiency by the following Eq. 2.4:

$$EE\ (\%) = \frac{Total\ initial\ DOX\ amount - unentrapped\ DOX}{Total\ initial\ DOX\ amount} \times 100 \qquad (2.4)$$

The loading capacity was calculated considering the *EE* (%), as follows:

$$LC\ (\%) = \frac{EE\ \times\ Total\ DOX\ amount}{Total\ lipid\ and\ surfactant\ amount} \times 100 \qquad (2.5)$$

2.4.6. Physical characterization of nanoparticles

NLCs hydrodynamic size, size distribution (polydispersity index - PDI) and surface charge (ξ-potential) were characterized using dynamic and electrophoretic light scattering (DLS and ELS) (ZetaPALS analyzer, Brookhaven Instruments Corporation, Holtsville, NY, USA), respectively. NLCs were diluted (1:400 in type 1 Milli-Q® Integral ultrapure water) and placed into clear disposable plastic cuvettes. All measurements were performed at 25 °C in triplicate. The stability of the prepared NLCs formulations was determined by measuring mean particle size and PDI for a period of 42 or 70 days maintaining the formulations in glass vials at room temperature.

2.4.6.1. Dynamic light scattering (DLS)

Dynamic light scattering (or photon correlation spectroscopy or quasi-elastic light scattering) is a technique that primarily measures the Brownian motion of particles in solution that arises due to bombardment from solvent molecules and relates this motion to the size of particles. This measures dependent on temperature and solvent viscosity [252].

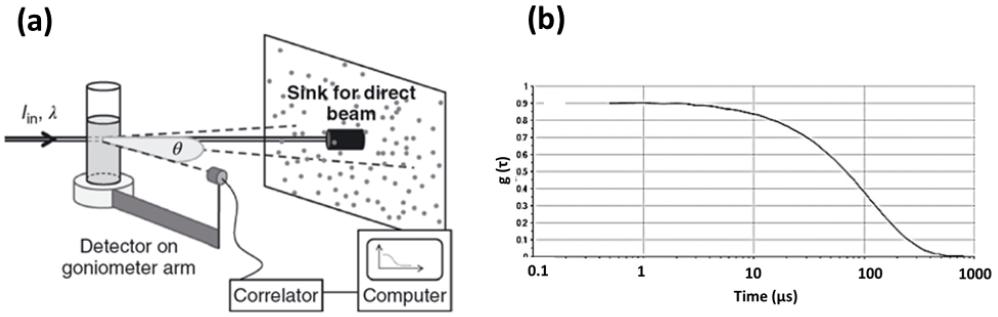

Fig. 2.15: (a) Schematic of a general DLS set-up. (b) Raw correlation function (RCF) (adapted of the [253, 254]).

The schematic of a general DLS set-up is present in the Fig. 2.15 (a). When the movement of particles over a time range is monitored, information on the size of particles can be obtained, as large particles diffuse slowly, resulting in similar positions at different time points, compared to small particles (such as solvent molecules) which move faster and therefore do not adopt a specific position. In a dynamic light-scattering instrument, when laser light encounters nanoparticles the incident light scatters in all directions and scattering intensity is recorded by a detector. The monochromatic incident light will undergo a phenomenon called Doppler broadening as the particles are in continuous motion in solution [252].The scattered light will either result in mutually destructive phases and cancel each other out, or in mutually constructive phases to produce a detectable signal.

In DLS instruments a correlogram is generated where RCF (raw correlation function) is plotted (Fig. 2.15 (b)) and the mathematical treatment of this curve allows to arrive at the Stokes-Einstein equation that define the hydrodynamic diameter of solid spherical particles [253, 255]:

$$d_H = \frac{K_b T}{3\pi\eta D} \tag{2.6}$$

where K_b is the Boltzmann constant (1.38064852 × 10−23 J/K), T the temperature, η the absolute viscosity and D the diffusion coefficient [253].

2.4.6.2. Zeta potential (ξ)

The zeta potential (ξ) reflects the potential difference between the electric double layer (EDL) of electrophoretically mobile particles and the dispersant layer around them in the sliding plane.

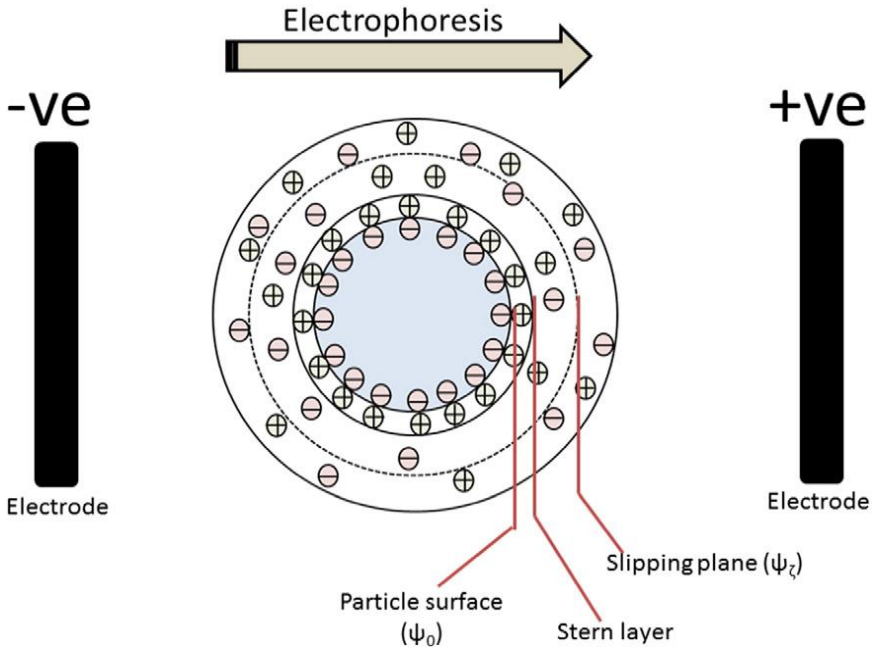

Fig. 2.16: Schematic showing the electric double layer (EDL) during electrophoresis [253].

The Fig. 1.16 shows the EDL in a negatively charged particle: immediately at the top of the particle surface there is a strongly adhered layer (stern layer) that comprises ions of opposite charge, that is, positive ions in this case. In addition to the stern layer, a diffuse layer develops consisting of negative and positive charges. During electrophoresis, the particle with adsorbed EDL moves towards the electrodes (positive electrode in this case) with the sliding plane becoming the interface between the moving particles and the dispersant. ξ is the electrokinetic potential in this sliding plane. The composition of this EDL is dynamic and varies depending on factors, for example, pH, ionic strength, concentration, etc. The Greek letter ζ (zeta) was originally used in mathematical equations when describing it and, therefore, the potential name zeta. As ξ cannot be measured directly it is deduced fromelectrophoretic mobility of charged particles under an applied electric field. The electrophoretic mobility (μe) of the particles is first calculated as [253]:

$$\mu_e = \frac{V}{E} \qquad 2.7$$

where V is particle velocity (μm/s) and E the electric field strength (Volt/cm). The ζ is then calculated from the obtained μ_e by the Henry's equation [253]:

$$\mu_e = \frac{2\varepsilon_r \varepsilon_0 \xi \, f(Ka)}{3\eta} \qquad 2.8$$

where ε_r is relative permittivity/dielectric constant, ε_0 the permittivity of vacuum, ζ the zeta potential, $f(Ka)$ the Henry's function and η the viscosity at experimental temperature. This equation applies to most of the pharmaceutical preparations and hence, very important for developing nanoparticles [256]

2.5. *In vitro* release studies

In vitro release studies were performed using a Slide-A-Lyzer MINI Dialysis Devices, 10K MWCO, 0.5 mL (Thermo Scientific) (Fig 2.17). In order to simulate the particles path in the body after oral administration, samples were incubated at 37 °C under stirring. To simulate the transit from stomach to intestine, samples were incubated first for 3 h in 14 mL of fasted state simulated gastric fluid (FaSSGF: NaCl/HCl solution, pH 1.6) - regime I - and then placed for 4 h in 14 mL of fasted state simulated intestinal fluid (FaSSIF: buffer solution containing potassium dihydrogen phosphate, pH 6.5) - regime II. Then the samples were placed in 14 mL of physiologic mimetic fluid (buffer solution at pH 7.4, with monopotassium phosphate) – regime III - for 14 h and finally placed for 24 h in 14 mL of tumor microenvironment mimetic fluid (citrate buffer solution at pH 6.3) - regime IV -, until the end of the experiment. At regular intervals, the vessels containing the formulations were transferred to a falcon with 14 mL of the same buffer or the buffer of the next regimen until the end of the process. These procedures ensured both the sink conditions and enough sensitivity of the analytical methodology.

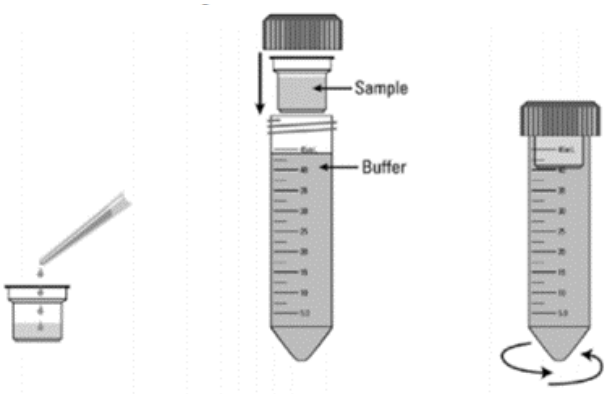

Fig. 2.17: Scheme of the experimental arrangement for dialysis in the *in vitro* release assay.

DOX release was previously analyzed by UV–Vis spectrophotometry, as described above. Free DOX was also analyzed by *in vitro* release, in the same conditions as the particles. The data analyses encompass the normalization with the free DOX results, in order to assess only the release from the particles and not the resistance of the drug towards the dialysis membrane.

Mathematical models for drug-release kinetics, including zero-order and first-order equations, Higuchi, Hixson–Crowell and Korsmeyer–Peppas [257], were applied to each release profile to evaluate the mechanism of drug release. The fitting of each model was evaluated based on the coefficients of determination (R^2) obtained.

2.6. Cellular studies

2.6.1. Dialysis of the formulations

For cell assays, it was necessary to filter the formulations containing the NLCs by dialysis to remove the free DOX. The experimental arrangement is shown in Fig. 2.18.

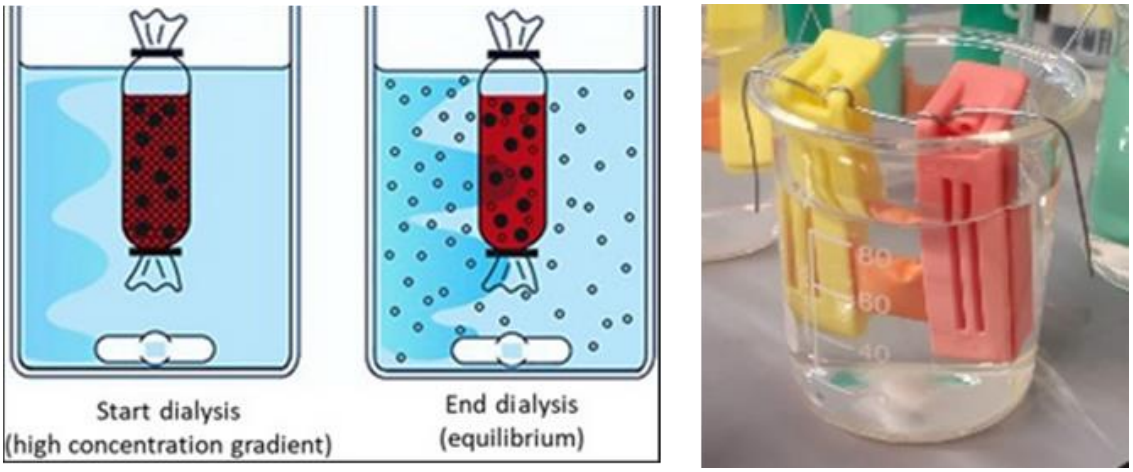

Fig. 2.18: Scheme of dialysis (left) and the set-up in our lab (right).

For each formulation, the dialysis was performed using a cellulose dialysis bag diffusion technique (Cellu.Sep®T1, 3500 NMWCO, Membrane Filtration Products, Inc.; Seguin, TX, USA) filled with 1 mL of the formulation immersed in 80 mL of buffer solution (HCl solution with pH = 1.5) for 45 min. For the calculation of concentrations in cell tests, the EE of each formulation was taken into account.

2.6.2. Cell culture

Breast cancer cells of the type MDA-MB-231 cells were cultivated at 37°C in a 5% CO_2 atmosphere (Unitherm CO_2 Incubator 3503 Uniequip; Planegg, Germany) in DMEM (Dulbecco's Modified Eagle's Medium**)** supplemented with 10% (v/v) fetal bovine serum (FBS) and 1% (v/v) penicilin-streptomicin. When the cell culture reached a 70% to 80% confluence, was detached using a 0.25% (w/v) trypsin-EDTA solution. Further, the cells were centrifuged using the Heraeus Multifuge X1R centrifuge (Thermo Fisher Scientific; Waltham, MA, USA) at 300 *xg* and re-suspended in fresh medium. Viable cells were counted using a Neubauer chamber (Improved Neubaur Bright-line, Boeco; Hamburg, Germany).

2.6.3. Cell Viability assays

The effect of the designed NLCs on cell viability was measured using the methylthiazolyldiphenyl-tetratozium bromide (MTT) conversion assay. MDA-MB-231 cells were seeded in 96-well microplates at a density of 10^6 cells per well in 100 µL supplemented DMEM and incubated for 24 h at 37°C in a 5% CO_2 atmosphere. Different concentrations of free DOX, DOX-loaded in functionalized and non-functionalized NLCs and the correspondent amounts of placebo NLCs were added, and cells were incubated for 72 h. Positive control (cells with only supplemented DMEM) was also included, and negative control exposing cells to 1% Triton X-100. After the incubation time, the content of the wells was discarded, and 200 µL of MTT solution (0.5 mg/mL in supplemented DMEM) was added to each well and incubated for 3 hours at 37°C in a 5% CO_2 atmosphere. MTT was then removed and replaced with 200 µL of DMSO. Upon 15 min incubation, protected from light, the absorbance was read using a microplate reader at 570 and 630 nm for background subtraction. Cell viability was determined according to the following equation:

$$Cell\ Viability\ (\%) = \frac{mean\ (n1,n2,n3) value}{mean\ positive\ control\ value} \times 100 \qquad (2.9)$$

The 50% cellular growth inhibition (IC_{50}) was determined.

2.6.4. Cell uptake assays

The NLCs uptake into MDA-MB 231 cells was studied by flow cytometry using the BD Accuri C6 (BD Biosciences, Belgium). Thus, NLCs were probed with a fluorescent agent during the production; 1% (w/w) coumarin-6 (Sigma-Aldrich, St Louis, Mo, USA) was added to the total mass of lipids and surfactant. These formulations were analyzed as size, PDI and zeta potential are concerned to ensure that the probe did not compromise the overall physical features of the particles. Cells were seeded in 24-well plates at the density of 10^5 cells per well in 300 µL of supplemented DMEM and incubated at 37°C in a 5% CO_2 atmosphere to allow cell attachment during 24 h. Afterwards, the culture medium was discarded, and replaced by 300 µL of fresh medium containing 0.25 mg/mL of the coumarin-6 marked non-functionalized and functionalized NLCs. A control (only culture medium) was included to normalize and compare the results. After each incubation time (15, 30, 45, 60, 75, 90 and 120 min for the $NLC_{(Gel)}$ and $NLC_{(Pal)}$ formulations, and 5, 10, 20, 30, 40, 50 and 60 min for the $NLC_{(Gel\text{-}PEG\text{-}FA)}$ and $NLC_{(Pal\text{-}PEG\text{-}FA)}$ formulations), cells were washed twice with phosphate buffered saline (PBS), detached with 150 µL of trypsin-EDTA and recovered in 100 µL of fresh culture medium. Before the measurements, 5 µL of Trypan Blue solution (0.5% (w/v) in PBS) was added. Finally, the samples were analyzed by flow cytometry. For each sample a minimum of 10,000 events was recorded and the auto-fluorescence of cells controlled. The cell uptake of all fluorescent NLCs formulations was expressed as a function of time. The results were analyzed using Michaelis-Menten function in OriginPro 8.5.

HaCaT cells (human keratinocytes cells) were cultivated under the same conditions as MDA-MB 231 cells. Cellular uptake studies were also conducted using HaCaT cells seeded in a 24-well plate at a concentration of 10^5 cells.mL^{-1}. Upon adherence, cells were incubated with 0.25 mg.mL^{-1} of the coumarin-6 marked non-functionalized and functionalized NLCs for 30 min. Cell recovery and flow cytometry analysis was performed as described for MDA-MB 231 cells.

2.6.5. Cellular internalization studies

To understand the endocytosis mechanisms of the NLCs in MDA-MB231 cells an internalization assay was set up as previously described [258]. Briefly, MDA-MB231 cells were grown in a 24-well plate at 10^5 cells.mL^{-1}, and for the energy-dependence mechanisms assessment, the cells were treated with either 1 mg.mL^{-1} of sodium azide or kept at 4 °C for 30 min. Then MDA-MB 231 cells were incubated with 0.25 mg.mL^{-1}

of the coumarin-6 marked non-functionalized and functionalized NLCs for 30 min. Afterwards, the cells were rinsed with cold phosphate buffer and analyzed by flow cytometry, as previously described. In the NLCs endocytosis study, MDA-MB 231 cells were pretreated with specific inhibitors (Cumarin for example) for 30 min, and then incubated with 0.25 $mg.mL^{-1}$ of the coumarin-6 marked non-functionalized and functionalized NLCs for 30 min, in the presence of the same inhibitors for 1 h. Subsequently, the cells were washed three times with cold phosphate buffer and collected for flow cytometric analysis.

2.6.6. Cellular internalization of nanowires

The monocytes were prepared in a 24-well plate with different NWs concentration in 300 mL of pH 7.4 buffer. Each well corresponded to 50.000 cells that were grown in DMEM supplemented with fetal bovine serum and penicillin/streptomycin at 37 °C with 5% CO_2. The MDA-MB 231 cells line was incubated with the NWs, also at 37 °C, for 19 h. The cells were examined in the BD AccuriTM C6 flow cytometer.

2.6.7. Statistical analysis

Statistical analyses were performed using GraphPad Prism6 software program (GraphPad Software Inc., CA, USA). The difference between four and more groups was, analyzed through two-way ANOVA multiple comparisons. Differences between two groups was evaluated by two-tailed Student's t-test. The differences were statistically significant when * $p < 0.05$, ** $p < 0.01$, *** $p < 0.001$ and **** $p < 0.0001$.

Chapter 3

Fe/Cu Multi-segmented Nanowires

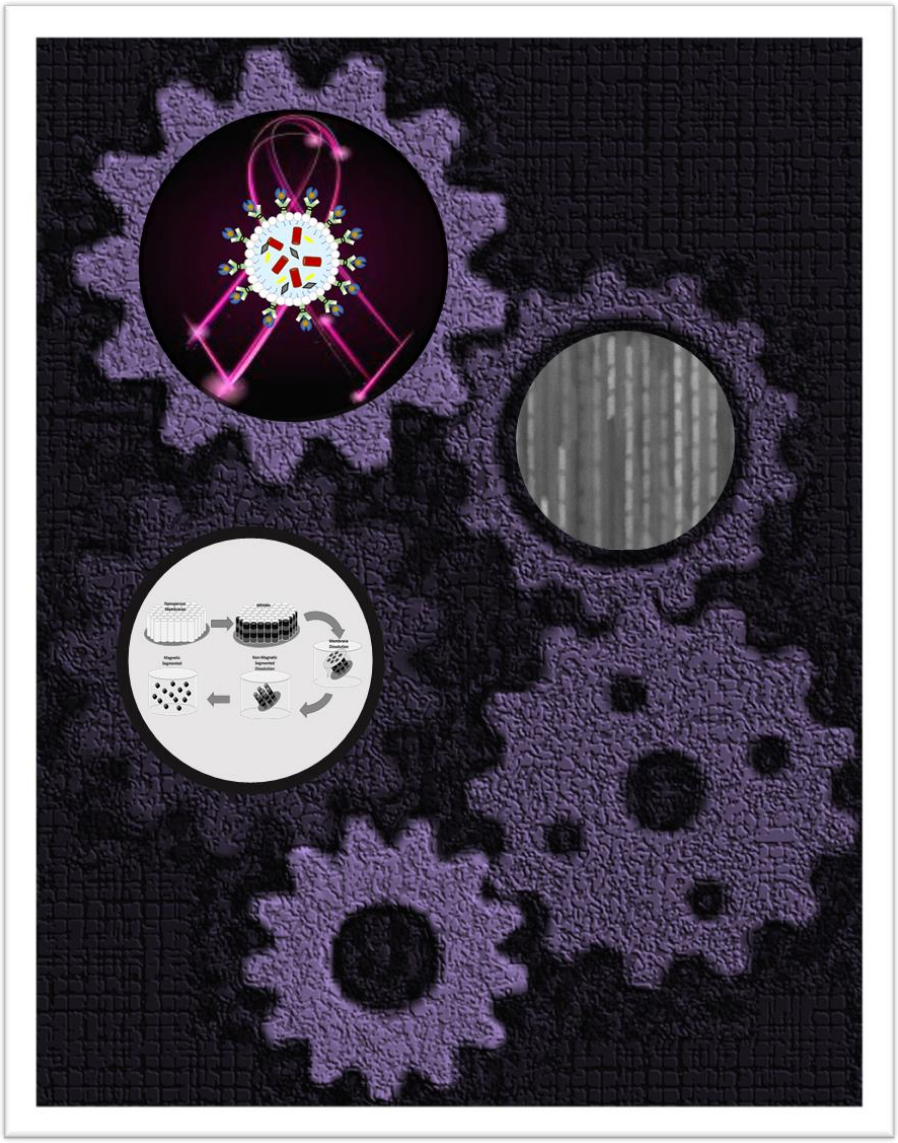

Chapter 3

Fe/Cu Multi-segmented Nanowires

In this chapter, we present the synthesis and characterization of Fe/Cu multi-segmented NWs obtained from electrodeposition in AAO templates. To better understand the main physical properties of these biocompatible NWs, the characterization was performed inside the pores of AAO templates by using various techniques such as SEM, TEM, XRD, VSM and SQUID (the characterization after the template removal, encapsulation in lipidic nanoparticles and internalization in cell lines is presented in chapter 6). To reveal the role of the Cu and Fe segment length in the NW magnetic properties, M(H) and FORC measurements were performed (part of this chapter is already published in Moraes, S.; Navas, D.; Béron, F.; Proenca, M.P.; Pirota, K.R.; Sousa, C.T.; Araújo, J.P. The Role of Cu Length on the Magnetic Behaviour of Fe/Cu Multi-Segmented Nanowires. Nanomaterials 2018, 8, 490).

3.1 Overview

Ferromagnetic nanostructures with complex and controlled magnetic behavior have been extensively studied during the last years. The need for emerging technologies and the recent advances in chemical and self-assembly synthesis techniques have boosted the growth of three-dimensional nano-objects [259]. This capacity to control size and shape, not only in the plane but also along the vertical direction, leads to the appearance of new effects in spin configurations [260, 261]. This potential is of great interest for a wide range of applications, such as novel magnetic sensors [262, 263], chemical and biological sensors [264], drug delivery systems [265] and medical treatment by hyperthermia [266]. Moreover, nanowires (NWs), nanorods (NRs) and nanodiscs (NDs) in vortex state with strong anisotropic and magnetic moments, covering a broad size range, are completely innovative [151]. Instead of the spherical counterparts, these systems suggest the possibility of performing magneto-mechanical cell death at lower field magnetic fields, low frequencies and low particle concentration [71]. At the same time, these magnetic nanostructures can significantly enhance the contrast in MRI [267].

Besides nanostructures in vortex state, also high-aspect ratio nanowires have been studied in the context of magnetomechanical induced cell damage by several authors. Fung *et al.* [28] studied the magneto-mechanical cell death of fibroblast (NIH/3T3) using ferromagnetic Ni NWs, with diameters ranging from 198 nm to 280 nm and an average length of 4.4 μm with longitudinal magnetic anisotropy. These nanostructures did not significantly affect the cell viability in the absence of a magnetic field, in spite of Ni being an agent of hypersensitivity and moderately cytotoxic. But, when the NWs were exposed to a weak (240 mT), and low-frequency (1 Hz) alternated magnetic field for 20 min, a viability reduction of the cell cultures by 89% was observed, indicating that this process effectively induced cell death. Ni, Fe and segmented NWs with different dimensions and optimized magneto-mechanical cell death were tested in several cell lines demonstrating promising results [74-76, 268].

Bearing in mind the improvement of this particular application using magnetic NWs, Martinez-Banderas *et al.* [28] developed a bimodal strategy to induce cancer cell death through the combination of an anticancer drug (doxorubicin) with the mechanical perturbation exerted by Fe NWs (average length of 6.4 μm and a diameter of 30 – 40 nm) exposed to a low frequency (10 Hz) AC magnetic field (1 mT) for 10 min. A large cytotoxic effect in the breast cancer cells caused by the dual effect of the functionalized NWs was also observed, with a maximum reduction of 73% in cell viability. Therefore, it was demonstrated that the combination of the chemotoxic and magneto-mechanical treatment modes, using magnetic nanowires, had synergistic effects, turning this technique into an attractive approach for novel cancer therapies.

Within several methods of NWs fabrication, template-assisted electrodeposition in anodic aluminum oxide (AAO) has been widely used [160, 162, 269] because of its ability to control the NW size and shape coupled with the simplicity and low cost of the involved processes. Moreover, the NWs inside AAO are organized in a closed-package array, which allows a better understanding of the inter-wire and intra-wire magnetic interactions [270].

An important class of NWs for applications in magnetic devices is the multi-segmented one [113, 131]. In particular, for biomedical applications segmented NWs present two key advantages: (1) segments of different materials can be functionalized with different moieties, namely with a drug and a target [271]; (2) the amount of magnetic nanostructures can be increased hundreds of times per sample since the non-magnetic layer can be used as a death layer and removed by selective chemical etching [112]. The combination of multilayers of different materials, both magnetic and non-magnetic, has been spreading much interest due to the magnetic capability to control the interactions and the effect of magnetic anisotropy obtained by only varying

the metal type and segment lengths [272-274]. In this sense, we can highlight some studies on multi-segmented NWs that employed Ni/Au [129, 275], Ni/Cu [113, 135, 250, 276-280], CoNi/Cu [281], NiFe/Cu [282], FeGa/Cu [273, 274], Co/Cu [283-286], and Co/Au [287]. Because of particular advantages, such as their high saturation magnetization [288] and the large possibility of modulation of their magnetic properties [289], systems with FeCo alloys (i.e., CoFeB/Cu [290], CoFe/Au [289], CoFe/Cu [27, 291-294]) have been extensively studied. As an example, Núñez *et al.* [291] investigated the magnetic behavior of CoFe/Cu multi-segmented NWs by varying the Cu spacer thickness. Complementarily, Palmero *et al.* [292] presented a study of first-order reversal curve (FORC) diagrams for CoFe/Cu multi-segmented NWs.

However, for biomedical applications, Co is usually considered toxic, and, thus, a magnetic segment with only Fe in its composition could be more interesting. Still, only a few studies are found in the literature about Fe/Cu multi-segmented NWs: Ramazani *et al.* [295] presented a comparative study between the multi-segmented NWs of Co/Cu, CoFe/Cu, and Fe/Cu, and Almasi-Kashi *et al.* [296] studied the effect of the magnetic layer thickness on the magnetic properties of Fe/Cu multi-segmented NWs. Moreover, most of these works are aimed at applications in electronic devices, leaving open the biotechnology field. In this field, the main challenge is to achieve better control and to understand the magnetic behavior of an array of 1D magnetic systems composed only of purely biocompatible materials that enable future biomedical applications.

3.2 Electrodeposition behavior of Fe/Cu multi-segmented nanowires

A representative example of the pulsed electrodeposition potential sequence employed for the syntheses of multi-segmented Fe/Cu NWs is showed in Fig. 3.1. (a) and (b). The possibility to perform co-deposition of Fe/Cu layers is based on the difference of the reduction potentials of Cu (+0.14 V versus Ag/AgCl) and Fe (−0.644 V versus Ag/AgCl) that are larger than - 0.6 V and also in the very low concentration of Cu (Cu^{2+}<<Fe^{2+}). Both conditions ensure low contaminated multilayers of Fe/Cu NWs [297, 298] since, for low Cu^{2+} concentration, the Cu deposition is diffusion-limited over a wide potential range from −0.15 to −0.7 V [269]. Therefore, for Fe deposition at higher potentials (−1.1 V), the molar fraction of Cu in Fe layers is expected to be lower than 10%, and Fe-rich segments are obtained. Figure 3.1. (a) shows all pulses to growth 15 Cu/Fe layers where it is possible to observe the homogeneous growth of the layers. Only 5 and 10% of current density increase was observed in Fe and Cu

deposition, respectively, between the first and the last electrodeposition pulse, as shown in Fig. 3.1 (b).

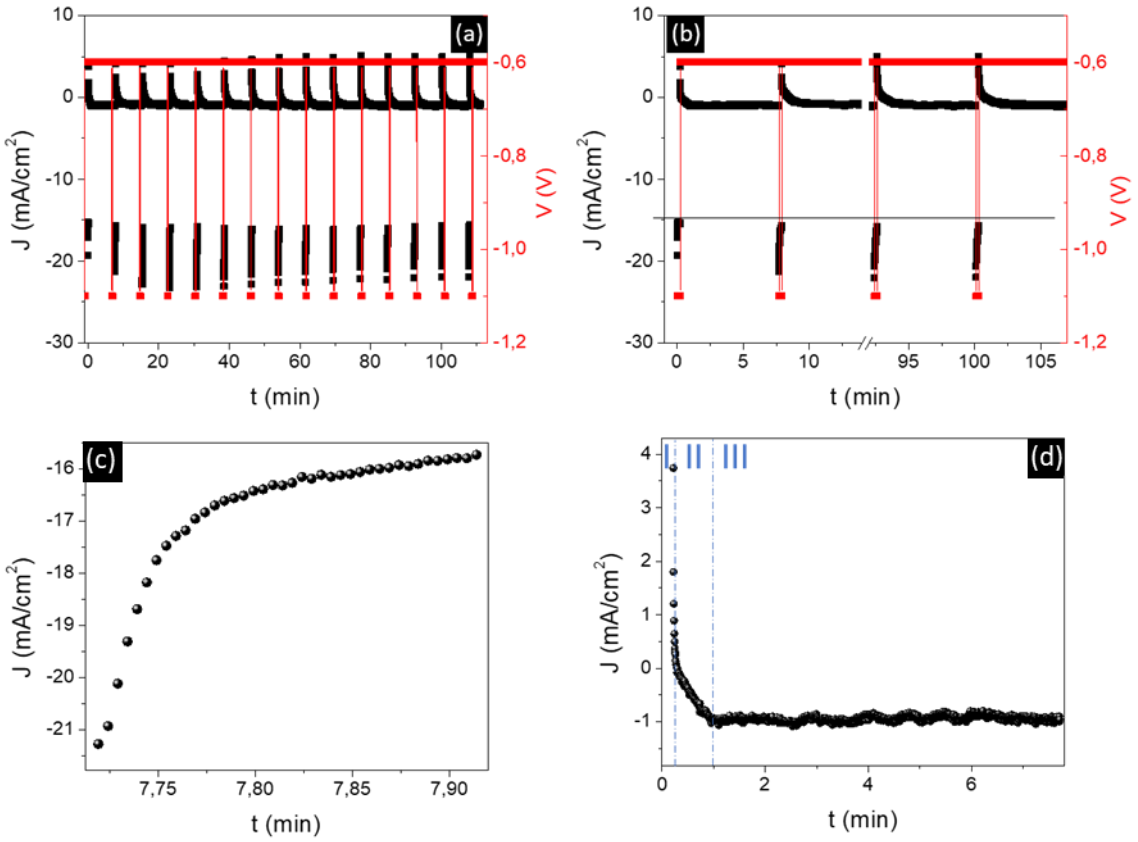

Fig. 3.1: Pulsed electrodeposition behavior in the synthesis of the multi-segmented Fe/Cu NWs in AAO templates: (a) all the 15 pulses for the Fe deposition pulse at -1.1 V and the Cu deposition pulses at -0.6 V and the respective current during the deposition process; (b) Inset shows a sequence of 4 double pulses (the firsts and the lasts); (c) current density during the Fe deposition and (d) Cu deposition.

The nucleation and growth mechanism as well as the electrodeposition rate, can be determined using the current transients as shown in a representative example presented in Fig. 3.1. In general, each metal layer nucleation mainly depends on the nature of the previous layer and the density of active sites on the surface, such as steps, kinks or other surface defects, whereas the growth mechanism depends on the applied potential and electrolyte [299]. Depending on the nucleation rate, two limiting cases can be identified corresponding to instantaneous nucleation and progressive nucleation, which corresponds to high and low nucleation rates, respectively [300, 301]. In both cases, the current density starts to increase with time due to 3D growth of the nuclei, which leads to an increase of the electrodeposition surface area. Then the

current achieves a quasi-constant value when the diffusion zones around the growing nuclei start to overlap, resulting in a 1D diffusion-limited current [300]. In the particular case of NWs growth in the nanopores of AAO membrane, the nucleation process may be only kinetically limited at the beginning in very short times, due to the large diffusion flux to small nuclei, but then the nuclei and NWs growth become diffusion limited [302, 303].

In the deposition of Fe layers (Fig. 3.1 (c)), a decrease in current density is observed associated with diffusion-limited growth. The expected initial increase in current due to nucleation is not observed due to the high deposition rate of Fe associated to the high deposition potential used (-1.1 V), indicating instantaneous nucleation where the nucleation sites become saturated after short times [5]. In the case of Cu, a more complex *j*(*t*) curve is observed with several phases, as shown in Fig. 3.1(d). The positive current observed in the first seconds can be associated to the metal oxidation in the previous Fe layer (Phase I). Then, the transients exhibit an increase in current due to the Cu layer nucleation (Phase II) followed by a quasi-constant current during the layer growth (Phase III). Taking into account the quite low deposition potential of Cu (-0.6 V) and the low concentration of Cu ions in the electrolyte, the Cu nucleation reveals a behavior of progressive nucleation where the density of nuclei increases linearly with time due to the low deposition rate [301, 304].

From the *j*(*t*) curves, the charge along the deposition process was determined and showed different slopes for Cu and Fe deposition, revealing that the deposition rate of Cu is lower than of Fe. From these deposition curves, the deposition rates of 0322 ± 0.001 nm/min and 0.0037 ± 0.0003 nm/min were determined for Fe NWs and Cu NWs, respectively. The low deposition rate of Cu compared with Fe is mainly associated with the low concentration of Cu ions present in the solution.

3.3 Morphological and structural characterization

Figure 3.2 display selected scanning electron microscopy (SEM) in cross-sectional views of the obtained (a) Fe NWs, (b) Cu NWs and (c) Fe/Cu multi-segmented NWs. The brighter part of the NWs observed on the bottom of the AAO membrane in all samples (Fig. 3.2) corresponds to one Au segment of 500 nm in length that is electrodeposited before the Cu and Fe layers to increase the samples homogeneity. The Cu contamination in the Fe NWs is practically null since Cu peaks are not observed in the EDS spectrum presented in the upper quadrant of the Fig 3.2 (a). Fe and Cu NWs present homogeneous diameters of 50 nm along the wire (Fig. 3.2 (a) and (b)), which corresponds to the AAO pore diameter (inset of figure 3.2. (b). The Fe and

Cu length are (1.6 ± 0.2) µm and (1.2 ± 0.1) µm, respectively. The deposition rate was calibrated through the SEM images of long NWs of each metal and correspondent deposition potential (Fig. 3.2. (a) and (b)): ≈ 2.5 nm/s at −1.1 V for Fe and ≈ 0.3 nm/s at −0.6 V for Cu. Then, considering these electrodeposition rates, the pulsed electrodeposition was used to accurately control the length (*L*) of each segment**.**

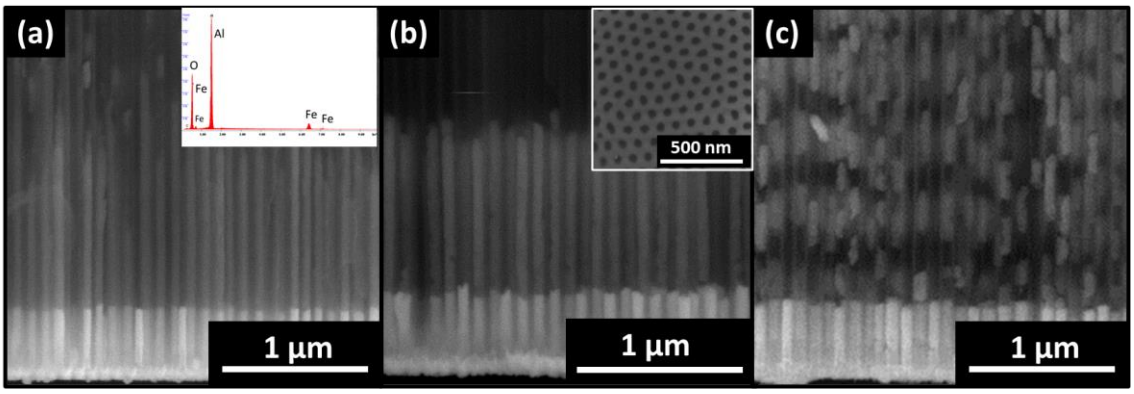

Fig. 3.2: Cross-sectional SEM images of (a) *Fe* NWs and EDS spectrum (inset) (b) Cu NWs and bottom of AAO (insert) and (c) Fe/Cu multi-segmented NWs grown in Anodic Aluminum Oxide (AAO) membranes.

The SEM images in Fig. 3.2. (c) show the Fe/Cu NWs, where the layered structure and the reproducibility of the layer thickness are clearly seen. The Cu segments (sections) alternated with Fe layers correspond to the bright and dark sections of the NWs, respectively (Fig. 3.2. (c)). Notice that due to the close atomic number of Fe and Cu, the segments are not easily distinguished using SEM and high contrast images need to be used that sometimes create artifacts. Nevertheless, the average diameter of both segments is the same (45 ± 5) nm, and the length of the segments was kept constant along the NW. The Fe and Cu segment length was (160 ± 20)/(200 ± 10) nm. The analysis of the interface between the segmented using high-resolution transmission electron microscopy has been previously reported by Chen *et al.* [276] in which sharp interfaces have been observed.

XRD analysis was performed for *Fe* and *Cu* NWs with (3.2 ± 0.2) µm and (1.2 ± 0.1) µm in length respectively, in AAO templates. The Fe NWs present a polycrystalline body-centered cubic (bcc) structure (Fig. 3.3 (a)). One main peak and two secondary peaks with lower intensities were identified at 44.52°, 65.04°, and 82.12°, which corresponded to the (110), (200), and (211) crystallographic planes, respectively. The *Cu* NWs presented a polycrystalline face-centered cubic (fcc) structure (Fig. 3.3 (b)). This Cu NWs spectrum also exhibited one main peak and two secondary peaks with

lower intensities at 43.28°, 50.55°, and 74.45°, which corresponded to the (111), (200), and (220) crystallographic planes, respectively.

A simple estimation of the average grain size (GS) was obtained using the Scherrer equation:

$$GS = \frac{k\lambda}{\omega \cos\theta} \tag{3.1}$$

where k is the shape factor (typically 0.9 for spherical grains), λ the X-ray wavelength (1.540593 Å, Cu K_α radiation), ω the line broadening taken at half the maximum intensity (FWHM) in radians, and θ the Bragg angle. From the Fe (110) and Cu (111) most intense peaks, a GS value of about 22 nm was estimated for both materials. The small GS can be related to the electrodeposition conditions, namely, the used high current density combined with the electrolyte nature [305, 306]

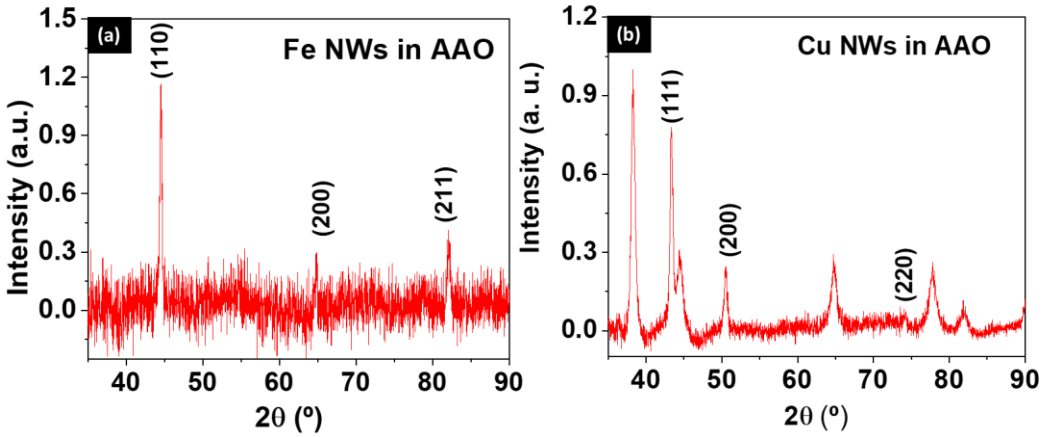

Fig. 3.3: X-ray diffractometry (XRD) pattern of an electrodeposited Fe (a) and Cu (b) NW array in AAO membranes. (*) represents peaks from Au NW deposited at the bottom of the pores.

3.4 The role of Cu length in the magnetic behavior

To study the role of the Cu non-magnetic layer between the Fe layers, a set of samples with constant Fe length and varying the Cu length was fabricated. For biomedical applications, non-interacting Fe segments are wanted to access the individual magnetic behavior of the Fe NDs or NWs. SEM images, shown in Fig. 3.4, display selected cross-sectional views of the Fe/Cu NWs grown in the AAO membranes. The layered structure and layer thickness homogeneity are clearly observed independent of the Cu length (in which brighter segments are composed of

Cu, while the darker ones correspond to Fe layers). The NWs presented an average diameter of (45 ± 5) nm, mimicking the pore size of the AAO template. The Cu segments' length (L_{Cu}) was varied, whereas the Fe electrodeposition parameters were maintained constant in all samples. As a result, the Fe segments length (L_{Fe}) presented an average of (30 ± 7) nm, and L_{Cu} varied from (15 ± 5) nm (Fig. 3.4 (a)) to (120 ± 10) nm (Fig. 3.4 (a)).

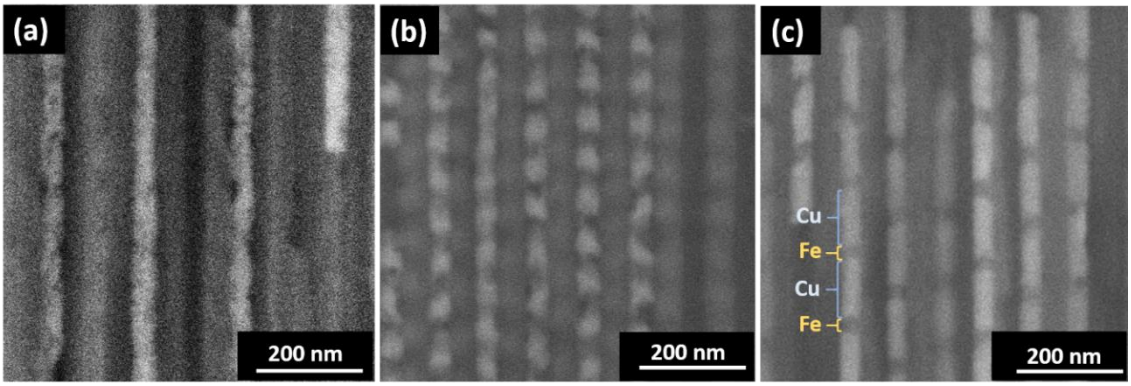

Fig. 3.4: Cross-sectional scanning electron microscopy (SEM) images of Fe/Cu nanowires (NWs) grown in anodic aluminum oxide (AAO) membranes. The average diameter and length of the Fe segments were kept constant to (45 ± 5) nm and (30 ± 7) nm, respectively, while the Cu segment length (L_{Cu}) was varied: (a) (15 ± 5) nm; (b) (60 ± 6) nm; (c) (120 ± 10) nm.

3.4.1 Magnetic properties

Figure 3.5 shows the magnetic hysteresis loops (Fig. 3.5 (a)–(c)) and their related FORC diagrams (Fig. 3.5 (d)–(f)) of the electrodeposited Fe/Cu NW arrays. Room temperature hysteresis loops were measured by applying the external magnetic field parallel (in red) and perpendicular (in black) to the NW long axis. Both coercive fields (H_c) and reduced remanence (m_r), given by the ratio M_r/M_{sat} (where M_r is the magnetization remanence and M_{sat} is the saturation magnetization), are summarized in Table 3.1. A decrease of the parallel coercivity $H_c^{||}$, (and increase of perpendicular coercivity $H_c^{\perp}$) was observed when the L_{Cu} was enlarged (Table 3.1). The same behavior was obtained for the parallel and perpendicular reduced remanence (m_r).

Therefore, and as a general idea extracted from the hysteresis loops, we could conclude that the easy magnetization axis evolved from parallel to the NW long axis for the *Fe* NWs with the thinnest Cu segments (L_{Cu} = 15 nm), to an almost isotropic behavior for the thickest case (L_{Cu} = 120 nm). This behavior suggests that *Fe* NWs exhibit different magnetization reversal regimes as a function of the *Cu* segments' thickness.

In order to achieve a deeper understanding of the evolution of the easy magnetization axis and the Fe NWs magnetization reversal processes as a function of the Cu spacer thickness, FORC measurements were performed with the external magnetic field applied parallel to the NW long axis (Fig.3.5 (d)-(f)). FORC diagrams clearly showed a striking behavior modification when increasing Cu thickness.

In a first approximation, one could suggest that, for 15 nm Cu thickness, the NW internal dipolar coupling (between nanoelements inside a NW) was still sufficiently large to sustain a magnetization reversal process for the array similar to the one obtained in homogenous Fe NWs with comparable dimensions [250]. This hypothesis arises from the FORC distribution elongation along the H_u axis, typical of a demagnetizing mean interaction field (H_{int} = k * M/M_{sat}), with the interaction field constant k < 0) and associated to the one-by-one NW reversal governed by this interaction field.

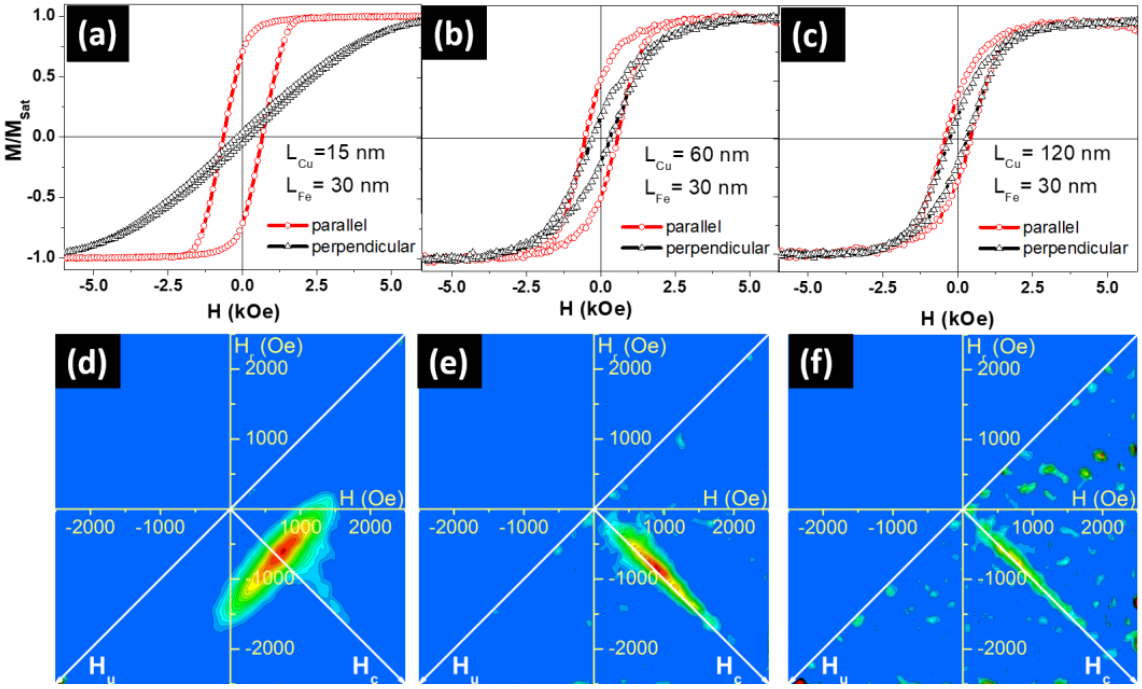

Fig. 3.5: Hysteresis loops of multi-segmented Fe/Cu NWs when the external magnetic field was applied parallel (in red) and perpendicular (in black) to the NW long axis and for LCu (a) 15 nm, (b) 60 nm, and (c) 120 nm. Their related first-order reversal curve (FORC) diagrams when the external magnetic field was applied parallel to the NWs' long axis and for LCu (d) 15 nm, (e) 60 nm, and (f) 120 nm.

Table 3.1: Magnetic characteristics of the multi-segmented nanowires: coercive field (H_c) and reduced remanence (m_r) measured with the magnetic field applied parallel (||) and perpendicular (⊥) to the nanowires' long axis.

Systems	$H_c^{\|\|}$(Oe)	$H_c^{\perp}$(Oe)	$m_r^{\|\|}$	$m_r^{\perp}$
$(Fe_{(30nm)}/Cu_{(15nm)})_{15}$	650 ± 50	190 ± 30	0.70 ± 0.03	0.04 ± 0.01
$(Fe_{(30nm)}/Cu_{(60nm)})_{15}$	480 ± 30	240 ± 40	0.45 ± 0.02	0.07 ± 0.02
$(Fe_{(30nm)}/Cu_{(120nm)})_{15}$	430 ± 30	280 ± 40	0.37 ± 0.02	0.20 ± 0.02

Note: $(Fe_{(Fe\ length)}/Cu_{(Cu\ length)})_{(layers)}$

A closer analysis of Fig. 3.5 (d) reveals that the FORC distribution exhibits two features: a slight counter-clockwise tilt and an additional elongation on the distribution right side, which is characteristic of a non-negligible coercivity distribution when submitted to a demagnetizing interaction field. In this case, the tilt arose from the fact that the magnetization reversal at negative H_u values only involved the NWs with the lowest coercivity. Following the procedure described in references [307] and [308], quantitative parameters could be estimated from the FORC diagram based on its distribution extremities. In the present case, the experimental result was comparable to a system consisting of a normal distribution of coercivity ((750 ± 45) Oe) with a mean interaction field constant k = -800 Oe.

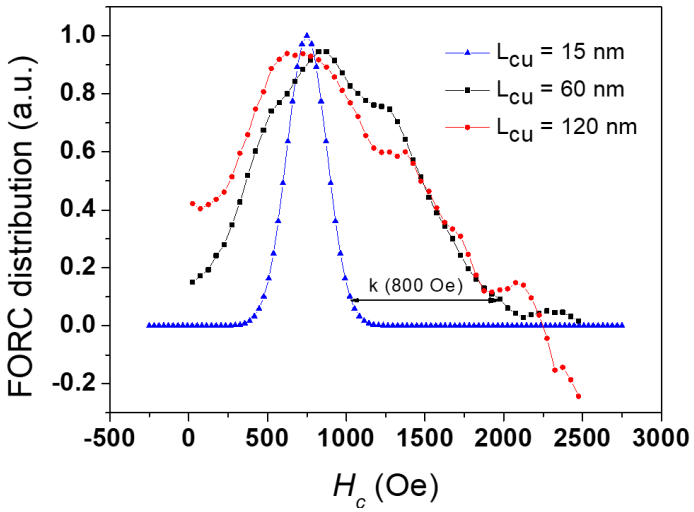

Fig. 3.6: Smoothed and normalized cross sections along the Hc axis for Cu thicknesses of 60 (in black) and 120 nm (in red), along with the coercivity distribution estimated from the FORC distribution for 15 nm Cu thickness (in blue).

By increasing Cu spacing to 60 and 120 nm, the FORC distribution drastically changed into a single feature, elongated along the H_c axis and narrower as Cu thickness was increased (Fig. 3.5 (e) and Fig. 3.5 (f)). The common explanation for this

type of distribution is through a collection of non-interacting magnetic entities, for which the coercivity distribution can be extracted by the cross-section along the H_c axis [308]. In the specific context of multilayer magnetic NW arrays, it could indicate that Cu thickness between the Fe disks was sufficiently large to magnetically decouple them (along the NW axis), thus destroying the one-by-one NW reversal mode.

Since the dimensions and quantity of Fe discs remained identical in Fig. 3.5 (e) and Fig. 3.5 (f) cases, it is interesting to compare their related H_c axis cross sections (See Fig. 3.6). According to Preisach model, this cross section, taken as the FORC distribution values along the H_c axis, i.e., at H_u = 0 Oe, would directly yield the nanodisc coercivity distribution if the nanodiscs are completely decoupled one from each other (non-interacting). Because of the small amount of magnetic material, the comparison was complicated by the large noise-to-signal ratio present in the experimental results. However, it is possible to conclude that the two distributions are globally similar, i.e., that the modification in Cu thickness did not influence the Fe disc coercivity, as expected. On the other hand, when including the estimated coercivity distribution for the sample with 15 nm-thick Cu discs on the same graph, we observed an important reduction of the distribution width, while its maximum remained around the same value as for the samples with thicker Cu spacers. Whereas this value (≈ 750 Oe) is reasonable for Fe nanowires/nanodiscs of 45 nm in diameter, the H_c cross sections spread until coercivity values considerably higher than expected for these Fe nanodiscs.

Therefore, we propose an alternative hypothesis to explain the large elongation along the H_c axis when the multi-segmented NWs are decoupled. Instead of resulting solely from the individual nanodisc coercivity, this elongation may arise from the neighbor-to-neighbor nanodisc dipolar interaction. This interaction field is highly inhomogeneous inside the array, thus not yielding a mean interaction field behavior. Instead, the signature of the FORC distribution appears on the H_c axis at higher values than the nanodisc coercivity. This phenomenon is based on the same process that yields the common artifact of the “tail” towards high H_c values, visible on experimental NW FORC distributions and explained by Stancu *et al.* [309]. In this specific case, the NWs located near the array border were submitted to a reduced interaction field compared to the NWs near the array center, due to the lack of neighbors. This interaction field spatial inhomogeneity and, thus, the different values for the same applied field, resulted in an apparent higher reversal field for these NWs near the array border. The highest apparent reversal field value is the magnetic entity intrinsic coercivity added to the maximum interaction field, when the array is almost saturated. In the present case of multilayer NW arrays decoupled along the NW axis but creating

a dipolar field on the neighbored discs, the intrinsic coercivity distribution of the Fe nanodiscs could be assumed to remain similar among the samples, despite the varying Cu nanodisc thickness. Therefore, the large elongation of their FORC distribution along the H_c axis arose from the same artifact explanation as for the homogeneous NW array.

3.4.2 Micromagnetic simulations

In order to identify the magnetization reversal modes in Fe/Cu NWs and obtain a deeper insight into the effects of the magnetostatic interactions between segments and NWs, three-dimensional micromagnetic simulations using MuMax3 software (Version 3.9.1) [310] were performed. According to our experimental results, we simulated multi-segmented individual NWs with a Fe segment 40 nm in diameter and 35 nm in length and with non-magnetic Cu spacer lengths ranging from 15 to 120 nm. As the electrodeposited Fe could be contaminated by small amounts of Cu, the magnetization of the Fe layers was set to M_{sat} = 1600 emu/cm^3, which was about 6% lower than Fe typical saturation magnetization value (1700 emu/cm^3) [311]. This assumption was experimentally verified in multi-segmented Co/Cu NWs prepared by electrodeposition into AAO templates, where a saturation magnetization value of 1200 emu/cm^3, instead of 1400 emu/cm^3, was determined for Co and was justified by the presence of Cu impurities in Co [312]. We used an exchange coupling constant A = 43 × 10^{-8} erg/cm [313, 314] and a Fe magneto-crystalline anisotropy value K = 4.8 × 105 erg/cm^3, based on the X-ray diffraction measurements. Cell size was chosen to be (2.5 × 2.5 × 2.5) nm^3, which was two times smaller than Fe exchange length $l_{ex} = \sqrt{2A/\mu_0 M_{sat}^2} \approx 5\ \mathrm{nm}$. Finally, the damping parameter was taken as 0.5 to ensure rapid convergence.

First of all, the magnetostatic interactions and the magnetization reversal modes of an isolated Fe disc and multi-segmented Fe/Cu NWs were analyzed as a function of Cu thickness, with Fe layers ranging from 1 to 15. The simulated hysteresis loops of 1 and 15 Fe discs, separated by 120 nm of Cu spacer, were nearly identical (see Fig. 3.7). This fact confirmed our FORC analysis indicating that this segmented NW behaved like a set of 15 non-interacting nanoparticles. Moreover, in the demagnetized state, each Fe segment showed a kind of vortex configuration with around 60% of the magnetization pointed parallel to the NW long axis (Fig. 3.7 (d)), as in the case of an isolated Fe nanodisc (Fig.3.7 (b)). Although the magnetic measurements performed in the NW array do not indicate the existence of a vortex state probably due to the dipolar interactions, the individual NWs after the AAO template removal should present a

vortex state which make these NWs promising nanostructures magneto-mechanical cell death.

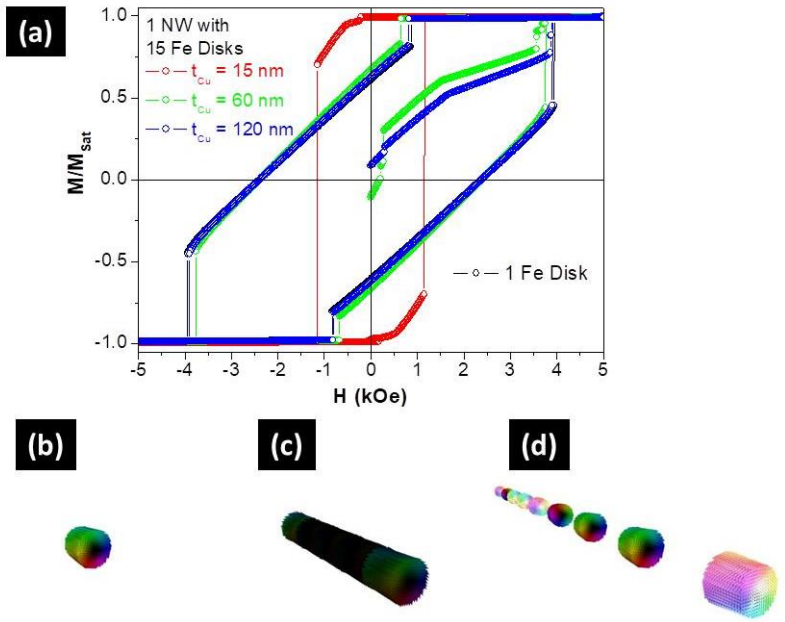

Fig. 3.7: (**a**) Simulated hysteresis loops and virgin curves of one Fe disc (in black) and isolated multi-segmented Fe/Cu NWs with 15 discs of L_{Fe} = 35 nm separated by L_{Cu} = 15 (in red), 60 (in green), and 120 nm (in blue). 3D simulated magnetic configurations of (**b**) one Fe disc and isolated multi-segmented Fe/Cu NWs separated by L_{Cu} of (**c**) 15 nm and (**d**) 120 nm, at the demagnetization state.

On the other hand, the hysteresis loop of a NW with 15 Fe discs separated by 15 nm of Cu spacer, was drastically different than that of the isolated Fe disc, thus confirming that they were strongly coupled (Fig. 3.7 (a)). Moreover, and like in long cylindrical Fe NWs [315], the reversal mode corresponded to the nucleation and propagation of a vortex domain wall from the NW extremities, which was predicted from the FORC curves (Fig. 5 (d)). For the intermediate thickness (60 nm of Cu spacer), and although the hysteresis loop was similar to the non-interacting case, the Fe discs were still slightly coupled.

Finally, the effect of the magnetostatic interactions between NWs was explored by simulating NW arrays with a hexagonal closest packet ordering and 105 nm of periodicity. However, and because of time consuming, our simulations were restricted to 7 and 23 NW arrays and up to 3 Fe segments.

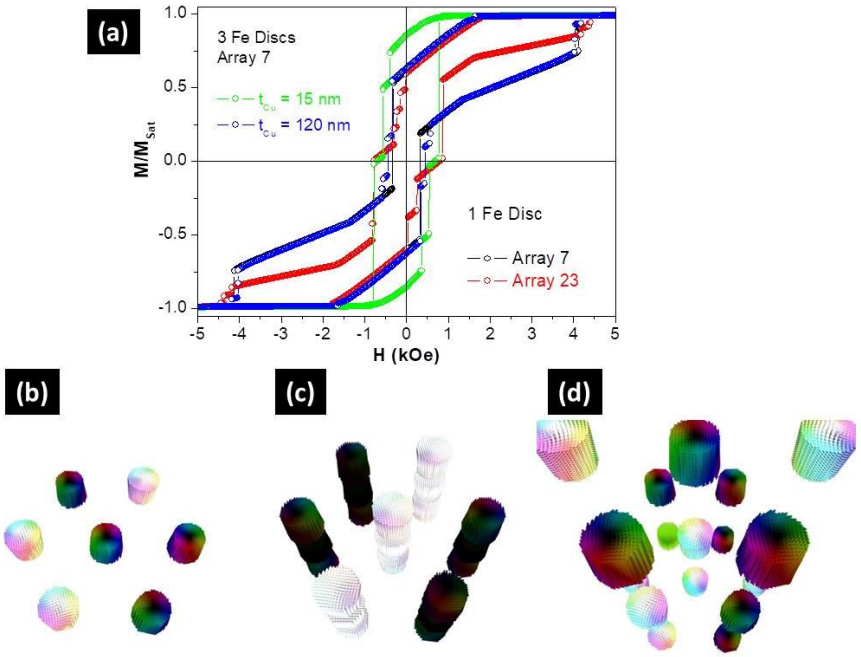

Fig. 3.8: (**a**) Simulated hysteresis loops of one Fe disc array with 7 (in black) and 23 discs (in red), and seven multi-segmented nanowire arrays with three discs separated by L_{Cu} = 15 nm (in green) and 120 nm (in blue). 3D simulated magnetic configuration of one Fe disc array (**b**) and multi-segmented Fe nanowire arrays separated by L_{Cu} = 15 nm (**c**) and 120 nm (**d**) at the demagnetization state.

For the NWs array with one segment of Fe, the hysteresis loop showed a drastic dependence on the wire quantity (Fig. 3.8 a). Although the normalized remanence was not affected by the wire quantity, the coercivity was reduced from about 2.4 kOe for an isolated Fe segment to lower than 0.8 kOe for an array with 23 nanoelements. A similar behavior was observed for the NWs array with three Fe segments separated by 120 nm of Cu. Therefore, our simulations confirmed that the magnetostatic interaction between NWs governed the magnetic behavior of the Fe/Cu multi-segmented NWs formed by a set of non-interacting (along the axis) magnetic discs.

On the other hand, the hysteretic loop of a NW array with three Fe segments and L_{Cu} = 15 nm (Fig. 3.8 a), was similar to that of the isolated multi-segmented NW (Fig.3.7 a) with small reductions of both coercivity and normalized remanence. In this case, we could conclude that the magnetic response was mainly controlled by the dipolar interactions between the Fe segments inside each NW.

Although simulations of the NW arrays allowed us to achieve good correlations with the experimental data, we should note that we studied a reduced number of NWs (7 or 23) and that the number of layers was also limited up to three elements. Therefore, the comparison with experiments, such as the coercive fields and remanence values, could

be only qualitative. Simulations using arrays with a higher number of NWs and layers will be required for a more proper and quantitative analysis.

3.5. Fe/Cu nanowires with different number of bi-segments

In this section, we assessed the magnetic behavior of segmented NWs as a function of bi-layers number. The prepared samples consisted of N = 1, 3, 5, 15 and 20 alternating bi-layers with Fe thickness of ~300 nm and Cu length between 60 and 120 nm. The hysteresis loops for the Fe/Cu NWs with 1 and 20 bilayers are presented in Figure 3.9. (a) and (b) respectively. In both cases, an increase in the coercivity and remanence values is observed when the magnetic field is applied parallel to the wire's axis, confirming the anisotropic behavior of the structures. A similar magnetic behavior has been observed for all the samples, independently of the number of bilayers, as presented in Figure 3.9. (c) and (d), where coercivity and remanence values, extrapolated from the parallel and perpendicular loops, are reported as a function of the number of Fe/Cu layers. From Figure 3.9. (c), it can be noticed that the coercivity of the samples slightly increase, either when the field is applied parallel or perpendicular to the wire's axis, when the number of bilayers increases. On the other hand, a steep slope in the remanence values along the parallel direction is observed up to 3 bi-layers, while the values are almost constant along the perpendicular direction.

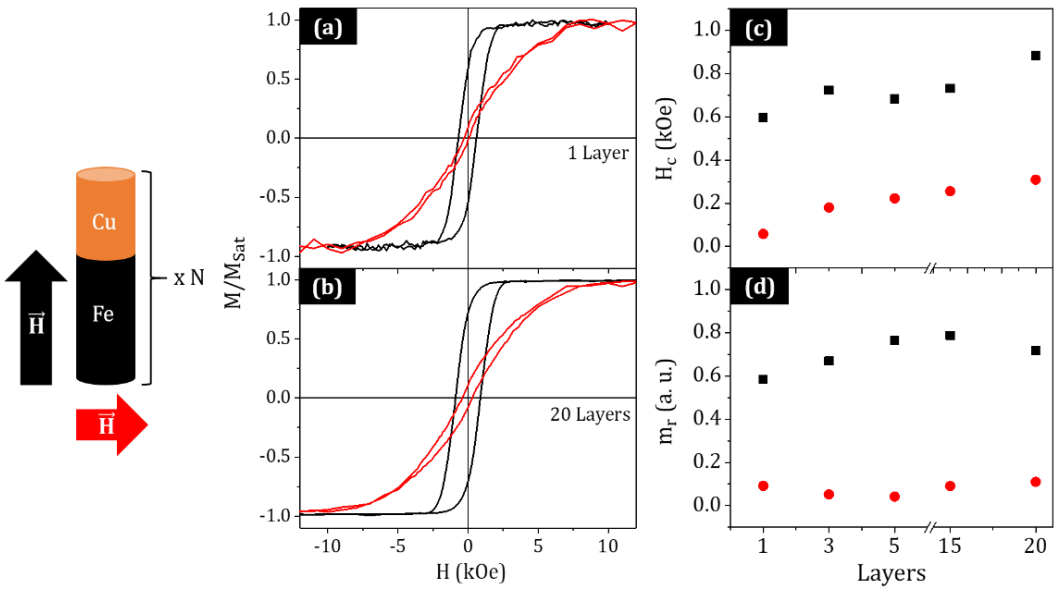

Fig. 3.9: Magnetic hysteresis loops of (a) 1 and (b) 20 Fe/Cu bilayers measured along the parallel (black) and perpendicular (red) directions. (c) Coercivity and (d) normalized remanence values as a function of the number of bi-segments, when applying a magnetic field parallel (black) and perpendicular (red) to the wire's axis.

This phenomenon might be associated with the complex behavior of the magnetization reversal mechanism in multilayered structures, in which interactions between neighboring NWs must be considered [316].

In order to identify the magnetization reversal modes in Fe/Cu NWs as a function of the number of bilayers, 3-D micro-magnetic simulations using MuMax3 software (Version 3.9.1) were performed [310]. According to the experimental results and our previous work presented in section 3.4.2., we simulated multi-segmented individual NWs with 40 nm in diameter and formed by 300 nm length ferromagnetic Fe layers with 120 nm length non-magnetic Cu spacers (see Fig. 3.10.) and ranging the number of bilayers from 1 to 15. For comparison, we also performed the micromagnetic simulations of an individual long Fe nanowire (3 µm length). All parameters used in these simulations (saturation magnetization, damping parameter, exchange coupling constant and magnetocrystalline anisotropy) are the same than used for NWs with different Cu length reported in section 3.4.2. The cell size was chosen to be (2.5 x 2.5 x 2.5) nm^3.

In agreement with literature, micromagnetic simulations shows that the magnetization reversal process in long cylindrical Fe NWs (3 µm length) occurs through the nucleation and propagation of a vortex domain wall from the NW extremities [317]. Like in the longer cylindrical Fe NWs (Fig. 3.10. (a)), the magnetic reversal mode in the 300 nm length segmented Fe NWs occurs through the nucleation and propagation of a vortex domain wall from the extremities of each segment and regardless of the number of bilayers (see Fig. 3.10 (b) and (c)).

From the simulated hysteresis loops with the magnetic field applied along the wire axis, we have extracted the coercivity fields as a function of the number of bilayers of the isolated Fe/Cu NWs (open symbols in Fig. 3.10 (d) and the long Fe NWs (red continuous line in Fig. 3.10 (d). Despite having simulated only one wire, a good quantitative correlation with the experimental data was achieved. Although we already concluded in the previous section that the 35 nm length Fe segments behave almost like a set of non-interacting nanoparticles when they are separated by 120 nm length non-magnetic Cu layers, we claim here that the contribution of the magnetostatic interactions is slightly greater for larger Fe segments. Therefore, we show how the coercive field progressively increases with the number of layers up to the maximum value corresponding to the long Fe NW.

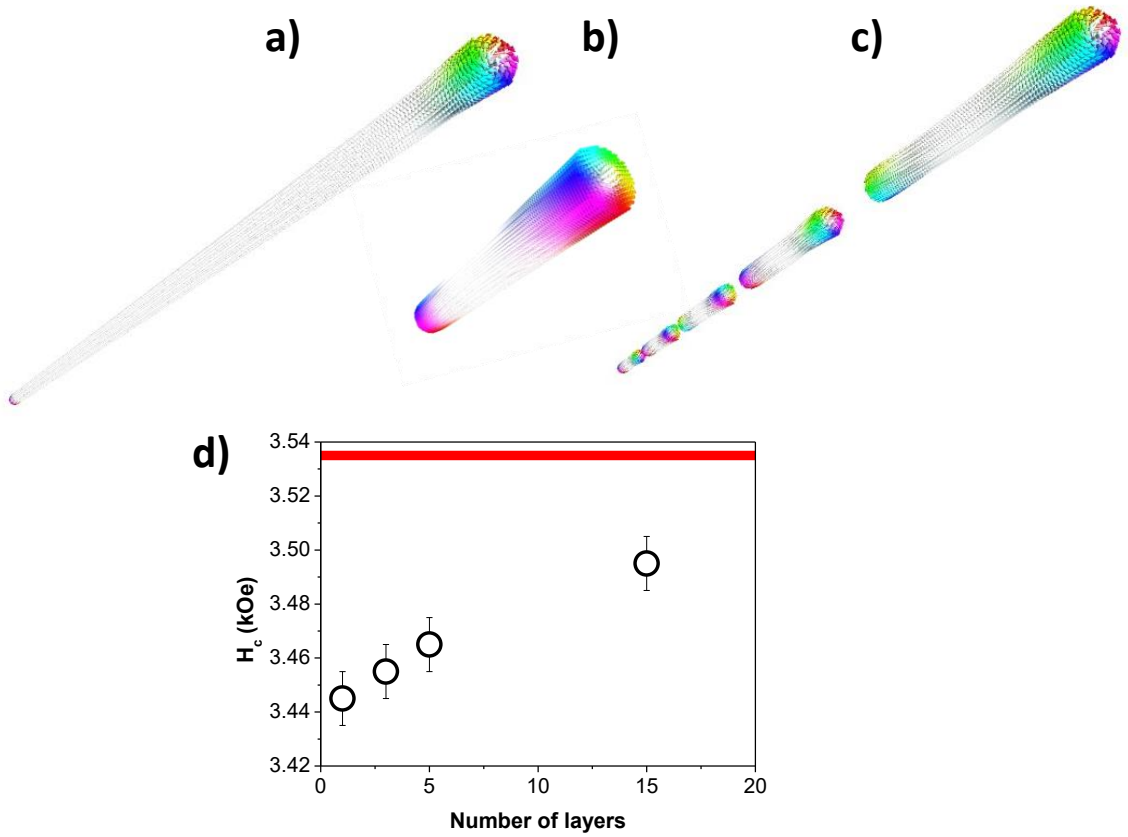

Fig. 3.10: 3D simulated magnetic configurations at the switching field state of (a) one Fe Nw with 3 µm length, and multi-segmented individual Fe (300 nm length)/Cu (120 nm length) NWs with (b) 1 and (c) 5 layers (d) The coercivity field as a function of the number of bilayers (open symbols) and the 3 µm length Fe isolated NW (red continuous line) extracted from the hysteresis loops when the external field was applied parallel to the NW axis.

3.6. Fe/Cu nanowires varying the Fe length

Once we have studied the influence of the non-magnetic spacer magnetic and the behavior of Fe/Cu NWs as a function of the number of bilayers, in this last section we focus our attention on understanding the magnetic behavior of the Fe layer thickness which is a crucial parameter to choose the dimensions of Fe nanostructures for biomedical applications. Therefore, we prepared Fe/Cu NWs where the number of Fe/Cu bilayers was fixed to 15 and the Fe segment thicknesses were range between 20 and 345 nm. In addition, the effect of the non-magnetic spacer thickness has been explored using Cu segments with lengths of 60 and 120 nm. While Fig. 3.11 presents the hysteresis loops of the 15 Fe/Cu bilayer samples, the thicknesses of the segments are reported in Table 3.2, together with the measured coercivity and remanence

values. In addition, the coercivity and reduced remanence values are also presented in Fig. 3.12, as a function of the Fe NWs length and when the external magnetic field was applied parallel to the long nanowire axis.

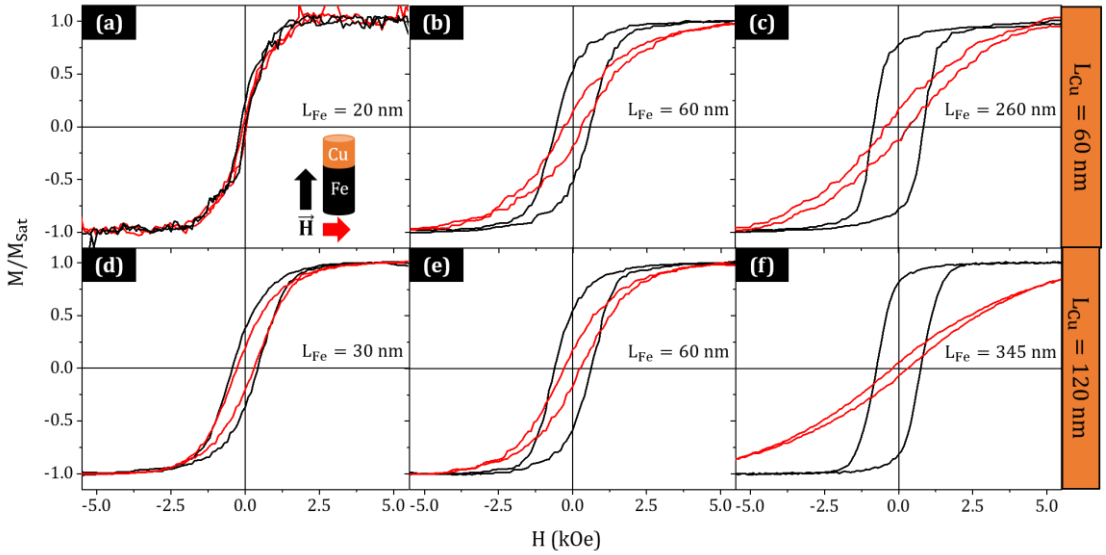

Fig. 3.11: Hysteresis loops of multi-segmented Fe/Cu NWs with different Fe lengths and Cu lengths of 60 nm (a-c) and 120 nm (d-f) measured along the parallel (black) and perpendicular (red) directions.

NWs with larger aspect-ratios, (length/diameter) > 1, shows that the magnetic anisotropy of the structure is dominated by the shape anisotropy factor, leading to align the magnetization easy axis along to the longitudinal NWs' axis (Fig. 3.11 (b-c), (e-f)), as it is usually observed in Fe NWs [318]. Regarding, the coercivity and remanence values along the parallel direction significantly increase by augmenting the Fe length of the samples, while no remarkable variation is noticed along the perpendicular direction. On the other hand, the hysteresis loops show that for small Fe segments (20-30 nm), or aspect-ratios < 1, the magnetization easy axis deviates from the longitudinal direction (Fig. 3.11 (a) and (d)) and confirms an isotropic-like behavior, in agreement with previous studies [128]. Furthermore, for small Fe segments (20 nm and 30 nm), a significant difference in the hysteresis loops can be observed when the Cu length is increased from 60 nm to 120 nm, respectively. In this context, it can be stated that the magnetization easy axis of Fe/Cu NWs with 20 nm of Fe length is perpendicular to the longitudinal axis of the wire and the system behaves like a synthetic antiferromagnet, presenting negligible coercivity and remanence values (Fig. 3.11 (a)). On the other hand, for Fe/Cu NWs with Fe and Cu lengths of 30 nm and 120 nm, respectively, it can be noticed that the magnetization easy axis deviates from the perpendicular direction

towards a more parallel one, as further confirmed by micromagnetic simulations presented in the next section.

Table 3.2: Magnetic properties of multi-segmented NWs: Coercive field (H_c) and reduced remanence (m_r) measured with the magnetic field applied parallel (∥) and perpendicular (⊥) to the NWs' long axis.

Systems	L_{Fe}(nm)	$H_c^{\parallel}$(Oe)	$H_c^{\perp}$(Oe)	$m_r^{\parallel}$ (a.u.)	$m_r^{\perp}$a.u.)
$(Fe_{(20\ nm)}/Cu_{(60\ nm)})_{15}$	20 ± 5	84 ± 40	60 ± 40	0.15 ± 0.04	0.09 ± 0.01
$(Fe_{(60\ nm)}/Cu_{(60\ nm)})_{15}$	60 ± 7	490 ± 60	350 ± 30	0.40 ± 0.10	0.25 ± 0.05
$(Fe_{(260\ nm)}/Cu_{(60\ nm)})_{15}$	260 ± 26	840 ± 40	390 ± 100	0.78 ± 0.03	0.11 ± 0.08
$(Fe_{(30\ nm)}/Cu_{(120\ nm)})_{15}$	30 ± 3	430 ± 30	280 ± 35	0.37 ± 0.02	0.20 ± 0.02
$(Fe_{(60\ nm)}/Cu_{(120\ nm)})_{15}$	60 ± 8	620 ± 45	260 ± 50	0.56 ± 0.04	0.17 ± 0.03
$(Fe_{(345\ nm)}/Cu_{(120\ nm)})_{15}$	345 ± 60	890 ± 40	363 ± 70	0.72 ± 0.02	0.09 ± 0.03

The coercivity values, in particular along the parallel direction, progressively increase by augmenting the Fe length until reaching the value corresponding to the long Fe NW (Fig. 3.12 (a)). On the other hand, the remanence values along the parallel direction increase by augmenting the Fe length, showing higher values when compared to the single Fe NW (Fig. 3.12 (b)).

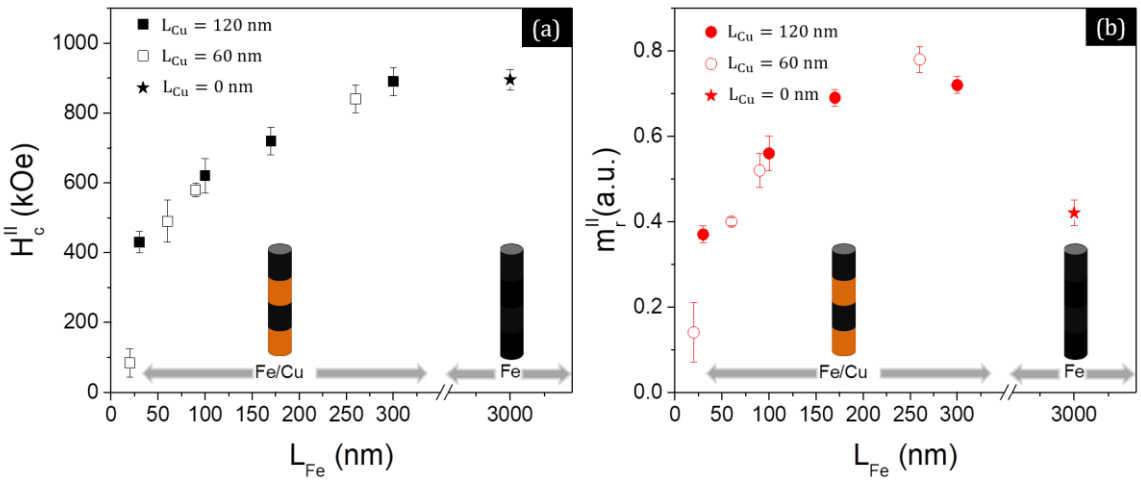

Fig. 3.12. Coercivity (a) and reduced remanence values (b) as a function of the Fe length when a magnetic field is applied in the parallel direction of the wires' long axis.

In order to confirm that NWs exhibit different magnetization reversal regimes as a function of the Fe segment aspect-ratios, the study was complemented also by performing 3D micromagnetic simulations as described in the previous sections. In this

case, we have simulated multi-segmented individual NWs with 40 nm in diameter, ranging the Fe layer lengths from 20 to 300 nm, with two different lengths for the non-magnetic Cu spacers (60 and 120 nm) and keeping fixed the total number of bilayers to 15. We used the same magnetic parameters and configurations described in the previous sections.

As it was claimed in our previous work [128], the micromagnetic simulations shows that the segmented Fe/Cu NW behaved like a set of 15 non-interacting nanoparticles when the Fe and Cu spacer lengths are 30 and 120 nm, respectively. In addition, it was confirmed that each Fe segment showed a kind of vortex configuration with around 60% of the magnetization pointed parallel to the NW long axis (see Fig. 3.13 (a)) like an isolated Fe nanodisc. As soon as the Fe segment lengths were increased (≥ 100 nm) and like in the longer cylindrical Fe NWs (Figure 3.10 (a)), the magnetic reversal mode occurs through the nucleation and propagation of a vortex domain wall from the extremities of each segment (see Figure 3.13 (b-c) and Figure 3.10 (c)). This behavior is more evident when the Fe segments length is increased.

In order to study the effect of the nonmagnetic Cu layer spacer, we also simulated Fe/Cu NWs with 60 nm length Cu spacers and ranging the Fe layer lengths from 20 to 260 nm. The 3D simulated magnetic configuration at remanence of the Fe/Cu NWs with 20 nm of Fe length shows that the easy magnetization axis lies in-plane or perpendicular to the longitudinal nanowire axis (see Fig.3.13 (e)). In addition, the magnetization in consecutive Fe segments is oriented in opposite directions and forming a synthetic antiferromagnetic system with coercivity and remanence values close to zero (see the hysteresis loops in Fig.3.13 (d). As it was observed in the samples with Cu spacer lengths of 120 nm, the magnetization reversal evolves from a kind of vortex configuration to the nucleation and propagation of a vortex domain wall from the extremities of each segment for NWs with larger Fe lengths (≥ 60 nm).

Regarding the evolution of the simulated coercivity fields as a function of the Fe segment length for Cu spacer lengths of 60 (open symbols in Fig. 3.13 (d)) and 120 nm (full symbols in Fig. 3.13 (d)), it progressively increases with the Fe length and approaches the value corresponding to the long Fe NW. Again, and despite having simulated only one wire, a good quantitative correlation with the experimental data was achieved. Then, we can claim that larger magnetostatic interactions are acting on the nanowires when the Fe segments are longer.

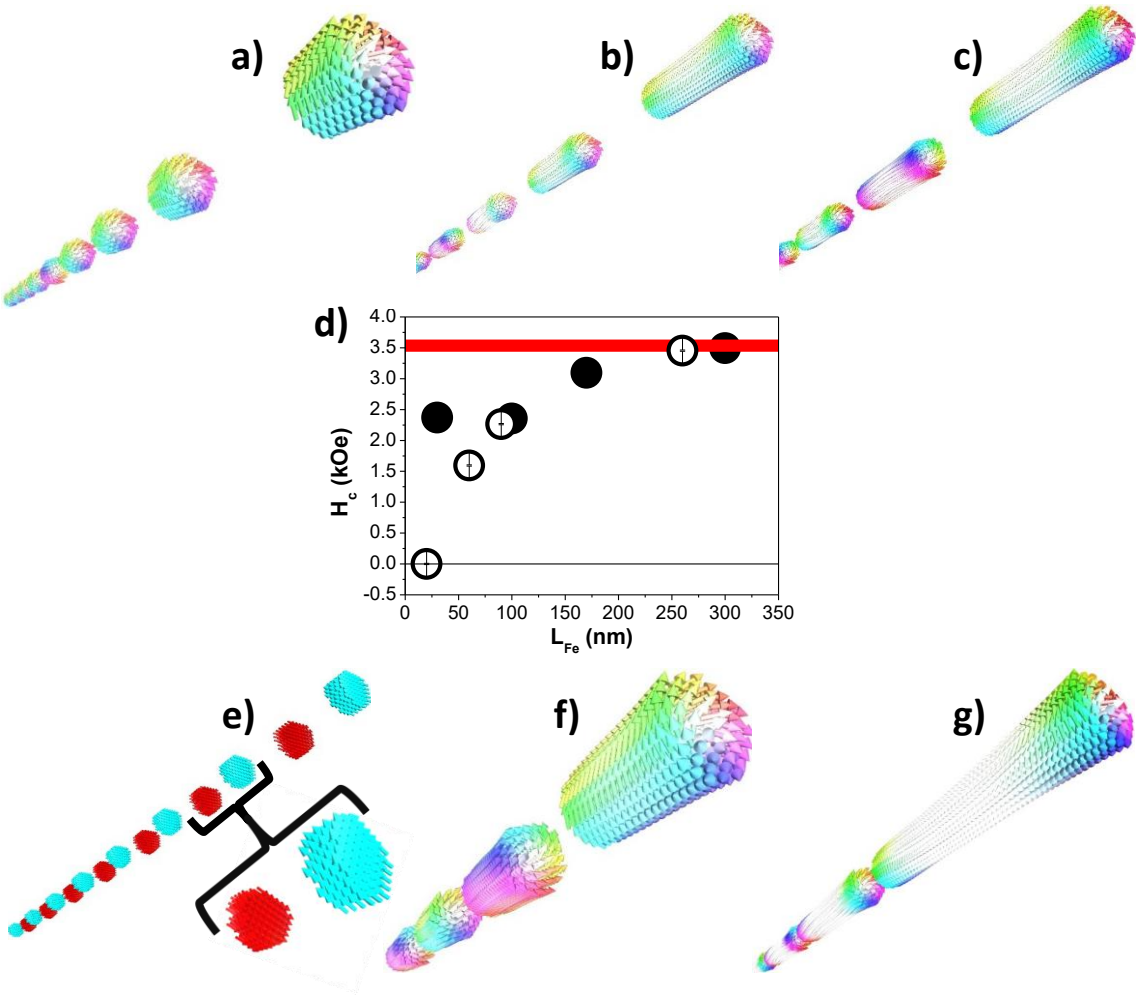

Fig. 3.13. 3D simulated magnetic configurations of Fe/Cu multi-segmented individual NWs with Cu spacer length of (a-c) 120 and (e-g) 60 nm, and different Fe segment lengths: (a) 30, (b) 100, (c) 170, (e) 20, (f) 60 and (g) 260 nm. (d) The coercivity field as a function of the Fe segment length in Fe/Cu NWs with a Cu spacer length of 120 (full symbol) and 60 nm (open symbol), as well as the 3 µm length Fe isolated NW (red continuous line) extracted from the hysteresis loops when the external field was applied parallel to the NW axis.

3.7. Conclusions

Fe/Cu multi-segmented NW arrays, with around 40 nm in diameter and made of alternating segments respective of Fe and Cu, having Fe length of 30 nm and Cu spacer length from 15 up to 120 nm have been synthesized by template assisted electrochemical deposition into the pores of AAO templates by alternately varying between two different deposition potentials. According to the electrodeposition curves, the NWs growth rate vary quasi-linearly with the deposition time. The nucleation process was found to be kinetically limited at the beginning of each layer growth, due to

the large diffusion flux to small nuclei, but then the nuclei and NWs growth becomes diffusion limited. XRD results indicate that Fe segments present a body-centered cubic (bcc) with a preferential (110) preferential crystalline direction.

Magnetic measurements, as a function of the applied field, illustrated a decrease in the coercivity, remanence with the Cu segments' length, when applying the magnetic field along the parallel direction whereas the opposite behavior was observed in perpendicular direction. To understand this behavior regarding the magnetic interactions between the magnetic layers, FORC diagrams were performed. From this analysis we can conclude that for Cu layers with thickness lower than 15 nm, the several Fe layers present a similar behavior to high-aspect ratio NWs (infinite wires). On the other hand, for Cu spacer higher that 60 nm a decoupling of the Fe layers along the axis was clearly observed.

Micromagnetic simulations illustrated the importance of the Cu segments' lengths on the tuning of the magnetic properties of the arrays. For multi-segmented (15 layers) individual NWs separated by 60 or 120 nm of Cu spacer, a behavior like a set of 15 non-interacting nanoparticles were found, which is in accordance with FORC results. The simulations also confirmed the FORC analysis for Fe discs separated by 15 nm of Cu, were strongly coupled Fe layers were identified. The micromagnetic simulations for an array of multi-segmented NWs showed a larger dipolar interaction between the Fe segments which induced a ferromagnetic coupling along the wires. In particularly, the coercivity was significantly reduced when the number of NWs was increased.

Since for biomedical applications non-interacting Fe nanostructures are needed, we also prepared samples with Cu spacer higher than 60 nm and varying the number of Fe layers from 1 to 20 and the thickness of the Fe layer from 20 to 300 nm. Experimental measurements showed only a small increase of the coercivity and remanence for the lower number of layers which can be associated to the complex behaviour the reversal magnetization due to the interactions between neighbour NWs. For the NWs with thicker Fe layers, we observed an anisotropic behaviour, consequence of the high-aspect-ratio that leads to a strong shape anisotropy with well-defined magnetic easy-axis lying along the NWs longitudinal direction. For the thinner Fe discs, similar M(H) cycles are observed in both directions. Finally, considering the industrial application of these high-aspect-ratio segmented nanoparticles, we can conclude that we developed an approach that enables the synthesis of nanostructures with high homogeneity in diameter and highly controllable length allowing an effective tune of their magnetic behaviors ultimately enabling reaching the superparamagnetic regime.

Chapter 4

Nanostructured Lipid Carriers for Doxorubicin Delivery

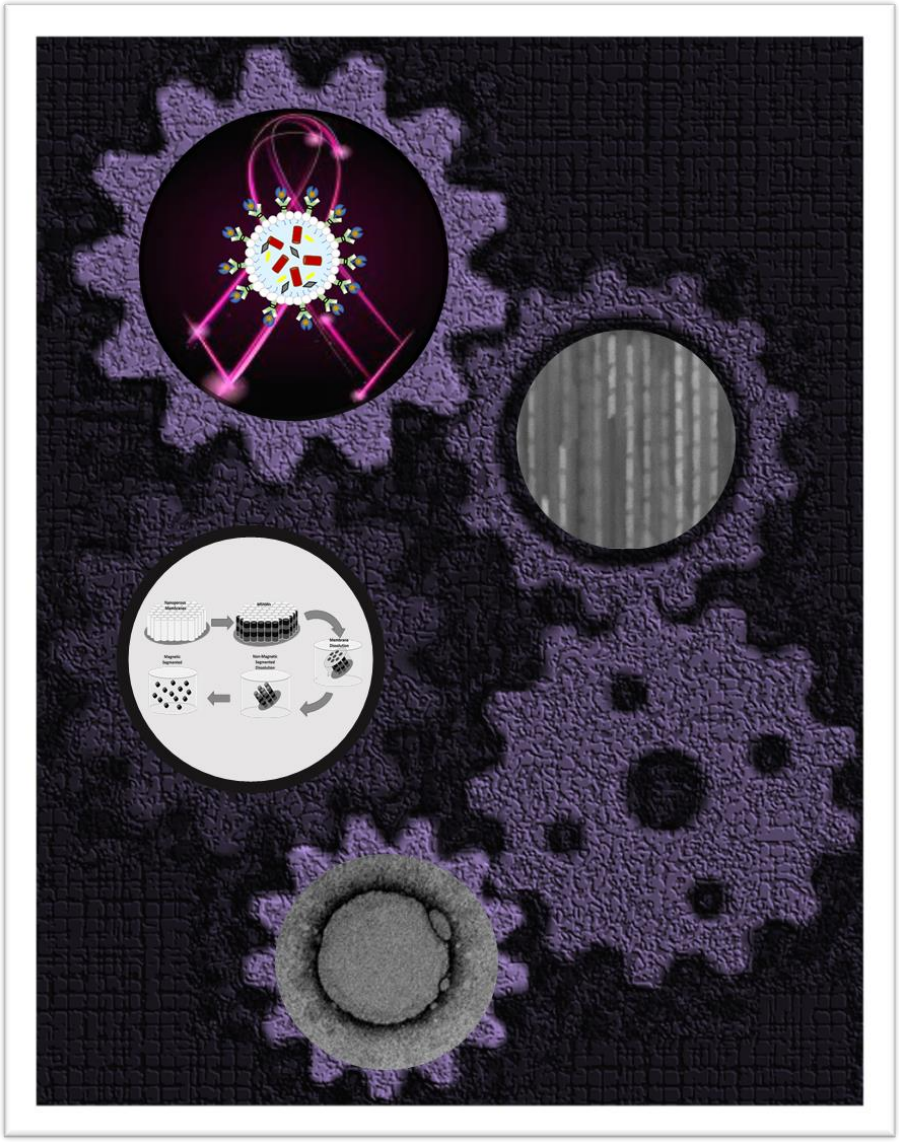

Chapter 4

Nanostructured Lipid Carriers for Doxorubicin Delivery

In this chapter, DOX loaded NLCs were produced using a hot ultrasonication method, which procedures have relatively low costs, exclude any use of organic solvents and, in this case, all the components are GRAS (generally recognized as safe). The study was performed using different NLCs matrixes, to assess the composition that held the most convenient physical features, as size, zeta potential and encapsulation. All other parameters were optimized so that the NLCs had good stability and sizes suitable for oral administration. A conjugate of PEG-FA was synthesized and added to the NLCs formulations to confer active targeting. Thus, this modification will allow DOX-NLCs to remain in circulation for longer periods of time and release the drug into site-specific targets (part of this chapter is already published in Moraes, S., Marinho, A., Lima, S., Granja, A., Araújo, J. P., Reis, S., Sousa,C.T. & Nunes, C. (2020). Targeted nanostructured lipid carriers for doxorubicin oral delivery. International Journal of Pharmaceutics, 592, 120029).

4.1. Overview

Cancer is expected to keep the rank as the leading cause of death and represents the main barrier impairing the increase of life expectancy in most developed countries in this century [319, 320]. Current therapies for solid cancers treatment, e.g. breast cancer, include chemotherapy, radiotherapy, and surgery. However, in most cases, surgery is not an option and, multidrug resistance and severe adverse effects on normal tissues are major causes for failure in clinical cancer chemotherapy and radiotherapy. In this sense, research in more efficient and less invasive cancer treatments is needed. Thus, nanotechnology applied to biomedicine is developing faster and faster and, in some cases, has already shown to improve some therapies [19]. This is the case of anticancer therapies that include the use of the anthracycline doxorubicin (DOX), which is an antitumor antibiotic used in oncologic practice since the late 1960s.

The tumors most commonly responding to DOX include breast and esophageal carcinomas, osteosarcoma, among others [14]. DOX has been showing to be effective for metastatic and early disease, but its use is limited due to its dose dependent cardiotoxicity and myelosuppression [321, 322]. Some DOX analogues such as mitoxantrone exhibited lower cardiotoxicity; however, they are less effective compared to the parent molecule which is key when it comes to cancer chemotherapy [323]. In this context, in 1995, the US Food and Drug Administration (FDA) approved a DOX-loaded liposome system (Doxil®), for the treatment of AIDS-related Kaposi sarcoma and until today is still used as a second-line breast cancer treatment [15].

Doxil®, and its analogs, are PEGylated liposomal doxorubicin formulations able to keep the structure and morphology of the drug, by entrapping it in the crystalline form inside the aqueous vacuoles of the liposomes [324]. These formulations are very effective in the treatments due to the high and stable loading of DOX by a transmembrane ammonium sulfate gradient that allows drug selective release at the tumor, with minimal release in plasma and healthy tissues [325, 326]. Moreover, the presence of the lipopolymer DSPE-PEG provides a highly hydrated, and flexible surface that enables prolonged circulation time and avoidance of the reticuloendothelial system. However, the intravenous administration and the associated high costs, limit the access to this therapy. Thereby, to implement a strategy equally efficient to the one in the market, but economically viable and with the possibility of enabling oral administration, this work emerges. In this sense, lipid nanoparticles of the type nanostructured lipid carriers (NLCs) are presented as an alternative to liposomes.

NLCs correspond to the second generation of lipid nanoparticles that includes the insertion of a liquid lipid into a solid lipid matrix, which creates imperfections in the crystal lattice and consequently allow a better accommodation of drug molecules, increasing the drug loading capacity, minimizing drug expulsion during storage and allowing a controlled drug release profile [327, 328]. In addition, NLCs have several advantages including biocompatibility and industrial scale production [329]. To inhibit protein adsorption and consequent opsonization, the NLCs surface can be functionalized with molecules that confer a more hydrophilic profile, such as polyethylene glycol (PEG) [326, 330]. Additionally, active targeting can be achieved and significantly decrease the non-specific action of passively targeted nanocarriers. The overexpression of folate receptors (FR) on the surface of several cancers, facilitates the transfer of folic acid (FA) functionalized nanocarriers through receptor mediated endocytosis [331, 332].

4.2. Optimization drug encapsulation

In a preliminary study, several Doxorubicin NLCs have been produced to optimize the best encapsulation rate and loading capacity with an average diameter of about 300 nm, suitable for oral administration. This study was divided into four phases. First, some parameters were fixed: a ratio of 9:1:3 between the solid lipid, liquid lipid and surfactant, all formulations were prepared in pH = 7 aqueous solutions and the sonication parameters remained constant. The variable to be tested was the solid lipid. Thus, several types of solid lipid were tested: cetyl palmitate, gelucire®43/1, compritol®ATO 888 and precirol®ATO 5.

Table 4.1 shows the parameters used and the results obtained (DLS, PDI, EE and LC) during the optimization process. It can be observed that the formulations with cetyl palmitate and gelucire®43/1 were the ones that presented better results in size (170 and 140 nm respectively) but with very low encapsulation rates (20% and 30% respectively).

After choosing the two solid lipids with the best results, a second phase was implemented using an HCl buffer instead of ultra-pure water. Different pH were tested to promote the affinity of DOX towards the lipids.

Regarding the results with the different pH values, there was no significant variation in the average size and PDI of the nanoparticles, however there was a significant increase in the encapsulated DOX rate, as the pH decreased (Table 4.1). Then, a longer sonication time was tested, however there were no significant changes.

Finally, one last parameter tested was the proportion of the surfactant. With the increase in the amount of surfactant, a significant improvement was observed in the DOX encapsulation, keeping the dimensions with a very low PDI. In addition, the replicas proved to be highly reproducible with very similar results. After all these optimization phases, two formulations had the suitable parameters for the desired application (experiments #13 and 14, Table 4.1): stability (minimum 30 days), encapsulation rate > 65%, loading capacity > 2% and diameter with about 300 nm and low PDI (< 0.2).

Once the encapsulation was optimized, the optimization of the nanoparticle surface functionalization with folic acid (FA) and PEG-2000 was started. The PEG-FA conjugate was added at the time of weighing the excipients. However, the first formulations were much larger than the previous ones (between 500 and 600 nm). Thus, it was then observed that the only uncontrolled variable was the cooling temperature of the formulation. Thereby, the cooling rate started to be controlled: the formulations were placed in a water bath at the same temperature that was used for

the fusion of the lipids and left until it reached room temperature. In these conditions, the formulations presented suitable parameters, has it can be seen in Table 4.1 (NLC_{15} and NLC_{16}).

Table 4.1: Parameters and the results obtained during the preliminary studies.

	Solid lipid	pH	M_{sfc} (mg)	t_{sc} (min)	Size (nm)	PDI	EE (%)	LC (%)
NLC_1	Gelucire	7	75	5	170 ± 07	0.11 ± 0.02	20	0.70
NLC_2	Cetil Palmitate	7	75	5	240 ± 06	0.08 ± 0.02	30	1.12
NLC_3	Compritol	7	75	5	1310 ± 10	0.23 ± 0.01	35	1.33
NLC_4	PrecirolAto 5	7	75	5	740 ± 34	0.30 ± 0.01	10	0.37
NLC_5	Gelucire	5	75	5	190 ± 05	0.10 ± 0.01	40	0.79
NLC_6	Cetil Palmitate	5	75	5	280 ± 07	0.11 ± 0.01	55	0.87
NLC_7	Gelucire	1	75	5	217 ± 05	0.05 ± 0.01	60	2.38
NLC_8	Cetil Palmitate	1	75	5	420 ± 10	0.21 ± 0.01	43	0.88
NLC_9	Gelucire	1	75	10	230 ± 11	0.21 ± 0.02	52	2.11
NLC_{10}	Cetil Palmitate	1	75	10	430 ± 20	0.31 ± 0.02	59	2.33
NLC_{11}	Gelucire	1	50	5	330 ± 06	0.16 ± 0.02	50	1.98
NLC_{12}	Cetil Palmitate	1	50	5	210 ± 05	0.09 ± 0.01	50	2.00
NLC_{13}	Gelucire	1	85	5	175 ± 05	0.09 ± 0.01	67	2.28
NLC_{14}	Cetil Palmitate	1	85	5	280 ± 03	0.06 ± 0.01	74	2.98
NLC_{15}	Gelucire*	1	85	5	255 ± 08	0.14 ± 0.01	91	3.56
NLC_{16}	Cetil Palmitate*	1	85	5	270 ± 06	0.13 ± 0.01	97	3.84

Note: (*) represents the addition of PEG-2000, M_{sfc} is the surfactant mass and t_{sc} is the sonication time.

4.3. Experimental validation

After an experimental optimization of the NLCs' manufacturing parameters by a univariate methodology, a RSM was implemented to assess whether the experimental set followed a multivariate mathematic model. The optimal ranges of variables were pre-selected to increase the accuracy of the statistical method. As an answer, size and

EE were analyzed, and for that, the pH and surfactant mass factors were considered the most critical dependent variables (assessed by preliminary assays) on the formulations features. Table 4.2 shows the effect summary report were the LogWorth and PValue for each effect in the model can be seen. The vertical blue line in the plot is set at the value 2. The LogWorth for each model effect is defined as $-\log_{10}(p\text{-value})$. This transformation adjusts *p*-values to provide an appropriate scale for graphing. A value that exceeds 2 is significant at the 0.01 level (once $-\log_{10}(0.01) = 2$). The results show that pH 1 and 7 for NLC $_{(Gel\text{-}DOX)}$ is significant at the 0.01 level. None of the other effects are significant at even 0.10 level, that is, there is no correspondence between variables. Table 4.2 also shows the *p*-value for each model effect. This is generally the *p*-value corresponding to the significance test displayed in the effect tests table or effect likelihood ratio tests table of the model report.

Table 4.2: Effect Summary: LogWorth for each model effect, defined as -log10(p-value) and PValue, which is the p-value corresponding to the significance.

NLC$_{(Gel\text{-}DOX)}$		
Source	**LogWorth**	**PValue**
pH (1,7)	2.485	0.00327
Surfactant mass (mg) (50,85)	1.854	0.01421

NLC$_{(Pal\text{-}DOX)}$		
Source	**LogWorth**	**PValue**
Surfactant mass (mg) (50,85)	1.789	0.01592
pH (1,7)	1.579	0.02638

In Fig. 4.1, the dependence profiles are presented. The mean size of the nanoparticles in the formulations containing gelucire ($NLC_{(Gel\text{-}DOX)}$), do not change much depending on the chosen variables. However, EE deeply changes with both factors, but mainly with pH. The maximization as a function of desirability shows that for this model the optimums are pH 1 and a surfactant mass of 85 mg, which corresponds to NLC with about 199 nm in size and EE of 60%. For $NLC_{(Pal\text{-}DOX)}$, the optimum value obtained for the surfactant mass is about 75 mg, however, a surfactant mass of 85 mg leads to a higher EE, which is more critical than the low size increase. Thereby, in Fig. 4.1, it can be observed that the values estimated as optimal for the factors evaluated, in the two types of solid lipids, are in accordance with those determined using a univariate optimization (pH 1 and surfactant mass 85 mg).

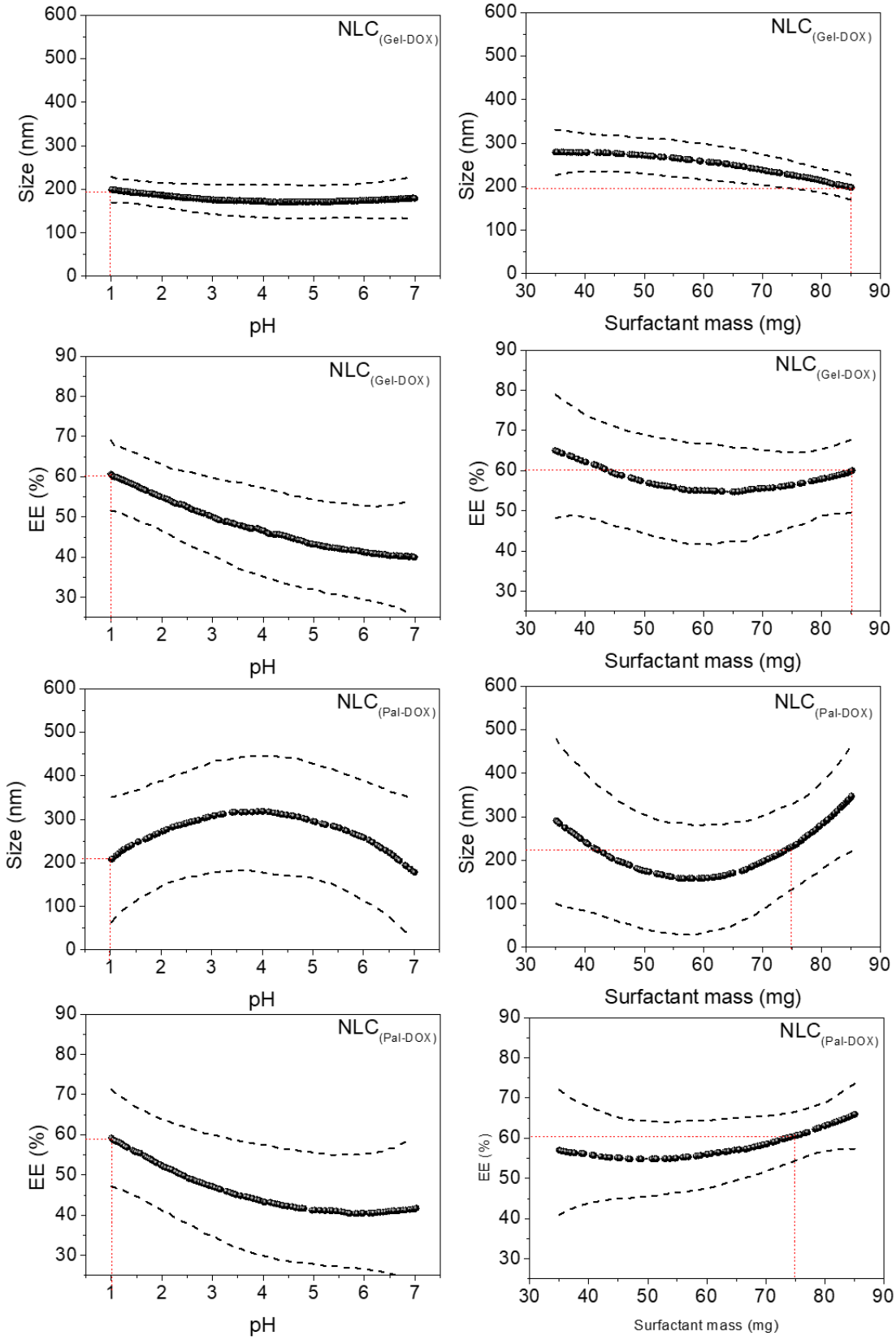

Fig. 4.1: Prediction profiles for NLC size (nm) and EE (%), based in a central composite design, depend in the formulation pH and used surfactant mass (mg). The dashed lines represent the confidence intervals.

4.4. Physicochemical characterization

After the production process, the obtained suspensions had low viscosity and it is also possible to notice different colors: white in the placebo NLCs, slightly yellow in the functionalized NLCs, orange in DOX loaded NLCs and bright red in the functionalized DOX loaded NLCs, as shown in Fig. 4.2.

Fig. 4.2: NLCs with different compositions and Dox-free. 1) $NLC_{(Pal)}$, 2) $NLC_{(Pal\text{-}PEG\text{-}FA)}$, 3) $NLC_{(Pal\text{-}DOX)}$, 4) $NLC_{(Pal\text{-}DOX\text{-}PEG\text{-}FA)}$, 5) $DOX_{(free)}$, 6) $NLC_{(Gel\text{-}DOX\text{-}PEG\text{-}FA)}$, 7) $NLC_{(Gel\text{-}DOX)}$, 8) $NLC_{(Gel\text{-}PEG\text{-}FA)}$, 9) $NLC_{(Gel)}$.

The main physicochemical characteristics of the developed NLCs in this study are summarized in Table 4.2. The measured properties influence the formulation's stability and their future interactions with cells and tissues [333]. The PDI of the all formulations were below 0.2 which is indicative of monodispersed formulations, with uniform diameters of nanoparticles populations [334]. These values also suggest a uniform functionalization process. NLCs with cetyl palmitate as a solid matrix ($NLC_{(Pal)}$) are considerably larger than those with gelucire ($NLC_{(GelL)}$) and have a higher encapsulation rate, which may be due to DOX affinity for lipids with more crystalline structures [335]. Moreover, the hydrodynamic diameter obtained for NLCs show a tendency to increase as they get more complex (Table 4.2). Nevertheless, the diameters of all NLCs are below 300 nm. Studies using different sized nanoparticles demonstrate that particles with 300 nm in size or less are ideal for oral administration since they are preferentially internalized by both enterocytes and M-cells, and reveal higher intestinal transport compared to larger sized particles [336, 337]. Furthermore, lipid nanoparticles have been reported to be taken up by the M-cells of Peyer's patches, which enables them to bypass first effect metabolism and undergo lymphatic absorption [338].

Regarding zeta potential, all values are higher than |20| mV and close to |30| mV. In general, particle aggregation or flocculation is prevented when zeta potential is ± 30 mV [339]. However, ± 25 mV is also considered an accepted value [340, 341], particularly when the particles have a steric stabilization agent. Additionally, negatively charged particles show less cytotoxicity than cationic nanoparticles, usually associated with cell membrane disruption and consequent cell death [342].

Table 4.3 also indicated the entrapment efficiency (EE) and drug loading capacity (LC) of drug-loaded NLCs. About 67% EE could be reached by the present preparation method. A small change was observed for EE and DL values between the NLCs with and without PEG-FA. These values are relatively close for NLCs presented in the literature synthesized by other methods, however with about twice the size of the NLCs presented here [219].

Table 4.3: Mean hydrodynamic particle size, polydispersity index (PDI), zeta potential, EE and LC.

Formulations	Size (nm)	PDI	Zeta potential (mV)	EE (%)	LC (%)
$NLC_{(Ge\text{-}SPIONsl)}$	185 ± 9	0.16 ± 0.03	-22.3 ± 0.6	−−	−−
$NLC_{(Gel\text{-}PEG\text{-}FA)}$	190 ± 14	0.11 ± 0.02	-26.3 ± 1.2	−−	−−
$NLC_{(Gel\text{-}DOX)}$	211 ± 37	0.08 ± 0.01	-22.8 ± 1.5	55 ± 2	2.18 ± 0.07
$NLC_{(Gel\text{-}DOX\text{-}PEG\text{-}FA)}$	220 ± 46	0.10 ± 0.02	-24.5 ± 1.7	60 ± 5	2.35 ± 0.10
$NLC_{(Pal)}$	245 ± 10	0.11 ± 0.01	-29.3 ± 0.5	−−	−−
$NLC_{(Pal\text{-}PEG\text{-}FA)}$	247 ± 20	0.18 ±0 .03	-30.0 ± 1	−−	−−
$NLC_{(Pal\text{-}DOX)}$	271 ± 29	0.10 ± 0.02	-28.9 ± 0.4	67 ± 5	2.45 ± 0.64
$NLC_{(Pal\text{-}DOX\text{-}PEG\text{-}FA)}$	281± 18	0.15 ± 0.04	-28.0 ± 0.9	66 ± 8	2.43 ± 0.33

Gel: Gelucire; Pal: Cetyl palmitate; DOX: Doxorubicin; PEG-FA: Polyethylene glycol-Folic acid. Values are expressed as mean ± standard deviation (n = 3).

4.5. Morphology

Transmission electron microscopy (TEM) studies were performed to evaluate the morphological features of the developed NLCs. Fig. 4.3 show the TEM images obtained for drug-free NLCs ($NLC_{(Gel)}$ and $NLC_{(Pal)}$) and DOX-loaded functionalized NLCs ($NLC_{(Gel\text{-}DOX\text{-}PEG\text{-}FA)}$ and $NLC_{(Pal\text{-}DOX\text{-}PEG\text{-}FA)}$). All images revealed NLCs' spherical shape and shown that the functionalization process did not considerably affect the particles shape. The average diameters were estimated using the ImageJ v1.48

software and the results obtained were 187 ± 70 nm for $NLC_{(Gel)}$, 300 ± 20 nm for $NLC_{(Gel\text{-}DOX\text{-}PEG\text{-}FA)}$, 315 ± 25 nm for $NLC_{(Pal)}$, and 335 ± 64 nm for $NLC_{(Pal\text{-}DOX\text{-}PEG\text{-}FA)}$ (n= 6). The values obtained are, in agreement with the average diameter obtained by DLS. However, the low sampling of images acquired prevented a statistical analysis. In the $NLC_{(Gel\text{-}DOX\text{-}PEG\text{-}FA)}$ and $NLC_{(Pal\text{-}DOX\text{-}PEG\text{-}FA)}$ it is possible to observe an all-around halo that is typical of a pegylated functionalized surface [237].

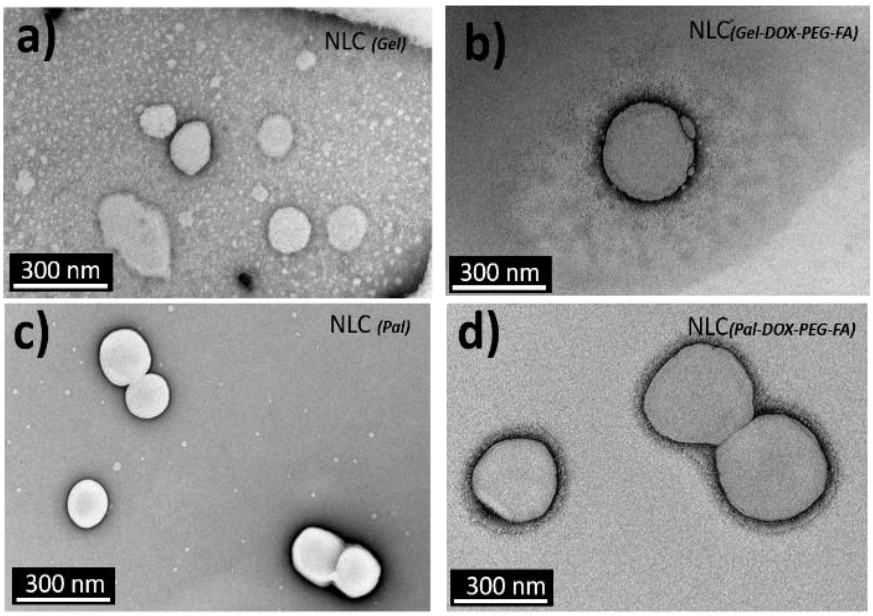

Fig. 4.3: Transmission electron microscopy (TEM) for (a) $NLC_{(Gel)}$, (b) $NLC_{(Gel\text{-}DOX\text{-}PEG\text{-}FA)}$, (c) $NLC_{(Pal)}$ and (d) $NLC_{(Pal\text{-}DOX\text{-}PEG\text{-}FA)}$.

4.6. Storage stability

The physical stability of all NLCs was verified periodically by analyzing the hydrodynamic diameter and polydispersity during storage conditions for 42 days at room temperature (Fig. 4.4). The results show that all NLCs formulations are stable for these parameters at least for 42 days. The ANOVA statistical analyses ($p < 0.05$ relatively to the correspondent week 0) show no significant change in the studied parameters during this period. Thus, the developed NLCs are appropriate for DOX incorporation and for therapeutic administration during this time and in these conditions of storage.

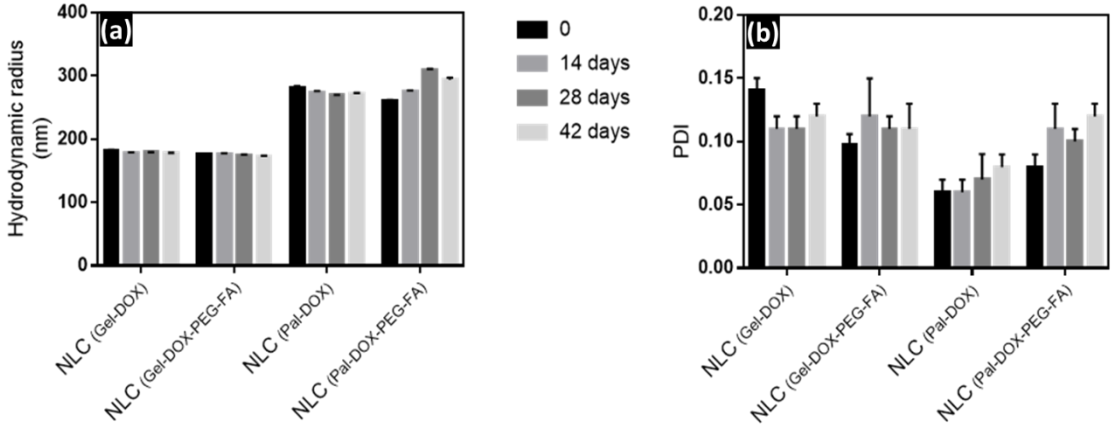

Fig. 4.4: Physical stability of the formulations over time (0, 14, 28 and 42 days). The graphics represent the size (left) and the PDI (right). Values corresponds mean of the readings (n=3) ± SD (The ANOVA analyses show $P < 0.05$ relatively to the correspondent day 0).

4.7. Structural characterization

The characterizations of X-ray diffraction were performed to better investigate the changes in the crystallization process of the solid lipids gelucire and cetyl palmitate used to produce the different NLCs. Diffraction patterns typical of nanoparticles are shown in Fig. 4.5. The diffraction patterns clearly show the presence of the crystalline structure in all formulations. The same characteristic peaks of each lipid were observed in all types of formulation, which shows that both the presence of the drug and of the conjugate does not interfere with the crystalline structure of the base NLCs.

The results were compared with the cetyl palmitate crystal data known from the literature [343] and no correlation with its monoclinic structure was found. This may indicate that the $NLC_{(Pal)}$ consists of crystallites from another modification of cetyl palmitate. The grain size was calculated for the cetyl palmitate group because its crystalline structure is better defined. The values obtained are: 33.6 ± 1.6 nm, 31.8 ± 1.8 nm, 23.9 ± 1 nm and 26.4 ± 2.6 nm for $NLC_{(Pal)}$, $NLC_{(Pal\text{-}PEG\text{-}FA)}$, $NLC_{(Pal\text{-}DOX)}$ and $NLC_{(Pal\text{-}DOX\text{-}PEG\text{-}FA)}$ respectively. It was observed that when the drug is inserted in the composition, there is a decrease in grain size. However, $NLC_{(Gel)}$ has the same crystalline configuration as the lipid phase of gelucire [344], which shows that the manufacturing process does not modify the crystalline nature of the lipid.

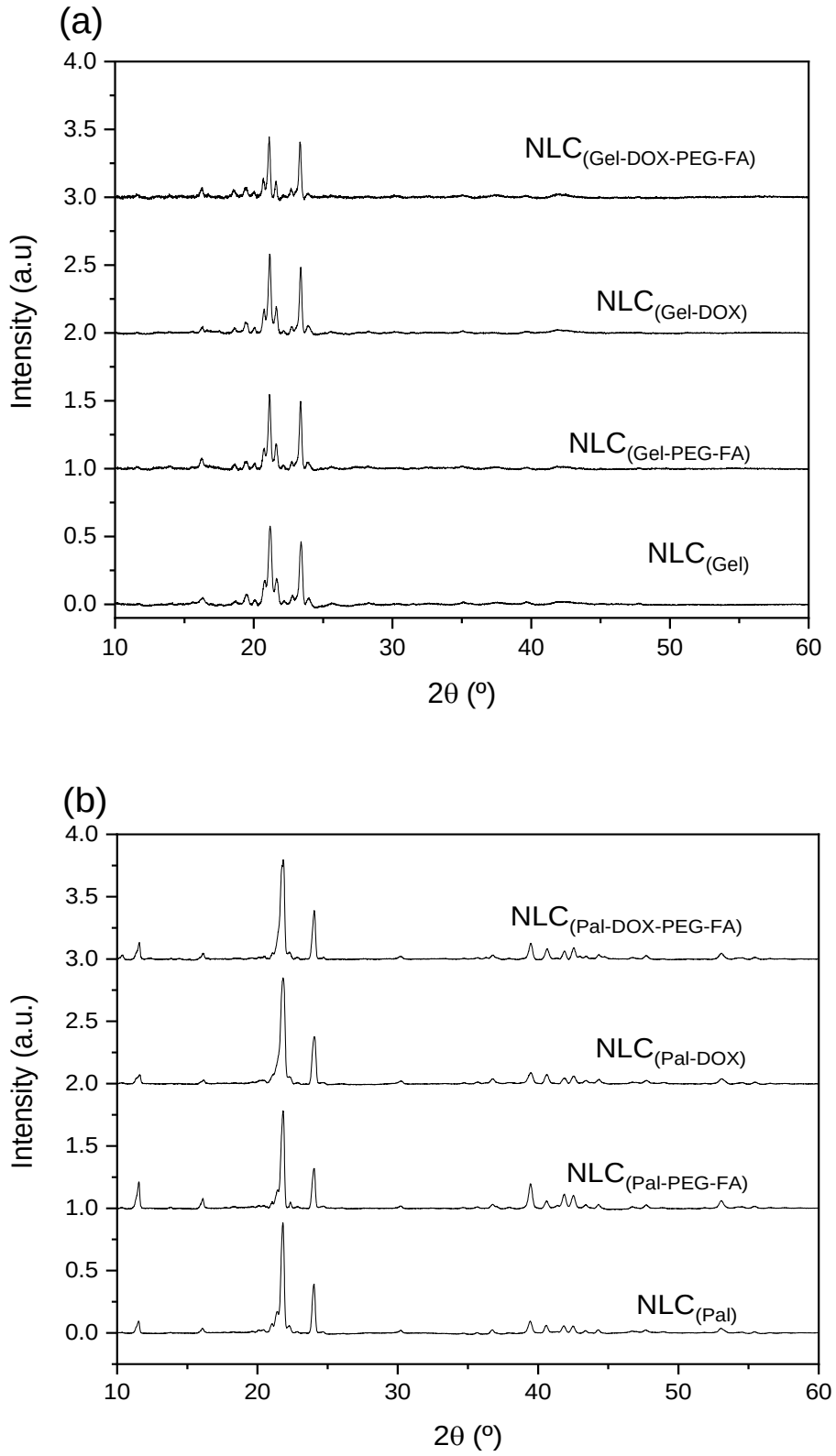

Fig. 4.5: X-ray diffraction pattern for formulations: a) $NLC_{(Gel\text{-}DOX\text{-}PEG\text{-}FA)}$, $NLC_{(Gel\text{-}PEG\text{-}FA)}$, $NLC_{(Gel\text{-}DOX)}$, $NLC_{(Gel)}$ and b) $NLC_{(Pal\text{-}DOX\text{-}PEG\text{-}FA)}$, $NLC_{(Pal\text{-}PEG\text{-}FA)}$, $NLC_{(Pal\text{-}DOX)}$, $NLC_{(Pal)}$.

4.8. Conclusion

The work presented in this chapter allowed the development of lipid-based delivery systems suitable for the oral delivery of doxorubicin. All the optimization steps were rationally designed in order to enable this administration route. The final optimized formulations present a mean size beneath 300 nm, which enable an efficient transport across intestinal cells. The PDI is lower than 0.18, which indicates a nearly monodisperse formulation, a key factor to ensure the same type of interactions with biological tissues and cells and the same pharmacokinetic and pharmacodynamics properties. The zeta potential near |30| mV, potentiates the physical stability across time. The negative charge provides less toxic interaction with non-target cells, once it doesn´t allow the establishment of electrostatic interaction with the cell membranes, which are mostly zwitterionic or slightly negatively charged.

Regarding the targetability towards cancer cells, the final formulations also present several features important features. The mean size allows the passive accumulation in tumor tissue as a consequence of the enhanced permeability and retention (EPR) effect. Moreover, the internalization can be greatly improved by the surface functionalization with a high-affinity targeting ligand, folic acid, which receptors are significantly overexpressed on cancer cells of the breast, lung, kidney, ovary,colon, brain, and myelogenous leukemias.

Regarding the encapsulation of DOX, the loaded amount is enough to achieve a therapeutic effect.

For all the stated reasons, these optimized formulations constitute the basis for the development of hybrid systems with loaded magnetic structures, addressed in the next chapter.

Chapter 5

Biotechnological Applications

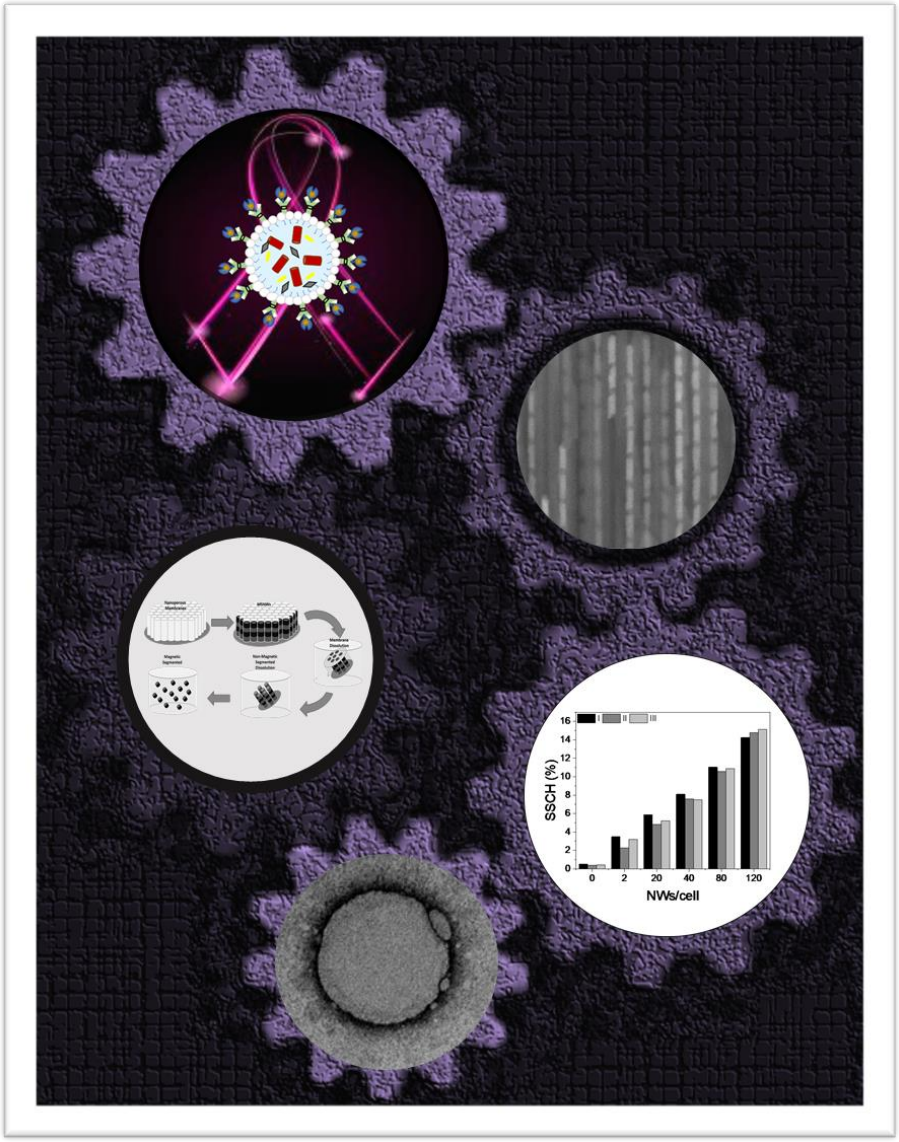

Chapter 5

Biotechnological Applications

In this chapter we describe the cytotoxic and targeting potential of a new targeted drug delivery system based on functionalized nanostructured lipid carriers (NLCs). The cytotoxicity and cell internalization were also evaluated for several types of magnetic nanostructures and for multifunctional nanostructures after the internalization of the magnetic core in the NLCs shell (part of this chapter is already published in Moraes, S., Marinho, A., Lima, S., Granja, A., Araújo, J. P., Reis, S., Sousa,C.T. & Nunes, C. (2020). Targeted nanostructured lipid carriers for doxorubicin oral delivery. International Journal of Pharmaceutics, 592, 120029).

5.1. Overview

When we talk about therapies for the treatment of cancer, it is evident that in recent years there have been substantial advances in the fields of surgery, chemotherapy, radiotherapy, and immunotherapy. However, there are still many disadvantages that require new approaches [345, 346]. Chemotherapy is the most common treatment for most tumors, even with the lack of specificity for cancer targets, which is mainly responsible for important serious side effects since healthy cells can also be affected [347-349]. Doxorubicin (DOX) is one of the most effective chemotherapeutics for the treatment of solid tumors and, in particular, breast cancer. However, DOX treatments can induce severe cardiotoxicity due to the accumulation of DOX in the cardiac tissue [350], which causes a narrow therapeutic dose to be imposed, thus limiting the effectiveness of DOX, which is also compromised by the generation of resistance by cancer cells [351].

As an alternative to this problem, nanocarriers can transport large quantities of drugs and provide controlled drug release at the tumor site [352-354]. In addition,

nanocarriers may allow passive targeting (improved permeability and retention at the microvasculature in the tumor mass), active targeting (functionalization of the nanoparticles with molecules able to recognize receptors) and/or molecular signaling [354-358]. Moreover, nanocarriers coupled with magnetic nanoparticles can also serve as agents of magnetic hyperthermia (MH), capable of inducing a local increased intra-tumoral temperature - around 43-46 ºC, when exposed to an alternating magnetic field (MFA) they. Thus, promoting an enhanced release of drugs or activation of therapeutic molecules, and increasing the concentration of drugs locally at the tumor site and stimulating the effectiveness of treatment [354, 359-362].

In this sense, nanostructured lipid carriers (NLC) are known in the literature as highly promising nanocarriers with advantages such as biocompatibility, low cost, and high stability. Moreover, they can load bioactive compounds and magnetic nanoparticles such as superparamagnetic iron oxide nanoparticles (SPIONs) and nanowire (NWs). In addition, they are usually composed of generally recognized as safe (GRAS) ingredients and their physicochemical features can be modulated to enable oral administration (Fig. 5.1) [363, 364].

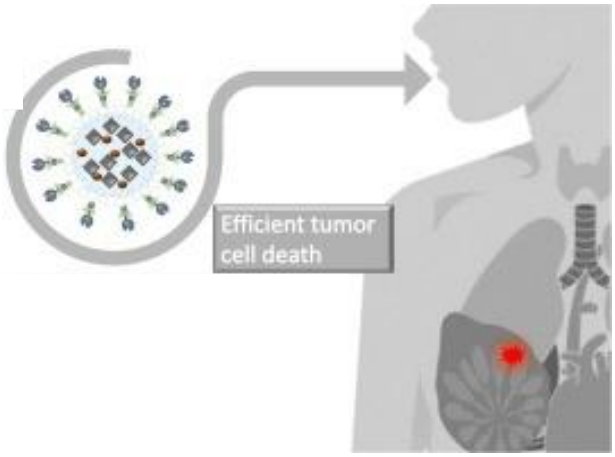

Fig. 5.1: Scheme of potential oral administration of multifunctional folic acid conjugated NLCs for controlled doxorubicin delivery to breast cancer cells.

5.2. Targeted nanostructures for doxorubicin oral delivery

5.2.1. *In vitro* release studies

The treatment with anticancer drugs remains a challenge, as available drugs still entail the risk of deleterious off-target effects. The present section describes folic acid conjugated nanostructured lipid carriers (NLCs) as an effective doxorubicin (DOX)

delivery approach targeted to breast cancer cells. Two distinct NLCs formulations were designed and optimized leading to an encapsulation efficiency over than 65% (Chapter 4). Cytotoxic and targeting potential of NLCs were studied *in vitro*, using a MDA-MB-231 cell line. Results showed an enhanced cellular uptake of conjugated NLCs. *In vitro* release studies, mimicking the path in the body after oral administration, show that the developed formulations would reach the tumor microenvironment bearing 50% of the encapsulated (DOX). Moreover, NLCs demonstrated storage stability at 25 °C for at least 42 days. Overall, results revealed that the developed NLCs enable the possibility of oral administration and are a promising approach for the targeted delivery of doxorubicin to breast cancer cells.

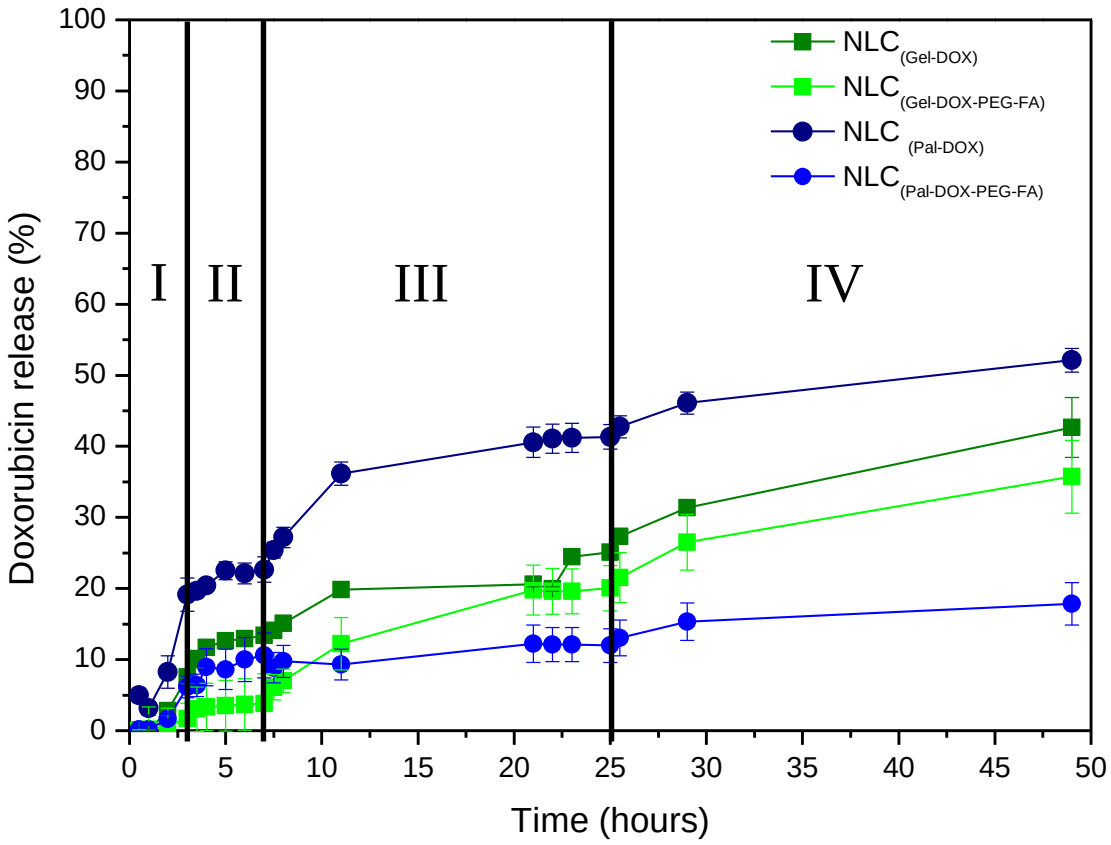

Fig. 5.2: Cumulative DOX release for $NLC_{(Gel\text{-}DOX)}$, $NLC_{(Gel\text{-}DOX\text{-}PEG\text{-}FA)}$, $NLC_{(Pal\text{-}DOX)}$ and $NLC_{(Pal\text{-}DOX\text{-}PEG\text{-}FA)}$. Formulations cumulative release profiles simulated in four conditions, regimes, after oral administration. Vertical dashed lines represent mimetic medium change: I) gastric media, II) intestinal media, III) physiologic media and IV) tumor microenvironment media. Values represent mean ± SD; n=3.

Figure 5.2 shows the *in vitro* release profiles from all drug-loaded NLCs following a set-up that simulates the path of the particles from the moment they enter the stomach until they reach the tumor microenvironment. After functionalization with polietileno-

glycol and folic acid (PEG-FA), DOX-loaded NLCs show notorious changes in the drug release profiles, principally for cetyl palmitate-based NLCs ($NLC_{(Pal\text{-}DOX\text{-}PEG\text{-}FA)}$) in comparison to non-functionalized nanoparticles. As rationally designed, only a small amount of DOX is released in the gastric and intestinal medium (a maximum of 20% for all formulations), which may prevent DOX side-effects on the intestinal epithelium [365]. Most of the release occurs in regimes III and IV, yet the amount of DOX that still remains in each formulation (more than 50% for all formulations) far exceeds the minimum limit to have a therapeutic response.

The release kinetics profile of DOX was studied by applying the mathematical models above described, the main results are presented in Table 5.1. Considering the values obtained for the determination coefficients (R^2), the models that best describe the release kinetics for DOX are mainly, taking out 3 exceptions, the Higuchi's model and the Korsmeyer-Peppas. However, in regime I (pH 1.6) of the gelucire-based formulation ($NLC_{(Gel\text{-}DOX)}$), zero-order kinetics rules. The zero-order equation indicates that the release of the active agent, DOX, occurs at a constant rate, regardless of the concentration of the active agent. On the other hand, for regime I of $NLC_{(Pal\text{-}DOX)}$ and $NLC_{(Pal\text{-}DOX\text{-}PEG\text{-}FA)}$, the first-order equation explains that the rate of drug release depends on its concentration [366]. Higuchi's model, predominant in 3 regimes of $NLC_{(Gel\text{-}DOX)}$, is linked to Fick's first law and describes the diffusion of drugs according to the concentration gradient [257].

Still, the model that best describes the mechanism of DOX release is the Korsmeyer-Peppas model in practically all cases. In this model, the value of *n* is used to characterize different types of mechanisms. Thus, $n \geq 0.43$ indicates a Fickian diffusion release mechanism; $0.43 < n < 0.85$ an anomalous transport mechanism; values of *n* equal to 0.85 represent case I transport; and for $n > 0.85$ indicates super case II transport (Fig. 5.1.) [257 , 366]. In the particular case of this model, the value of *n* is given by the slope of the line obtained. For $NLC_{(Pal\text{-}DOX\text{-}PEG\text{-}FA)}$ at pH values of 6.5 and 6.3, regime II and III (Fig. 5.1.), values of $n \geq 0.43$ were obtained. The mechanism associated with these values occurs by diffusion where the diffusion rate of the solvent is greater than the relaxation process of the surfactant. For $NLC_{(Gel\text{-}DOX\text{-}PEG\text{-}FA)}$, at pH 1.6, regime I, it is found that $n > 0.83$. This represents the super case II, where the sorption process governs the release mechanism, leading to the breakdown of the particle. In the remaining cases, $0.43<n<0.85$, the release mechanism is governed by diffusion and swelling. The rearrangement of the nanoparticles structure occurs slowly, and the diffusion process simultaneously cause the time-dependent anomalous effects.

Table 5.1: Determination coefficients (R^2) and k values from various drug release models for each developed NLC formulation (n = 3).

	Regime	Zero-order		First-order		Higuchi		Hixson-Crowell		Korsmeyer-Peppas	
		R^2	k_0	R^2	k_1	R^2	k_H	R^2	k_{HC}	R^2	k_{KP}
$NLC_{(Gel)}$	I	**†0.9814**	0.006	0.960	0.6746	0.902	0.0167	0.930	-3.075	0.950	2.172
	II	0.9813	0.0034	0.885	0.1664	**†0.995**	0.0094	0.874	-0.916	0.989	0.686
	III	0.9545	0.0023	0.812	0.0733	**†0.980**	0.0104	0.814	-0.666	0.971	0.773
	IV	0.967	0.0008	0.835	0.027	**†0.999**	0.005	0.982	-0.640	0.999	0.444
$NLC_{(Gel-PEG-FA)}$	I	0.949	0.0008	0.978	0.477	0.919	0.0075	0.946	-0.666	**†0.986**	1.551
	II	0.992	0.0024	0.934	0.1502	0.987	0.0066	0.914	-0.201	**†0.993**	0.604
	III	0.946	0.0029	0.834	0.0734	0.985	0.0134	0.933	-1.080	**†0.984**	0.770
	IV	0.927	0.0008	0.729	0.03	0.988	0.0049	0.9492	-0.569	**†0.985**	0.530
$NLC_{(Pal)}$	I	0.953	0.0088	**†0.987**	0.3367	0.884	0.0224	0.834	-5.818	0.9081	1.045
	II	0.984	0.0031	0.906	0.1526	0.985	0.008	0.776	-0.850	**†0.986**	0.621
	III	0.934	0.003	0.822	0.0626	0.982	0.0139	0.847	-1.136	**†0.980**	0.660
	IV	0.910	0.0005	0.740	0.0253	0.981	0.0029	0.935	-0.383	**†0.989**	0.440
$NLC_{(Pal-PEG-FA)}$	I	0.898	0.0052	**†0.989**	0.5302	0.859	0.0143	0.867	-2.369	0.9416	1.674
	II	0.957	0.0014	0.899	0.0958	0.975	0.0038	0.782	-1.005	**†0.979**	0.390
	III	0.956	0.0015	0.901	0.0556	0.978	0.0068	0.898	-0.254	**†0.986**	0.561
	IV	0.847	0.0004	0.680	0.0224	0.945	0.0023	0.866	-0.185	**†0.972**	0.403

†Represents models that best fit each release profile. K_0: Zero-order constant; K_1: First-order constant; K_H: release constant of Higuchi; K_{HC}: release constant of Hixson-Crowell; K_{KP}: release constant of Korsmeyer-Peppas

5.2.2. Hemolysis

After administration, nanoparticles face a series of biological barriers that can limit the achievement of adequate therapeutic results. Blood is one of those barriers since after administration, nanoparticles end up inevitably in contact with this fluid. When exposed to blood, nanoparticles interact with biomolecules that can lead to changes in their surface, which consequently, can lead to changes in biological responses. These interactions with blood components are not preventable and are also potentially dangerous, so hemolytic activity must be assessed.

Figure 5.3 shows the results obtained for the study of the interactions between developed NLC, in the presence and absence of DOX and PEG-FA, with red blood cells. Hemolysis assay was carried out in a DOX concentration range from 1 to 50 $\mu g \cdot mL^{-1}$, and possible toxicity was analysed after 1h, through the percentage of

hemolysis. In the case of NLC with gelucire up to a value of 20 µg ·mL^{-1}, all formulations have a lower hemolysis percentage than the free drug, in the corresponding concentration. However, at a concentration of 50 µg·mL^{-1}, formulations, where DOX was incorporated, have a higher hemolysis rate than the free drug. On the other hand, in NLC with cetyl palmitate the percentage of hemolysis obtained is, in most cases, equal to or greater than the percentage of hemolysis caused by the free drug. Nevertheless, hemolysis rate below 5% is generally considered non-toxic [367].

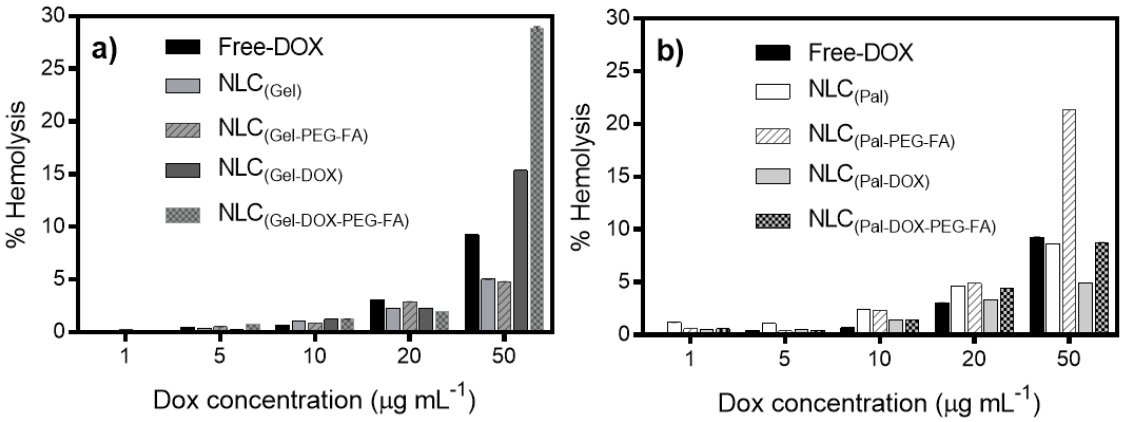

Fig. 5.3: Hemolysis rate obtained for the different NLC, where A) represents the gelucire based NLC and B) the cetyl palmitate based NLC. Data expressed as mean ± SD (n = 3) ***P < 0.001 in relation to control of free DOX at each concentration; ****P < 0.0001 in relation to control of free DOX at each concentration.

This shows that NLCs with gelucire may be a viable alternative for the administration of DOX, up to a concentration of 20 µg·mL^{-1}. Although in these conditions the differences with the free drug are not significantly different, the administration of DOX through the NPs allows a more controlled and targeted delivery, which will be an asset in clinical practice.

5.2.3. *In vitro* cytotoxicity study

The cell viability of NLCs with and without DOX was evaluated for 72 h of incubation. As shown in Fig.5.4 (a), treatment with unloaded NLCs up to 180 µg·mL^{-1}, in lipid, did not affect the cell viability, exhibiting over 98% viability for the studied conditions, suggesting that both lipid matrixes are safe for the use as drug carriers. The viability of DOX-loaded NLCs is shown in the graphs of Fig. 5.4 (b) and (c). All DOX-loaded NLCs presented the same trend of enhanced cytotoxicity with the increase in DOX-loaded concentration. The 50% cellular growth inhibitions (IC_{50}) of the

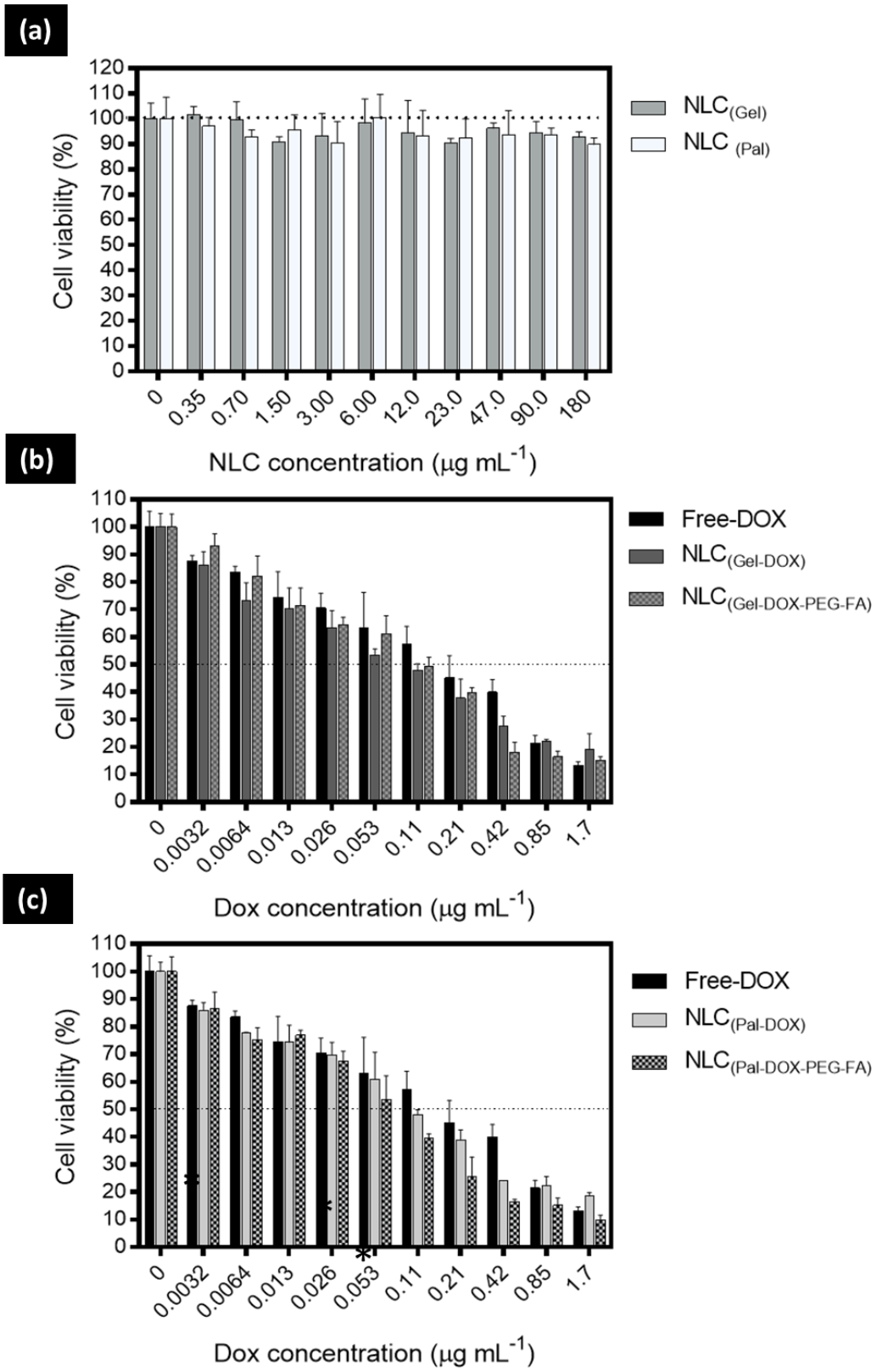

Fig. 5.4: MDA-MB 231 cells viability for different NLCs concentrations A). Viability MDA-MB 321 cells exposed to doxorubicin solution, freshly prepared doxorubicin loaded NLCs with and without PEG-FA. B) Formulations made with gelucire, and C) formulations made with cetyl palmitate, as a solid lipid. (n = 3).

DOX-loaded NLCs are shown in Table 5.2. It can be observed that the concentrations for IC_{50} are very low and close to that obtained for free-DOX. Moreover, when functionalized the NLCs have higher toxicity compared to non-functionalized NLCs, and between the two groups $NLC_{(Pal\text{-}DOX\text{-}PEG\text{-}FA)}$ can be highlighted as being more cytotoxic to this breast cancer cell line. The table also shows the values of the NLCs concentrations corresponding to the DOX concentrations for IC_{50}. It can be observed that the concentrations of NLCs are within the viability range observed in Fig.5.4 (a) for NLCs without DOX, therefore all observed effects occur exclusively by the presence of DOX.

Table 5.2: IC_{50} of NLCs (Mean ± SD, n = 3).

Formulation	IC_{50} ($\mu g \cdot mL^{-1}$)
$DOX_{(Free)}$	0.163 ± 0.026
$NLC_{(Gel-DOX)}$	0.206 ± 0.006
$NLC_{(Gel-DOX-PEG-FA)}$	0.200 ± 0.033*
$NLC_{(Pal-DOX)}$	0.207 ± 0.002
$NLC_{(Pal-DOX-PEG-FA)}$	0.132 ± 0.033$^{\#}$

IC_{50} value of drug solution against drug resistance cells; $DOX_{(free)}$ vs NLC formulations * $P < 0.05$; $NLC_{(Pal\text{-}DOX)}$ vs $NLC_{(Pal\text{-}Dox\text{-}PEG\text{-}FA)}$ $^{\#}$ $P < 0.03$.

5.2.4. *In vitro* cell uptake assessment

The uptake study was performed for drug-free NLCs with and without functionalization up to 120 min. Figure 5.5 (a) shows the cellular uptake percentages of NLCs at different incubation times when the MDA-MB 231 cells were incubated with $NLC_{(Gel)}$ formulations with and without PEG-FA. Comparing the two types of $NLC_{(Gel)}$ we can see that both formulations are internalized very quickly, reaching more than 80% in less than 30 min. The cellular uptake percentages of NLCs functionalized with PEG-FA increased comparing with NLCs non-functionalized, following the purposed of the designed nanoparticles.

Figure 5.5 (b) shows the cellular uptake percentages of NLCs at different incubation time when the MDA-MB 231 cells were incubated with cetyl-palmitate formulations with and without PEG-FA. Comparing the two types, $NLC_{(Pal)}$ and $NLC_{(Pal\text{-}PEG\text{-}FA,)}$ we can see that both cellular uptakes are very different, for $NLC_{(Pal)}$ more than 80% are already internalized before 1 h, while for $NLC_{(Pal\text{-}PEG\text{-}FA)}$ the same 80% was reached before 40 min. Also for this group of formulations, the cellular uptake percentages of NLCs functionalized with PEG-FA increased comparing with that of NLCs non-functionalized. It was clear that the cell uptake of gelucire-based NLCs is faster than cetyl palmitate-based NLCs. This fact can be attributed to the smaller sizes

of $NLC_{(Gel)}$ and $NLC_{(Gel\text{-}PEG\text{-}FA)}$; however, this difference decreases when NLCs are functionalized. These results also lead to the conclusion that for the same time of exposure the rapid uptake of functionalized NLCs causes a greater amount of DOX to be internalized in the cell, increasing the toxicity of this type of nanoparticles making it equivalent to the performance of free DOX ($P < 0.05$).

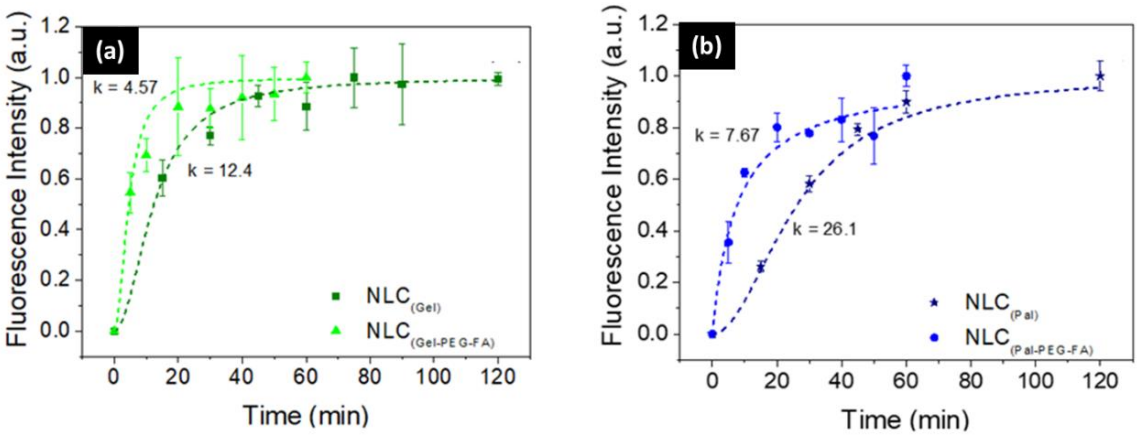

Fig. 5.5: MDA-MB 231 cells uptake of fluorescent labelled non-functionalized NLCs and PEG-FA functionalized NLCs over time (0 at 60 and 120 min). Values represent mean ± SD; n = 3.

To clarify the uptake mechanism of the FA-functionalized NLC by MDA-MB-231 that are high FA-receptor expressing cells, a study was conducted with HaCaT cells, a human keratinocytes cell line, with low FA-receptors expression. FA-functionalized NLC exhibited an enhanced selectivity to FR-positive MDA-MB231 cells, revealing about 1.5-fold higher cellular uptake. Non-functionalized NLC were internalized at similar extent by both MDA-MB231 and HaCaT cell lines while FA-functionalized NLC exhibited a decrease uptake in the low FA-receptor expressing cells (Fig. 5.6).

To gain information on the internalization pathway of the functionalized NLCs, MDA-MB231 cells were incubated at 4 °C and with sodium azide, both inhibitors of active transport [368]. Cellular uptake of functionalized NLCs exhibited a significant decrease in relation to the endocytosis of non-functionalized nanoparticles and to the control condition (37 °C) (Fig. 5.7). At low temperatures, there is a significant decrease in membrane recycling. In the presence of FA-functionalized nanoparticles, MDA-MB231 cells average cellular fluorescence decreased by ca. 50 to 60% with low temperature treatment and about 35 to 45% for sodium azide treatment, for $NLC_{(Gel\text{-}PEG\text{-}FA)}$ and $NLC_{(Pal\text{-}PEG\text{-}FA)}$, respectively. The sodium azide condition inhibits active transport, so about 25% of NLCs uptake is due to passive diffusion (assessed by the 4 °C condition). Non-functionalized NLC internalization is also affected by the incubation at low temperature and with sodium azide, but to a less extent. The energy-dependent internalization pathway was further studied using specific inhibitors (Table 5.3) of the

most often used pathways clathrin- and caveolae-mediated endocytosis and micropinocytosis [369].

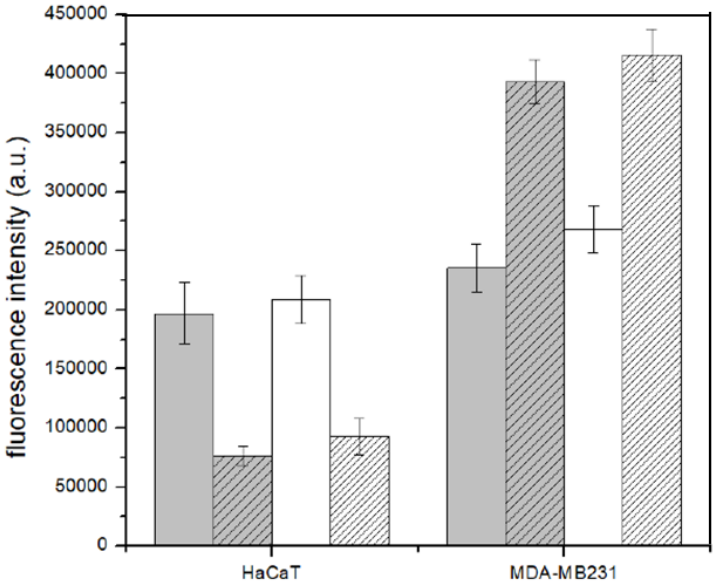

Fig. 5.6: Selective uptake of FA-functionalized NLC by FR-positive expressing MDA-MB231 cells. $NLC_{(Gel)}$ (light grey bar), $NLC_{(Gel\text{-}PEG\text{-}FA)}$ (dashed light grey bar), $NLC_{(Pal)}$ (white bar), $NLC_{(Pal\text{-}PEG\text{-}FA)}$(dashed white bar) were incubated for 30 min with MDA-MB231 and HaCaT cell lines.

Table 5.3: Selected inhibitors and respective functions applied to mechanistic studies of NLCs transport by MDA-MB231 cells.

	Inhibitor	Concentration	Function
Energy-dependence	4ºC	-	Passive diffusion and active transport inhibitor
	Sodium azide	1 mg·mL^{-1}	Active transport inhibitor
docytosis inhibitors	Chlorpromazine	10 µg·mL^{-1}	Clathrin-mediated endocytosis
	Cytochalasin D	5 µg·mL^{-1}	Disrupt actin filaments and macropinocytosis
	Filipin	1 µg·mL^{-1}	Caveolae-mediated endocytosis

The results shown in Fig. 5.7 (b) demonstrated that uptake of FA-functionalized NLCs was remarkably reduced (ca. 40%) compared to control cells, in the presence of chlorpromazine, an inhibitor of clathrin-mediated endocytosis. This is the “classical route” of cellular entry, which is present and active in all mammalian cells and is responsible for the uptake of nutrients and molecules able to bind the surface cell receptors. The results indicate that the internalization of FA-functionalized NLCs is

mainly mediated by the chlatrin-coated pits present in the FA receptor. About 10% of the internalization of FA-functionalized NLCs was hampered by the presence of cytochalasin D, a non-selective uptake process dependent on actin present in the cytoskeleton structure. Similar outcome was observed with the non-functionalized NLCs internalization by MDA-MB231 cells. In sum, data shows the involvement of the actin filaments as well as clathrin-coated pits in the internalization of FA-functionalized and non-functionalized NLCs.

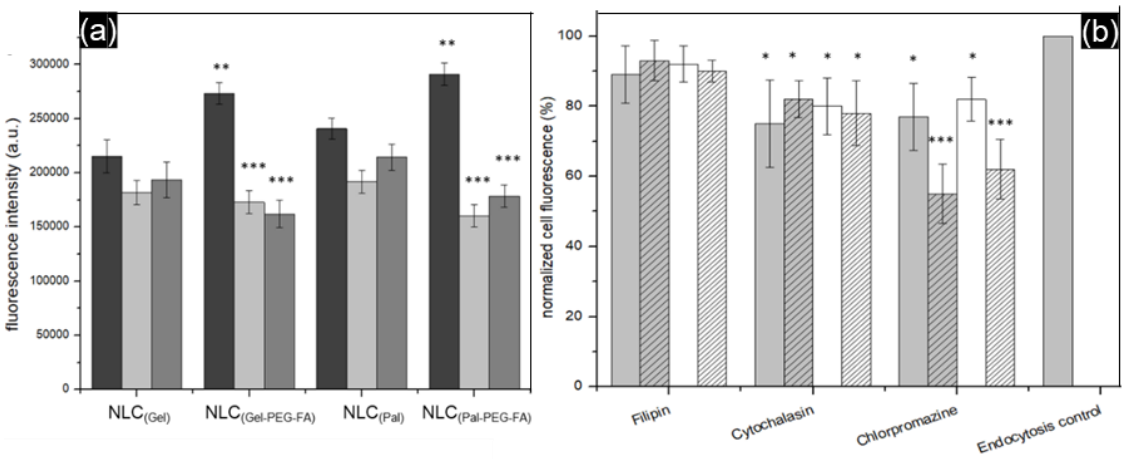

Fig. 5.7: Uptake of NLCs in MDA-MB231 cells. (a) Role of energy assessed by sodium azide (light grey) and low temperature (4 °C, dark grey) in endocytosis of NLCs in relation to 37 °C cell incubation temperature (back bar). Data expressed as mean ± SD (n = 3) ***P* < 0.01 in relation to control of non-functionalized NLC; and *** *P* < 0.001 in comparison to the control (37 °C). (b) The effects of different inhibitors on the endocytosis of $NLC_{(Gel)}$ (light grey bar), $NLC_{(Gel-á estPEG-FA)}$ (dashed light grey bar), $NLC_{(Pal)}$ (white bar), $NLC_{(Pal-PEG-FA)}$ (dashed white bar). Data expressed as mean ± SD (n=3) as normalized mean fluorescence intensity relative to control cells incubated with coumarin 6 marked NLCs without the respective inhibitors. **P* < 0.01 and *** *P* < 0.001 in comparison to the endocytosis control (absence of inhibitors at 37 °C).

5.3. Magneto-lipid nanocarriers for magnetic fluidic hyperthermia

Superparamagnetic iron oxide nanoparticles (SPIONs) are promising magnetic nanoheating agents for diagnostic and therapeutic applications [28]. The combination of its magnetic properties, chemical stability and biocompatibility enables SPIONs to be applied as drug delivery systems, magnetic fluid hyperthermia (MFH) [370, 371] and contrast agents for magnetic resonance image (MRI) techniques [372]. Magnetic hyperthermia emerged in the mid-1950s as a promising non-invasive therapeutic approach for the thermal treatment of cancer [373]. In this sense, we can apply

SPIONs as therapy agents, since it releases heat when exposed to an alternating magnetic field of appropriate frequency and amplitude, converting magnetic energy into thermal energy [374, 375]. This phenomenon leads to a controlled and local heating of the tissue tumor above 40°C [376, 377], which activates mechanisms of cell death (apoptosis or/and necrosis) while altering the functionality of proteins causing high sensitivity of cancer cells to traditional treatments such as radiotherapy and chemotherapy [378]. The SPION's ability to be activated and accumulated in the desired tissue is highly dependent on its surface and magnetic properties. Size, morphology and composition can increase heating efficiency by avoiding overdosing of magnetic fluid to achieve the treatment condition [379-381]. In addition, for the success of hyperthermia therapy, the encapsulation and functionalization of SPIONs are of great importance for anchoring specific ligands of cancer cells, while improving colloidal stability [382, 383]. In this section we report the physicochemical characterization of SPIONs and DOX encapsulated in $NLC_{(Gel)}$. Preliminary MFH measurements show the potential medical application of these multifunctional nanocarriers.

5.3.1. Physicochemical characterization of the nanocarriers

The methodology for SPIONs encapsulation into NLCs was described in section 2.3.2. According to the results obtained in the previous sections, the gelucire-based formulation ($NLC_{(Gel)}$) was adopted for SPIONs encapsulation ($NLC_{(Gel\text{-}SPION)}$). The obtained samples were also functionalized with the conjugated PEG-FA ($NLC_{(Gel\text{-}SPION\text{-}PEG\text{-}FA)}$), before and after de DOX encapsulation ($NLC_{(Gel\text{-}SPION\text{-}DOX\text{-}PEG\text{-}FA)}$). The main physical and chemical characteristics of the NLCs with SPIONs developed in this study are summarized in Table 5.4. These results correspond to the optimized formulation for each type of composition, in respect to size, zeta potential, polydispersity index (PDI), entrapment efficiency (EE) and drug loading capacity (LC).

$NLC_{(Gel\text{-}SPION)}$ when compared with the NLCs presented in Chapter 4 ($NLC_{(Gel)}$), show similar properties regarding the size, zeta potential and PDI once again showing the great reproducibility of the manufacturing process. The PDI of all formulations close to 0.2, is indicative that the formulations are nearly monodispersed, with uniform diameters of nanoparticle populations even with the magnetic core incorporated [334]. $NLC_{(Gel\text{-}SPION)}$ particles are slightly larger than those without SPIONs $NLC_{(Gel)}$, which is due to the SPIONs incorporation within the NLCs core. In addition, the diameters of all $NLC_{(Gel\text{-}SPION)}$ are around 300 nm, which remain within the size range acceptable for

oral administration, since they are preferentially internalized by enterocytes and cells, and reveal higher intestinal transport compared to larger particles [336, 337].

Table 5.4: Mean hydrodynamic particle size, polydispersity index (PDI) and zeta potential.

Formulations	**Size (nm)**	**PDI**	**Zeta potential (mV)**	EE (%)	LC (%)
$NLC_{(Gel\text{-}SPION)}$	258 ± 27	0.21 ± 0.02	-22.6 ± 2.2	--	--
$NLC_{(Gel\text{-}SPION\text{-}PEG\text{-}FA)}$	303 ± 37	0.22 ± 0.02	-23.1 ± 0.8	--	--
$NLC_{(Gel\text{-}SPION\text{-}DOX)}$	256 ± 29	0.19 ± 0.02	-22.7 ± 2.6	72 ± 2	2.8 ± 0.1
$NLC_{(Gel\text{-}SPION\text{-}DOX\text{-}PEG\text{-}FA)}$	277 ± 10	0.19 ± 0.02	-25.9 ± 2.3	85 ± 12	3.3 ± 0.5

Gel: Gelucire; SPION: superparamgnetic iron oxide nanoparticles; DOX: Doxorubicin; PEG-FA: Polyethylene glycol-Folic acid. Values are expressed as mean ± standard deviation (n = 3).

Regarding the zeta potential, all values are greater than | 20 | mV and even it is established that the aggregation or flocculation of particles is avoided when the zeta potential is ± 30 mV [339]. Studies already show that for values close to ± 25 mV an accepted value is also considered [377], particularly when the particles have a spherical stabilizing agent. In addition, the particles are negatively charged which causes them to show less cytotoxicity than cationic nanoparticles, usually associated with rupture of the cell membrane and consequent cell death [342]. The entrapment efficiency of DOX in the $NLC_{(Gel\text{-}SPION\text{-}DOX)}$ was (72 ± 2) % with a drug loading of (2.8 ± 0.1) % and in the $NLC_{(Gel\text{-}SPION\text{-}DOX\text{-}PEG\text{-}FA)}$ was (85 ± 12) % with a drug loading of (3.3 ± 0.5) %. Previously, we have reported that encapsulation of the DOX in NLC without SPIONs, was among 55-60%, thus we can conclude that the co-encapsulation of DOX and SPIONs did not affect the drug loading, on the contrary, promoted an increase of DOX encapsulation [384].

5.3.2. Nanoparticles morphology

Transmission electron microscopy (TEM) studies were performed in an aqueous suspension of SPIONs. Figure 5.8.(a) is a typical TEM image of SPIONs, where the agglomerated nanoparticles with nearly spherical shape are observed with an average diameter of approximately 12 ± 3 nm and low size distribution.

In the NLCs with internalized SPIONs (Fig 5.8. (b)), the spherical shape of the lipid nanoparticles is highly visible and SPIONs are not observed outside the lipid structure. However, it is not possible to see SPIONs within the NLCs, which may be explained

due the presence of the uranyl contrast agent that may have camouflaged the SPIONs. We can also observe that the sizes are similar to those obtained in the DLS characterization. However, it was not possible to make a statistical analysis. In Fig. 5.8 (d) we can also see the presence of functionalization by PEG-FA through the most accentuated outline of the nanoparticle.

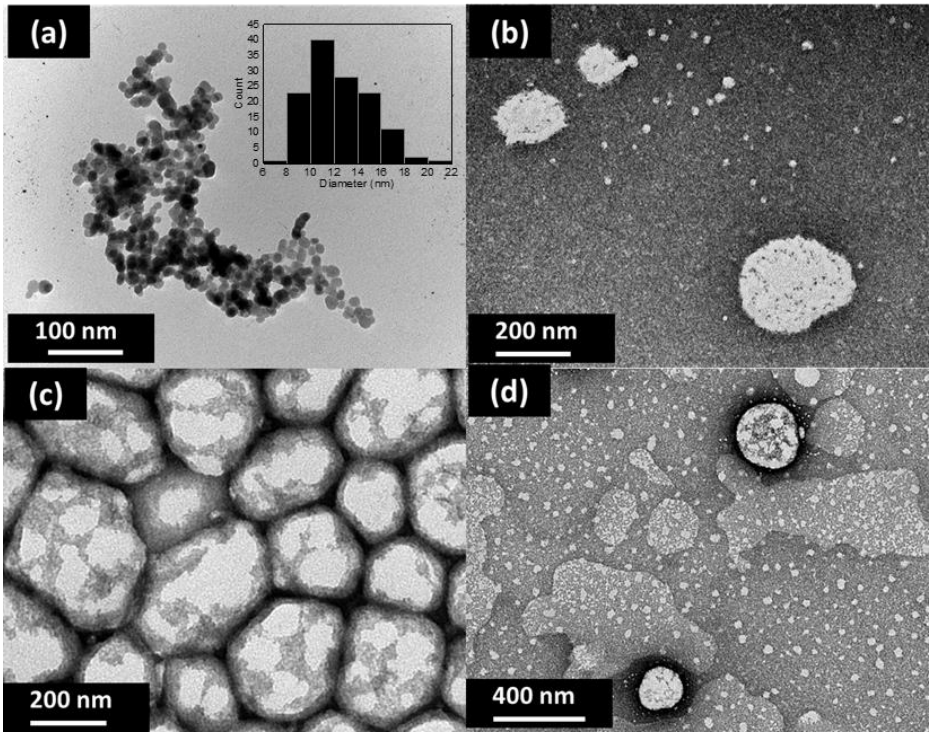

Fig. 5.8: Transmission electron microscopy for (a) SPIONs (b) $NLC_{(Gel\text{-}SPIONs)}$, (c) $NLC_{(Gel\text{-}DOX\text{-}SPIONs)}$, (d) $NLC_{(Gel\text{-}DOX\text{-}PEG\text{-}FA\text{-}SPONs)}$.

5.3.3. Storage stability

The physical stability of all NLCs formulations were checked periodically by analyzing the hydrodynamic diameter, polydispersity, zeta potential, EE and LC during storage conditions for 10 weeks at 4ºC (Fig. 5.9). The results show that all formulations are stable for these parameters for at least 10 weeks. ANOVA statistical analyzes ($p < 0.05$ in relation to the corresponding week zero do not show any significant change in the parameters studied during this period. As for EE and LC, it was observed that at the end of the first two weeks the release of DOX was significantly higher, nevertheless after 8 weeks the values stabilized between 50 and 60 percent. Thus, the developed NLCs are suitable for incorporating DOX in conjunction with SPIONs and for therapeutic administration during this time and under the described storage conditions.

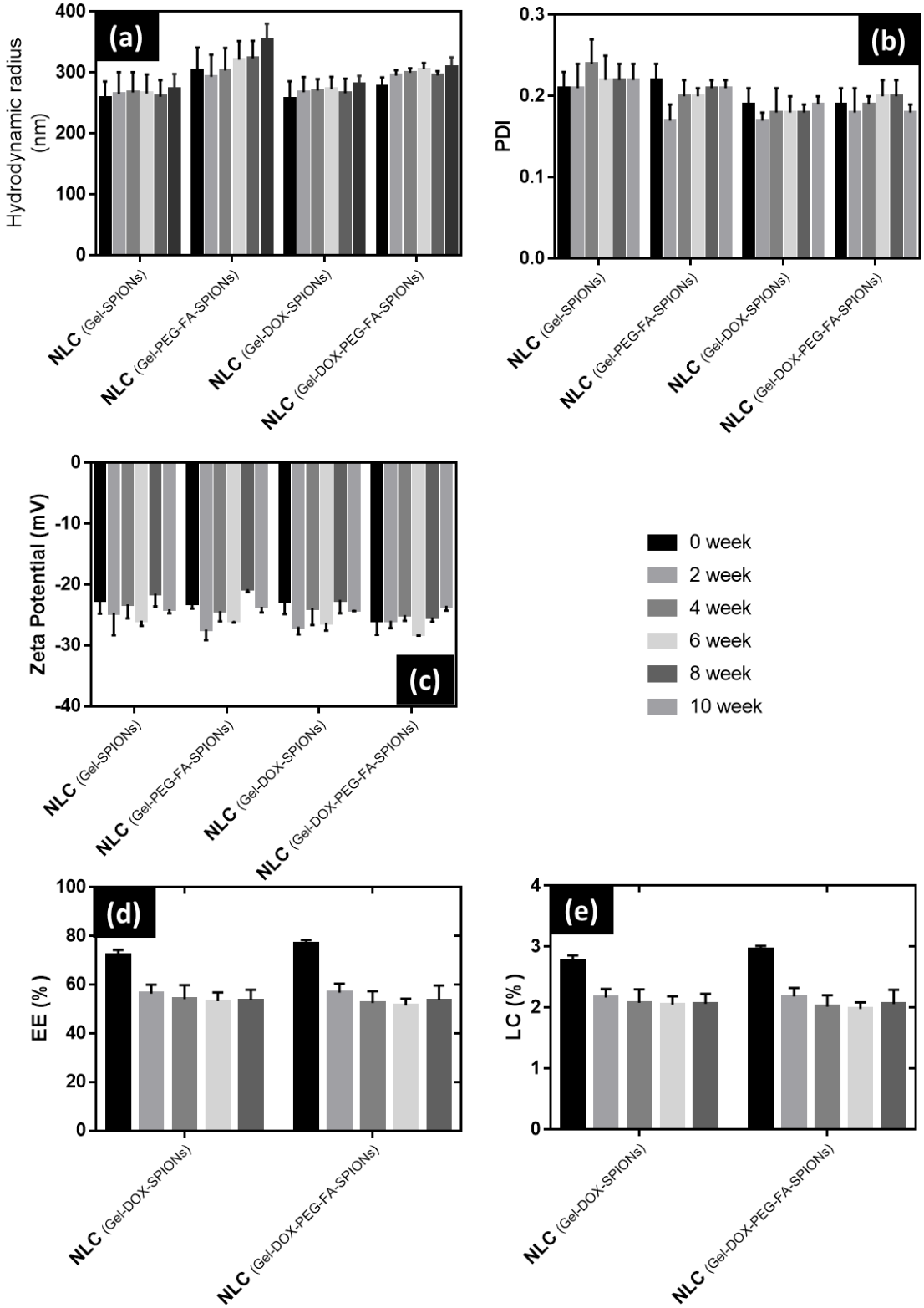

Fig. 5.9: Physical stability of the formulations over time (for up to 10 weeks). The graphics represent the mean hydrodynamic diameter (a), PDI (b), Zeta potential (c, EE (d) and LC (e). Values corresponds mean of the readings (n=3) ± SD (The ANOVA analyses show $P < 0.05$ relatively to the correspondent day 0).

5.3.4. Structural characterization

The structural characterization of the prepared formulations with and without SPIONs was made by XRD. The XRD pattern of the SIPONs (Fig. 5.10 a) reveals the cubic ferrite structure of the magnetite phase. The characteristic XRD peaks marked by their Bragg indices (220), (311), (400), (422), (511), (440) and (533) are in correspondence with Fe_3O_4 phase [385]. The average x-ray crystallite diameter (D_{XRD}), calculated using the Scherrer's equation [386] by using the B value of the (311), (511) and (440) planes peaked at 35.7°, 57.2° and 62.9° as the representative planes of the magnetite phase was 12.6 ± 0.6 nm The D_{XRD} value obtained is comparable with other SPIONs synthesized by different techniques in the literature [59] and it is in good agreement with the diameter calculated from the TEM images.

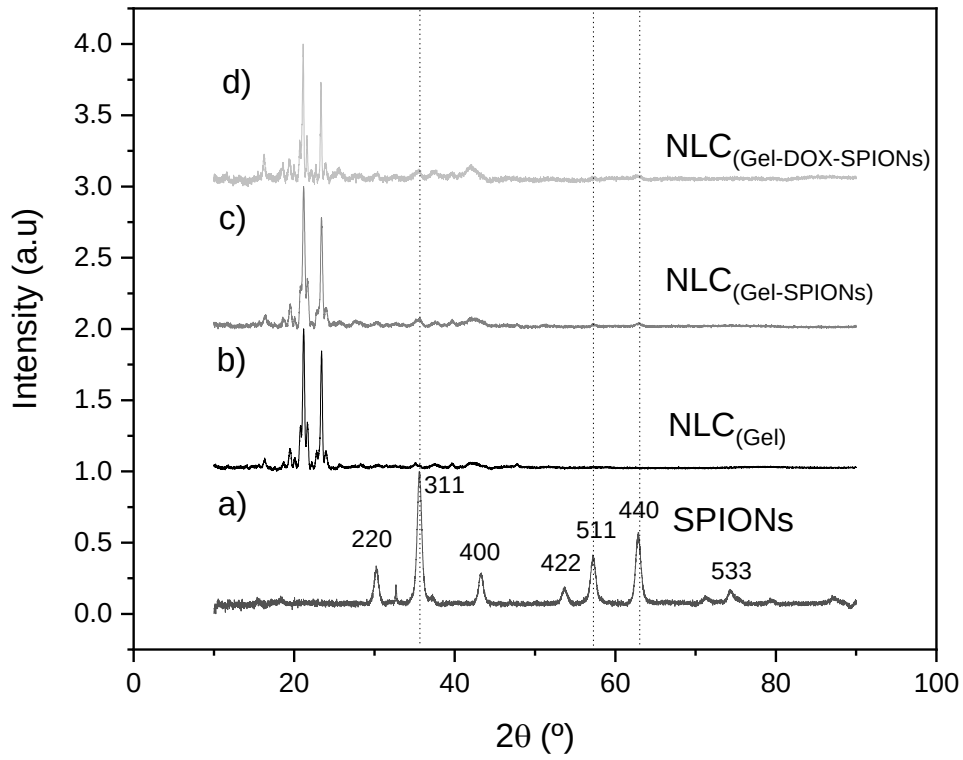

Fig. 5.10: X-ray diffraction pattern for formulations: a) SPIONs, b) $NLC_{(Gel)}$, c) $NLC_{(Gel\text{-}SPIONs)}$ and d) $NLC_{(Gel\text{-}DOX\text{-}SPIONs)}$.

In order to investigate the changes in the NLCs crystalline structure due to the drug and/or SPIONS encapsulation and to confirm the SPIONs encapsulation, XRD measurements were also performed in NLC_{Gel}, $NLC_{Gel\text{-}SPIONs}$, $NLC_{Gel\text{-}DOX\text{-}SPIONs}$ and the respective spectra are represented in Fig. 5.10. b, c, d. The diffraction pattern of NLC_{Gel} (Fig. 5.10 b) clearly show a crystalline phase with two more intense peaks at 21º and 23º that can be associated to gelucire, the solid lipid used in all formulations [387]. The

same characteristic peaks of the solid lipid were observed in all formulation, which indicates that the presence of the drug and SPIONs do not interfere in the crystalline structure of the NLCs. We can also observe the presence of the three main peaks of the SPIONs in the NLCs (highlighted by dashed lines) (Fig. 5.9 c and d), proving, once again, that the nanomagnets are internalized in the NLCs. The low intensity of the peaks related to the SPIONs, compared with the peaks of the solid lipid, leads us to conclude that the ratio between SPIONs and NLCs is low. In this sense, an optimization procedure to increase SPIONs concentration in the NLCs may be further performed.

5.3.5. Magnetic characterization

Magnetic properties of the as prepared SPIONs were evaluated using magnetic hysteresis loops. Samples were measured in liquid. The masses were determined by the concentration of SPIONs in the aqueous suspension while for SPIONs in the NLCs an estimate was made based on the proportion of Ms (magnetization of saturation) at 5 K for all. The magnetization versus magnetic field curves shows that all samples, SPIONs and $NLC_{(Gel\text{-}DOX\text{-}SPIONs)}$ is showed in Fig 5.11. The results show that symmetry and reversibility of all magnetization curves represent superparamagnetic behavior [388]. At the room temperature superparamagnetic characteristic of all samples with nearly zero remanence magnetization (Mr) confirmed the single-domain structure of the SPIONs obtained from TEM image and D_{XRD}. The magnetization saturation for SPIONs is 78 emu/g, which is near to the values obtained for bulk magnetite [389]. In both samples at 5 K, the superparamagnetic behavior were not observed, because in those temperature the nanoparticles do not have enough thermal energy to come to

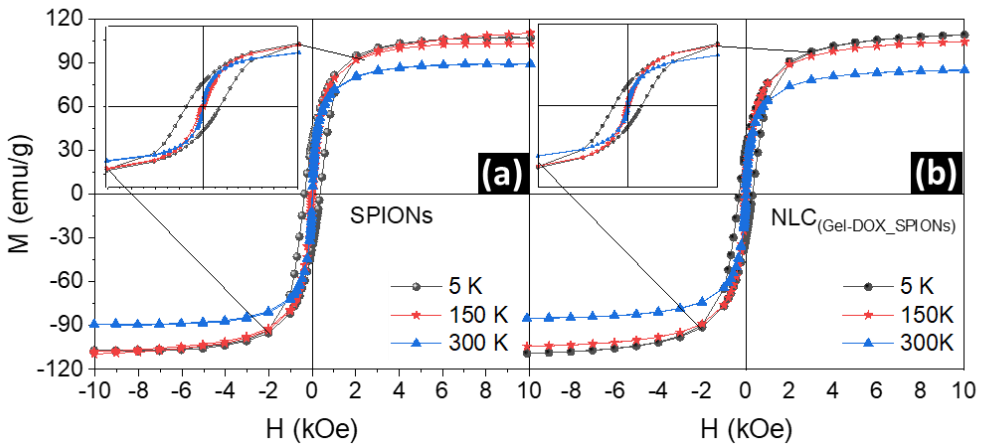

Fig. 5.11: Hysteresis loops with different temperatures measured for: (a) SPIONs and (b) $NLC_{(Gel\text{-}DOX\text{-}SPIONs)}$.

complete thermal equilibrium with the applied field during the time required for the measurement, and hysteresis appears [388]. As can be seen comparing the M (H) at 300 K for both SPIONs and SPIONs encapsulated in NLCs, the magnetization does not decrease after the encapsulation in the NLCs, which is a very advantageous feature from the point of view of SPIONs' usage as a targeted drug delivery platform.

Figure 5.12 present a study of the coercivity field and remanence magnetization as a function of temperature. In Fig. 5.12 (a) the curves of the coercivity field and remanence magnetization for SPIONs as a function of temperature also confirmed the superparamagnetism of SPIONs since the same trend of Mr and Hc vs T plot is observed and in the ideal conditions these curves would overlap [121]. In Fig. 5.12 (b) remanence magnetization and (c) coercivity field are presented for SPIONs, $NLC_{(Gel\_SPIONs)}$ and $NLC_{(Gel\text{-}DOX\_SPIONs)}$ respectively and the same behavior is observed which confirms that NLCs encapsulation doesn't affects the magnetic performance of the magnetic core.

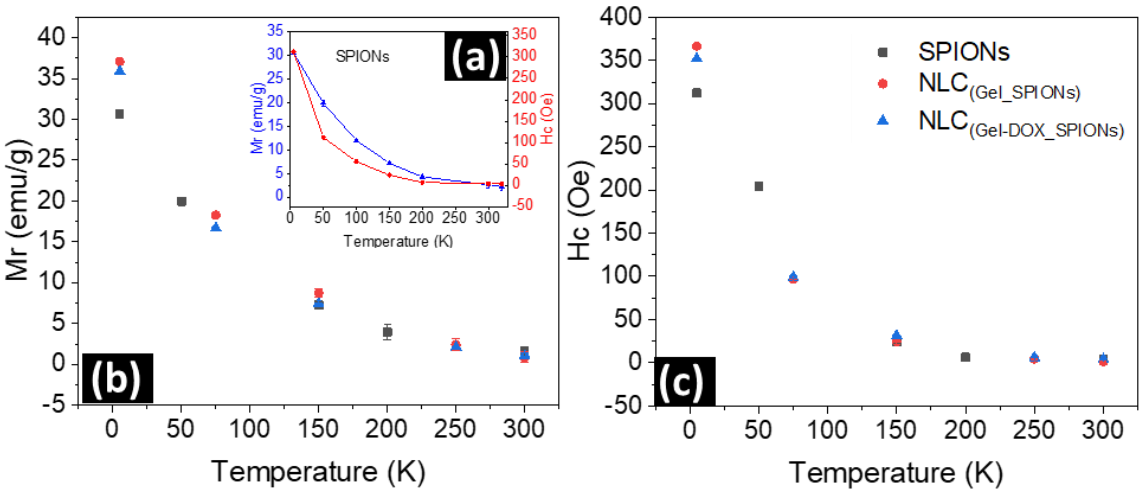

Fig. 5.12: Study of the coercivity field and remanence magnetization as a function of temperature. (a) coercivity field and remanence magnetization for SPIONs, (b) coercivity field and (c) remanence magnetization for SPIONs, $NLC_{(Gel\_SPIONs)}$ and $NLC_{(Gel\text{-}DOX\_SPIONs)}$.

The zero field cooled- field cooled (ZFC-FC) curves obtained for the SPIONs powder and for the NLC $_{(Gel\text{-}DOX\text{-}SPIONs)}$ can be seen in Fig. 5.13. (a) and (b) respectively. For SPIONs it is not possible to observe T_{max}, as it is well above room temperature, this may be occurs due to the separation between the particles that is not sufficient to reduce dipolar interactions. However, there is a transition at 230 K which shows that a significant number of particles are unblocked at this temperature. Within NLCs, SPIONs reach a T_{max} of around 236 K, also above room temperature. In both cases

there is an irregularity in the curves between 50 and 100 K, which may be an O_2 contamination inside the SQUID.

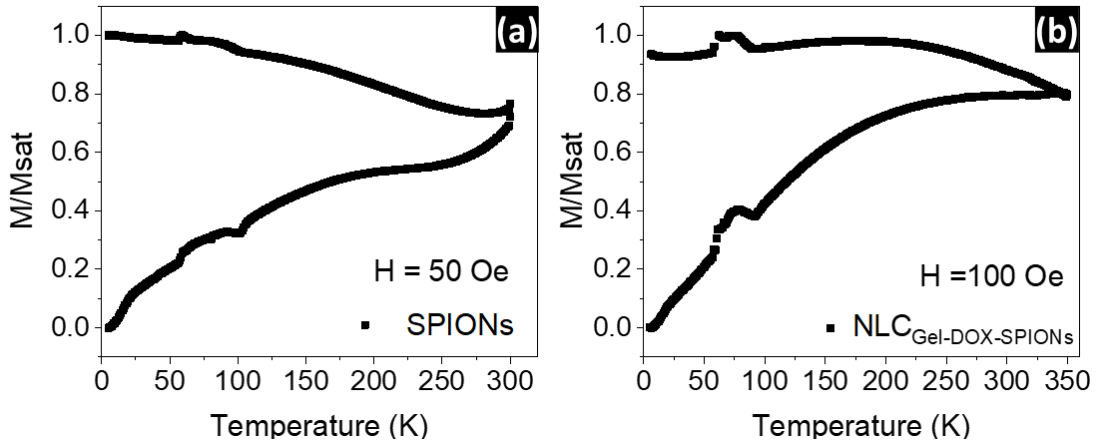

Fig. 5.13: Zero field cooled- field cooled (ZFC-FC) cures obtained for the SPIONs (a) and $NLC_{(Gel\text{-}DOX\text{-}SPIONs)}$ (b).

5.3.6. Magnetic fluidic hyperthermia

A heating study was performed for SPIONs, measured under equal experimental conditions (volumes, temperature and types of tubes), in water. The SAR parameter is changed if different magnetic strengths and frequencies are carried out to evaluate the heating of the same sample. Figure 5.14 shows the heating curves for different frequency conditions and alternating magnetic field. Based on the results obtained, the SAR was calculated using equation 1.1. and Fig. 5.14 (a) shows that for a frequency of 103 kHz and a magnetic field (H) of 20 mT (200 Oe) a SAR of 64 W/g was obtained. In Fig. 5.14 (b) the magnetic field (H) was reduced by half while the frequency was increased to 556 kHz resulting in a SAR of 62 W/g. In both analyzes, the temperature variation in less than 5 min can reach values greater than 42 ºC showing that SPIONs are potentially effective for hyperthermia treatment. Frequency can also be used to tune the heat generation. Thus, heat generated by SPION can be optimized by adjusting the properties of the applied magnetic field and frequency to obtain the highest values of SAR [390, 391].

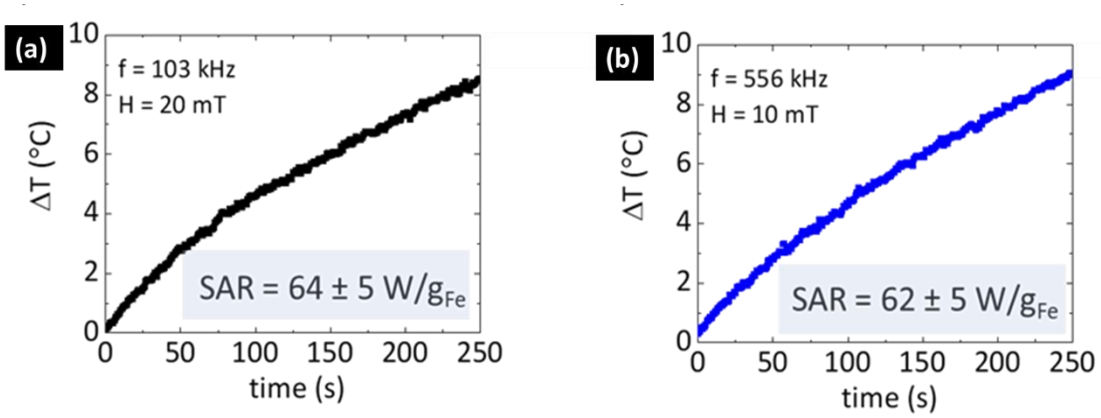

Fig. 5.14: Temperature elevation curves of SPIONs, upon magnetic induced hyperthermia under different conditions: a) f = 103 KHz and H = 20 mT; b) f = 556 KHz and H = 10 mT.

5.4. Conclusions

The *in vitro* DOX release profile revealed that the developed NLC formulations can be suitable for oral administration and enable a sustained release that may allow a significant amount of drug to reach the cancer cells, where DOX has its therapeutic target. *In vitro* cellular studies demonstrated the cytotoxic potential of the formulations towards breast cancer cells and the influence of FA conjugation in the intracellular uptake. Taking these *in vitro* studies results, it is possible to realize the FA-PEG-NLCs potential as DOX delivery systems to increase its bioavailability and improve the target therapeutic effectiveness in situ, while minimizing the well-known side-effects. Besides their potential to enable a more convenient route of administration the oral one.

SPIONs where been encapsulated in the NLCs for MFH application. The magnetic beads can be encapsulated with DOX in the NLCs without affect the physical-chemical properties of the lipid shell and the magnetic properties of the core. The preliminary MFH measurements showed the potential application of the fabricated SPIONs for MFH treatment combined with DOX release.

Chapter 6

Work in Progress

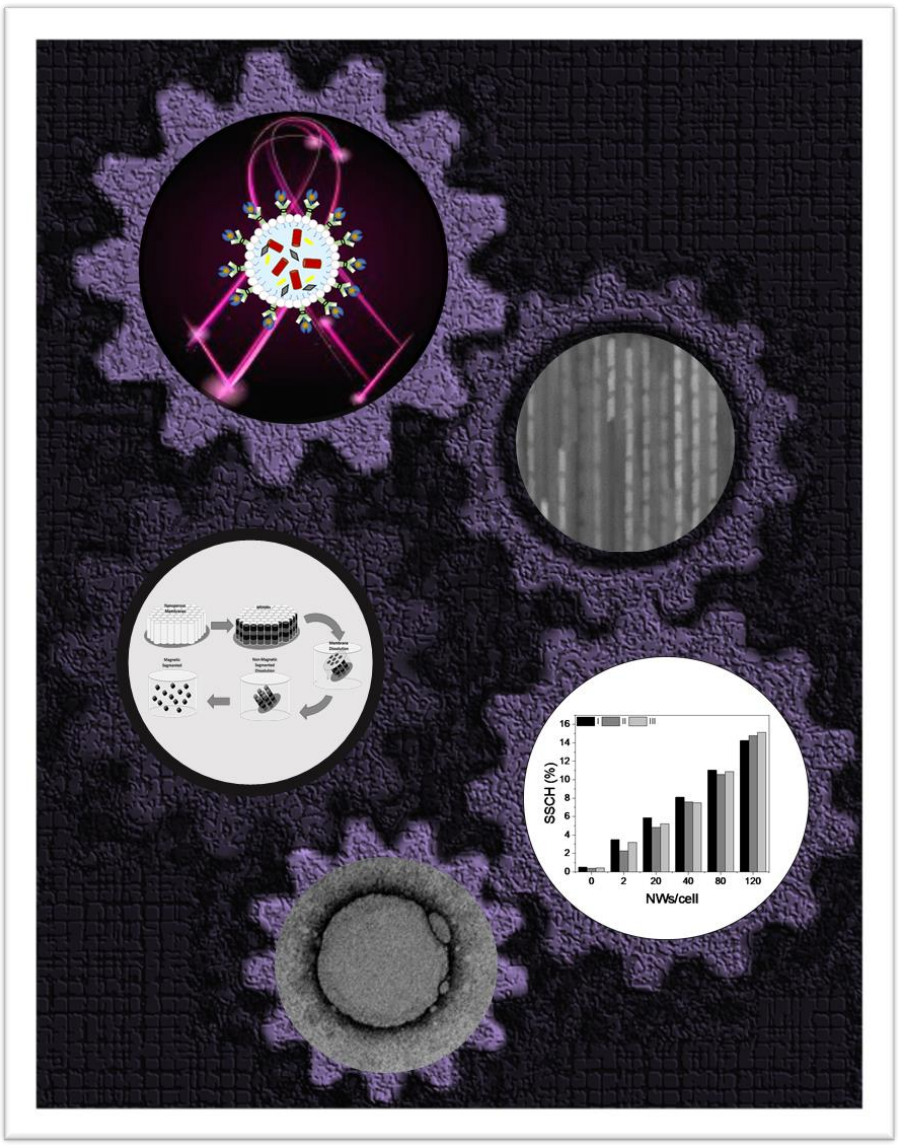

Chapter 6

Work in Progress

In this chapter we present several researches works that are currently under study.

6.1 Overview

In recent years, to overcome many limitations in the current therapeutics of cancer treatment, new approaches based on multifunctional hybrid-design nanostructure appears to be a promising route. A multifunctional nanohybrid with a magnetic part optimized for magnetic hyperthermia or/and magneto-mechanical induce cellular death, and a plasmonic metal, with tunable plasmonic properties in the near infra-red (NIR) region, for photothermal therapy, is defined as the cooperation among different treatments integrated into a single nanoplatform whose yields enhanced therapeutic effects compared to the individual treatments [392].

The combination of iron (magnetic) and gold (plasmonic) nanoparticles has been constantly chosen in the studies involving multi thermo-therapy because those materials are biocompatible and have good physical properties [393]. In the case of magnetic nanoparticles, application of a high frequency alternating magnetic field can result in three phenomena pertinent to use in cancer therapy, depending on the physical properties of the nanomaterials: (1) excites the fluctuations of the magnetic moment, the resulting magnetic energy being released and dissipated as heat (magnetic hyperthermia); (2) the minimization of energy forces the spins into a curling state, change gradually spin directions, starting parallel to the surface, canceling the total dipole energy, and also not losing too much exchange energy consequently, near the center of the disk, the angles between adjacent spins increase until it is no longer possible to remain confined in-plane, resulting in a vortex core (vortex state) [394-396]; (3) there is a homogeneous rotation of the magnetization along the wire (transverse domain wall and vortex domain wall modes) [397, 398] and for optical excitation of plasmonic nanoparticles by an infrared laser causes localized heating that can destroy surrounding cancer cells (photothermia) [399, 400].

Evidently in all cases, the size and shape of the nanoparticles are crucial for optimizing these specific physical properties in agreement biological processes [400, 401].

This chapter presents a set of works that are under development involving two different multifunctional hybrid nanostructures for potential application in cancer therapy. Firstly, our main objective was to develop nanostructured lipid carriers (NLC) that would include, in addition to the drug, magnetic Fe nanorods (NRs) for magneto-mechanical cancer therapy with an additional segment of Au for magneto-plasmonic cancer therapy. However, these objectives present some challenges that implied the development of new approaches and future strategies.

6.2 Magnetic nanorods for magneto-mechanical cancer therapy

The main motivation of this study is to use Fe NRs for application in magneto-mechanical cancer therapy. Figure 6.1 shows the schematic steps planned for the fabrication of a multifunctional nanoparticle with a magneto-lipidic core-shell structure as described in the section 2.3, but with an improved release capability of the drug and even damage the cell itself due to the presence of Fe NRs and its mechanical movement induced by an alternating magnetic field (AMF). The first step consists in the synthesis of Fe/Cu multi-segmented NWs by electrodeposition in anodic alumina oxide (AAO) as described in section 2.1.2, where we chose a dimension of about 250 nm of Fe segments obeying a compromise between an acceptable length for oral administration, resistance to chemical attack during the removal process from the template and the guaranteed vortex domain wall from the extremities of each segment, as shown in the study presented in section 3.5. Despite being biocompatible and having great advantages for bioapplications, the greatest difficulty in obtaining Fe nanostructures is its oxidation during the manufacturing process; some processes may even oxidize it completely and in the sense, the second step refers to the removal of the NRs from the anodic aluminum oxide (AAO) membranes and then the chemical etching of the Cu segments, which was performed as described in section 2.1.3, always avoiding as much as possible the Fe dissolution and oxidation. Once the Fe NRs are released, a study of biocompatibility and internalization in cells were carried out and, on the other hand, it follows the manufacturing process of nanostructured lipid nanocarriers (NLCs) loaded with NRs, which in turn are also studied for the same parameters used for NRs in cells.

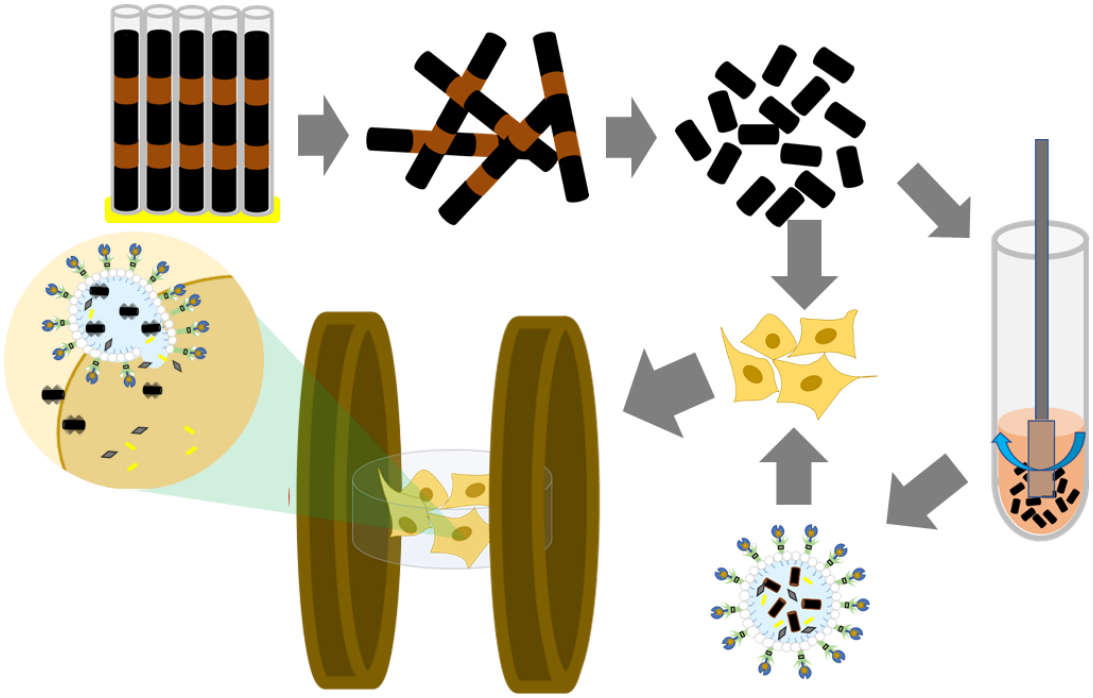

Fig. 6.15: Scheme of Fe NRs fabrication steps and internalization in NLCs for application in magneto-mechanical cancer therapy.

Figure 6.2 (a) shows TEM images of Fe/Cu NWs with L_{Fe} 250 ± 20 nm and L_{Cu} 60 ± 5 nm after AAO removal. Notice that alumina was successfully removed, leaving clean the NWs. Although the Fe/Cu interface is expected to be a fragile spot of these NWs, the structures are seen to withstand the process of dissolution/washing, showing mechanical robustness, and thus making this approach extremely viable for high-yield synthesis. Finally, the Fe/Cu NWs were immersed in a solution of 10% HNO_3 about 2 min to remove Cu segments which is enough to completely dissolve all Cu and no evidence of Fe oxidation was found in the STEM images (Fig. 6.2 (b)). Also, the easy magnetic rescued is an evidence of the lower oxidation of the magnetic segments.

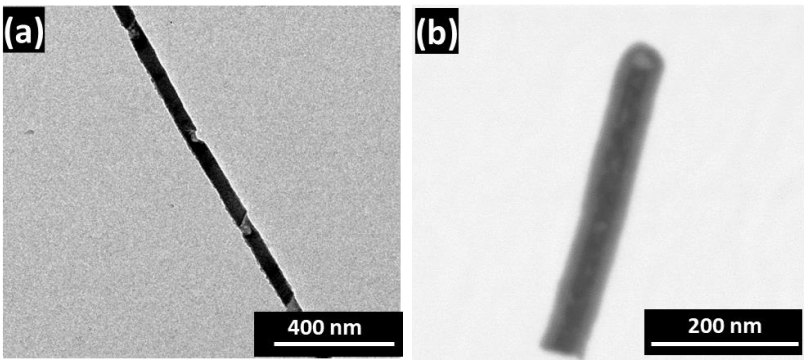

Fig. 6.16: (a) STEM images of the Fe/Cu NWs dispersed after AAO membrane removal. The average diameter is 40 ± 5 nm and length of the Fe and Cu segments is and 60 ± 5 nm, 250 ± 20 nm. (b) STEM images of the nanowires Fe dispersed after removal Cu segments.

The toxicity of the Fe NRs was evaluated in MDA-MB 231 cells line, for different concentrations. The results of the cell viability studies are shown in Fig. 6.3 (a). All tested concentrations have less than 15% of dead cells, which leads us to believe that this NRs are innocuous without an applied magnetic field.

The difference in the height of the side scattered light (SSC-H) was measured to infer particle uptake. The results are summarized in Fig. 6.3 (b). As mentioned before, the analysis of the SSC-H allows for an assessment of the internal complexity or relative granularity. So, by comparing these results, we can conclude that Fe NRs was internalized up to 120 NRs per cell.

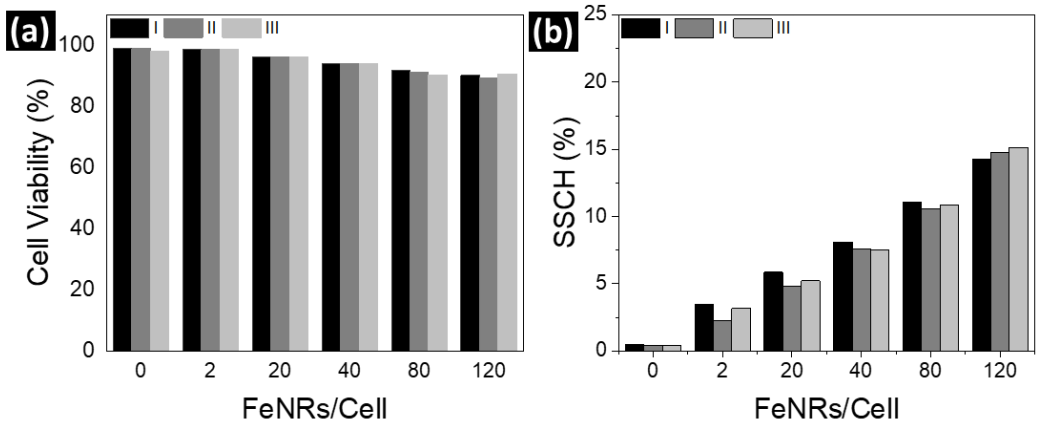

Fig. 6.17: (a) Percentage of cell viability with the number of Fe NRs per cell. (b) Cellular uptake of the Fe NRs in MDA-MB 231 cells line. NRs/cell were internalized by the cells for 24 h for n = 3 (I,II and III) replicas. P <0.05.

In order to internalize the Fe NRs in the NLCs, the previously optimized NLC manufacturing protocol was carried out (see section 4.2), but with one-step where the NRs were added directly to the lipid emulsion phase. The main physical and chemical characteristics of NLC loaded Fe NRs are shown in the graphics of Fig. 6.4, where the formulations with and without NRs are compared. The particle dimensions are in accordance with the previously obtained in the optimization process (see section 4.4) being 224 ± 5, 239 ± 12 and 236 ± 9 nm for $NLC_{(Gel)}$, $NLC_{(Gel\text{-}DOX)}$ and $NLC_{(Gel\text{-}DOX\text{-}Fe\_NRs)}$ respectively. Unpredictably, the overall diameter in the formulation with the drug and the magnetic core did not increase, what would be expected due to the size of the NRs in the long axis.

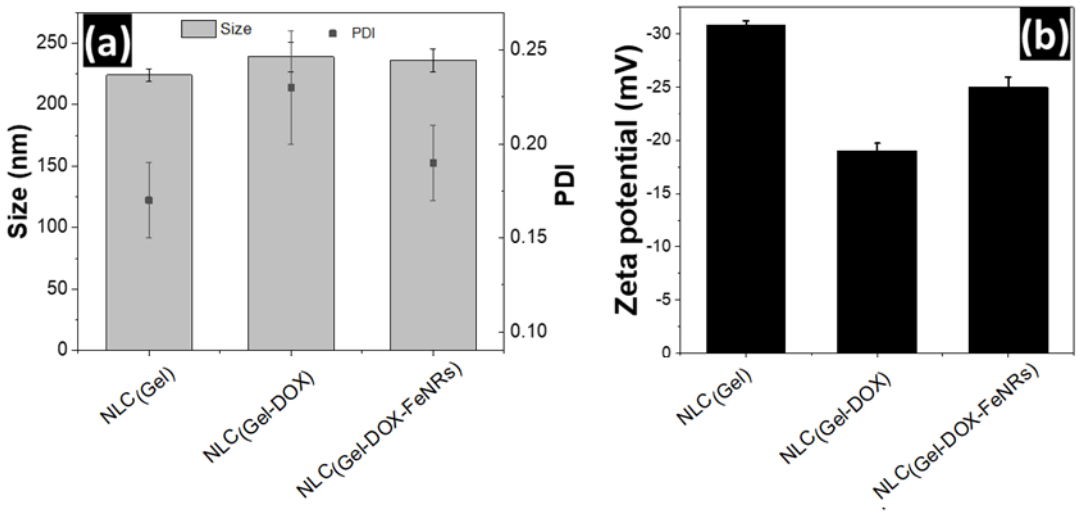

Fig. 6.18: (a) Mean hydrodynamic particle diameter and (b) zeta potential of the produced NLCs.

Transmission electron microscopy (TEM) studies were performed to evaluate the morphological features of the developed formulations. Fig. 6.5 show the TEM images obtained for drug-free NLCs ($NLC_{(Gel)}$), DOX-loaded NLCs ($NLC_{(Gel\text{-}DOX)}$ and $NLC_{(Pal\text{-}DOX\text{-}NRs)}$). All images revealed NLCs keep the spherical shape even with after the NRs incorporation. The average diameters were estimated using the imageJ v1.48 software and the results obtained were 288 ± 66 nm for $NLC_{(Gel)}$, 221 ± 60 nm for $NLC_{(Gel\text{-}DOX)}$ and 244 ± 41 nm for $NLC_{(Gel\text{-}DOX\text{-}NWs)}$ with n = 6. The values obtained are, in agreement with the average diameter obtained by DLS. Figure. 6.5 (c) provides the explanation for the overall size of the NLCs didn´t increase with the incorporation of the NRs; the wires are shorter than they were as prepared. This might happen due to the sonication involved in the preparation of the NLCs that broken the NRs. Thus, a different methodology for the incorporation of NRs in the NLCs should be explored.

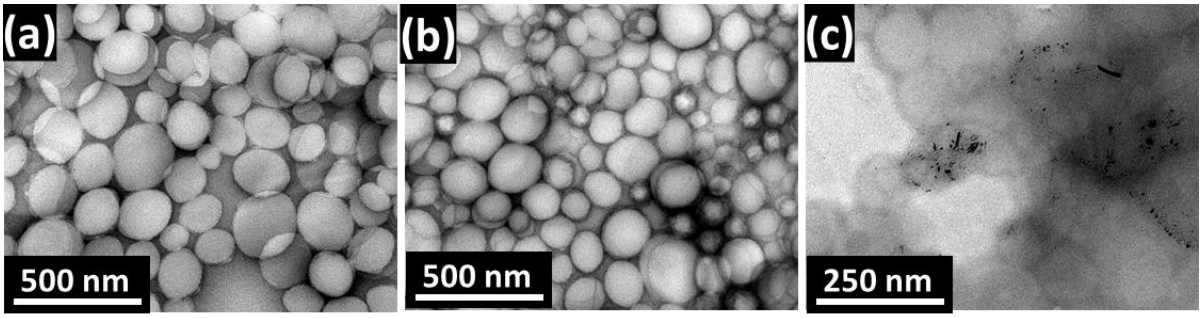

Fig. 6.19: Transmission electron microscopy (TEM) for (a) $NLC_{(Gel)}$, (b) $NLC_{(Gel\text{-}DOX)}$ and (c) $NLC_{(Gel\text{-}DOX\text{-}NRs)}$.

Following these results, new samples are being synthesized in order to continue the optimization of the encapsulation of NRs in NLCs, such as the variation of

parameters such as sonication amplitude time or even the change of strategy, such as the functionalization of the Fe NRs surface and the study of a joint action with drug-loaded NLCs.

6.3 Fe/Au nanorods for magneto-plasmonic cancer therapy

The Fe NRs described in the previous sections can be used for magneto-mechanical cell death applications as already reported, however vortex state nanodics (NDs) can be also very interesting nanostructures for such application [105, 151, 402]. To obtain a vortex state in NDs with 40 nm in diameter (typical diameter of nanostructures obtained by mild anodization of AAO membranes), a thickness of 5 nm is needed, which is very difficult to achieve by electrodeposition methods [402]. Therefore, hard anodization (HA) allows the fabrication of larger pore diameter and greater inter-pore distance favoring the growth of vortex nanostructures. On the other hand, for plasmonic effect, in the literature several studies reported Au nanostructures with different shapes, showing that nanostructures with more complex geometries such as NRs exhibit a shape and dimensional dependence on absorption and scattering. Since NRs can be easily controlled in dimensions and aspect ratio, they can be tunned to improve the absorption efficiency in the near-infrared region (NIR) [403].

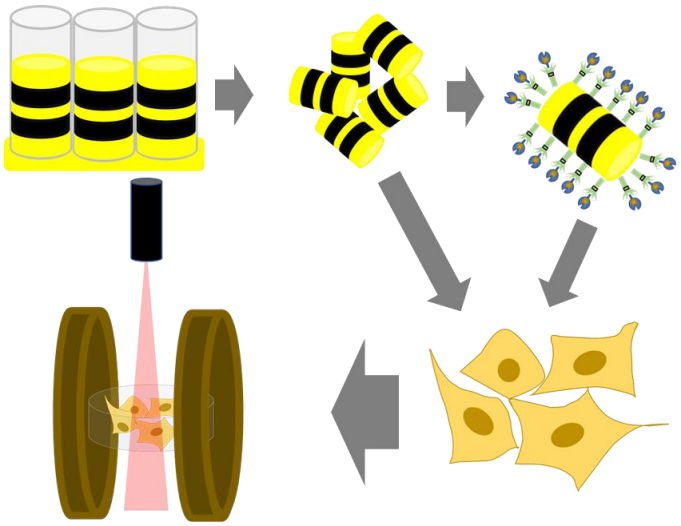

Fig. 6.20: Scheme of segmented Fe/Au NRs production steps for magneto-plasmonic cancer therapy combined with phototherapy.

Figure 6.6 shows the steps of the study of potential applications of segmented Fe/Au NRs in magneto-plasmonic cancer therapy. The NDs were obtained by electrodeposition as shown in section 2.1.1 in AAO by hard anodization (described in

detail in section 2.2.1.2.2). In this approach, after being synthesized and released from the AAO, the NDs biocompatibility and internalization were evaluated. Finally, when internalized by the cells, they would be subjected to a combined magneto-plasmonic technique with an AMF source and a laser source.

The process to obtain AAO membranes by hard anodization was optimized in the framework of this thesis, namely regarding the pore enlargement and deposition rate. SEM images of the optimized membranes are shown in Fig. 6.7 (a) top surface of the AAO grown, (b) surface of the bottom of the AAO after opening the base of the pores and enlargement with a dimension of diameters of such pores have been found to be around 130 nm, with interpore distance of 300 nm and (c) Cross-section of the AAO with a total length of 150 µm.

The Fe and Au NRs presented in this section were deposited by DC electrodeposition using the electrolyte and electrodeposition conditions used in MA membrane (section 2.12), where the cross-sectional images of Fe/Cu nanorods (NRs) grown in AAO membranes show in Fig. 6.7 (d). The average diameter and length of the Fe segments (135 ± 5) nm, (340 ± 25) nm respectively, Au center segment length (50 ± 10) nm.

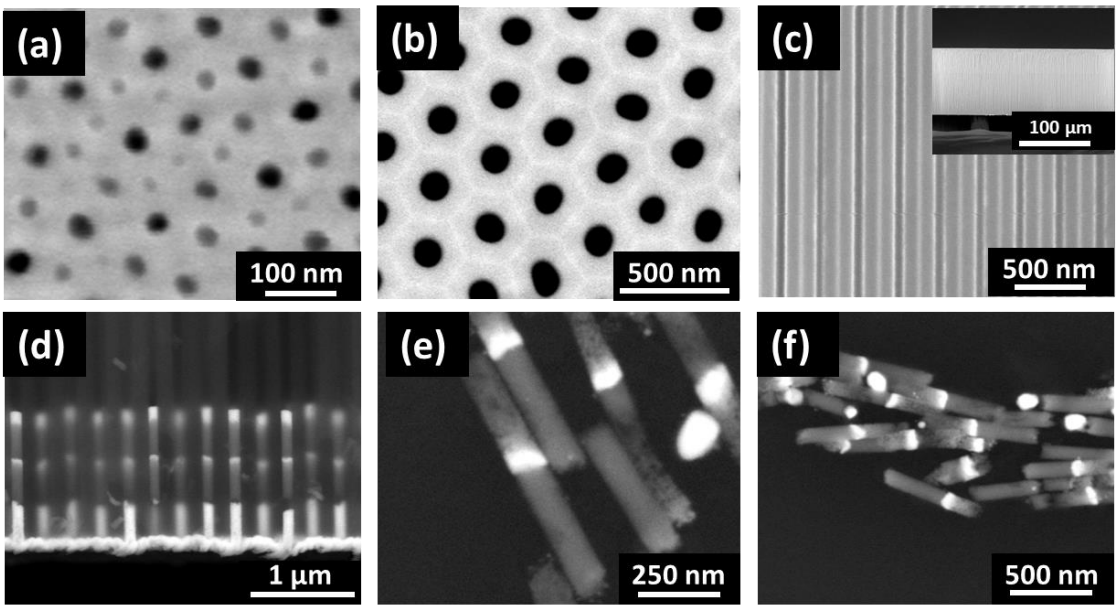

Fig. 6.21: (a) Scanning Electron Microscopy (SEM) image of the top surface of the anodic aluminum oxide (AAO) grown by the hard anodization method, (b) surface of the bottom of the AAO after opening the base of the pores, (c) Cross-section of the AAO with a total length of 150 µm; (d) Cross-sectional images of Fe/Cu nanorods (NRs) grown in AAO membranes and (e) and (f) Surface of the same NRs after removing the AAO.

The removal process was also done by dipping the AAO in $H_2Cr_2O_7$, (0.2 M) and H_3PO_4 (0.4M) at 40 ºC. However, due to the stiffness of the membranes made by hard anodization being lower, the dissolution of the AAO was slower taking a few days, therefore this process needs to be optimized. The NRs was then magnetically rescued and reserved in 99% ethanol. SEM images were obtained using a silicon substrate where a drop of suspended NRs in ethanol was placed followed by air drying (Fig. 6.7 (e) and (f)). The bottom and top of Au segments were broken during removal and washing processes and some Fe segments were also separated, suggesting that the nucleation at the interface of these segments is quite fragile. However, the length of the Fe segments remains like when they were protected by AAO, which suggests low chemical attack to the Fe NRs during the lengthy AAO dissolution process.

Magnetic characterization of the Fe/Au/Fe (340/50/340 nm) NRs were performed as a function of the applied magnetic field and temperature. Hysteresis loops M(H) obtained with temperature ranging from 10 to 330 K and the magnetic field applied in the parallel direction are shown in Fig.6.8 (a). The parallel direction was chosen to perform the measurements at several temperatures since the easy axis of magnetization is parallel to the wire axis. Note that, the diamagnetic signal of the AAO template and the Au segment were subtracted to the sample measurements by data treatment.

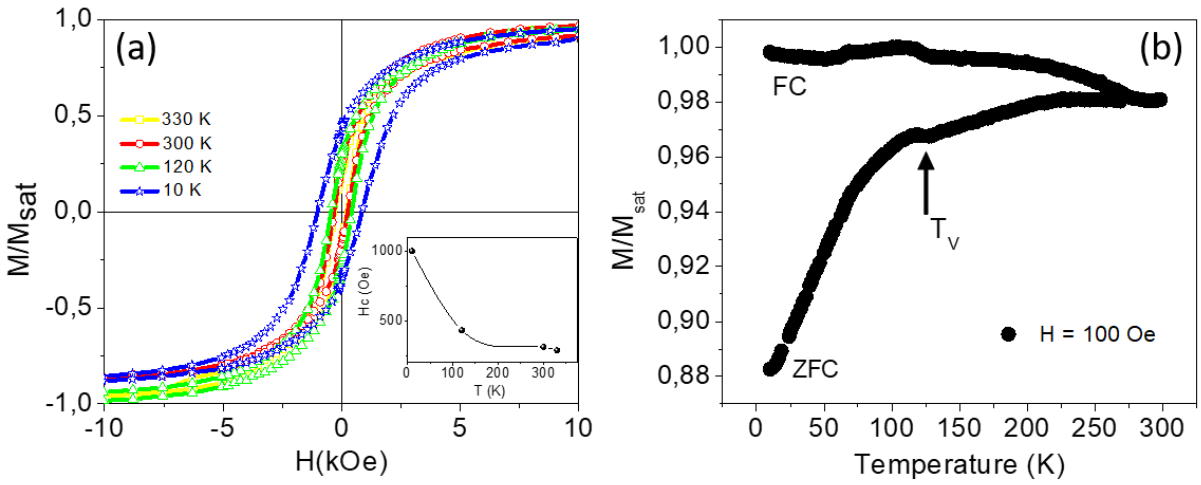

Fig. 6.22: (a) Hysteresis loops measured with the magnetic field applied parallel to the NRs axis at different temperatures and values of coercive field (Hc) as a function of the temperature (inset); (b) Magnetization versus temperature after zero field cooling (ZFC) and field cooling (FC) conditions. Both were taken under a magnetic field of 100Oe where the Verwey (T_V) transition is observed.

The coercivity and squareness (Mr/M_{sat}), i.e., the ratio between remanence and saturation magnetization, decrease as the measurement temperature increases (inset of Fig. 6.8 (a)). Samples at room temperature (300K) and heated to 330 K present an almost isotropic M(H) behavior, whereas by decreasing the temperature until 10 K, the coercivity and squareness increases significantly indicating a well-defined magnetization easy axis parallel to the NR longitudinal axis, evidencing a dominant shape anisotropy.

Figure 6.8 (b) shows the induced magnetization of Fe/Au/Fe (340/50/340 nm) NRs. The measurements were carried out in heating run, after previous cooling down to 5 K with zero field (zero field cooled, ZFC) and under an applied magnetic field of 100 Oe (field cooled, FC). Comparing the FC and ZFC curves, three different features can be observed. Both curves collapse above a temperature Ts ≈ 280 K. Bellow T_S irreversibilities are observed with $M_{ZFC} < M_{FC}$ increasing with decreasing temperature. The ZFC curve shows an initial low magnetization and thereafter increases sharply until it reached a maximum value at T ≈ Ts, that can be associated to the blocking temperature (T_B ≈ 280 K). The Fe/Au/Fe NRs array suggest that a significant competition between short and long-range magnetic interactions takes place in the nanograins presents in the polycrystalline NRs [28]. The transition observed at 121 K can be associated to the Verwey phase transition (T_V) indicating the presence of a magnetite phase due to the partial oxidation of the NRs [404].

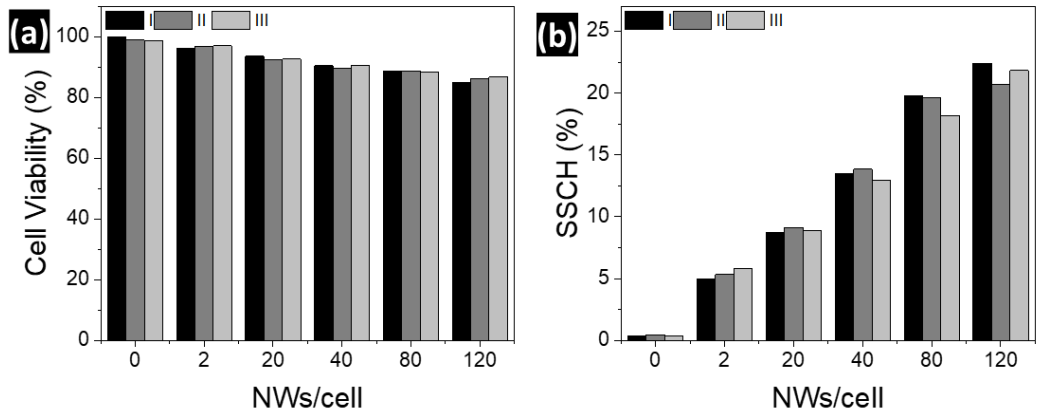

Fig. 6.23: (a) Percentage of cell viability with the number of of Fe/Au/Fe NWs per cell**. (b)** Cellular uptake of the of Fe/Au/Fe NWs in MDA-MB 231 cells line. NWs/cell were internalized by the cells for 24 h for n = 3 (I, II and III) replicas. P <0.05.

The toxicity of the Fe/Au/Fe NRs was also evaluated in MDA-MB 231 cells line, for different concentrations. The results of the cell viability studies are shown in Fig. 6.9 (a). The results show a cell viability above 80% for all concentrations. According to ISO

10993-5, percentages of cell viability above 80% are considered as non-cytotoxicity; within 80% - 60% weak; 60% - 40% moderate and below 40% strong cytotoxicity respectively [28]. Thus, it can be considered that the Fe/Au/Fe NRs were innocuous inside the range of studied concentrations.

The difference in the height of the side scattered light (SSC-H) was measured to infer particle uptake. The results are summarized in Fig. 6.9. As mentioned in the previous section, the analysis of the SSC-H allows for an assessment of the internal complexity or relative granularity, so by comparing these results, it can be seen that the discs were internalized. The smaller differences for higher concentrations of 120 NWs/cell may reveal to be because of some form of saturation. Moreover, when compared with Fe NRs (Fig. 6.3) the Fe/Au/Fe NRs seems to present a higher uptake.

6.4 Conclusions

Porous alumina templates were fabricated using mild and hard anodization methods and used for electrodepositing Fe NRs and Fe/Au segmented NRs. The objective here was to begin operating with a high-aspect ratio NRs and vortex NDs, using the knowledge obtained from the micromagnetic simulations. The magnetic NRs were then analyzed with SQUID but the vortex state was not observable. The electrodeposition process also needs to be optimized and NRs with low lengths need to be deposited to achieve the NDs dimensions (L < D).

Both Fe NRs and Fe/Au NRs were observed to have been internalized in MDA-MB 231 cells. It was observed for Fe/Au NRs that the increase in particle uptake between 80 and 120 discs/cell was small, meaning that we could be reaching a saturation region. None of the concentrations or NRs composition resulted in a cell survivability of less than 80%, which means that the discs are innocuous, without an applied magnetic field. In the future, the discs fabricated would be used to progress the study with cell lines towards the application of magneto-mechanically induced damage.

Chapter 7

Conclusions and Perspectives

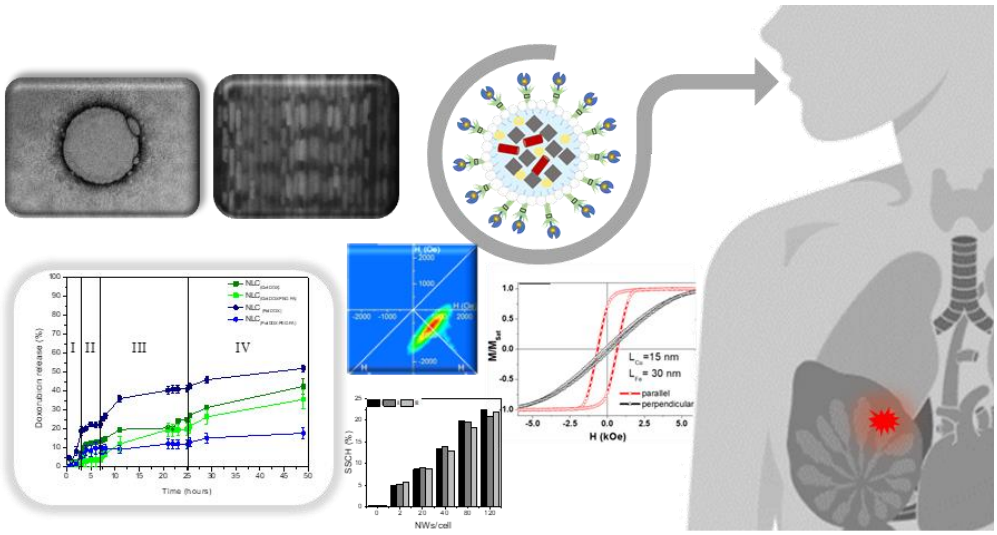

Chapter 7

Conclusions and Perspectives

This thesis is based in a multidisciplinary work that involved two main research lines: (i) the design and optimization of nanostructured lipid carriers (NLC) with encapsulated doxorubicin (DOX) and (ii) development of high aspect ratio magnetic nanostructures namely nanowires (NWs) with tailored dimensions and improved magnetic properties. Besides, superparamagnetic iron oxide nanoparticles (SPIONs) were also loaded in NLC. Both nanostructures were integrated into multifunctional nanocarriers with a magnetic core and a lipid vehicle with a functionalized surface with potential for biomedical applications. Regarding the nanofabrication of magnetic nanostructures, the results show that the pulsed electrodeposition method using a single bath successfully leads to the fabrication of well-controlled multi-segmented NW arrays with magnetic (Fe) and non-magnetic (Cu) segments. The obtained length for the Fe segments was tuned from (30 ± 7) nm to 340 nm, while the Cu segments varied between (15 ± 5) nm and (120 ± 10) nm, up to 20 bilayers with uniform layer thickness. Structural analysis revealed the formation of preferential Fe (110) crystalline directions in a body-centered cubic (bcc) structure. Magnetic measurements demonstrated that the Cu segments' length played a role in the magnetization reversal regimes of the Fe NWs. FORC diagrams were obtained for all samples and showed that for Cu thicknesses of 15 nm, the system behaved like a NW array, while a decoupling of the Fe discs along the axis was observed for Cu spacer lengths greater than 60 nm. Regarding the extracted quantitative parameters, there was a normal distribution of coercivity (750 ± 45 Oe) with a mean interaction field constant k = −800 Oe.

According to our experimental results, we performed micromagnetic simulations in multi-segmented individual NWs with a Fe segment of 40 nm in diameter and 35 nm in length and with the non-magnetic Cu spacer length ranging from 15 to 120 nm. We concluded that the simulated hysteresis loops of one and 15 Fe discs, separated by 120 nm of Cu spacer, were nearly identical, which is in accordance with FORC analysis, where these segmented NWs behaved as a set of 15 non-interacting nanoparticles. On the other hand, the simulations also confirmed our FORC analysis

where the Fe discs, separated by 15 nm of Cu spacer, were strongly coupled and behaved like a homogeneous Fe NW. Regarding the effect of the magnetostatic interactions between NWs, the hysteresis loop showed a drastic dependence on the number of wires for the NWs array with 120 nm of Cu spacer. The normalized remanence was not affected by the wire quantity, but the coercivity was significantly reduced when the number of NWs was increased. From these findings, it is possible to conclude that the micromagnetic model can be used to describe the magnetic behavior of multi-segmented NWs.

Based on these results, another study was carried out involving the variation of the lengths of Fe between (20 ± 5) nm and (300 ± 60) nm, with Cu segments greater than 60 nm, ensuring non-interacting Fe segments. From this study the coercivity in the parallel direction was 84 ± 40 Oe (L_{Fe} = 20 nm) to 890 ± 40 Oe (L_{Fe} = 300nm) showing an increasing behavior as the length of Fe increases, tending to the coercivity of an infinite wire (972 ± 40) Oe. We can also conclude that the 20 nm Fe segment is possibly in a superparamagnetic state, due to its low coercivity and reduced remanence, however for this to be proven, it will be necessary to characterize and study the magnetization curves as a function of temperature (zero-field-cooling (ZFC) and field-cooling (FC)).

To develop multifunctional nanocarriers with the Fe NWs as a magnetic core, NLCs with DOX, were designed and optimized. Also, to selectively deliver the carriers to breast cancer, FA conjugated NLCs were developed aiming for a targeted therapy. The study started with the optimization of the NLC features regarding lipid and surfactant composition, ratio between all components, pH of the aqueous media and experimental conditions. NLCs' characterization in terms of size, surface charge, size distribution, drug loading capacity and encapsulation efficiency show that two formulations with two different types of solid lipids (cetyl palmitate and gelucire) ended up with optimized characteristics for either intravenous or oral administration. The *in vitro* DOX release profile revealed that the developed formulations canbe suitable for oral administration and enable a sustained release that may allow a significant amount of drug to reach cancer cells, where DOX has its therapeutic target. Additionally, the morphological analysis allowed assessing NLCs´ structure and underlining the differences between PEG-FA conjugated and unconjugated NLCs. *In vitro* cellular studies demonstrated the cytotoxic potential of the formulations towards breast cancer cells and the influence of FA conjugation in the intracellular uptake. Taking these *in vitro* studies results, it is possible to realize the FA-PEG-NLCs potential as DOX delivery systems to increase its bioavailability and improve the target therapeutic effectiveness *in situ*, while minimizing the well-known side-effects. From the presented results, it is possible to observe that

both final formulations present overall suitable features to proceed to future studies. However, due to the hemolytic activity, gelucire-based NLCs seem the most promising. Additionally, their low cost and their potential to enable a more convenient route of administration, the oral one, can boost their translation from the bench to the bedside.

Before performing the encapsulation of Fe NWs, superparamagnetic iron oxide nanoparticles were encapsulated in the developed NLCs. SPIONs were obtained by an ultra-sound assisted co-precipitation method and present a spherical shape with an average diameter of approximately 12 ± 3 nm with low size distribution. The characteristic XRD peaks marked by their Bragg indices are in correspondence with Fe_3O_4 phase and the magnetic measurements show a superparamagnetic behavior. After encapsulation in the NLCs with DOX, the final size of the nanoparticles seems not to be significantly affected and shelf stability was achieved for more than 10 weeks. Preliminary results regarding the application of these SPIONs in magnetic fluidic hyperthermia (MFH) showed a specific absorption rate (SAR) of 64 W/g (20 mT and 103 Hz). The temperature variation of 8 ºC in less than 5 min, showsthat SPIONs are potential candidates for MFH treatment.

After chemical removal of the anodic aluminum oxide (AAO) membrane and the Cu layers by chemical etching, the Fe NWs with 40 nm in diameter and 320 ± 50 nm in length were suspended in water. Also, Fe/Au/Fe NWs with 135 nm in diameter and 730 nm in length were also obtained by template-assisted electrodeposition in AAO, removed from the template, and suspended in water. Both NWs were used to test cell viability and cellular uptake, with different concentrations (0, 2, 20, 40, 80, 120 NWs/cell), by flow cytometry. The NWs were observed to have been internalized up to the tested concentration. None of the concentrations resulted in a cell survivability of less than 85%, which means that the discs are innocuous, without an applied magnetic field. Fe NWs was also successfully encapsulated in the NLCs with DOX and functionalized with FA-PEG. In the future, the NWs fabricated can be used to progress the study with cell lines towards the application of magneto-mechanically induced damage combined with DOX release.

This thesis constitutes the basis for the advance of research and the start of new works in the following fields:

- New Fe nanostructures with discs shape will be fabricated to achieve the vortex state and improve the encapsulation in the NLCs.
- Magneto-mechanical cell death experiments will be performed to evaluate the magnetic field and frequency needed to perform the cell death. The drug delivery will be also determined in this condition.

- Evaluation of drug delivery combined with MFH for nanocarriers with SPIONs as a magnetic core.
- Optimization of new formulations of lipid nanoparticles with other drugs or even the combination of drugs.
- Development of formulations with different types of nanoparticles for combined action on the target.

List of Contributions

As part of this thesis, 4 research articles were published in international scientific journals (2 more in preparation) and 2 invited oral presentation, 7 oral presentations and 10 poster communications, which contributed with important scientific improvements and advances, not only in the studies of the physical properties of the nanostructures synthesized for drug delivery, but also in the practical application in cancer therapy. Recognition of the work was also granted by the two awards obtained for the best poster, one of which was at an international conference.

Papers in international scientific periodicals with referees:

- Tuning the magnetic properties of multisegmented Ni/Cu electrodeposited nanowires with controllable Ni lengths, M. Susano, M.P. Proenca, S. Moraes, C.T. Sousa, and J.P. Araujo, Nanotechnology,. 27, (2016), 1-10. DOI: 10.1088/0957-4484/27/33/335301.
- The Role of Cu Length on the Magnetic Behaviour of Fe/Cu Multi-Segmented Nanowires. S. Moraes, D. Navas, F. Béron, M.P. Proenca, K.R. Pirota, C.T.Sousa and J. P. Araújo, Nanomaterials, 8 (2018) 490. doi:10.3390/nano8070490.
- Magnetic nanostructures for emerging biomedical applications, L. Peixoto, R. Magalhães, D. Navas, S. Moraes, C. Redondo, R. Morales,J. P. Araújo, C.T. Sousa, Applied Physics Reviews 7(2020), 011310 doi.org/10.1063/1.5121702.
- Targeted Nanostructured Lipid Carriers for Doxorubicin Oral Delivery, Suellen Moraes; Andreia Marinho; Sofia Lima; Andreia Granja; João P Araújo; Salette Reis; Célia T Sousa; Cláudia Nunes. International Journal of Pharmaceutics, 10(2020), 120029 https://doi.org/10.1016/j.ijpharm.2020.120029

Oral Communications:

- C. Nunes, S. Moraes, F. Soares, S. Lima, M. Horta, R. Leal, C.T. Sousa, S. Reis. Tailoring lipid based nanoparticles to fight cancer. 2nd International Conference on Nanomaterials Applied to Life Sciences 2020 (NALS 2020). 01/2020, Madrid, Spain.
- Magnetic behaviour of Fe/Cu multisegmented nanowires: the influence of non-magnetic layer thickness, S. Moraes*, D. Navas, F. Beron, M. P. Proenca, K. R. Pirota, C. T. Sousa and J. P. Araújo, 17 to 21 June 2019, 10th International Symposium on Metallic Multilayers.Madrid, Spain

- A New Doxorubicin Nanoformulation for Cancer Treatment,. S. Moraes, S. Lima, S. Reis, J. P. Araújo, C. Nunes and C. T. Sousa, SBAN, June 5-6, 2019, Madrid, Spain.
- The role of Cu length on the magnetic behaviour of Fe/Cu multi-segmented nanowires, S. Moraes, D. Navas, F. Béron, M.P. Proenca, K.R. Pirota, C.T. Sousa and J. P. Araújo. XIII EDNANO, 29 August to 01 Setember , 2018, Bristol, England.
- Tuning the magnetic properties of multisegmented Ni/Cu electrodeposited nanowires with controllable Ni lengths. C.T. Sousa, M. Susano, M. Proenca, S. Moraes, J. Araújo 12th International Workshop on Electrodeposited Nanostructures (EDNANO-12), March 15-16, 2017, Bulgary.
- Magnetic nanostructures for biotechnological applications. L. Peixoto, M. Luz, C.T. Sousa, D. Navas, S. Moraes, B. Mora, C. Redondo, R. Morales, J.P. Araújo.11º IJUP, February, 2018 Porto, Portugal.
- Magnetic nanostructures for biotechnological applications. L. Peixoto, C.T. Sousa, M. Luz, D. Navas, S. Moraes, B. Mora, C. Redondo, R. Morales, J.P. Araújo. 3ª Jornadas em Engenharia Física, Física e Astronomia, 18 May, 2018, Porto, Portugal.

Poster Communications:

- Iron-based nanostructures encapsulated in lipid nanoparticles as a multifunctional nanocarriers for doxorubicin controlled delivery, Célia T. Sousa,L. Peixoto, D. Navas, S. Moraes, R. Magalhães, S. Caspani C. Redondo, R. Morales, S. Lima, C. Nunes, S. Reis, J.P. Araújo, 2nd International Conference on Nanomaterials Applied to Life Sciences 2020 (NALS 2020) 29th to 31th January 2020, Madrid, Spain.
- Vortex nano-discs for magneto-mechanically induced damage in cancer cells S. Moraes, S. Lima, S. Reis, J. P. Araújo, C. Nunes, C. T. Sousa, 2nd International Conference on Nanomaterials Applied to Life Sciences 2020 (NALS 2020) 29th to 31th January 2020, Madrid, Spain.
- In the Trail of a New Doxorubicin Nanoformulation Loading Magnetic Nanoparticles, S. Moraes, S. Lima, S. Reis, J. P. Araújo, C. Nunes, C. T. Sousa, 3nd Doctoral Congress in Engineering 27th to 28th of June, 2019 Porto, Portugal.
- Doxorubicin Nanoformulation Loading Magnetic Nanoparticles, S. Moraes, S. Lima, S. Reis, J. P. Araújo, C. Nunes, C. T. Sousa, 3rd COST Action Workshop Brillouin Scattering Microspectroscopy for Biology and Biomedical Research and Applications (“BioBrillouin”), 25-27th September 2019, Faculdade de Ciências da Universidade do Porto, Porto, Portugal.

- Fe Nanowires Encapsulated in Lipid Nanoparticles as a Multifunctional Nanocarriers for Biomedical Applications, S. Moraes, C. T. Sousa, C. Nunes, S. Reis, J. P.Araújo. 3ª Jornadas em Engenharia Física, Física, Física Médica e Astronomia,18 , March 2018, Porto, Portugal.
- Magnetic Nanowires and Nanodiscs Encapsulated in Lipid Nanoparticles as a Mul tifunctional Nanocarriers for Biomedical Applications,S.S.Moraes, C.T.Sousa, J.P.Araújo, C.Nunes, and S. Reis, 1st BioBrillouin Meeting, 13-15 september de 2017, Vienna, Austria.
- High Aspect Ratio Magnetic Nanoparticles as a Multimodal Nanocarriers for Cancer Therapies, S. Moraes, C. T. Sousa, C. Nunes, S. Reis, J. P. Araújo. 2nd Doctoral Congress in Engineering, 08 - 09 June de 2017, Porto, Portugal.
- Magnetic Nanoparticles as a Multimodal Nanocarriers for Cancer Therapies, S. Moraes, C. T. Sousa, J. P. Araújo. 2ª Jornadas em Engenharia Física, Física, Física Médica e Astronomia, 24 March 2017, Porto, Portugal.
- Electrodeposition: A tool to grow tuned nanowires for biomedical and magnetic recording applications. M. P. Proença, C. T. Sousa, S. Moraes, J. Azevedo, J. Ventura and J. P. Araújo IN Institute of Nanoscience and Nanotechnology Workshop, 7 July 2016, IST, Lisboa, Portugal.
- Tuning the magnetic properties of multisegmented Ni/Cu electrodeposited nanowires with controllable Ni lengths M. Susano, C.T. Sousa, M.P. Proença, S. Moraes and J.P. Araújo 11 th International Workshop on Electrodeposited Nanostructures (EDNANO-11), 10-12 September, 2015, Balatonfüred, Hungary.

Best Poster Award

- Iron-based nanostructures encapsulated in lipid nanoparticles as a multifunctional nanocarriers for doxorubicin controlled delivery, Célia T. Sousa,L. Peixoto, D. Navas, S. Moraes, R. Magalhães, S. Caspani C. Redondo, R. Morales, S. Lima, C. Nunes, S. Reis, J.P. Araújo, 2nd International Conference on Nanomaterials Applied to Life Sciences 2020 (NALS 2020) 29th to 31th January 2020, Madrid, Spain.

- High Aspect Ratio Magnetic Nanoparticles as a Multimodal Nanocarriers for Cancer Therapies, S. S. Moraes, C. T. Sousa, C. Nunes, S. Reis, J. P. Araújo. 2ndDoctoral Congress in Engineering 08 e 09 Junho de 2017, Porto, Portugal.

Bibliography

[1] C.T.d. Sousa, Development of Nanoporous Alumina Templates for Biotechnological Applications, Department of Physics and Astronomy Faculty of Sciences, University of Porto 2011.

[2] S. Hossen, M.K. Hossain, M. Basher, M. Mia, M. Rahman, M.J. Uddin, Smart nanocarrier-based drug delivery systems for cancer therapy and toxicity studies: A review, J Journal of advanced research 15 (2019) 1-18.

[3] L. Hajba, A. Guttman, The use of magnetic nanoparticles in cancer theranostics: Toward handheld diagnostic devices, Biotechnology Advances 34(4) (2016) 354-361.

[4] N. Griffete, J. Fresnais, A. Espinosa, C. Wilhelm, A. Bée, C. Ménager, Design of magnetic molecularly imprinted polymer nanoparticles for controlled release of doxorubicin under an alternative magnetic field in athermal conditions, Nanoscale 7(45) (2015) 18891-18896.

[5] Juan Lao, Julia Madani, Teresa Puértolas, María Álvarez, Alba Hernández, Roberto Pazo-Cid, Ángel Artal, A.A. Torres, Liposomal Doxorubicin in the Treatment of Breast Cancer Patients: A Review, Journal of Drug Delivery 2013 (2013) 12.

[6] J. Kreuter, Drug delivery to the central nervous system by polymeric nanoparticles: What do we know?, Advanced Drug Delivery Reviews 71 (2014) 2-14.

[7] N.K. Mehra, S. Palakurthi, Interactions between carbon nanotubes and bioactives: a drug delivery perspective, Drug Discovery Today 21(4) (2016) 585-597.

[8] R.H. Müller, K. Mäder, S. Gohla, Solid lipid nanoparticles (SLN) for controlled drug delivery – a review of the state of the art, European Journal of Pharmaceutics and Biopharmaceutics 50(1) (2000) 161-177.

[9] V.R. Salvi, P. Pawar, Nanostructured lipid carriers (NLC) system: A novel drug targeting carrier, Journal of Drug Delivery Science and Technology 51 (2019) 255-267.

[10] S. Mannucci, L. Ghin, G. Conti, S. Tambalo, A. Lascialfari, T. Orlando, D. Benati, P. Bernardi, N. Betterle, R. Bassi, P. Marzola, A. Sbarbati, Magnetic Nanoparticles from Magnetospirillum gryphiswaldense Increase the Efficacy of Thermotherapy in a Model of Colon Carcinoma, PLOS ONE 9(10) (2014) e108959.

[11] Y. Oh, M.S. Moorthy, P. Manivasagan, S. Bharathiraja, J. Oh, Magnetic hyperthermia and pH-responsive effective drug delivery to the sub-cellular level of human breast cancer cells by modified CoFe2O4 nanoparticles, Biochimie 133 (2017) 7-19.

[12] D.A. LaVan, T. McGuire, R. Langer, Small-scale systems for in vivo drug delivery, Nature Biotechnology 21(10) (2003) 1184-1191.

[13] I. Charlie-Silva, L.F. Fraceto, N.F.S. de Melo, Progress in nano-drug delivery of artemisinin and its derivatives: towards to use in immunomodulatory approaches, Artificial cells, nanomedicine, biotechnology Advances 46(sup3) (2018) S611-S620.

[14] A.D. Bangham, M.M. Standish, J.C. Watkins, Diffusion of univalent ions across the lamellae of swollen phospholipids, Journal of Molecular Biology 13(1) (1965) 238-IN27.

[15] N.D. James, R.J. Coker, D. Tomlinson, J.R.W. Harris, M. Gompels, A.J. Pinching, J.S.W. Stewart, Liposomal doxorubicin (Doxil): An effective new treatment for Kaposi's sarcoma in AIDS, Clinical Oncology 6(5) (1994) 294-296.

[16] M.R. Green, G.M. Manikhas, S. Orlov, B. Afanasyev, A.M. Makhson, P. Bhar, M.J. Hawkins, Abraxane®, a novel Cremophor®-free, albumin-bound particle form of paclitaxel for the treatment of advanced non-small-cell lung cancer, Annals of Oncology 17(8) (2006) 1263-1268.

[17] C.L. Ventola, Progress in nanomedicine: approved and investigational nanodrugs, J Pharmacy Therapeutics 42(12) (2017) 742.

[18] A.C. Anselmo, S. Mitragotri, Nanoparticles in the clinic: An update, Bioengineering Translational Medicine 4(3) (2019) e10143.

[19] Z. Li, Tan, S., Li, S., Shen, Q., Wang, K, Cancer drug delivery in the nano era: An overview and perspectives (Review), Oncology Reports 38(2) (2017) 611-624.

[20] S. Ahadian, J.A. Finbloom, M. Mofidfar, S.E. Diltemiz, F. Nasrollahi, E. Davoodi, V. Hosseini, I. Mylonaki, S. Sangabathuni, H. Montazerian, Micro and nanoscale technologies in oral drug delivery, Advanced Drug Delivery Reviews (2020).

[21] S.B. Dhadde, J.S. Patil, B.N. Chandakavathe, B. Thippeswamy, M.G. Kavatekar, Relevance of Nanotechnology in Solving Oral Drug Delivery Challenges: A Perspective Review, Critical Reviews™ in Therapeutic Drug Carrier Systems 37(5) (2020).

[22] S.J. Son, X. Bai, S.B. Lee, Inorganic hollow nanoparticles and nanotubes in nanomedicine: Part 1. Drug/gene delivery applications, Drug Discovery Today 12(15) (2007) 650-656.

[23] F. Assa, H. Jafarizadeh-Malmiri, H. Ajamein, N. Anarjan, H. Vaghari, Z. Sayyar, A. Berenjian, A biotechnological perspective on the application of iron oxide nanoparticles, Nano Research 9(8) (2016) 2203-2225.

[24] J. Alonso, H. Khurshid, V. Sankar, Z. Nemati, M.H. Phan, E. Garayo, J.A. García, H. Srikanth, FeCo nanowires with enhanced heating powers and controllable dimensions for magnetic hyperthermia, Journal of Applied Physics 117(17) (2015) 17D113.

[25] C.T. Sousa, C. Nunes, M.P. Proença, D.C. Leitão, J.L.F.C. Lima, S. Reis, J.P. Araújo, M. Lúcio, pH sensitive silica nanotubes as rationally designed vehicles for NSAIDs delivery, Colloids and Surfaces B: Biointerfaces 94 (2012) 288-295.

[26] A.O. Fung, V. Kapadia, E. Pierstorff, D. Ho, Y. Chen, Induction of Cell Death by Magnetic Actuation of Nickel Nanowires Internalized by Fibroblasts, The Journal of Physical Chemistry C 112(39) (2008) 15085-15088.

[27] B. Özkale, N. Shamsudhin, G. Chatzipirpiridis, M. Hoop, F. Gramm, X. Chen, X. Martí, J. Sort, E. Pellicer, S. Pané, Multisegmented FeCo/Cu Nanowires: Electrosynthesis, Characterization, and Magnetic Control of Biomolecule Desorption, ACS Applied Materials & Interfaces 7(13) (2015) 7389-7396.

[28] H. Abbas, H. Refai, N. El Sayed, Superparamagnetic iron oxide–loaded lipid nanocarriers incorporated in thermosensitive in situ gel for magnetic brain targeting of clonazepam, Journal of Pharmaceutical Sciences
107(8) (2018) 2119-2127.

[29] S. Sharma, N. Shrivastava, F. Rossi, N.T.K. Thanh, Nanoparticles-based magnetic and photo induced hyperthermia for cancer treatment, J Nano Today 29 (2019) 100795.

[30] E.S. Shibu, M. Hamada, N. Murase, V. Biju, Nanomaterials formulations for photothermal and photodynamic therapy of cancer, Journal of Photochemistry and Photobiology C: Photochemistry Reviews 15 (2013) 53-72.

[31] A. Espinosa, R. Di Corato, J. Kolosnjaj-Tabi, P. Flaud, T. Pellegrino, C. Wilhelm, Duality of Iron Oxide Nanoparticles in Cancer Therapy: Amplification of Heating Efficiency by Magnetic Hyperthermia and Photothermal Bimodal Treatment, ACS Nano 10(2) (2016) 2436-2446.

[32] X. Huang, M.A. El-Sayed, Gold nanoparticles: Optical properties and implementations in cancer diagnosis and photothermal therapy, J Journal of advanced research 1(1) (2010) 13-28.

[33] J. Estelrich, M.A. Busquets, Iron oxide nanoparticles in photothermal therapy, J Molecules 23(7) (2018) 1567.

[34] A.I. Martínez-Banderas, A. Aires, M. Quintanilla, J.A. Holguin-Lerma, C. Lozano-Pedraza, F.J. Teran, J.n.A. Moreno, J.E. Perez, B.S. Ooi, T. Ravasi, Iron-based core–shell nanowires for combinatorial drug delivery and photothermal and magnetic therapy, ACS Applied Materials Interfaces 11(47) (2019) 43976-43988.

[35] K.-C. Li, H.-C. Chu, Y. Lin, H.-Y. Tuan, Y.-C. Hu, PEGylated copper nanowires as a novel photothermal therapy agent, ACS applied materials interfaces 8(19) (2016) 12082-12090.

[36] A. Rajan, N.K. Sahu, Review on magnetic nanoparticle-mediated hyperthermia for cancer therapy, J Journal of Nanoparticle Research 22(11) (2020) 1-25.

[37] C.S.S.R. Kumar, F. Mohammad, Magnetic nanomaterials for hyperthermia-based therapy and controlled drug delivery, Advanced Drug Delivery Reviews 63(9) (2011) 789-808.

[38] V. Nikiforov, Magnetic induction hyperthermia, J Russian Physics Journal 50(9) (2007) 913-924.

[39] P. Lemal, C. Geers, B. Rothen-Rutishauser, M. Lattuada, A. Petri-Fink, Measuring the heating power of magnetic nanoparticles: An overview of currently used methods, Materials Today: Proceedings 4 (2017) S107-S117.

[40] P. Guardia, R. Di Corato, L. Lartigue, C. Wilhelm, A. Espinosa, M. Garcia-Hernandez, F. Gazeau, L. Manna, T. Pellegrino, Water-soluble iron oxide nanocubes with high values of specific absorption rate for cancer cell hyperthermia treatment, J ACS nano 6(4) (2012) 3080-3091.

[41] R.R. Shah, T.P. Davis, A.L. Glover, D.E. Nikles, C.S. Brazel, Impact of magnetic field parameters and iron oxide nanoparticle properties on heat generation for use in magnetic hyperthermia, Journal of magnetism magnetic materials 387 (2015) 96-106.

[42] R.E. Rosensweig, Heating magnetic fluid with alternating magnetic field, Journal of Magnetism and Magnetic Materials 252 (2002) 370-374.

[43] M. Harabech, J. Leliaert, A. Coene, G. Crevecoeur, D. Van Roost, L. Dupré, The effect of the magnetic nanoparticle's size dependence of the relaxation time constant on the specific loss power of magnetic nanoparticle hyperthermia, J Journal of Magnetism Magnetic Materials 426 (2017) 206-210.

[44] N.Ž. Knežević, I. Gadjanski, J.-O. Durand, Magnetic nanoarchitectures for cancer sensing, imaging and therapy, J Journal of Materials Chemistry B 7(1) (2019) 9-23.

[45] W.S. Seo, J.H. Lee, X. Sun, Y. Suzuki, D. Mann, Z. Liu, M. Terashima, P.C. Yang, M.V. McConnell, D.G. Nishimura, FeCo/graphitic-shell nanocrystals as advanced magnetic-resonance-imaging and near-infrared agents, J Nature materials 5(12) (2006) 971-976.

[46] E.L. Verde, G.T. Landi, J.d.A. Gomes, M.H. Sousa, A.F.J.J.o.A.P. Bakuzis, Magnetic hyperthermia investigation of cobalt ferrite nanoparticles: Comparison between experiment, linear response theory, and dynamic hysteresis simulations, 111(12) (2012) 123902.

[47] C.L. Dennis, R. Ivkov, Physics of heat generation using magnetic nanoparticles for hyperthermia, International Journal of Hyperthermia 29(8) (2013) 715-729.

[48] R. Das, J. Alonso, Z. Nemati Porshokouh, V. Kalappattil, D. Torres, M.-H. Phan, E. Garaio, J.A.n. García, J.L. Sanchez Llamazares, H. Srikanth, Tunable high aspect ratio iron oxide nanorods for enhanced hyperthermia, The Journal of Physical Chemistry C 120(18) (2016) 10086-10093.

[49] Z. Nemati, J. Alonso, L. Martinez, H. Khurshid, E. Garaio, J. Garcia, M. Phan, H. Srikanth, Enhanced magnetic hyperthermia in iron oxide nano-octopods: size and anisotropy effects, J The Journal of Physical Chemistry C 120(15) (2016) 8370-8379.

[50] P. Pradhan, J. Giri, G. Samanta, H.D. Sarma, K.P. Mishra, J. Bellare, R. Banerjee, D. Bahadur, Comparative evaluation of heating ability and biocompatibility of different ferrite-based magnetic fluids for hyperthermia application, Journal of Biomedical Materials Research Part B: Applied Biomaterials 81(1) (2007) 12-22.

[51] E.C. Abenojar, S. Wickramasinghe, M. Ju, S. Uppaluri, A. Klika, J. George, W. Barsoum, S.J. Frangiamore, C.A. Higuera-Rueda, A.C.S. Samia, Magnetic glycol chitin-based hydrogel nanocomposite for combined thermal and D-amino-acid-assisted biofilm disruption, ACS infectious diseases 4(8) (2018) 1246-1256.

[52] G.T. Landi, Role of dipolar interaction in magnetic hyperthermia, J Physical Review B 89(1) (2014) 014403.

[53] J. Carrey, B. Mehdaoui, M. Respaud, Simple models for dynamic hysteresis loop calculations of magnetic single-domain nanoparticles: Application to magnetic hyperthermia optimization, Journal of Applied Physics 109(8) (2011) 083921.

[54] R. Tan, J. Carrey, M. Respaud, Magnetic hyperthermia properties of nanoparticles inside lysosomes using kinetic Monte Carlo simulations: Influence of key parameters and dipolar interactions, and evidence for strong spatial variation of heating power, J Physical Review B 90(21) (2014) 214421.

[55] M. Suto, Y. Hirota, H. Mamiya, A. Fujita, R. Kasuya, K. Tohji, B. Jeyadevan, Heat dissipation mechanism of magnetite nanoparticles in magnetic fluid hyperthermia, Journal of Magnetism Magnetic Materials 321(10) (2009) 1493-1496.

[56] A. Roca, B. Wiese, J. Timmis, G. Vallejo-Fernandez, K. O'grady, Effect of frequency and field amplitude in magnetic hyperthermia, J IEEE transactions on magnetics 48(11) (2012) 4054-4057.

[57] W.-K. Fong, T.L. Moore, S. Balog, D. Vanhecke, L. Rodriguez-Lorenzo, B. Rothen-Rutishauser, M. Lattuada, A. Petri-Fink, Nanoparticle Behaviour in Complex Media: Methods for Characterizing Physicochemical Properties, Evaluating Protein Corona Formation, and Implications for Biological Studies, Biological Responses to Nanoscale Particles, Springer2019, pp. 101-150.

[58] S. Del Sol-Fernández, Y. Portilla-Tundidor, L. Gutiérrez, O. Odio, E. Reguera, D.F. Barber, M. Morales, Flower-like Mn-Doped Magnetic Nanoparticles Functionalized with α v β3-Integrin-Ligand to Efficiently Induce Intracellular Heat after Alternating Magnetic Field Exposition, Triggering Glioma Cell Death, ACS Applied Materials & Interfaces
11(30) (2019) 26648-26663.

[59] Z. Hedayatnasab, A. Dabbagh, F. Abnisa, H. Karimian, N.H.A. Kasim, W.M.A.W. Daud, Synthesis, characterization and in vitro analysis of superparamagnetic iron oxide nanoparticles for targeted hyperthermia therapy, J Chemical Papers (2020) 1-11.

[60] X. Hopkins, W.A. Gill, R. Kringel, G. Wang, J. Hass, S. Acharya, J. Park, I.T. Jeon, B.H. An, J.S. Lee, Radio frequency-mediated local thermotherapy for destruction of pancreatic tumors using Ni–Au core–shell nanowires, J Nanotechnology 28(3) (2016) 03LT01.

[61] W.-S. Lin, H.-M. Lin, H.-H. Chen, Y.-K. Hwu, Y.-J. Chiou, Shape Effects of Iron Nanowires on Hyperthermia Treatment, Journal of Nanomaterials 2013 (2013) 237439.

[62] P.W. Egolf, N. Shamsudhin, S. Pané, D. Vuarnoz, J. Pokki, A.-G. Pawlowski, P. Tsague, B. de Marco, W. Bovy, S. Tucev, Hyperthermia with rotating magnetic nanowires inducing heat into tumor by fluid friction, Journal of Applied Physics 120(6) (2016) 064304.

[63] K. Maier-Hauff, F. Ulrich, D. Nestler, H. Niehoff, P. Wust, B. Thiesen, H. Orawa, V. Budach, A. Jordan, Efficacy and safety of intratumoral thermotherapy using magnetic iron-oxide nanoparticles combined with external beam radiotherapy on patients with recurrent glioblastoma multiforme, Journal of neuro-oncology 103(2) (2011) 317-324.

[64] E. Blanco, H. Shen, M. Ferrari, Principles of nanoparticle design for overcoming biological barriers to drug delivery, Nature Biotechnology 33(9) (2015) 941-951.

[65] S. Leulmi, X. Chauchet, M. Morcrette, G. Ortiz, H. Joisten, P. Sabon, T. Livache, Y. Hou, M. Carrière, S. Lequien, B. Dieny, Triggering the apoptosis of targeted human renal cancer cells by the vibration of anisotropic magnetic particles attached to the cell membrane, Nanoscale 7(38) (2015) 15904-15914.

[66] Z. Hartmut, Radiology, Lasers, Nanoparticles and Prosthetics, De Gruyter, Berlin, Boston, 2017.

[67] N. Wang, Review of cellular mechanotransduction, Journal of Physics D: Applied Physics 50(23) (2017) 233002.

[68] R. Mansell, T. Vemulkar, D.C. Petit, Y. Cheng, J. Murphy, M.S. Lesniak, R.P. Cowburn, Magnetic particles with perpendicular anisotropy for mechanical cancer cell destruction, Scientific reports 7(1) (2017) 1-7.

[69] D.W. Wong, W.L. Gan, N. Liu, W.S. Lew, Magneto-actuated cell apoptosis by biaxial pulsed magnetic field, Scientific Reports 7(1) (2017) 10919.

[70] S.W. Lowe, A.W. Lin, Apoptosis in cancer, Carcinogenesis 21(3) (2000) 485-495.

[71] A.I. Martínez-Banderas, A. Aires, F.J. Teran, J.E. Perez, J.F. Cadenas, N. Alsharif, T. Ravasi, A.L. Cortajarena, J. Kosel, Functionalized magnetic nanowires for chemical and magneto-mechanical induction of cancer cell death, Scientific Reports 6(1) (2016) 35786.

[72] E.A. Vitol, V. Novosad, E.A. Rozhkova, Multifunctional Ferromagnetic Disks for Modulating Cell Function, IEEE Transactions on Magnetics 48(11) (2012) 3269-3274.

[73] D.-H. Kim, E.A. Rozhkova, I.V. Ulasov, S.D. Bader, T. Rajh, M.S. Lesniak, V. Novosad, Biofunctionalized magnetic-vortex microdiscs for targeted cancer-cell destruction, Nature Materials 9(2) (2010) 165-171.

[74] D.S. Choi, X. Hopkins, R. Kringel, J. Park, I.T. Jeon, Y. Keun Kim, Magnetically driven spinning nanowires as effective materials for eradicating living cells, Journal of Applied Physics 111(7) (2012) 07B329.

[75] M.F. Contreras, R. Sougrat, A. Zaher, T. Ravasi, J. Kosel, Non-chemotoxic induction of cancer cell death using magnetic nanowires, Int J Nanomedicine 10 (2015) 2141.

[76] M.F. Contreras, Magnetic nanowires as materials for cancer cell destruction, Biological and Environmental Sciences and Engineering (BESE) Division, 2015.

[77] V. Kuperman, Magnetic resonance imaging: physical principles and applications, Elsevier2000.

[78] H. Shokrollahi, Contrast agents for MRI, J Materials Science Engineering: C 33(8) (2013) 4485-4497.

[79] J. Lohrke, T. Frenzel, J. Endrikat, F.C. Alves, T.M. Grist, M. Law, J.M. Lee, T. Leiner, K.-C. Li, K.J.A.i.t. Nikolaou, 25 years of contrast-enhanced MRI: developments, current challenges and future perspectives, 33(1) (2016) 1-28.

[80] J. Wahsner, E.M. Gale, A. Rodríguez-Rodríguez, P. Caravan, Chemistry of MRI contrast agents: current challenges and new frontiers, J Chemical reviews 119(2) (2018) 957-1057.

[81] Y.-D. Xiao, R. Paudel, J. Liu, C. Ma, Z.-S. Zhang, S.-K. Zhou, MRI contrast agents: Classification and application, J International journal of molecular medicine 38(5) (2016) 1319-1326.

[82] T. Lam, P. Pouliot, P.K. Avti, F. Lesage, A.K. Kakkar, Superparamagnetic iron oxide based nanoprobes for imaging and theranostics, J Advances in colloid interface science 199 (2013) 95-113.

[83] C.C. Berry, A.S. Curtis, Functionalisation of magnetic nanoparticles for applications in biomedicine, Journal of physics D: Applied physics 36(13) (2003) R198.

[84] N.J. Hobson, X. Weng, B. Siow, C. Veiga, M. Ashford, N.T. Thanh, A.G. Schätzlein, I.F. Uchegbu, Clustering superparamagnetic iron oxide nanoparticles produces organ-targeted high-contrast magnetic resonance images, J Nanomedicine 14(9) (2019) 1135-1152.

[85] J.S. Michael, B.-S. Lee, M. Zhang, J.S. Yu, Nanotechnology for Treatment of Glioblastoma Multiforme, J Transl Int Med 6(3) (2018) 128-133.

[86] A. Arrott, B. Heinrich, A. Aharoni, Point singularities and magnetization reversal in ideally soft ferromagnetic cylinders, IEEE Transactions on Magnetics 15(5) (1979) 1228-1235.

[87] E. Frei, S. Shtrikman, D. Treves, Critical size and nucleation field of ideal ferromagnetic particles, J Physical Review 106(3) (1957) 446.

[88] E. Stoner, E. Wohlfarth, A mechanism of magnetic hysteresis in heterogeneous alloys, J IEEE Transactions on Magnetics 27(4) (1991) 3475-3518.

[89] R.M. Fratila, S. Rivera-Fernández, M. Jesús, Shape matters: synthesis and biomedical applications of high aspect ratio magnetic nanomaterials, J Nanoscale 7(18) (2015) 8233-8260.

[90] D. Shore, S.L. Pailloux, J. Zhang, T. Gage, D.J. Flannigan, M. Garwood, V.C. Pierre, B.J.J.C.C. Stadler, Electrodeposited Fe and Fe–Au nanowires as MRI contrast agents, 52(85) (2016) 12634-12637.

[91] P.C. Naha, A. Al Zaki, E. Hecht, M. Chorny, P. Chhour, E. Blankemeyer, D.M. Yates, W.R. Witschey, H.I. Litt, A. Tsourkas, Dextran coated bismuth–iron oxide nanohybrid contrast agents for computed tomography and magnetic resonance imaging, J Journal of Materials Chemistry B 2(46) (2014) 8239-8248.

[92] D. Bates, S. Abraham, M. Campbell, I. Zehbe, L. Curiel, Development and characterization of an antibody-labeled super-paramagnetic iron oxide contrast agent targeting prostate cancer cells for magnetic resonance imaging, PLoS One 9(5) (2014).

[93] C. Kaittanis, T.M. Shaffer, A. Ogirala, S. Santra, J.M. Perez, G. Chiosis, Y. Li, L. Josephson, J. Grimm, Environment-responsive nanophores for therapy and treatment monitoring via molecular MRI quenching, J Nature communications 5(1) (2014) 1-11.

[94] C. Fang, K. Wang, Z.R. Stephen, Q. Mu, F.M. Kievit, D.T. Chiu, O.W. Press, M. Zhang, Temozolomide nanoparticles for targeted glioblastoma therapy, J ACS applied materials interfaces
7(12) (2015) 6674-6682.

[95] D. Li, X. Tang, B. Pulli, C. Lin, P. Zhao, J. Cheng, Z. Lv, X. Yuan, Q. Luo, H. Cai, Theranostic nanoparticles based on bioreducible polyethylenimine-coated iron oxide for reduction-responsive gene delivery and magnetic resonance imaging, Int J Nanomedicine 9 (2014) 3347.

[96] J. Kolosnjaj-Tabi, R. Di Corato, L. Lartigue, I. Marangon, P. Guardia, A.K. Silva, N. Luciani, O. Clement, P. Flaud, J.V. Singh, Heat-generating iron oxide nanocubes: subtle "destructurators" of the tumoral microenvironment, J ACS nano 8(5) (2014) 4268-4283.

[97] D.K. Kirui, D.A. Rey, C.A. Batt, Gold hybrid nanoparticles for targeted phototherapy and cancer imaging, J Nanotechnology 21(10) (2010) 105105.

[98] M. Nafiujjaman, V. Revuri, M. Nurunnabi, K.J. Cho, Y.-k. Lee, Photosensitizer conjugated iron oxide nanoparticles for simultaneous in vitro magneto-fluorescent imaging guided photodynamic therapy, J Chemical Communications 51(26) (2015) 5687-5690.

[99] R.A. Revia, M. Zhang, Magnetite nanoparticles for cancer diagnosis, treatment, and treatment monitoring: recent advances, Materials Today 19(3) (2016) 157-168.

[100] P.C. Pinheiro, C.T. Sousa, J.P. Araújo, A.J. Guiomar, T. Trindade, Functionalization of nickel nanowires with a fluorophore aiming at new probes for multimodal bioanalysis, Journal of Colloid and Interface Science 410 (2013) 21-26.

[101] A. Espinosa, J. Reguera, A. Curcio, Á. Muñoz-Noval, C. Kuttner, A. Van de Walle, L.M. Liz-Marzán, C. Wilhelm, Janus Magnetic-Plasmonic Nanoparticles for Magnetically Guided and Thermally Activated Cancer Therapy, J Small Science 16(11) (2020) 1904960.

[102] K. Hayashi, A. Tokuda, J. Nakamura, A. Sugawara-Narutaki, C. Ohtsuki, Tearable and Fillable Composite Sponges Capable of Heat Generation and Drug Release in Response to Alternating Magnetic Field, J Materials 13(16) (2020) 3637.

[103] M.-M. Song, W.-J. Song, H. Bi, J. Wang, W.-L. Wu, J. Sun, M. Yu, Cytotoxicity and cellular uptake of iron nanowires, Biomaterials 31(7) (2010) 1509-1517.

[104] D.H. Reich, M. Tanase, A. Hultgren, L.A. Bauer, C.S. Chen, G.J. Meyer, Biological applications of multifunctional magnetic nanowires (invited), 93(10) (2003) 7275-7280.

[105] C. Naud, C. Thébault, M. Carrière, Y. Hou, R. Morel, F. Berger, B. Diény, H. Joisten, Cancer treatment by magneto-mechanical effect of particles, a review, Nanoscale Advances 2(9) (2020) 3632-3655.

[106] L.H. Reddy, J.L. Arias, J. Nicolas, P. Couvreur, Magnetic nanoparticles: design and characterization, toxicity and biocompatibility, pharmaceutical and biomedical applications, J Chemical reviews 112(11) (2012) 5818-5878.

[107] H. Soo Choi, W. Liu, P. Misra, E. Tanaka, J.P. Zimmer, B. Itty Ipe, M.G. Bawendi, J.V. Frangioni, Renal clearance of quantum dots, Nature Biotechnology 25(10) (2007) 1165-1170.

[108] F. Braet, E. Wisse, P. Bomans, P. Frederik, W. Geerts, A. Koster, L. Soon, S. Ringer, Contribution of high-resolution correlative imaging techniques in the study of the liver sieve in three-dimensions, Microscopy research and technique 70(3) (2007) 230-42.

[109] S.K. Hobbs, W.L. Monsky, F. Yuan, W.G. Roberts, L. Griffith, V.P. Torchilin, R.K. Jain, Regulation of transport pathways in tumor vessels: Role of tumor type and microenvironment, Proceedings of the National Academy of Sciences 95(8) (1998) 4607-4612.

[110] L.T. Chen, L. Weiss, The role of the sinus wall in the passage of erythrocytes through the spleen, Blood 41(4) (1973) 529-37.

[111] Y. Geng, P. Dalhaimer, S. Cai, R. Tsai, M. Tewari, T. Minko, D.E. Discher, Shape effects of filaments versus spherical particles in flow and drug delivery, Nature Nanotechnology 2(4) (2007) 249-255.

[112] C.T. Sousa, D.C. Leitao, J. Ventura, P.B. Tavares, J.P. Araújo, A versatile synthesis method of dendrites-free segmented nanowires with a precise size control, J Nanoscale research letters 7(1) (2012) 1-7.

[113] M. Susano, M.P. Proenca, S. Moraes, C.T. Sousa, J.P. Araújo, Tuning the magnetic properties of multisegmented Ni/Cu electrodeposited nanowires with controllable Ni lengths, Nanotechnology 27(33) (2016) 335301.

[114] J.M. Coey, Magnetism and magnetic materials, Cambridge university press2010.

[115] M.P. Proenca, C.T. Sousa, J. Ventura, J. Garcia, M. Vazquez, J.P. Araujo, Identifying weakly-interacting single domain states in Ni nanowire arrays by FORC, Journal of Alloys and Compounds 699 (2017) 421-429.

[116] J. Escrig, M. Daub, P. Landeros, K. Nielsch, D. Altbir, Angular dependence of coercivity in magnetic nanotubes, J Nanotechnology 18(44) (2007) 445706.

[117] Q.A. Pankhurst, J. Connolly, S.K. Jones, J. Dobson, Applications of magnetic nanoparticles in biomedicine, J Journal of physics D: Applied physics 36(13) (2003) R167.

[118] L. Néel, Thermoremanent magnetization of fine powders, J Reviews of Modern Physics 25(1) (1953) 293.

[119] J. Sherwood, Shape dependent iron oxide nanoparticles for simultaneous imaging and therapy, University of Alabama Libraries, 2018.

[120] M. Vazquez, C. Luna, M. Morales, R. Sanz, C. Serna, C. Mijangos, Magnetic nanoparticles: synthesis, ordering and properties, J Physica B: Condensed Matter 354(1-4) (2004) 71-79.

[121] C. Xu, S. Sun, Monodisperse magnetic nanoparticles for biomedical applications, Polymer International 56(7) (2007) 821-826.

[122] V.F. Cardoso, A. Francesko, C. Ribeiro, M. Bañobre-López, P. Martins, S. Lanceros-Mendez, Advances in magnetic nanoparticles for biomedical applications, Advanced healthcare materials 7(5) (2018) 1700845.

[123] B.D. Plouffe, S.K. Murthy, L.H. Lewis, Fundamentals and application of magnetic particles in cell isolation and enrichment: a review, J Reports on Progress in Physics 78(1) (2014) 016601.

[124] A. Guimaraes, Nano-science and technology: principles of nanomagnetism, Springer-Verlag Berlin Heidelberg: Wiley-IEEE Press, 2009.

[125] R.M. Fratila, S. Rivera-Fernández, J.M. de la Fuente, Shape matters: synthesis and biomedical applications of high aspect ratio magnetic nanomaterials, Nanoscale 7(18) (2015) 8233-8260.

[126] E.H. Frei, S. Shtrikman, D. Treves, Critical Size and Nucleation Field of Ideal Ferromagnetic Particles, Physical Review 106(3) (1957) 446-455.

[127] E.C. Stoner, E.P. Wohlfarth, A mechanism of magnetic hysteresis in heterogeneous alloys, Philosophical Transactions of the Royal Society of London. Series A, Mathematical and Physical Sciences 240(826) (1948) 599-642.

[128] S. Moraes, D. Navas, F. Béron, P.M. Proenca, R.K. Pirota, T.C. Sousa, P.J. Araújo, The Role of Cu Length on the Magnetic Behaviour of Fe/Cu Multi-Segmented Nanowires, Nanomaterials 8(7) (2018).

[129] S. Ishrat, K. Maaz, K.-J. Lee, M.-H. Jung, G.-H. Kim, Fabrication and temperature-dependent magnetic properties of one-dimensional multilayer Au–Ni–Au–Ni–Au nanowires, Journal of Solid State Chemistry 210(1) (2014) 116-120.

[130] L.-F. Liu, W.-Y. Zhou, S.-S. Xie, O. Albrecht, K. Nielsch, Microstructure and temperature-dependent magnetic properties of Co/Pt multilayered nanowires, Chemical Physics Letters 466(4) (2008) 165-169.

[131] T. Böhnert, A.C. Niemann, A.-K. Michel, S. Bäßler, J. Gooth, B.G. Tóth, K. Neuróhr, L. Péter, I. Bakonyi, V. Vega, V.M. Prida, K. Nielsch, Magnetothermopower and magnetoresistance of single Co-Ni/Cu multilayered nanowires, Physical Review B 90(16) (2014) 165416.

[132] R. Ferré, K. Ounadjela, J.M. George, L. Piraux, S. Dubois, Magnetization processes in nickel and cobalt electrodeposited nanowires, Physical Review B 56(21) (1997) 14066-14075.

[133] S. Pal, S. Saha, D. Polley, A. Barman, Magnetization reversal dynamics in Co nanowires with competing magnetic anisotropies, Solid State Communications 151(24) (2011) 1994-1998.

[134] A. Elmekawy, E. Iashina, I. Dubitskiy, S. Sotnichuk, I. Bozhev, D. Kozlov, K. Napolskii, D. Menzel, A. Mistonov, Magnetic properties of ordered arrays of iron nanowires: The impact of the length, Journal of Magnetism Magnetic Materials 532 (2021) 167951.

[135] L.-P. Carignan, C. Lacroix, A. Ouimet, M. Ciureanu, A. Yelon, D. Ménard, Magnetic anisotropy in arrays of Ni, CoFeB, and Ni/Cu nanowires, Journal of Applied Physics 102(2) (2007) 023905.

[136] D.C. Leitao, A.V. Silva, R. Ferreira, E. Paz, F.L. Deepack, S. Cardoso, P.P. Freitas, Linear nanometric tunnel junction sensors with exchange pinned sensing layer, Journal of Applied Physics 115(17) (2014) 17E526.

[137] D.C. Leitao, J. Ventura, C.T. Sousa, A.M. Pereira, J.B. Sousa, M. Vazquez, J.P. Araujo, Insights into the role of magnetoelastic anisotropy in the magnetization reorientation of magnetic nanowires, Physical Review B 84(1) (2011) 014410.

[138] I.D. Mayergoyz, Mathematical Models of Hysteresis, Physical Review Letters 56(15) (1986) 1518-1521.

[139] C.R. Pike, A.P. Roberts, K.L. Verosub, Characterizing interactions in fine magnetic particle systems using first order reversal curves, Journal of Applied Physics 85(9) (1999) 6660-6667.

[140] M.A. Valdez-Grijalva, A.R. Muxworthy, W. Williams, P. Ó Conbhuí, L. Nagy, A.P. Roberts, D. Heslop, Magnetic vortex effects on first-order reversal curve (FORC) diagrams for greigite dispersions, Earth and Planetary Science Letters 501 (2018) 103-111.

[141] C. Pike, A. Fernandez, An investigation of magnetic reversal in submicron-scale Co dots using first order reversal curve diagrams, Journal of Applied Physics 85(9) (1999) 6668-6676.

[142] C.R. Pike, C.A. Ross, R.T. Scalettar, G. Zimanyi, First-order reversal curve diagram analysis of a perpendicular nickel nanopillar array, Physical Review B 71(13) (2005) 134407.

[143] M.V. Vaganov, J. Linke, S. Odenbach, Y.L. Raikher, Model FORC diagrams for hybrid magnetic elastomers, Journal of Magnetism and Magnetic Materials 431 (2017) 130-133.

[144] F. Beron, L. Clime, M. Ciureanu, D. Menard, R.W. Cochrane, A. Yelon, First-Order Reversal Curves Diagrams of Ferromagnetic Soft Nanowire Arrays, IEEE Transactions on Magnetics 42(10) (2006) 3060-3062.

[145] E. Jafari-Khamse, M. Almasi Kashi, A. Ramazani, First-order-reversal-curve (FORC) diagrams of alternative chain of soft/ hard magnetic CoFe/Cu multilayer nanowires, Current Applied Physics 16(4) (2016) 486-496.

[146] C.R. Pike, First-order reversal-curve diagrams and reversible magnetization, Physical Review B 68(10) (2003) 104424.

[147] F. Beron, L.P. Carignan, D. Menard, A. Yelon, Extracting Individual Properties from Global Behaviour: First-Order Reversal Curve Method Applied to Magnetic Nanowire Arrays, ChemInform 44(43) (2013) no-no.

[148] N. Lupu, Electrodeposited nanowires and their applications, BoD–Books on Demand2010.

[149] E. Torre, Effect of interaction on the magnetization of single-domain particles, IEEE Transactions on Audio Electroacoustics 14(2) (1966) 86-92.

[150] T. Shinjo, T. Okuno, R. Hassdorf, K. Shigeto, T. Ono, Magnetic vortex core observation in circular dots of permalloy, J Science 289(5481) (2000) 930-932.

[151] L. Peixoto, R. Magalhães, D. Navas, S. Moraes, C. Redondo, R. Morales, J.P. Araújo, C.T. Sousa, Magnetic nanostructures for emerging biomedical applications, Applied Physics Reviews 7(1) (2020) 011310.

[152] K.Y. Guslienko, V. Novosad, Y. Otani, H. Shima, K. Fukamichi, Field evolution of magnetic vortex state in ferromagnetic disks, Applied Physics Letters 78(24) (2001) 3848-3850.

[153] R.P. Cowburn, D.K. Koltsov, A.O. Adeyeye, M.E. Welland, D.M. Tricker, Single-Domain Circular Nanomagnets, Physical Review Letters 83(5) (1999) 1042-1045.

[154] M. Schneider, H. Hoffmann, S. Otto, T. Haug, J. Zweck, Stability of magnetic vortices in flat submicron permalloy cylinders, Journal of Applied Physics 92(3) (2002) 1466-1472.

[155] A.L. Koh, W. Hu, R.J. Wilson, S.X. Wang, R. Sinclair, Preparation, structural and magnetic characterization of synthetic anti-ferromagnetic (SAF) nanoparticles, Philosophical Magazine 88(36) (2008) 4225-4241.

[156] B. Schoeman, J. Sterte, J.-E. Otterstedt, Colloidal zeolite suspensions, J Zeolites 14(2) (1994) 110-116.

[157] Hamley, Ordering in thin films of block copolymers: Fundamentals to potential applications, Progress in polymer science 34(11) (2009) 1161-1210.

[158] J. Yao, Z. Liu, Y. Liu, Y. Wang, C. Sun, G. Bartal, A.M. Stacy, X. Zhang, Optical negative refraction in bulk metamaterials of nanowires, J Science 321(5891) (2008) 930-930.

[159] W. Li, J. Zhang, T. Shen, G.A. Jones, P.J. Grundy, Magnetic nanowires fabricated by anodic aluminum oxide template—a brief review, Science China Physics, Mechanics and Astronomy 54(7) (2011) 1181-1189.

[160] K. Nielsch, F. Müller, A.P. Li, U. Gösele, Uniform Nickel Deposition into Ordered Alumina Pores by Pulsed Electrodeposition, Advanced Materials 12(8) (2000) 582-586.

[161] H. Masuda, H. Asoh, M. Watanabe, K. Nishio, M. Nakao, T. Tamamura, Square and Triangular Nanohole Array Architectures in Anodic Alumina, Advanced Materials 13(3) (2001) 189-192.

[162] C.T. Sousa, D.C. Leitao, M.P. Proenca, J. Ventura, A.M. Pereira, J.P. Araujo, Nanoporous alumina as templates for multifunctional applications, Appl. Phys. Rev. 1(3) (2014) 031102.

[163] F. Li, L. Zhang, R.M. Metzger, On the Growth of Highly Ordered Pores in Anodized Aluminum Oxide, Chemistry of Materials 10(9) (1998) 2470-2480.

[164] P. Skeldon, K. Shimizu, G.E. Thompson, G.C. Wood, Fundamental studies elucidating anodic barrier-type film growth on aluminium, Thin Solid Films 123(2) (1985) 127-133.

[165] J.C.A.M. Azevedo, Preparation and Characterization of Photoanodes of Hematite Nanostructures for Solar Water Splitting Applications, Department of Physics and Astronomy, Faculty of Sciences of the University of Porto, 2011, p. 137.

[166] J.W. Diggle, T.C. Downie, C. Goulding, Anodic oxide films on aluminum, Chemical Reviews 69(3) (1969) 365-405.

[167] R. Wehrspohn, A. Li, K. Nielsch, F. Müller, W. Erfurth, U. Gösele, Highly ordered alumina films: pore growth and applications, Electrochem. Soc. Proc, 2000, pp. 271-282.

[168] W. Lee, R. Ji, U. Gösele, K. Nielsch, Fast fabrication of long-range ordered porous alumina membranes by hard anodization, Nature Materials 5(9) (2006) 741-747.

[169] Y.D.a.Z. Gamburg, Giovanni, Theory and Practice of Metal Electrodeposition, Springer New York2011.

[170] S. Shidhaye, R. Vaidya, S. Sutar, A. Patwardhan, V. Kadam, Solid lipid nanoparticles and nanostructured lipid carriers-innovative generations of solid lipid carriers, J Current drug delivery 5(4) (2008) 324-331.

[171] S.A. Belachew, D.A. Erku, A.B. Mekuria, B.M. Gebresillassie, Pattern of chemotherapy-related adverse effects among adult cancer patients treated at Gondar University Referral Hospital, Ethiopia: A cross-sectional study, Drug, healthcare patient safety 8 (2016) 83.

[172] M. Haider, S.M. Abdin, L. Kamal, G. Orive, Nanostructured lipid carriers for delivery of chemotherapeutics: A review, Pharmaceutics 12(3) (2020) 288.

[173] K.K. Sawant, S.S. Dodiya, Recent advances and patents on solid lipid nanoparticles, J Recent patents on drug delivery formulation 2(2) (2008) 120-135.

[174] R.H. Müller, K. Mäder, S. Gohla, Solid lipid nanoparticles (SLN) for controlled drug delivery–a review of the state of the art, European Journal of Pharmaceutics 50(1) (2000) 161-177.

[175] C. Zylberberg, S. Matosevic, Pharmaceutical liposomal drug delivery: a review of new delivery systems and a look at the regulatory landscape, J Drug Delivery 23(9) (2016) 3319-3329.

[176] R. H Muller, R. Shegokar, C. M Keck, 20 years of lipid nanoparticles (SLN & NLC): present state of development & industrial applications, J Current drug discovery technologies 8(3) (2011) 207-227.

[177] C. Tapeinos, M. Battaglini, G. Ciofani, Advances in the design of solid lipid nanoparticles and nanostructured lipid carriers for targeting brain diseases, Journal of Controlled Release 264 (2017) 306-332.

[178] K. Jores, W. Mehnert, K. Mäder, Physicochemical investigations on solid lipid nanoparticles and on oil-loaded solid lipid nanoparticles: a nuclear magnetic resonance and electron spin resonance study, J Pharmaceutical research 20(8) (2003) 1274-1283.

[179] G. Abdelbary, M. Haider, In vitro characterization and growth inhibition effect of nanostructured lipid carriers for controlled delivery of methotrexate, Pharmaceutical development technology 18(5) (2013) 1159-1168.

[180] R. Müller, M. Radtke, S. Wissing, Nanostructured lipid matrices for improved microencapsulation of drugs, International journal of pharmaceutics 242(1-2) (2002) 121-128.

[181] W. Mehnert, K. Mäder, Solid lipid nanoparticles: production, characterization and applications, J Advanced drug delivery reviews 64 (2012) 83-101.

[182] L. Battaglia, M. Gallarate, Lipid nanoparticles: State of the art, new preparation methods and challenges in drug delivery, Expert opinion on drug delivery 9 (2012) 497-508.

[183] V.R. Salvi, P. Pawar, Nanostructured lipid carriers (NLC) system: A novel drug targeting carrier, J Journal of Drug Delivery Science Technology 51 (2019) 255-267.

[184] R.H. Müller, M. Radtke, S.A. Wissing, Solid lipid nanoparticles (SLN) and nanostructured lipid carriers (NLC) in cosmetic and dermatological preparations, Advanced drug delivery reviews 54 (2002) S131-S155.

[185] K.W. Kasongo, M. Jansch, R.H. Müller, R.B. Walker, Evaluation of the in vitro differential protein adsorption patterns of didanosine-loaded nanostructured lipid carriers (NLCs) for potential targeting to the brain, J Journal of liposome research
21(3) (2011) 245-254.

[186] T. Waghule, V.K. Rapalli, S. Gorantla, R.N. Saha, S.K. Dubey, A. Puri, G. Singhvi, Nanostructured lipid carriers as potential drug delivery systems for skin disorders, J Current Pharmaceutical Design (2020).

[187] M.L. Bondì, E.F. Craparo, G. Giammona, M. Cervello, A. Azzolina, P. Diana, A. Martorana, G. Cirrincione, Nanostructured lipid carriers-containing anticancer compounds: preparation, characterization, and cytotoxicity studies, Drug Delivery 14(2) (2007) 61-67.

[188] Y.-P. Fang, Y.-K. Lin, Y.-H. Su, J.-Y. Fang, Tryptanthrin-loaded nanoparticles for delivery into cultured human breast cancer cells, MCF7: the effects of solid lipid/liquid lipid ratios in the inner core, J Chemical Pharmaceutical Bulletin
59(2) (2011) 266-271.

[189] Y. Wang, H. Zhang, J. Hao, B. Li, M. Li, W. Xiuwen, Lung cancer combination therapy: co-delivery of paclitaxel and doxorubicin by nanostructured lipid carriers for synergistic effect, Drug delivery 23(4) (2016) 1398-1403.

[190] M. Sabzichi, N. Samadi, J. Mohammadian, H. Hamishehkar, M. Akbarzadeh, O. Molavi, Sustained release of melatonin: A novel approach in elevating efficacy of tamoxifen in breast cancer treatment, J Colloids Surfaces B: Biointerfaces 145 (2016) 64-71.

[191] E. Souto, R. Müller, Investigation of the factors influencing the incorporation of clotrimazole in SLN and NLC prepared by hot high-pressure homogenization, Journal of microencapsulation 23(4) (2006) 377-388.

[192] M. Cirri, L. Maestrini, F. Maestrelli, N. Mennini, P. Mura, C. Ghelardini, L. Di Cesare Mannelli, Design, characterization and in vivo evaluation of nanostructured lipid carriers (NLC) as a new drug delivery system for hydrochlorothiazide oral administration in pediatric therapy, Drug delivery 25(1) (2018) 1910-1921.

[193] P. Carvajal-Vidal, M.-J. Fábrega, M. Espina, A.C. Calpena, M.L. García, Development of Halobetasol-loaded nanostructured lipid carrier for dermal administration: Optimization, physicochemical and biopharmaceutical behavior, and therapeutic efficacy, Nanomedicine: Nanotechnology, Biology and Medicine
20 (2019) 102026.

[194] A. Chinsriwongkul, P. Chareanputtakhun, T. Ngawhirunpat, T. Rojanarata, W. Sila-on, U. Ruktanonchai, P. Opanasopit, Nanostructured lipid carriers (NLC) for parenteral delivery of an anticancer drug, Aaps Pharmscitech 13(1) (2012) 150-158.

[195] C. Carbone, A. Campisi, D. Manno, A. Serra, M. Spatuzza, T. Musumeci, R. Bonfanti, G. Puglisi, The critical role of didodecyldimethylammonium bromide on physico-chemical, technological and biological properties of NLC, Colloids surfaces B: Biointerfaces 121 (2014) 1-10.

[196] J. Yostawonkul, S. Surassmo, T. Iempridee, W. Pimtong, K. Suktham, W. Sajomsang, P. Gonil, U.R. Ruktanonchai, Surface modification of nanostructure lipid carrier (NLC) by oleoyl-quaternized-chitosan as a mucoadhesive nanocarrier, J Colloids Surfaces B: Biointerfaces 149 (2017) 301-311.

[197] A. Mendes, A. Silva, J. Catita, F. Cerqueira, C. Gabriel, C. Lopes, Miconazole-loaded nanostructured lipid carriers (NLC) for local delivery to the oral mucosa: improving antifungal activity, J Colloids Surfaces B: Biointerfaces 111 (2013) 755-763.

[198] M. Elmowafy, A. Samy, M.A. Raslan, A. Salama, R.A. Said, A.E. Abdelaziz, W. El-Eraky, S. El Awdan, T. Viitala, Enhancement of bioavailability and pharmacodynamic effects of thymoquinone via nanostructured lipid carrier (NLC) formulation, Aaps Pharmscitech 17(3) (2016) 663-672.

[199] S. Abdolahpour, T. Toliyat, K. Omidfar, H. Modjtahedi, A.J. Wong, M.J. Rasaee, S. Kashanian, M. Paknejad, Targeted delivery of doxorubicin into tumor cells by nanostructured lipid carriers conjugated to anti-EGFRvIII monoclonal antibody, Artificial cells, nanomedicine, biotechnology Advances 46(1) (2018) 89-94.

[200] B. Sjöström, B. Bergenståhl, Preparation of submicron drug particles in lecithin-stabilized o/w emulsions I. Model studies of the precipitation of cholesteryl acetate, International journal of pharmaceutics 88(1-3) (1992) 53-62.

[201] D. Liu, Z. Liu, L. Wang, C. Zhang, N. Zhang, Nanostructured lipid carriers as novel carrier for parenteral delivery of docetaxel, J Colloids Surfaces B: Biointerfaces
85(2) (2011) 262-269.

[202] X. Ding, X. Xu, Y. Zhao, L. Zhang, Y. Yu, F. Huang, D. Yin, H. Huang, Tumor targeted nanostructured lipid carrier co-delivering paclitaxel and indocyanine green for laser triggered synergetic therapy of cancer, Rsc Advances 7(56) (2017) 35086-35095.

[203] X.-G. Zhang, J. Miao, Y.-Q. Dai, Y.-Z. Du, H. Yuan, F.-Q. Hu, Reversal activity of nanostructured lipid carriers loading cytotoxic drug in multi-drug resistant cancer cells, J International journal of pharmaceutics 361(1-2) (2008) 239-244.

[204] M. Cirri, M. Bragagni, N. Mennini, P. Mura, Biopharmaceutics, Development of a new delivery system consisting in “drug–in cyclodextrin–in nanostructured lipid carriers” for ketoprofen topical delivery, European Journal of Pharmaceutics and Biopharmaceutics 80(1) (2012) 46-53.

[205] J.-Y. Fang, C.-L. Fang, C.-H. Liu, Y.-H. Su, Lipid nanoparticles as vehicles for topical psoralen delivery: solid lipid nanoparticles (SLN) versus nanostructured lipid carriers (NLC), J European Journal of Pharmaceutics Biopharmaceutics 70(2) (2008) 633-640.

[206] Y. Chen, L. Pan, M. Jiang, D. Li, L. Jin, Nanostructured lipid carriers enhance the bioavailability and brain cancer inhibitory efficacy of curcumin both in vitro and in vivo, Drug delivery 23(4) (2016) 1383-1392.

[207] C.-L. Fang, S. A Al-Suwayeh, J.-Y. Fang, Nanostructured lipid carriers (NLCs) for drug delivery and targeting, J Recent patents on nanotechnology 7(1) (2013) 41-55.

[208] M. Sun, S. Nie, X. Pan, R. Zhang, Z. Fan, S. Wang, Quercetin-nanostructured lipid carriers: characteristics and anti-breast cancer activities in vitro, J Colloids Surfaces B: Biointerfaces
113 (2014) 15-24.

[209] R. Müller, R. Petersen, A. Hommoss, J. Pardeike, Nanostructured lipid carriers (NLC) in cosmetic dermal products, Advanced drug delivery reviews 59(6) (2007) 522-530.

[210] R.V. Tikekar, N. Nitin, Distribution of encapsulated materials in colloidal particles and its impact on oxidative stability of encapsulated materials, J Langmuir 28(25) (2012) 9233-9243.

[211] S.V. Talluri, G. Kuppusamy, V.V.S.R. Karri, S. Tummala, S.V. Madhunapantula, Lipid-based nanocarriers for breast cancer treatment–comprehensive review, Drug Delivery 23(4) (2016) 1291-1305.

[212] X. Li, X. Jia, H. Niu, Nanostructured lipid carriers co-delivering lapachone and doxorubicin for overcoming multidrug resistance in breast cancer therapy, Int J Nanomedicine 13 (2018) 4107.

[213] Y.S. Ong, L. Saiful Yazan, W.K. Ng, R. Abdullah, N.M. Mustapha, S. Sapuan, J.B. Foo, Y.S. Tor, C.W. How, N. Abd Rahman, Thymoquinone loaded in nanostructured lipid carrier showed enhanced anticancer activity in 4T1 tumor-bearing mice, J Nanomedicine 13(13) (2018) 1567-1582.

[214] L. Wang, Q. Luo, T. Lin, R. Li, T. Zhu, K. Zhou, Z. Ji, J. Song, B. Jia, C. Zhang, PEGylated nanostructured lipid carriers (PEG–NLC) as a novel drug delivery system for biochanin A, J Drug Development Industrial Pharmacy
41(7) (2015) 1204-1212.

[215] L.M. Ensign, R. Cone, J. Hanes, Oral drug delivery with polymeric nanoparticles: the gastrointestinal mucus barriers, Advanced drug delivery reviews 64(6) (2012) 557-570.

[216] A. Banerjee, J. Qi, R. Gogoi, J. Wong, S. Mitragotri, Role of nanoparticle size, shape and surface chemistry in oral drug delivery, Journal of Controlled Release Bioengineering 238 (2016) 176-185.

[217] C. He, L. Yin, C. Tang, C. Yin, Size-dependent absorption mechanism of polymeric nanoparticles for oral delivery of protein drugs, J Biomaterials 33(33) (2012) 8569-8578.

[218] M. Haider, S.M. Abdin, L. Kamal, G. Orive, Nanostructured Lipid Carriers for Delivery of Chemotherapeutics: A Review, Pharmaceutics 12(3) (2020) 288.

[219] X.-G. Zhang, J. Miao, Y.-Q. Dai, Y.-Z. Du, H. Yuan, F.-Q. Hu, Reversal activity of nanostructured lipid carriers loading cytotoxic drug in multi-drug resistant cancer cells, International Journal of Pharmaceutics 361(1) (2008) 239-244.

[220] Y. Wang, H. Zhang, J. Hao, B. Li, M. Li, W. Xiuwen, Lung cancer combination therapy: co-delivery of paclitaxel and doxorubicin by nanostructured lipid carriers for synergistic effect, Drug Delivery 23(4) (2016) 1398-1403.

[221] S. Abdolahpour, T. Toliyat, K. Omidfar, H. Modjtahedi, A.J. Wong, M.J. Rasaee, S. Kashanian, M. Paknejad, Targeted delivery of doxorubicin into tumor cells by nanostructured lipid carriers conjugated to anti-EGFRvIII monoclonal antibody, Artificial Cells, Nanomedicine, and Biotechnology 46(1) (2018) 89-94.

[222] M. Sun, S. Nie, X. Pan, R. Zhang, Z. Fan, S. Wang, Quercetin-nanostructured lipid carriers: Characteristics and anti-breast cancer activities in vitro, Colloids and Surfaces B: Biointerfaces 113 (2014) 15-24.

[223] C.W. How, A. Rasedee, S. Manickam, R. Rosli, Tamoxifen-loaded nanostructured lipid carrier as a drug delivery system: Characterization, stability assessment and cytotoxicity, Colloids and Surfaces B: Biointerfaces 112 (2013) 393-399.

[224] D.C. Leitao, Micro and Nano Patterned Magnetic Structures, Universidade do Porto, 2010.

[225] D. Leitao, C. Sousa, J. Ventura, F. Carpinteiro, J. Correia, M. Amado, J. Sousa, J. Araujo, Influence of surface pre-treatment in the room temperature fabrication of nanoporous alumina, J physical status solidic
5(11) (2008) 3488-3491.

[226] D. Leitao, A. Apolinario, C. Sousa, J. Ventura, J. Sousa, M. Vazquez, J. Araujo, Nanoscale topography: a tool to enhance pore order and pore size distribution in anodic aluminum oxide, The Journal of Physical Chemistry C 115(17) (2011) 8567-8572.

[227] V.V. Yuzhakov, H.-C. Chang, A.E. Miller, Pattern formation during electropolishing, Physical Review B 56(19) (1997) 12608.

[228] M.P. Proenca, C.T. Sousa, D.C. Leitao, J. Ventura, J.B. Sousa, J.P. Araujo, Nanopore formation and growth in phosphoric acid Al anodization, Journal of Non-Crystalline Solids 354(47) (2008) 5238-5240.

[229] M.P. Proenca, C.T. Sousa, J. Ventura, M. Vazquez, J.P. Araujo, Distinguishing nanowire and nanotube formation by the deposition current transients, Nanoscale Research Letters 7(1) (2012) 280.

[230] H. Masuda, K. Fukuda, Ordered Metal Nanohole Arrays Made by a Two-Step Replication of Honeycomb Structures of Anodic Alumina, Science 268(5216) (1995) 1466-1468.

[231] M. Ohring, Chapter 5 - Plasma and Ion Beam Processing of Thin Films, in: M. Ohring (Ed.), Materials Science of Thin Films (Second Edition), Academic Press, San Diego, 2002, pp. 203-275.

[232] D. Depla, S. Mahieu, J.E. Greene, Chapter 5 - Sputter Deposition Processes A2 - Martin, Peter M, Handbook of Deposition Technologies for Films and Coatings (Third Edition), William Andrew Publishing, Boston, 2010, pp. 253-296.

[233] Sputtering, Available at: http://www.lithoguru.com/scientist/CHE323/Lecture22.pdf (Accessed January 18, 2021).

[234] Sputter Coater Principles, Available at: https://www.emsdiasum.com/microscopy/technical/datasheet/sputter_coating.aspx (Accessed January 18, 2021).

[235] H.H. Gatzen, V. Saile, J. Leuthold, Deposition Technologies, Micro and Nano Fabrication: Tools and Processes, Springer Berlin Heidelberg, Berlin, Heidelberg, 2015, pp. 65-203.

[236] Sputter deposition, Available at: https://en.wikipedia.org/wiki/Sputter_deposition (Accessed January 14, 2021).

[237] J. Lopes-de-Araújo, A.R. Neves, V.M. Gouveia, C.C. Moura, C. Nunes, S. Reis, Oxaprozin-Loaded Lipid Nanoparticles towards Overcoming NSAIDs Side-Effects, Pharmaceutical Research 33(2) (2016) 301-314.

[238] W. Zhou, R. Apkarian, Z.L. Wang, D. Joy, Fundamentals of Scanning Electron Microscopy (SEM), in: W. Zhou, Z.L. Wang (Eds.), Scanning Microscopy for Nanotechnology: Techniques and Applications, Springer New York, New York, NY, 2007, pp. 1-40.

[239] J. Goldstein, Scanning electron microscopy and x-ray microanalysis, Kluwer Academic/Plenum Publishers, New York, 2003.

[240] MATERIALS CHARACTERIZATION SERIES A2 - Brundle, C. Ricbard, in: C.A. Evans, S. Wilson (Eds.), Encyclopedia of Materials Characterization, Butterworth-Heinemann, Boston, 1992, p. ii.

[241] V. Kazmiruk, Scanning Electron Microscopy, InTech, Chapters 2012.

[242] SEM: Types of Electrons and the Information They Provide. Available at: https://www.thermofisher.com/blog/microscopy/sem-types-electrons-and-the-information-they-provide/ (Accessed February 12, 2020).

[243] C.A. Schneider, W.S. Rasband, K.W. Eliceiri, NIH Image to ImageJ: 25 years of image analysis, Nat. Methods 9(7) (2012) 671-675.

[244] J. Bergström, 2 - Experimental Characterization Techniques, in: J. Bergström (Ed.), Mechanics of Solid Polymers, William Andrew Publishing2015, pp. 19-114.

[245] Transmission Electron Microscopy vs Scanning Electron Microscopy, Available at: https://www.thermofisher.com/pt/en/home/materials-science/learning-center/applications/sem-tem-difference.html (Accessed January 17, 2021).

[246] T. Ungár, Microstructural parameters from X-ray diffraction peak broadening, Scr. Mater. 51(8) (2004) 777-781.

[247] N.I. Stresstech, X-ray diffraction, Available at: https://www.stresstech.com/en-fi/products/x-ray-diffraction-equipment/x-ray-diffraction/ (Accessed May 01, 2020).

[248] W.H. Bragg, W.L. Bragg, The reflection of X-rays by crystals, Proceedings of the Royal Society of London. Series A, Containing Papers of a Mathematical and Physical Character 88(605) (1913) 428-438.

[249] A.L. Patterson, The Scherrer Formula for X-Ray Particle Size Determination, Phys. Rev. 56(10) (1939) 978-982.

[250] F. Béron, L.P. Carignan, D. MÉnard, A. Yelon, Magnetic Behavior of Ni/Cu Multilayer Nanowire Arrays Studied by First-Order Reversal Curve Diagrams, IEEE Transactions on Magnetics 44(11) (2008) 2745-2748.

[251] C. De Caro, C. Haller, UV/VIS Spectrophotometry - Fundamentals and Applications, 2015.

[252] S.E. Harding, K. Jumel, Light scattering, J Current protocols in protein science 11(1) (1998) 7.8. 1-7.8. 14.

[253] S. Bhattacharjee, DLS and zeta potential–what they are and what they are not?, J Journal of controlled release 235 (2016) 337-351.

[254] E. Eiser, Dynamic light scattering, J Multi Length-Scale Characterisation 1 (2014) 233.

[255] D.J. Pine, D.A. Weitz, P.M. Chaikin, E. Herbolzheimer, Diffusing wave spectroscopy, J Physical review letters 60(12) (1988) 1134.

[256] F.J.M. Ruiz-Cabello, G. Trefalt, P. Maroni, M. Borkovec, Electric double-layer potentials and surface regulation properties measured by colloidal-probe atomic force microscopy, J Physical Review E 90(1) (2014) 012301.

[257] M.S. Gautam Singhvi, REVIEW: IN-VITRO DRUG RELEASE CHARACTERIZATION MODELS International Journal of Pharmaceutical Studies and Research II (2011) 77-84

[258] E. Silva, L. Barreiros, M.A. Segundo, S.A. Costa Lima, S. Reis, Cellular interactions of a lipid-based nanocarrier model with human keratinocytes: Unravelling transport mechanisms, Acta Biomater 53 (2017) 439-449.

[259] A. Fernández-Pacheco, R. Streubel, O. Fruchart, R. Hertel, P. Fischer, R.P. Cowburn, Three-dimensional nanomagnetism, Nature Communications 8 (2017) 15756.

[260] P.M. Paulus, F. Luis, M. Kröll, G. Schmid, L.J. de Jongh, Low-temperature study of the magnetization reversal and magnetic anisotropy of Fe, Ni, and Co nanowires, Journal of Magnetism and Magnetic Materials 224(2) (2001) 180-196.

[261] C.A. Ross, M. Hwang, M. Shima, J.Y. Cheng, M. Farhoud, T.A. Savas, H.I. Smith, W. Schwarzacher, F.M. Ross, M. Redjdal, F.B. Humphrey, Micromagnetic behavior of electrodeposited cylinder arrays, Physical Review B 65(14) (2002) 144417.

[262] E.C. Walter, K. Ng, M.P. Zach, R.M. Penner, F. Favier, Electronic devices from electrodeposited metal nanowires, Microelectronic Engineering 61-62 (2002) 555-561.

[263] R. Skomski, Nanomagnetics, Journal of Physics: Condensed Matter 15(20) (2003) R841.

[264] J.F. Fennell, S.F. Liu, J.M. Azzarelli, J.G. Weis, S. Rochat, K.A. Mirica, J.B. Ravnsbæk, T.M. Swager, Nanowire Chemical/Biological Sensors: Status and a Roadmap for the Future, Angewandte Chemie International Edition 55(4) (2016) 1266-1281.

[265] W.-S. Lin, H.-M. Lin, Y.-K. Hwu, Y.-J. Chiou, Synthesis and Characterization of Functionalied Iron Nanowires, Procedia Engineering 92 (2014) 42-45.

[266] T. Kumeria, S. Maher, Y. Wang, G. Kaur, L. Wang, M. Erkelens, P. Forward, M.F. Lambert, A. Evdokiou, D. Losic, Naturally Derived Iron Oxide Nanowires from Bacteria for Magnetically Triggered Drug Release and Cancer Hyperthermia in 2D and 3D Culture Environments: Bacteria Biofilm to Potent Cancer Therapeutic, Biomacromolecules 17(8) (2016) 2726-2736.

[267] M. Bañobre-López, C. Bran, C. Rodríguez-Abreu, J. Gallo, M. Vázquez, J. Rivas, A colloidally stable water dispersion of Ni nanowires as an efficient T 2-MRI contrast agent, Journal of Materials Chemistry B 5(18) (2017) 3338-3347.

[268] A. Serrà, G. Vázquez-Mariño, J. García-Torres, M. Bosch, E. Vallés, Magnetic actuation of multifunctional nanorobotic platforms to induce cancer cell death, Advanced Biosystems 2(2) (2018) 1700220.

[269] M. Vázquez, K. Pirota, M. Hernández-Vélez, V.M. Prida, D. Navas, R. Sanz, F. Batallán, J. Velázquez, Magnetic properties of densely packed arrays of Ni nanowires as a function of their diameter and lattice parameter, Journal of Applied Physics 95(11) (2004) 6642-6644.

[270] T.M. Whitney, P.C. Searson, J.S. Jiang, C.L. Chien, Fabrication and Magnetic Properties of Arrays of Metallic Nanowires, Science 261(5126) (1993) 1316.

[271] B. Wildt, P. Mali, P.C. Searson, Electrochemical template synthesis of multisegment nanowires: Fabrication and protein functionalization, J Langmuir 22(25) (2006) 10528-10534.

[272] Q. Kuo, L. Xinghua, Z. Hong, W. Li, X. Desheng, Z. Haoli, Z. Baofan, J.M. Nigel, P. Yong, Nanoscale characterization and magnetic property of NiCoCu/Cu multilayer nanowires, Nanotechnology 23(50) (2012) 505707.

[273] J.J. Park, M. Reddy, B.J.H. Stadler, A.B. Flatau, Hysteresis measurement of individual multilayered Fe-Ga/Cu nanowires using magnetic force microscopy, Journal of Applied Physics 113(17) (2013) 17A331.

[274] S.M. Reddy, J.J. Park, M.M. Maqableh, A.B. Flatau, B.J.H. Stadler, Magnetization reversal mechanisms in 35-nm diameter Fe1-xGax/Cu multilayered nanowires, Journal of Applied Physics 111(7) (2012) 07A920.

[275] L. Clime, S.Y. Zhao, P. Chen, F. Normandin, H. Roberge, T. Veres, The interaction field in arrays of ferromagnetic barcode nanowires, Nanotechnology 18(43) (2007) 435709.

[276] M. Chen, C.-L. Chien, P.C. Searson, Potential Modulated Multilayer Deposition of Multisegment Cu/Ni Nanowires with Tunable Magnetic Properties, Chemistry of Materials 18(6) (2006) 1595-1601.

[277] M. Chen, P.C. Searson, C.L. Chien, Micromagnetic behavior of electrodeposited Ni/Cu multilayer nanowires, Journal of Applied Physics 93(10) (2003) 8253-8255.

[278] N. Maleak, P. Potpattanapol, N.N. Bao, J. Ding, W. Wongkokuo, I.M. Tang, S. Thongmee, Fabrication and magnetic properties of electrodeposited Ni/Cu nanowires using the double bath method, Journal of Magnetism and Magnetic Materials 354 (2014) 262-266.

[279] A. Shirazi Tehrani, M. Almasi Kashi, A. Ramazani, A.H. Montazer, Axially adjustable magnetic properties in arrays of multilayered Ni/Cu nanowires with variable segment sizes, Superlattices and Microstructures 95 (2016) 38-47.

[280] S.H. Xu, G.T. Fei, X.G. Zhu, L.D. Zhang, Orientation-dependent growth rate of crystalline plane study in electrodeposited Ni/Cu superlattice nanowires, CrystEngComm 15(20) (2013) 4070-4076.

[281] X.-T. Tang, G.-C. Wang, M. Shima, Magnetic layer thickness dependence of magnetization reversal in electrodeposited CoNi/Cu multilayer nanowires, Journal of Magnetism and Magnetic Materials 309(2) (2007) 188-196.

[282] S. Krimpalis, O.-G. Dragos, A.-E. Moga, N. Lupu, H. Chiriac, Magnetization processes in electrodeposited NiFe/Cu multilayered nanowires, Journal of Materials Research 26(9) (2011) 1081-1090.

[283] A. Blondel, B. Doudin, J.P. Ansermet, Comparative study of the magnetoresistance of electrodeposited Co/Cu multilayered nanowires made by single and dual bath techniques, Journal of Magnetism and Magnetic Materials 165(1) (1997) 34-37.

[284] J.D.L.T. Medina, M. Darques, A. Encinas, L. Piraux, Dipolar interactions in multilayered Co0.96Cu0.04/Cu nanowire arrays, physica status solidi (a) 205(8) (2008) 1813-1816.

[285] J. Wong, P. Greene, R.K. Dumas, K. Liu, Probing magnetic configurations in Co/Cu multilayered nanowires, Applied Physics Letters 94(3) (2009) 032504.

[286] L. Piraux, J.M. George, J.F. Despres, C. Leroy, E. Ferain, R. Legras, K. Ounadjela, A. Fert, Giant magnetoresistance in magnetic multilayered nanowires, Applied Physics Letters 65(19) (1994) 2484-2486.

[287] B. Jang, E. Pellicer, M. Guerrero, X. Chen, H. Choi, B.J. Nelson, J. Sort, S. Pané, Fabrication of Segmented Au/Co/Au Nanowires: Insights in the Quality of Co/Au Junctions, ACS Applied Materials & Interfaces 6(16) (2014) 14583-14589.

[288] J. YangChunxiang CuiWei Yang, C. Cui, W. Yang, B. Hu, J.-B. Sun, Electrochemical fabrication and magnetic properties of Fe 7 Co 3 alloy nanowire array, 2011.

[289] B.C. Park, B.G. Kim, H.W. Seo, Y.K. Kim, Magnetic Anisotropy Evolution in CoFe/Au Barcode Nanowire Arrays, IEEE Transactions on Magnetics 50(1) (2014) 1-4.

[290] A. Akhtari-Zavareh, L.P. Carignan, A. Yelon, D. Ménard, T. Kasama, R. Herring, R.E. Dunin-Borkowski, M.R. McCartney, K.L. Kavanagh, Off-axis electron holography of ferromagnetic multilayer nanowires, Journal of Applied Physics 116(2) (2014) 023902.

[291] A. Núñez, L. Pérez, M. Abuín, J.P. Araujo, M.P. Proenca, Magnetic behaviour of multisegmented FeCoCu/Cu electrodeposited nanowires, Journal of Physics D: Applied Physics 50(15) (2017) 155003.

[292] M.P. Ester, B. Fanny, B. Cristina, P.d.R. Rafael, V. Manuel, Magnetic interactions in compositionally modulated nanowire arrays, Nanotechnology 27(43) (2016) 435705.

[293] T. Sahin, H. Kockar, M. Alper, Properties of electrodeposited CoFe/Cu multilayers: The effect of Cu layer thickness, Journal of Magnetism and Magnetic Materials 373 (2015) 128-131.

[294] A. Ramazani, M.A. Kashi, F. Eghbal, E. Jafari-Khamse, The effect of deposition parameters on the magnetic behavior of CoFe/Cu multilayer nanowires, The European Physical Journal Plus 130(1) (2015) 2.

[295] A. Ramazani, M. Ghaffari, M.A. Kashi, F. Kheiry, F. Eghbal, A new approach to fabricating magnetic multilayer nanowires by modifying the ac pulse electrodeposition in a single bath, Journal of Physics D: Applied Physics 47(35) (2014) 355003.

[296] M. Almasi-Kashi, A. Ramazani, F. Kheyri, E. Jafari-Khamse, The effect of magnetic layer thickness on magnetic properties of Fe/Cu multilayer nanowires, Materials Chemistry and Physics 144(3) (2014) 230-234.

[297] M. Chen, P. Searson, Potential modulated multilayer deposition of multisegment Cu/Ni nanowires with tunable magnetic properties Chemistry of Materials 18 (2006) 1595.

[298] Guo, L.-J. Wan, C.-F. Zhu, D.-L. Yang, D.-M. Chen, C.-L. Bai, Ordered Ni−Cu Nanowire Array with Enhanced Coercivity, Chemistry of Materials 15(3) (2003) 664-667.

[299] Y.D. Gamburg, G. Zangari, Theory and practice of metal electrodeposition, Springer Science & Business Media2011.

[300] G. Gunawardena, G. Hills, I. Montenegro, B. Scharifker, Electrochemical nucleation: Part I. General considerations, Journal of Electroanalytical Chemistry and Interfacial Electrochemistry 138(2) (1982) 225-239.

[301] B. Scharifker, G. Hills, Theoretical and experimental studies of multiple nucleation, Electrochim. Acta 28(7) (1983) 879-889.

[302] M. Proenca, C. Sousa, J. Ventura, M. Vazquez, J. Araujo, Ni growth inside ordered arrays of alumina nanopores: Enhancing the deposition rate
Electrochim. Acta 72 (2012).

[303] J.W.M. Jacobs, Note on a theory of three-dimensional electrochemical nucleation with diffusion-controlled growth, Journal of Electroanalytical Chemistry and Interfacial Electrochemistry 247(1) (1988) 135-144.

[304] G. Oskam, J.G. Long, A. Natarajan, P.C. Searson, Electrochemical deposition of metals onto silicon, Journal of Physics D: Applied Physics 31(16) (1998) 1927-1949.

[305] J. Qin, J. Nogués, M. Mikhaylova, A. Roig, J.S. Munoz, M. Muhammed, Differences in the magnetic properties of Co, Fe, and Ni 250− 300 nm wide nanowires electrodeposited in amorphous anodized alumina templates, J Chemistry of materials 17(7) (2005) 1829-1834.

[306] H. Wang, E. Jia, L. Zhang, L. Li, M. Li, On low-temperature ordering of FePt nanowires, J Physics Letters A 372(35) (2008) 5712-5715.

[307] B. Fanny, A.S.d.O. Luiz, K. Marcelo, R.P. Kleber, A novel method for identifying the local magnetic viscosity process of heterogeneous magnetic nanostructures, Journal of Physics D: Applied Physics 46(4) (2013) 045003.

[308] F. Béron, D. Ménard, A. Yelon, First-order reversal curve diagrams of magnetic entities with mean interaction field: A physical analysis perspective, Journal of Applied Physics 103(7) (2008) 07D908.

[309] C.-I. Dobrotă, A. Stancu, Tracking the individual magnetic wires' switchings in ferromagnetic nanowire arrays using the first-order reversal curves (FORC) diagram method, Physica B: Condensed Matter 457 (2015) 280-286.

[310] A. Vansteenkiste, J. Leliaert, M. Dvornik, M. Helsen, F. Garcia-Sanchez, B. Van Waeyenberge, The design and verification of MuMax3, AIP Advances 4(10) (2014) 107133.

[311] Y.-P. Xie, S.-J. Zhao, The energetic and structural properties of bcc NiCu, FeCu alloys: A first-principles study, Computational Materials Science 50(9) (2011) 2586-2591.

[312] D. Reyes, N. Biziere, B. Warot-Fonrose, T. Wade, C. Gatel, Magnetic Configurations in Co/Cu Multilayered Nanowires: Evidence of Structural and Magnetic Interplay, Nano Letters 16(2) (2016) 1230-1236.

[313] J.L. Palma, C. Morales-Concha, B. Leighton, D. Altbir, J. Escrig, Micromagnetic simulation of Fe asymmetric nanorings, Journal of Magnetism and Magnetic Materials 324(4) (2012) 637-641.

[314] V.R. Igor, L. Chang-Peng, S. Harry, B. Xavier, S. Roy, K.S. Sunil, S. Park, P. Roger, M.R. Fitzsimmons, M.-L. Jose, A. Dora, A.H. Romero, K.S. Ivan, Measurement of the vortex core in sub-100 nm Fe dots using polarized neutron scattering, EPL (Europhysics Letters) 86(6) (2009) 67008.

[315] P.I. Yu, M. Vázquez, O. Chubykalo-Fesenko, Magnetic reversal modes in cylindrical nanowires, Journal of Physics D: Applied Physics 46(48) (2013) 485001.

[316] M. Susano, M. Proenca, S. Moraes, C. Sousa, J. Araújo, Tuning the magnetic properties of multisegmented Ni/Cu electrodeposited nanowires with controllable Ni lengths, Nanotechnology 27 (2016) 335301.

[317] Y.P. Ivanov, M. Vazquez, O. Chubykalo-Fesenko, Magnetic reversal modes in cylindrical nanowires, J. Phys. D: Appl. Phys. 46 (2013) 485001.

[318] V. Haehnel, S. Faehler, P. Schaaf, M. Miglierini, C. Mickel, L. Schultz, H. Schloerb, Towards smooth and pure iron nanowires grown by electrodeposition in self-organized alumina membranes, Acta Materialia 58(7) (2010) 2330-2337.

[319] F. Bray, J. Ferlay, I. Soerjomataram, R.L. Siegel, L.A. Torre, A. Jemal, Global cancer statistics 2018: GLOBOCAN estimates of incidence and mortality worldwide for 36 cancers in 185 countries, CA: A Cancer Journal for Clinicians 68(6) (2018) 394-424.

[320] L.A. Torre, F. Islami, R.L. Siegel, E.M. Ward, A. Jemal, Global Cancer in Women: Burden and Trends, Cancer Epidemiology Biomarkers & Prevention 26(4) (2017) 444-457.

[321] K. Chatterjee, J. Zhang, N. Honbo, J.S. Karliner, Doxorubicin cardiomyopathy, Cardiology 115(2) (2010) 155-162.

[322] P.K. Singal, N. Iliskovic, Doxorubicin-Induced Cardiomyopathy, New England Journal of Medicine 339(13) (1998) 900-905.

[323] D.R. Kalaria, Sharma, G., Beniwal, V., Design of Biodegradable Nanoparticles for Oral Delivery of Doxorubicin: In vivo Pharmacokinetics and Toxicity Studies in Rats, Pharmaceutical Research 26(3) (2008) 492–501.

[324] Y. Schilt, T. Berman, X. Wei, Y. Barenholz, U. Raviv, Using solution X-ray scattering to determine the high-resolution structure and morphology of PEGylated liposomal doxorubicin nanodrugs, Biochimica et Biophysica Acta (BBA) - General Subjects 1860(1, Part A) (2016) 108-119.

[325] T.J. Anchordoquy, Y. Barenholz, D. Boraschi, M. Chorny, P. Decuzzi, M.A. Dobrovolskaia, Z.S. Farhangrazi, D. Farrell, A. Gabizon, H. Ghandehari, B. Godin, N.M. La-Beck, J. Ljubimova, S.M. Moghimi, L. Pagliaro, J.-H. Park, D. Peer, E. Ruoslahti, N.J. Serkova, D. Simberg, Mechanisms and Barriers in Cancer Nanomedicine: Addressing Challenges, Looking for Solutions, ACS Nano 11(1) (2017) 12-18.

[326] L. Silverman, Y. Barenholz, In vitro experiments showing enhanced release of doxorubicin from Doxil® in the presence of ammonia may explain drug release at tumor site, Nanomedicine: Nanotechnology, Biology and Medicine 11(7) (2015) 1841-1850.

[327] J.-S. Baek, C.-W. Cho, Controlled release and reversal of multidrug resistance by co-encapsulation of paclitaxel and verapamil in solid lipid nanoparticles, International Journal of Pharmaceutics 478(2) (2015) 617-624.

[328] S. Weber, A. Zimmer, J. Pardeike, Solid Lipid Nanoparticles (SLN) and Nanostructured Lipid Carriers (NLC) for pulmonary application: A review of the state of the art, European Journal of Pharmaceutics and Biopharmaceutics 86(1) (2014) 7-22.

[329] S.V. Mussi, R. Sawant, F. Perche, M.C. Oliveira, R.B. Azevedo, L.A.M. Ferreira, V.P. Torchilin, Novel Nanostructured Lipid Carrier Co-Loaded with Doxorubicin and Docosahexaenoic Acid Demonstrates Enhanced in Vitro Activity and Overcomes Drug Resistance in MCF-7/Adr Cells, Pharmaceutical Research 31(8) (2014) 1882-1892.

[330] J.S. Suk, Q. Xu, N. Kim, J. Hanes, L.M. Ensign, PEGylation as a strategy for improving nanoparticle-based drug and gene delivery, Advanced Drug Delivery Reviews 99 (2016) 28-51.

[331] B. Farran, R.C. Montenegro, P. Kasa, E. Pavitra, Y.S. Huh, Y.-K. Han, M.A. Kamal, G.P. Nagaraju, G.S. Rama Raju, Folate-conjugated nanovehicles: Strategies for cancer therapy, Materials Science and Engineering: C 107 (2020) 110341.

[332] B. Bahrami, M. Mohammadnia-Afrouzi, P. Bakhshaei, Y. Yazdani, G. Ghalamfarsa, M. Yousefi, S. Sadreddini, F. Jadidi-Niaragh, M. Hojjat-Farsangi, Folate-conjugated nanoparticles as a potent therapeutic approach in targeted cancer therapy, Tumor Biology 36(8) (2015) 5727-5742.

[333] S.N. Manzoor Ahmad Gatoo, Mir Yasir Arfat, Ayaz Mahmood Dar, Khusro Qasim,3and Swaleha Zubair, Physicochemical Properties of Nanomaterials: Implication in Associated Toxic Manifestations, BioMed Research International 2014 (2014).

[334] M.D. Danaei, M.; Ataei, S.; Hasanzadeh Davarani, F.; Javanmard, R.; Dokhani, A.; Khorasani, S.; Mozafari, M. R., Impact of Particle Size and Polydispersity Index on the Clinical Applications of Lipidic Nanocarrier Systems, Pharmaceutics 10 (2018) 57.

[335] C. Peetla, S. Vijayaraghavalu, V. Labhasetwar, Biophysics of cell membrane lipids in cancer drug resistance: Implications for drug transport and drug delivery with nanoparticles, Advanced Drug Delivery Reviews 65(13) (2013) 1686-1698.

[336] C. He, L. Yin, C. Tang, C. Yin, Size-dependent absorption mechanism of polymeric nanoparticles for oral delivery of protein drugs, Biomaterials 33(33) (2012) 8569-8578.

[337] A. Banerjee, J. Qi, R. Gogoi, J. Wong, S. Mitragotri, Role of nanoparticle size, shape and surface chemistry in oral drug delivery, Journal of Controlled Release 238 (2016) 176-185.

[338] L.B.a.E. Ugazio, Lipid Nano- and Microparticles: An Overview of Patent-Related Research, Journal of Nanomaterials 2019 (2019) 22.

[339] J.D.P. Clogston, A. K. , Characterization of Nanoparticles Intended for Drug Delivery, Methods in Molecular Biology 697 (2018) 63–70.

[340] A. Kumar, C.K. Dixit, Methods for characterization of nanoparticles, in: S. Nimesh, R. Chandra, N. Gupta (Eds.), Advances in Nanomedicine for the Delivery of Therapeutic Nucleic Acids, Woodhead Publishing2017, pp. 43-58.

[341] S. Nimesh, R. Chandra, N. Gupta, Advances in Nanomedicine for the Delivery of Therapeutic Nucleic Acids, Elsevier Science2017.

[342] A.M. Farnoud, S. Nazemidashtarjandi, Emerging investigator series: interactions of engineered nanomaterials with the cell plasma membrane; what have we learned from membrane models?, Environmental Science: Nano 6(1) (2019) 13-40.

[343] G. Lukowski, J. Kasbohm, P. Pflegel, A. Illing, H. Wulff, Crystallographic investigation of cetylpalmitate solid lipid nanoparticles, International Journal of Pharmaceutics 196(2) (2000) 201-205.

[344] A.E.-H.I. El Assasy, N.F. Younes, A.I.A. Makhlouf, Enhanced Oral Absorption of Amisulpride Via a Nanostructured Lipid Carrier-Based Capsules: Development, Optimization Applying the Desirability Function Approach and In Vivo Pharmacokinetic Study, AAPS PharmSciTech 20(2) (2019) 82.

[345] C. Fitzmaurice, T.F. Akinyemiju, F.H. Al Lami, T. Alam, R. Alizadeh-Navaei, C. Allen, U. Alsharif, N. Alvis-Guzman, E. Amini, B.O. Anderson, Global, regional, and national cancer incidence, mortality, years of life lost, years lived with disability, and disability-adjusted life-years for 29 cancer groups, 1990 to 2016: a systematic analysis for the global burden of disease study, J JAMA oncology 4(11) (2018) 1553-1568.

[346] R.L. Siegel, K.D. Miller, A. Jemal, Cancer statistics, 2016, CA: a cancer journal for clinicians 66(1) (2016) 7-30.

[347] A.S. Garanina, V.A. Naumenko, A.A. Nikitin, E. Myrovali, A.Y. Petukhova, S.V. Klimyuk, Y.A. Nalench, A.R. Ilyasov, S.S. Vodopyanov, A.S. Erofeev, Temperature-controlled magnetic nanoparticles hyperthermia inhibits primary tumor growth and metastases dissemination, J Nanomedicine: Nanotechnology, Biology
Medicine 25 (2020) 102171.

[348] J. Dobson, Magnetic micro-and nano-particle-based targeting for drug and gene delivery, Nanomedicine 1:1 (2006) 31-37.

[349] C. Sun, J.S. Lee, M. Zhang, Magnetic nanoparticles in MR imaging and drug delivery, J Advanced drug delivery reviews 60(11) (2008) 1252-1265.

[350] Y. Octavia, C.G. Tocchetti, K.L. Gabrielson, S. Janssens, H.J. Crijns, A.L. Moens, Doxorubicin-induced cardiomyopathy: from molecular mechanisms to therapeutic strategies, Journal of molecular cellular cardiology
52(6) (2012) 1213-1225.

[351] C. Humber, J. Tierney, R. Symonds, M. Collingwood, J. Kirwan, C. Williams, J. Green, Chemotherapy for advanced, recurrent or metastatic endometrial cancer: a systematic review of Cochrane collaboration, J Annals of Oncology 18(3) (2007) 409-420.

[352] J.-S. Au, S. Jang, J. Zheng, C.-T. Chen, S. Song, L. Hu, M.G. Wientjes, Determinants of drug delivery and transport to solid tumors, Journal of controlled release 74(1-3) (2001) 31-46.

[353] G. Garcia Rubia, A. Peigneux, Y. Jabalera, J. Puerma, F. Oltolina, K. Elert, D. Colangelo, J. Gómez Morales, M. Prat, C. Jimenez-Lopez, pH-dependent adsorption release of doxorubicin on MamC-biomimetic magnetite nanoparticles, J Langmuir
34(45) (2018) 13713-13724.

[354] A. Peigneux, F. Oltolina, D. Colangelo, G.R. Iglesias, A.V. Delgado, M. Prat, C. Jimenez-Lopez, Functionalized biomimetic magnetic nanoparticles as effective nanocarriers for targeted chemotherapy, J Particle Particle Systems Characterization
36(6) (2019) 1900057.

[355] R. Duncan, The dawning era of polymer therapeutics, Nature reviews Drug discovery 2(5) (2003) 347-360.

[356] Y. Matsumura, H. Maeda, A new concept for macromolecular therapeutics in cancer chemotherapy: mechanism of tumoritropic accumulation of proteins and the antitumor agent smancs, Cancer research 46(12 Part 1) (1986) 6387-6392.

[357] D. Zhi, T. Yang, J. Yang, S. Fu, S. Zhang, Targeting strategies for superparamagnetic iron oxide nanoparticles in cancer therapy, J Acta biomaterialia 102 (2020) 13-34.

[358] F. Oltolina, D. Colangelo, I. Miletto, N. Clemente, M. Miola, E. Verné, M. Prat, A. Follenzi, Tumor targeting by monoclonal antibody functionalized magnetic nanoparticles, J Nanomaterials 9(11) (2019) 1575.

[359] R.D. Issels, Hyperthermia adds to chemotherapy, J European journal of cancer 44(17) (2008) 2546-2554.

[360] D. Liu, F. Yang, F. Xiong, N. Gu, The smart drug delivery system and its clinical potential. Theranostics 6, 1306–1323, 2016.

[361] Y. Jabalera, A. Sola-Leyva, A. Peigneux, F. Vurro, G.R. Iglesias, J. Vilchez-Garcia, I. Pérez-Prieto, F.J. Aguilar-Troyano, L.C. López-Cara, M.P. Carrasco-Jiménez, Biomimetic Magnetic Nanocarriers Drive Choline Kinase Alpha Inhibitor inside Cancer Cells for Combined Chemo-Hyperthermia Therapy, J Pharmaceutics 11(8) (2019) 408.

[362] G. Iglesias, F. Reyes-Ortega, B. Checa Fernandez, Á.V. Delgado, Hyperthermia-triggered gemcitabine release from polymer-coated magnetite nanoparticles, J Polymers 10(3) (2018) 269.

[363] A.Z. Wilczewska, K. Niemirowicz, K.H. Markiewicz, H. Car, Nanoparticles as drug delivery systems, J Pharmacological reports 64(5) (2012) 1020-1037.

[364] P. Severino, T. Andreani, A.S. Macedo, J.F. Fangueiro, M.H.A. Santana, A.M. Silva, E.B. Souto, Current state-of-art and new trends on lipid nanoparticles (SLN and NLC) for oral drug delivery, J Journal of drug delivery 2012 (2012).

[365] A. Pugazhendhi, T.N.J.I. Edison, B.K. Velmurugan, J.A. Jacob, I. Karuppusamy, Toxicity of Doxorubicin (Dox) to different experimental organ systems, Life Sciences 200 (2018) 26-30.

[366] 5 - Mathematical models of drug release, in: M.L. Bruschi (Ed.), Strategies to Modify the Drug Release from Pharmaceutical Systems, Woodhead Publishing2015, pp. 63-86.

[367] K. Golla, B. Cherukuvada, F. Ahmed, A.K. Kondapi, Efficacy, safety and anticancer activity of protein nanoparticle-based delivery of doxorubicin through intravenous administration in rats, PLoS One 7(12) (2012) e51960.

[368] G. Sahay, D.Y. Alakhova, A.V. Kabanov, Endocytosis of nanomedicines, J Control Release 145(3) (2010) 182-95.

[369] N.D. Donahue, H. Acar, S. Wilhelm, Concepts of nanoparticle cellular uptake, intracellular trafficking, and kinetics in nanomedicine, Adv Drug Deliv Rev 143 (2019) 68-96.

[370] A. Hervault, N.T.K. Thanh, Magnetic nanoparticle-based therapeutic agents for thermo-chemotherapy treatment of cancer, J Nanoscale 6(20) (2014) 11553-11573.

[371] M.L. Tebaldi, C.M. Oda, L.O. Monteiro, A.L. de Barros, C.J. Santos, D.C.F. Soares, Biomedical nanoparticle carriers with combined thermal and magnetic response: Current preclinical investigations, Journal of Magnetism Magnetic Materials
461 (2018) 116-127.

[372] K. Li, H. Nejadnik, H.E. Daldrup-Link, Next-generation superparamagnetic iron oxide nanoparticles for cancer theranostics, Drug discovery today 22(9) (2017) 1421-1429.

[373] M.O. Ansari, M.F. Ahmad, G. Shadab, H.R. Siddique, Technology, Superparamagnetic iron oxide nanoparticles based cancer theranostics: A double edge sword to fight against cancer, Journal of Drug Delivery Science and Technology 45 (2018) 177-183.

[374] Z. Hedayatnasab, F. Abnisa, W.M.A.W. Daud, Review on magnetic nanoparticles for magnetic nanofluid hyperthermia application, J Materials Design 123 (2017) 174-196.

[375] E. Cazares-Cortes, S. Cabana, C. Boitard, E. Nehlig, N. Griffete, J. Fresnais, C. Wilhelm, A. Abou-Hassan, C. Ménager, Recent insights in magnetic hyperthermia: From the “hot-spot” effect for local delivery to combined magneto-photo-thermia using magneto-plasmonic hybrids, Advanced drug delivery reviews 138 (2019) 233-246.

[376] D. Chang, M. Lim, J.A. Goos, R. Qiao, Y.Y. Ng, F.M. Mansfeld, M. Jackson, T.P. Davis, M. Kavallaris, Biologically targeted magnetic hyperthermia: potential and limitations, Frontiers in pharmacology 9 (2018) 831.

[377] C.S. Kumar, F. Mohammad, Magnetic nanomaterials for hyperthermia-based therapy and controlled drug delivery, J Advanced drug delivery reviews 63(9) (2011) 789-808.

[378] B. Kozissnik, A.C. Bohorquez, J. Dobson, C. Rinaldi, Magnetic fluid hyperthermia: advances, challenges, and opportunity, J International Journal of Hyperthermia 29(8) (2013) 706-714.

[379] E.A. Perigo, G. Hemery, O. Sandre, D. Ortega, E. Garaio, F. Plazaola, F.J. Teran, Fundamentals and advances in magnetic hyperthermia, Applied Physics Reviews 2(4) (2015) 041302.

[380] M. Gonzalez-Fernandez, T. Torres, M. Andrés-Vergés, R. Costo, P. De la Presa, C. Serna, M. Morales, C. Marquina, M. Ibarra, G.J.J.o.S.S.C. Goya, Magnetic nanoparticles for power absorption: Optimizing size, shape and magnetic properties, 182(10) (2009) 2779-2784.

[381] B. Mehdaoui, A. Meffre, J. Carrey, S. Lachaize, L.M. Lacroix, M. Gougeon, B. Chaudret, M. Respaud, Optimal size of nanoparticles for magnetic hyperthermia: a combined theoretical and experimental study, Advanced Functional Materials 21(23) (2011) 4573-4581.

[382] D. Ramimoghadam, S. Bagheri, S.B. Abd Hamid, Stable monodisperse nanomagnetic colloidal suspensions: an overview, J Colloids Surfaces B: Biointerfaces 133 (2015) 388-411.

[383] S. Rana, N.G. Shetake, K. Barick, B. Pandey, H. Salunke, P. Hassan, Folic acid conjugated Fe 3 O 4 magnetic nanoparticles for targeted delivery of doxorubicin, Dalton Transactions 45(43) (2016) 17401-17408.

[384] S. Moraes, A. Marinho, S. Lima, A. Granja, J. Araújo, S. Reis, C. Sousa, C. Nunes, Targeted nanostructured lipid carriers for doxorubicin oral delivery, International Journal of Pharmaceutics 592 (2021) 120029.

[385] Á. de Jesús Ruíz-Baltazar, S.Y. Reyes-López, R. Pérez, Magnetic structures synthesized by controlled oxidative etching: Structural characterization and magnetic behavior, Results in physics 7 (2017) 1828-1832.

[386] B.D. Cullity, Answers to problems: elements of X-ray diffraction, Addison-Wesley Publishing Company1978.

[387] E.T. Maggio, Polysorbates, peroxides, protein aggregation, and immunogenicity–a growing concern, J Journal of Excipients Food Chemicals
3(2) (2016) 1108.

[388] B.D. Cullity, C.D. Graham, Introduction to magnetic materials, John Wiley & Sons2011.

[389] M. Osial, P. Rybicka, M. Pękała, G. Cichowicz, M.K. Cyrański, P. Krysiński, Easy synthesis and characterization of holmium-doped SPIONs, J Nanomaterials 8(6) (2018) 430.

[390] R.D. Piazza, W.R. Viali, C.C. Dos Santos, E.S. Nunes, R.F.C. Marques, P.C. Morais, S.W. Da Silva, J.A.H. Coaquira, M. Jafelicci, PEGlatyon-SPION surface functionalization with folic acid for magnetic hyperthermia applications, J Materials Research Express 7(1) (2020) 015078.

[391] R.R. Shah, T.P. Davis, A.L. Glover, D.E. Nikles, C.S. Brazel, Impact of magnetic field parameters and iron oxide nanoparticle properties on heat generation for use in magnetic hyperthermia, Journal of Magnetism and Magnetic Materials 387 (2015) 96-106.

[392] S. Stafford, R. Serrano Garcia, Y.K. Gun'ko, Multimodal Magnetic-Plasmonic Nanoparticles for Biomedical Applications, 8(1) (2018) 97.

[393] A. Espinosa, J. Kolosnjaj-Tabi, A. Abou-Hassan, A. Plan Sangnier, A. Curcio, A.K. Silva, R. Di Corato, S. Neveu, T. Pellegrino, L.M. Liz-Marzán, Magnetic (hyper) thermia or photothermia? Progressive comparison of iron oxide and gold nanoparticles heating in water, in cells, and in vivo, J Advanced Functional Materials 28(37) (2018) 1803660.

[394] K.Y. Guslienko, V. Novosad, Y. Otani, H. Shima, K. Fukamichi, Field evolution of magnetic vortex state in ferromagnetic disks, J Applied Physics Letters 78(24) (2001) 3848-3850.

[395] V. Novosad, K.Y. Guslienko, H. Shima, Y. Otani, S. Kim, K. Fukamichi, N. Kikuchi, O. Kitakami, Y. Shimada, Effect of interdot magnetostatic interaction on magnetization reversal in circular dot arrays, J Physical Review B 65(6) (2002) 060402.

[396] J. Neal, H. Roberts, M. Connolly, S. Crampin, S. Bending, G. Wastlbauer, J. Bland, Magnetisation reversal in epitaxial Fe (1 0 0) disks studied by high resolution scanning Hall probe microscopy, J Ultramicroscopy 106(7) (2006) 614-619.

[397] H. Xiang, D. Jiang, J. Yao, Y. Zheng, W. Lu, G. Li, H. Saito, S. Ishio, X. Tan, Y. Lin, Micromagnetic simulations of magnetization reversal of iron nanowire, Journal of Physics: Conference Series, IOP Publishing, 2011, p. 012022.

[398] X. Qin, C. Deng, Y. Liu, X. Meng, J. Zhang, F. Wang, X. Xu, Magnetization reversal of high aspect ratio iron nanowires grown by electrodeposition, J IEEE transactions on magnetics 48(11) (2012) 3136-3139.

[399] R. Bardhan, S. Lal, A. Joshi, N.J. Halas, Theranostic nanoshells: from probe design to imaging and treatment of cancer, Accounts of chemical research 44(10) (2011) 936-946.

[400] A. Espinosa, M. Bugnet, G. Radtke, S. Neveu, G.A. Botton, C. Wilhelm, A. Abou-Hassan, Can magneto-plasmonic nanohybrids efficiently combine photothermia with magnetic hyperthermia?, J Nanoscale 7(45) (2015) 18872-18877.

[401] H. Jans, Q. Huo, Gold nanoparticle-enabled biological and chemical detection and analysis, J Chemical Society Reviews 41(7) (2012) 2849-2866.

[402] L. Peixoto, Magnetic nanostructures for biotechnological applications, Engenharia Física, Porto University, 2018.

[403] J. Chen, Z. Ye, F. Yang, Y. Yin, Plasmonic Nanostructures for Photothermal Conversion, J Small Science 1(2) (2021) 2000055.

[404] M. Iizumi, T. Koetzle, G. Shirane, S. Chikazumi, M. Matsui, S. Todo, Structure of magnetite (Fe3O4) below the Verwey transition temperature, J Acta Crystallographica Section B: Structural Crystallography Crystal Chemistry
38(8) (1982) 2121-2133.